Cape Peninsula
University of Technology

A MULTI-OBJECTIVE OPTIMISATION APPROACH FOR SMALL-SCALE STANDING WAVE THERMOACOUSTIC COOLERS DESIGN

by

LAGOUGE TARTIBU KWANDA

Thesis submitted in fulfilment of the requirements for the degree

Doctor of Technology: Mechanical Engineering

in the Faculty of Engineering

at the Cape Peninsula University of Technology

Supervisor: Prof Bohua Sun
Co-supervisor: Prof Modify Andrew Elton Kaunda

Bellville
June 2014

DECLARATION

I, Lagouge Tartibu Kwanda, declare that the contents of this thesis represent my own unaided work, and that this thesis has not previously been submitted for academic examination towards any qualification. Furthermore, it represents my own opinions and not necessarily those of the Cape Peninsula University of Technology.

Lagouge Tartibu **22/06/2014**

Signed **Date**

ABSTRACT

Thermoacoustic heat engines provide a practical solution to the problem of heat management where heat can be pumped or spot cooling can be induced. This is new among emerging technology with a strong potential towards the development of sustainable and renewable energy systems by utilising solar energy or wasted heat. The most inhibiting characteristic of current thermoacoustic cooling devices is the lack of efficiency. Although simple to fabricate, the designing of thermoacoustic coolers involves significant technical challenges. The stack has been identified as the heart of the device where the heat transfer takes place. Improving its performance will make thermoacoustic technology more attractive. Existing efforts have not taken thermal losses to the surroundings into account in the derivation of the models. Although thermal losses can be neglected for large-scale applications, these losses need to be adequately covered for small-scale applications.

This work explores the use of a multi-objective optimisation approach to model and to optimise the performance of a simple thermoacoustic engine. This study aims to optimise its geometrical parameters—namely the stack length, the stack height, the stack position, the number of channels and the plate spacing—involved in designing thermoacoustic engines. System parameters and constraints that capture the underlying thermoacoustic dynamics have been used to define the models. Acoustic work, viscous loss, conductive heat loss, convective heat loss and radiative heat loss have been used to measure the performance of the thermoacoustic engine. The optimisation task is formulated as a five-criterion mixed-integer nonlinear programming problem. Since we optimise multiple objectives simultaneously, each objective component has been given a weighting factor to provide appropriate user-defined emphasis. A practical example is provided to illustrate the approach. We have determined a design statement of a stack describing how the design would change if emphasis is placed on one objective in particular. We also considered optimisation of multiple objective components simultaneously and identified global optimal solutions describing the stack geometry using the augmented ε-constraint method. This approach has been implemented in GAMS (General Algebraic Modelling System).

In addition, this work develops a novel mathematical programming model to optimise the performance of a simple thermoacoustic refrigerator. This study aims to optimise its geometrical parameters—namely the stack position, the stack length, the blockage ratio and the plate spacing—involved in designing thermoacoustic refrigerators. System parameters and constraints that capture the underlying thermoacoustic dynamics have been used to define the models. The cooling load, the coefficient of performance and the acoustic power loss have been used to measure the performance of the device. The optimisation task is formulated as a three-criterion nonlinear programming problem with discontinuous

derivatives (DNLPs). Since we optimise multiple objectives simultaneously, each objective component has been given a weighting factor to provide appropriate user-defined emphasis. A practical example is provided to illustrate the approach. We have determined a design statement of a stack describing how the geometrical parameters described would change if emphasis is placed on one objective in particular. We also considered optimisation of multiple objective components simultaneously and identified global optimal solutions describing the stack geometry using a lexicographic multi-objective optimisation scheme. The unique feature of the present mathematical programming approach is to compute the stack geometrical parameters describing thermoacoustic refrigerators for maximum cooling or maximum coefficient of performance.

The present study highlights the importance of thermal losses in the modelling of small-scale thermoacoustic engines using a multi-objective approach. The proposed modelling approach for thermoacoustic engines provides a fast estimate of the geometry and position of the stack for maximum performance of the device. The use of a lexicographic method introduced in this study improves the modelling and the computation of optimal solutions and avoids subjectivity in aggregation of weight to objective functions in the formulation of mathematical models. The unique characteristic of this research is the computing of all efficient non dominated Pareto optimal solutions allowing the decision maker to select the most efficient solution.

The present research experimentally examines the influence of the stack geometry and position on the performance of thermoacoustic engines and thermoacoustic refrigerators. Thirty-six different cordierite honeycomb ceramic stacks are studied in this research. The influence of the geometry and the stack position has been investigated. The temperature difference across the stack and radiated sound pressure level at steady state are considered indicators of the performance of the devices. The general trends of the proposed mathematical programming approach results show satisfactory agreement with the experiment.

One important aspect revealed by this study is that geometrical parameters are interdependent and can be treated as such when optimising the device to achieve its highest performance. The outcome of this research has direct application in the search for efficient stack configurations of small-scale thermoacoustic devices for electronics cooling.

ACKNOWLEDGEMENTS

First and foremost, I wish to express my gratitude to both my supervisor and co-supervisor, Prof. Bohua Sun and Prof. Modify Andrew Elton Kaunda, for giving me the freedom and the encouragement to pursue my own ideas and to manage my own research. Their support has contributed to my academic development, in particular my confidence in undertaking independent and rigorous research. With their skilled supervision and inspirational advice, my doctoral research has been an enjoyable experience. In addition, their wisdom made it easier for me to accomplish my work, despite difficult circumstances throughout the study. I look forward to future opportunities to interact with them on projects and papers.

Moreover, I wish to express my warm thanks and appreciation to the most helpful people at Mangosuthu University of Technology (MUT) and Cape Peninsula University of Technology (CPUT) during my studies: my HOD, Prof. Ewa Zawilska; Research Director, Dr Mienie; Research Coordinator, Sfiso Qwabe; HR Development Officer, Mrs Smangele Gumede; CPUT BTech Coordinator, Fareed Ismail; BTech graduates, Welcome Mawisile Mdabula and Maria Antonio; my colleagues in both CPUT and MUT department of Mechanical Engineering; all my friends from the Congolese Engineers community of Cape Town; all my family members; and every single person who had either direct or indirect contact with me during my studies and who had a positive influence on my progress and outcomes.

Special Thanks to Dr Laura Budler for proofreading and editing my thesis and thereby significantly improved its readability. In addition, i would also like to express my gratitude to my thesis external examiners Prof. Sarp Adali (University of Kwazulu Natal), Prof. Feng Liu (University of California) and Prof. Ya-Pu Zhao (Chinese Academy of Sciences) for their thoughtful and detailed comments.

Financial support from Mangosuthu University of Technology and the Department of Mechanical Engineering of Cape Peninsula University of Technology is acknowledged and sincerely appreciated.

Last, but not least, in acknowledgement to God, my only statement is “Ebenezer”.

DEDICATION

This thesis is dedicated to my entire Family, particularly:

My wife: Myra *TARTIBU*

My parents: Jean-Louis *TARTIBU NYEMBO,* and Georgette Ngala Tshoba

My brothers: Willy, Herve, Nel, Tony and Joseph *TARTIBU*

My sisters: Lysette, Linda, Laeticia *TARTIBU*

My father and mother in-laws: Charles and Olga *NZABA*

My brother and sister in-laws: Olivier Bomolo, Jerry Kilumbu and Nicole *TARTIBU*

My nephew and nieces: Oredi, Olivia, Odavia and Othiniela Bomolo.

My uncle and aunt: Francois and Vicky Asani.

Last, but not least, my sweet daughter: Anais *TARTIBU*

*A*nd my handsome son: Yanis *TARTIBU*

for their endless love, support and encouragement

TABLE OF CONTENTS

LIST OF FIGURES

LIST OF TABLES

NOMENCLATURE

Symbol	Parameter	Units
A	Total cross-sectional area	[m^2]
BR	Blockage ratio	
c or a	Speed of sound	[m/s]
c_p	Isobaric specific heat	[J/kgK]
c_v	Isochoric specific heat	[J/kgK]
COP	Coefficient of performance of refrigerator	
COPC	Carnot coefficient of performance	
COPR	Relative coefficient of performance	
d	Diameter	[m]
dc	Channel dimension	[m]
DR	Drive ratio	
f	Frequency	[Hz]
f_k	Thermal Rott function	
f_v	Viscous Rott function	
H	Stack height	[m]
Im[]	Imaginary part of a complex variable	
j	Imaginary unit	
k	Wave number	[m^{-1}]
K	Thermal conductivity	[W/m K]
k_B	Boltzmann constant	
l	Plate half thickness	[m]
L or L_S	Stack length	[m]
L_p	Sound pressure level	[dB]
L_{Sn}	Normalised stack length	
N	Number of channels	
Nu	Nusselt number	

p	Pressure	[Pa]
p_m	Mean pressure	[Pa]
p_1,p_0	Fluctuating pressure amplitude	[Pa]
Pr	Prandtl number	
Q	Heat flux	[W]
Ra	Rayleigh number	
Re[]	Real part of complex variable	
S	Entropy	
T	Temperature	[K]
T_C	Cold end temperature	[K]
T_H	Hot end temperature	[K]
T_m	Mean temperature	[K]
u	Velocity	[m/s]
U	Internal energy	[J]
x	Axial distance	[m]
X_S	Stack centre position	[m]
X_{Sn}	Normalised stack position	
w	Objective function component weight	
W	Acoustic work	[W]
y_o	Plate half-gap	[m]
Za	Stack position	[m]

Greek symbols

α	Thermal diffusion rate	[m^2/s]
β	Thermal expansion coefficient	[K^{-1}]
δ_k	Gas thermal penetration depth	[m]
δ_{kn}	Normalised thermal penetration depth	
δ_v	Viscous penetration depth	[m]
δ_s	Solid thermal penetration depth	[m]

ε	Surface emissivity	
γ	Isentropic coefficient	
Γ	Temperature gradient ratio	
λ	Wavelength	[m]
μ	Dynamic viscosity	[kg/m s]
ω	Angular frequency	[rad/s]
ρ	Density	[kg/m^3]
σ	Prandtl number	
Π	Perimeter	[m]
∇T	Temperature gradient	[K/m]
θ	Normalised temperature difference	
η	Efficiency	

CHAPTER 1: INTRODUCTION

1.1 Background

The market for small-scale electronic devices, including smartphones, mobile phones and tablets, is growing rapidly and is expected to increase further thanks to immense customer demand. Research conducted by Gartner, Inc. (2014) has reported, “Worldwide mobile communication device sales to end users totalled 1.8 billion units in 2013, an increase of 3.5% from 2012.” In particular, the International Data Corporation (IDC) forecasts global smartphone sales of 1,925.9 million units for 2014, reaching 2,227.5 million units in 2018 (IDC Corporate, 2014). Further, Gartner predicts Worldwide combined shipments of devices—PCs, tablets, ultra mobiles and mobile phones—will reach a total 2.5 billion units in 2014, a 7.6% increase from 2013 (IDC Worldwide Mobile Phone Tracker, 2014).

Customers’ various needs and high expectations have engendered tremendous improvement in both hardware and software for these handheld devices. The power consumption of most of these handheld devices is currently lower than 3W, with a junction temperature of 115^{o}C. Using heat spreaders as a passive cooling method, it is possible to maintain the devices at temperatures below the junction temperature. The anticipated doubling of power consumption levels will require more effective thermal management and more aggressive approaches to improve cooling performance and to prevent malfunctions. However, due to constraints in the volume and power consumption, the thermal management of these devices has been particularly challenging.

Thermal management has always been a concern for computer systems and other electronics. Computational speeds will always be limited by the amount of noise produced by computer chips. Since most noise is generated by wasted heat, computer components and other semiconductor devices operate faster and more efficiently at lower temperatures (Yuan & Jung, 1999). The need to manage heat fluxes of orders 10–50 W/cm^2 and higher in microcircuits has emphasised the importance of developing devices which can cope with such heat levels. Many interesting devices have been proposed for such applications, ranging from forced convection cooling devices to thermoelectric devices, heat pipes, liquid coolants, and evaporative spray cooling devices (Joshi & Garimella, 2003).

Here, thermoacoustic devices are proposed (Figure 1.1); such engines can convert heat to sound or use sound to pump heat. They represent a new application in the area of thermal management, but based on their performance and adaptability to microcircuits, they show significant promise (Abdel-Rahman *et al.,* 2003; Tsai *et al*., 2002). If thermoacoustic cooling

devices could be scaled down for computer applications, the electronic industry would realise longer lifetimes for microchips, increased speed and capacity for telecommunications, as well as reduced energy costs (Garrett *et al*., 1993).

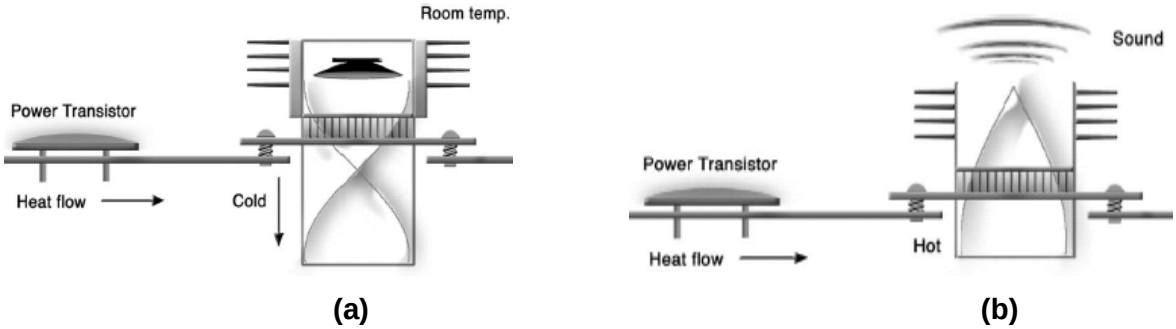

Figure 1.1: (a) Acoustic spot-cooler interfaced with circuit (b) Prime mover interfaced with circuit

(Adapted from Symko et al., 2004)

Thermoacoustics combines the branches of acoustics and thermodynamics together to move heat by using sound. While acoustics is primarily concerned with the macroscopic effects of sound transfer, like coupled pressure and motion oscillations, thermoacoustics focuses on the microscopic temperature oscillations that accompany these pressure changes. Thermoacoustics takes advantage of these pressure oscillations to move heat on a macroscopic level. This results in a large temperature difference between the hot and cold sides of the device and causes refrigeration (Swift, 1988).

Thermoacoustic refrigerators can be classified based on the source of acoustic energy input. If the acoustic energy is provided by an acoustic driver (e.g. a loudspeaker), it is termed as an ‘acoustically-driven thermoacoustic refrigerator’ or ‘thermoacoustic refrigerator’ (TAR).

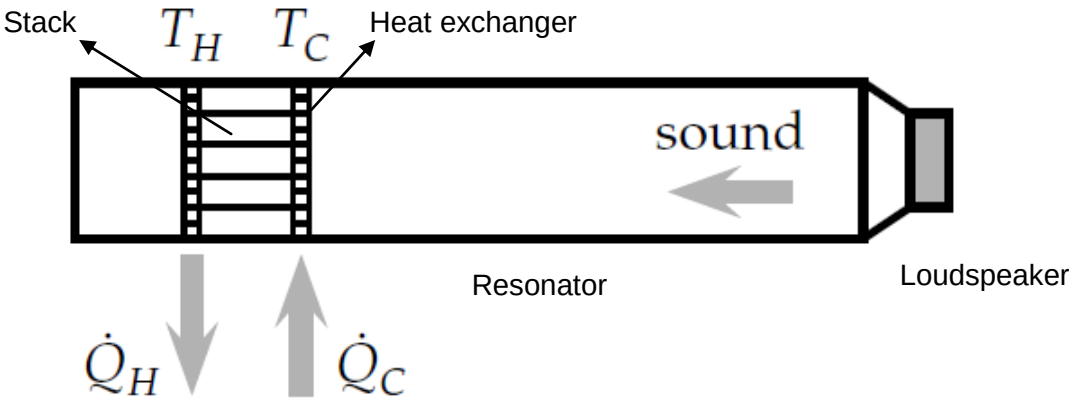

Figure 1.2: Acoustically driven thermoacoustic refrigerator

Alternatively, if the acoustic energy is provided by the thermoacoustic engine (TAE), the refrigerator is called a 'thermoacoustically-driven thermoacoustic refrigerator' (TADTAR). During the past decades, several acoustically-driven thermoacoustic refrigerators have been developed (Garrett *et al*., 1993; Tijani *et al.,* 2002). Recently, there has been an increased interest in the development of thermoacoustically-driven thermoacoustic refrigerators. These devices are built by coupling a thermoacoustic refrigerator to a thermoacoustic engine. Thermoacoustic engines are capable of producing acoustic energy from any source of heat energy. Thus, the primary energy source to drive the refrigerator could be conventional or unconventional, including industrial waste heat, solar energy and fossil fuels.

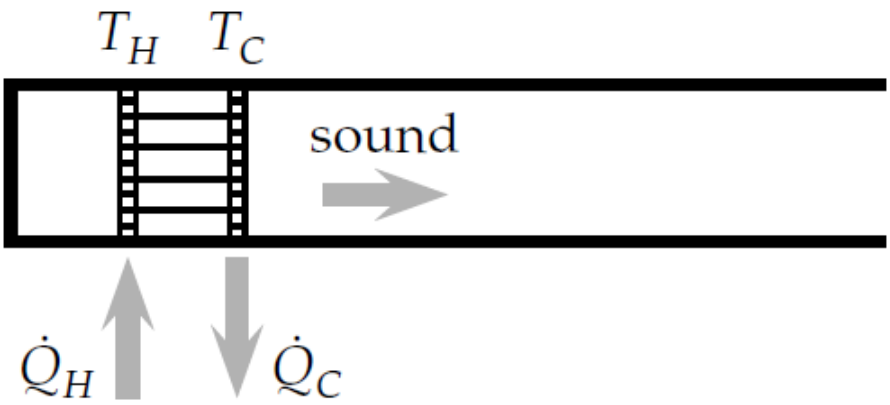

Figure 1.3: Thermoacoustic engine or prime mover

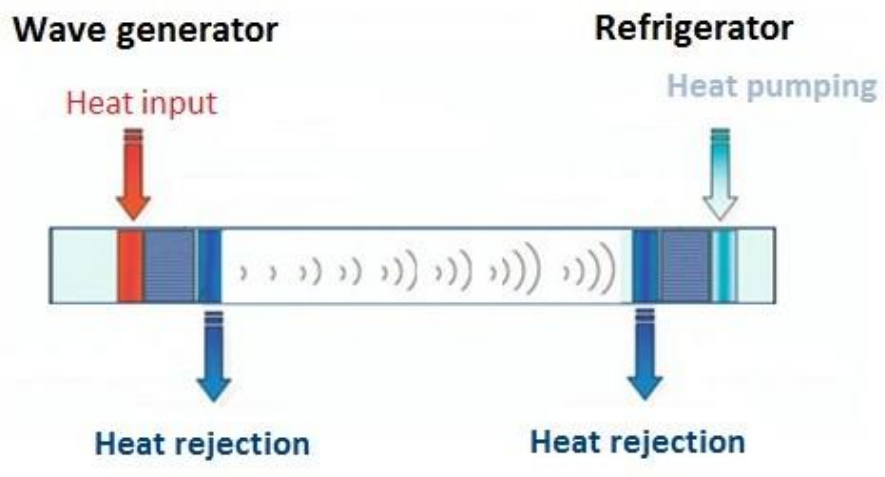

Figure 1.4: Thermoacoustically-driven thermoacoustic refrigerator

Merkli and Thomann were the first to show that sound in a resonant tube produces cooling (Merkli & Thomann, 1975). Wheatley *et al.* (1983) built the first acoustic refrigerator and demonstrated its potentials: the acoustic frequency was around 500 Hz. This was followed by a variety of large scale devices (Garrett & Hofler, 1992). The presence of a stack provides heat exchange with the sound field and the generation or absorption of acoustic power. With a suitable geometry, substantial amounts of heat can be moved, as demonstrated for example by Garrett and Hofler (1991). An interesting and important feature of such engines is that the performance depends on geometric factors and gas parameters, but is independent of the device temperature (Swift, 1995).

Scaling down thermoacoustic systems is challenging due to an increased role of thermoviscous losses, thermal management and fabrication issues and difficulty in integrating with heat sources. There have been several attempts aimed at developing miniature thermoacoustic engines. The construction and performance of a relatively small 14 cm tube was documented by Hofler and Adeff (2001). Much smaller systems, down to a few centimeters in length, were also built by Symko *et al.* (2004), but their design was not reported in detail sufficient for reproduction. However, one common trait of these small-scale devices is that their efficiency, which depends on geometrical factors, is an appreciable fraction of Carnot. Working models and modeling show that power densities of several watts per cubic centimeter can be achieved by optimising the parameters and working conditions.

1.2 Motivations for research

As a result of miniaturisation, electronic products are shrinking in size and weight, but with greater pressure for cost reduction. Heat fluxes have increased considerably and hence thermal management has become critical from the reliability point of view. Thermoacoustic heat engines provide a practical solution to the problem of heat management in microcircuits where they can be used to pump heat or produce spot cooling of specific circuit elements. Such devices are relatively simple, they can be efficient, and they are readily adaptable to microcircuit interfacing. However, the most inhibiting characteristic of thermoacoustic cooling is its current lack of efficiency. In order for a thermoacoustic refrigerator or prime mover system as well as a thermoacoustic prime mover driving a thermoacoustic refrigerator to be competitive in the current market, they must be optimised to improve their overall performance.

McLaughlin (2008) has thoroughly analysed the heat transfer for a Helmholtz-like resonator, 1.91 cm in diameter and 3.28 cm in length. The loss to conduction has been estimated as

40% of the input power. The losses from convection inside and outside of the device have been estimated as 38%. Radiation accounts for 10% of the input power. This leaves only 12% of input power that can be used to produce acoustic work (Figure 1.5). Although these losses are approximations not meant to be highly accurate determinations, they suggest that these losses are significant when compared to total heat input and should be considered as design criterion. Therefore, this work aims to highlight one methodology to incorporate thermal losses in the design process.

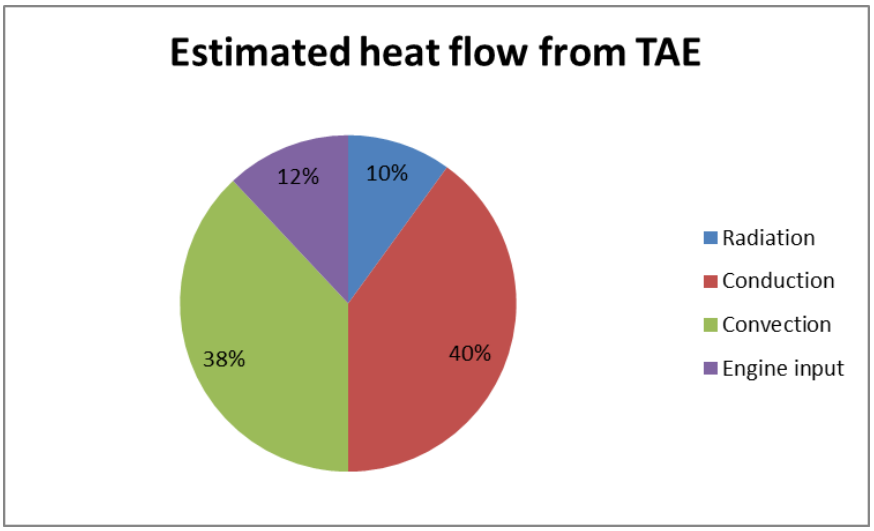

Figure 1.5: Heat flow from the power supply partitioned by the losses from radiation, conduction, convection and the power input.

(Adapted from McLaughlin, 2008)

Considering the previous optimisation efforts of Zink et al. (2009) and Trapp et al. (2011), this work illustrates the use of a new mathematical approach to incorporate thermal losses in the modelling of thermoacoustic engine. These losses have been incorporated in the modelling as objectives functions. An effort to effectively implement the Epsilon-constraint method for producing the Pareto optimal solutions of the multi-objective optimisation problem is carried out in this work. This has been implemented in the widely used modelling language GAMS (General Algebraic Modelling System, www.gams.com). As a result, GAMS codes are written to define, analyse, and solve optimisation problems to generate sets of Pareto optimal solutions unlike in previous studies.

Considering a simple thermoacoustic refrigerator, comprised of a stack inside of a resonance tube, the energy flows are obvious. Acoustic work (sound) can be used to generate temperature differences that allow heat to move from a low temperature reservoir to an ambient at higher temperature, thus forming a thermoacoustic refrigeration system.

Therefore, the goal of the optimisation is to achieve the highest performance for a particular configuration and set of operating conditions. Interestingly, Herman and Travnicek (2006) found that sets of parameters leading to two seemingly similar outcomes, maximum efficiency and maximum cooling were not the same. Therefore, they have considered two optimisation criteria in the design optimisation of thermoacoustic refrigerators. For a particular set of operating conditions and system configuration, one goal is to achieve the highest COP. This criteria is useful when designing large thermoacoustic systems or comparing the performance of refrigeration systems. For small-scale thermoacoustic systems, the cooling load was found to be critical for the success of the design (Herman & Travnicek, 2006). This work is undoubtedly a valuable addition to the thermoacoustic community. However, this optimisations effort relies heavily on studying the effect of a single design parameter on device performance. In all likelihood, each optimal design is a local optimum as the optimisation performed considers one variable while all else are fixed. In this work, we propose a novel mathematical programming approach to handling design and choice between maximum cooling and maximum coefficient of performance of thermoacoustic refrigerators. Additionally, we have identified the blockage ratio, the stack spacing, the stack length and the position of the stack as design parameters and have taken their interdependency into account while computing the optimal set of design parameters describing optimal performance of TARs, a perspective lacking in previous studies.

1.3 Objectives of the research

The purpose of the stack is to provide a medium where the walls are close enough so that each time a parcel of gas moves, the temperature differential is transferred to the wall of the stack. Their geometry and position are crucial for the performance of the device. With regards to miniaturization, performance inefficiencies arise from heat transfer problems and viscous losses within a viscous penetration depth (δ_v) from stack plates and from resonator walls (Abdel-Rahman *et al.,* 2002). Stack resistance to sound waves causes intensity attenuation and introduces nonlinearities (Kuntz & Blackstock, 1987).

The efficiency of thermoacoustic engines and refrigerators depend critically on stack properties. This component of an engine or refrigerator is where the energy conversion of heat into sound or the pumping of heat by a sound wave takes place. The most common stack geometries encountered in practical devices have a constant cross-section along the direction of the flow (e.g. parallel plates, narrow tubes, spiral mimicking parallel plates). This work focuses on parallel plates and square pores (Figure 1.6).

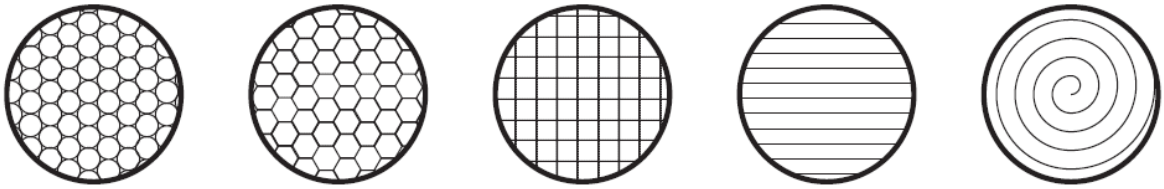

Figure 1.6: Schematic picture of thermoacoustic stack geometries.

The primary objectives of the present research are as follows:

- developing a new optimisation scheme combining acoustic work, viscous resistance and thermal losses as objective functions in small-scale thermoacoustic engine design; and
- developing a new optimisation scheme to clarify the design choice between maximum cooling and maximum coefficient of performance of thermoacoustic refrigerators for applications to electronics cooling.

Specific sub-objectives are as follows:

- providing guidance on the computation of optimal solutions describing the geometry of the stack;
- providing guidance to the decision maker on the choice of optimal geometry of thermoacoustic devices;
- analysing the influence of stack geometry on the performance of thermoacoustic engines; and
- analysing the influence of stack geometry on the performance of thermoacoustic refrigerators.

1.4 Solution approach

As outlined previously, this work aims to investigate thermoacoustics in three areas:

- incorporating losses in new modelling approaches;
- using mathematical analysis and optimisation to model small-scale thermoacoustic devices; and
- computing optimal geometrical parameters describing the stack.

The use of a parametric approach to model thermoacoustic devices and the lack of inclusion of thermal losses in the modelling that occurs during operation is a large obstacle that can hinder progress for improving the performance of small-scale devices. Thus, this work can be divided into the following parts:

- a development of a new mathematical approach to model thermoacoustic devices;
- a detailed case study on the design and optimisation of a small-scale stack of a thermoacoustic engine;
- a detailed case study on the design and optimisation of a small-scale stack of a thermoacoustic refrigerator; and
- an experimental analysis to investigate the influence of the geometrical parameters on the performance of thermoacoustic devices.

These main goals will be targeted as follows:

- First, a new mathematical programming approach is proposed in this current study. The methods used to formulate and solve the problem are presented in detail. We have implemented the mathematical equations describing the models proposed in the software GAMS. The development of mathematical programming models for thermoacoustic devices is in itself a significant contribution to the field of thermoacoustics.
- Next, in order to justify the inclusion of thermal losses in the design of small-scale thermoacoustic engines, a case study is used to model the device. A multi-objective optimisation approach is implemented to calculate Pareto optimal solutions describing the geometry of the device. The magnitude of thermal losses will be estimated.
- In order to clarify the design choice between maximum cooling and maximum efficiency of TAR, a multi-objective optimisation approach is implemented in GAMS to calculate Pareto optimal solutions. Through this means, it is possible to illustrate the difference of the choice between the design for maximum cooling and for maximum coefficient of performance. The presented effort should lead to the utilisation of mathematical analysis and optimisation for future modelling of small-scale refrigerators.
- Finally, the findings from optimisation investigations have been tested experimentally to evaluate the influence of the geometry of the stacks on the performance of the devices.

1.5 Major contributions of the thesis

Figure 1.7 illustrates the major contributions of this present research. The stack element of thermoacoustic devices is the predominant focus of the current study. The primary objective of the present research is to develop a new mathematical programming approach for the modelling and optimisation of TAR and TAE. An ε-constraint method, combined with a lexicographic method, is used to formulate and solve the models. These models considered

thermal losses for TAE and have applications in TAR design for electronics cooling. Physical parameters describing the devices are treated as non-independents to identify the global optimal solution corresponding to the highest performance of the devices. Experiments in the present study are performed on cordierite honeycomb stacks to evaluate the influence of the geometry and the stack position on the performance of the device and to verify the validity of the models. These issues are absent from the current literature and thus are significant contributions of this current research.

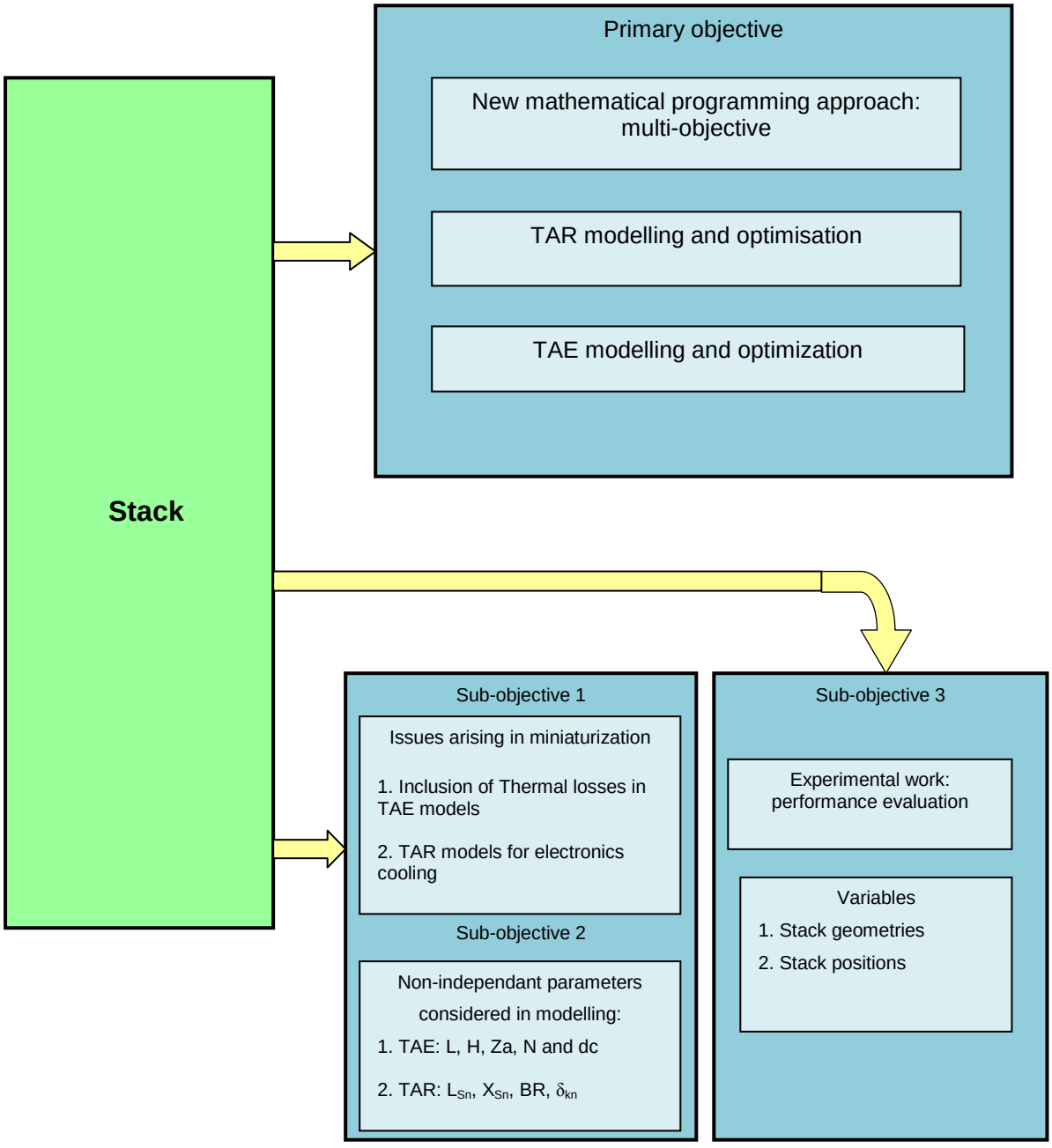

Figure 1.7: Pictorial representation of the major contributions of the present study.

1.6 Outline of Thesis

The thesis consists of seven chapters and 22 appendices.

Chapter 1 presents a brief description of the background of this thesis, the motivations for research, the objectives of the current study and the proposed approach to the solution.

Chapter 2 defines basics concepts of thermoacoustics, a description of successful applications of the approach as well as issues of optimisation in thermoacoustics, is presented.

Chapter 3 reviews the background of thermoacoustics and the principle of thermoacoustic theory. Governing equations and model development are presented.

Chapter 4 is dedicated to the thermoacoustic modelling development. The fundamental components of the mathematical model characterising the standing wave thermoacoustic engine are presented. This chapter includes equations involved in the models proposed in this study.

Chapter 5 gives a detailed description of the proposed new mathematical approach. Two different case studies are examined related to the proposed approach for the modelling and optimisation of thermoacoustic engines and refrigerators. Results obtained are discussed.

Chapter 6 is dedicated to the experimental set-up along with the measurements on simple thermoacoustic engines and thermoacoustic refrigerators. This chapter primarily investigates the effect of the geometry and the stack position on the performance of the devices. Results obtained are discussed.

Chapter 7, finally, presents conclusions and recommendations for future work.

CHAPTER 2: LITERATURE REVIEW

2.1 Thermoacoustics

The interaction between heat and sound has interested acousticians since 1816 when Newton's earlier calculation of the speed of sound in air was corrected by Laplace. Just as a temperature difference creates sound, sound produces a temperature difference: cool at one side and hot at the other side. In thermoacoustic engines (TAEs), the pistons of ordinary Stirling engines are replaced by the sound waves maintained in the resonator for compression and expansion. The displacement of the working gas is caused by the velocity component of the sound waves so that the gas is transported from the hot heat exchanger to the cold heat exchanger. Equation 2.1 is an illustration (for ideal gas) of the isentropic relationship between a temperature change and the pressure change,

$$\left(\frac{T_1}{T_2}\right)=\left(\frac{p_1}{p_2}\right)^{\frac{\gamma-1}{\gamma}} \qquad \textbf{Equation 2.1}$$

where γ represents the ratio of the specific heat capacity at constant pressure and constant volume. This change in temperature occurs in all pressure waves. To illustrate this, we can consider the following example: in ordinary conversation, the sound pressure level (SPL) can be approximated as 70 decibels (or dB). The associated pressure change can be evaluated to 0.06 Pa using Equation 2.2. The resulting temperature difference is a mere ten thousandth of a degree Celsius.

$$SPL = 20\log\left(\frac{p_{rms}}{20\mu Pa}\right) \qquad \textbf{Equation 2.2}$$

Most refrigerators and air conditioners pump heat over a temperature range of 20 degrees and more, so the temperature swings created by sound waves are too small to be useful. Therefore, a solid material with generally higher heat capacity per unit volume than gasses is introduced in the vicinity of the sound wave to handle larger temperature spans. With respect to the length of the plate, the displacement of one fluid parcel is usually small. Thus, an entire train of adjacent fluid parcels, each confined to a short region of length $2x_1$, transfer the heat as in a bucket brigade. Although a heat δQ is transported by a single parcel over a very small interval, δQ is shuttled along the entire plate, as illustrated in Figure 2.1, because there are many parcels in a series.

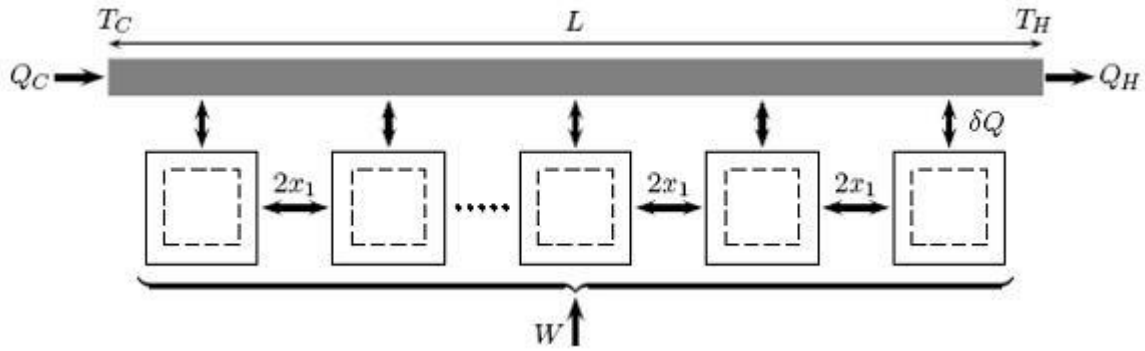

Figure 2.1: Heat and work flow inside a thermoacoustic refrigerator.

As heat is shuttled along the stack plate from one parcel of gas to the next, oscillating fluid parcels work as a bucket brigade. As a result, heat is pumped from the left to the right using acoustic work W. Inside a thermoacoustic engine or prime mover, the arrows will be reversed. The heat will be pumped, or transported, from the right to the left and acoustic work is produced.

The net amplification of pressure amplitude for driving thermoacoustic effect is possible in the following conditions:

- if there is a temperature change within the gas; and
- if the temperature gradient of the wall is sufficiently large relative to the gas displacement (Swift, 2002).

For amplification to occurs, the temperature gradient of the walls has to equal the 'critical temperature gradient' given by Equation 2.3:

$$\nabla T_{crit} = \left(\frac{\omega p_1^s}{\rho_m c_p u_1^s} \right) \qquad \textbf{Equation 2.3}$$

where ω represents the operating frequency; p_1^s and u_1^s are respectively the first order pressure and velocity of the standing wave; and c_p and ρ_m are respectively the specific capacity and the mean gas density. In terms of the ratio of the temperature gradient along the stack and the critical temperature gradient, there are two modes of operation characterising thermoacoustic effect:

- when the temperature gradient over the stack is smaller than the critical temperature gradient, or $\Gamma = \frac{\nabla T_m}{(\nabla T)_{crit}} < 1$, the device operates as a refrigerator as external power is needed to transport the heat;

- when the temperature gradient over the plate is larger than the temperature gradient, or $\Gamma = \frac{\nabla T_m}{(\nabla T)_{crit}} > 1$, the device operates as a prime mover as work is produced.

There are two fundamental modes of operation of thermoacoustic engines based on the phasing between the pressure and the velocity component of the acoustic wave: standing wave and traveling wave devices.

2.1.1 Standing wave engine

The main criterion to identify the type of wave excitation within the system is the phase difference between pressure wave and velocity wave. There is a phase lag of 90° between pressure and velocity waves in pure standing wave devices (Figure 2.2). Most commonly, a quarter wavelength resonator $(\lambda/4)$ is used in standing wave devices. The maximum change in pressure (at the pressure antinode) takes place at the closed end and there is zero change in pressure with respect to time (at the pressure node) at the opening. With respect to pressure, the velocity is phase shifted (between 0^oC and 90^oC) as seen in Figure 2.2. While a velocity antinode is located at the opening, a velocity node is located at the closed end. Considering the fact that the engine is driven based on pressure oscillations and requires gas displacement, it becomes obvious why the stack is to be placed next to the closed end rather than the opening. Additionally, positioning the stack closer to the velocity node than the pressure node avoids the increase of viscous losses which can disable the engine.

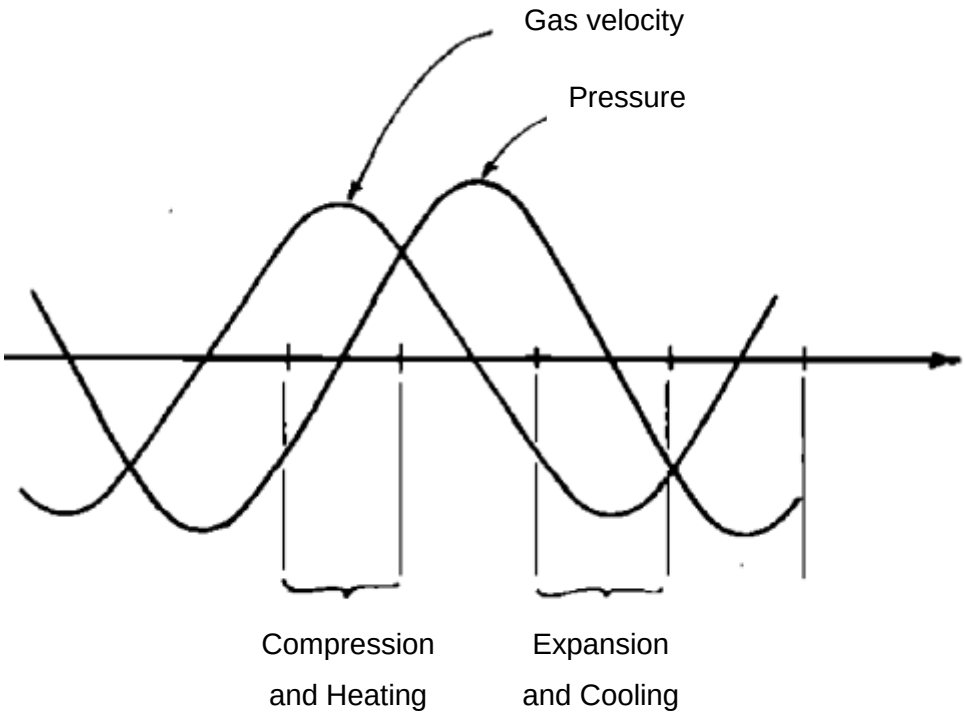

Figure 2.2: Pressure and velocity variation with time in a standing wave thermoacoustic device

(Adapted from Ceperley, 1979)

The phase difference between pressure wave and velocity wave results in a compression and displacement within the device. A delay in the heat exchange is required to heat the gas when it is most compressed and reject heat at the point of expansion. For this reason, the thermal penetration depth of the gas (defined as the length across which a sound field interacts thermally within a time of $1/\omega$) is smaller than the flow channels. According to Swift (2002), it is defined as follows:

$$\delta_k = \sqrt{\frac{2K}{\omega \rho c_p}}$$ **Equation 2.4**

where K is the thermal conductivity, and c_p and ρ are respectively the specific heat capacity and the gas density. The irreversibility of the heat transfer in addition to its artificial delay results in a poor performance of the device (Ceperley, 1979) with an efficiency of around 20% (Backhaus & Swift, 2000).

2.1.2 Traveling wave engine

As opposed to the standing wave engine, the pressure and velocity waves within a traveling wave device will essentially be in phase (Figure 2.3). Thus the gas experiences its maximum compression or expansion when it is at a peak of its displacement (zero velocity).

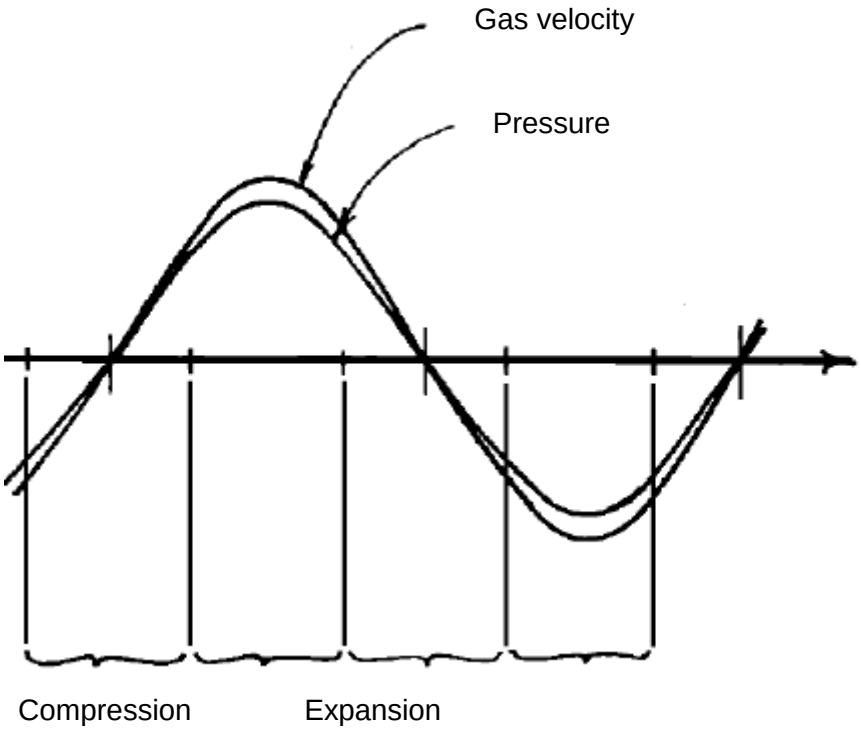

Figure 2.3: Pressure and velocity variation with time in a traveling-wave thermoacoustic device

(Adapted from Ceperley, 1979)

This change in pressure/velocity phasing is achieved by introducing a feedback inertance around the regenerator (DeBlok *et al.,* 2001; Bastyr & Keolian, 2003) or by utilising a looped compliance (Ceperley, 1982; Backhaus & Swift, 1999; Ueda *et al.,* 2003). A traveling wave design is illustrated in Figure 2.4.

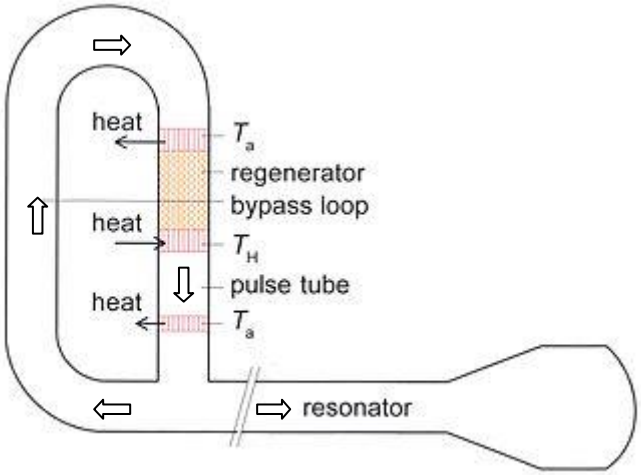

Figure 2.4: Thermoacoustic engine with looped feedback

(Arrows indicate the acoustic power flow).

Because of this more ideal pressure-velocity phasing, the regenerator in a traveling wave engine can be designed differently than the stack of a standing wave engine. The walls can be spaced much closer together, more specifically, smaller than the thermal penetration depth. This results in fewer losses and in improved heat transfer (Swift, 2002). Therefore, unlike the standing wave engine, the regenerator-based thermoacoustic engine can theoretically reach the Carnot efficiency (Poese, 2004).

2.2 Practical thermoacoustic apparatus

Los Alamos National Laboratory (LANL) developed the first practical thermoacoustic apparatus in the early eighties (Wheatly *et al.,* 1983; Hofler, 1986). Since then, thermoacoustic technology has become as a new research area of heat pumps and heat engines. Many thermoacoustic systems have been developed, mostly at LANL, Naval Postgraduate School (NPS) in Monterey, California, and at Pennsylvania State University. A detailed description of the design and construction of thermoacoustic apparatus is available in Tijani (2001) and Mahmud (2005).

Many of the attempts at LANL focused primarily on the development of large thermoacoustic engines using heat to generate sound. This sound can be used to produce electricity or to drive coolers to liquefy natural gas. An example of such an application is a thermoacoustic Stirling engine (LANL, 2004) which produces power up to 8.1 W per kilogramme and operates at an efficiency of 18%. The sound wave produced by the engine drives a piston

which moves a coil through a magnetic field and results in a current flowing through the coil. The electricity generated can be used for space. The efficiency of existing spaceship thermoelectric power converters is about 7% and produces 5.2 watts per kilogram. This thermoacoustic engine can generate electricity for space. A Stirling cooler to pump heat out of drill tip electronics to a temperature of 200^{o}C (LANL, 2010) has been developed as a result of a collaboration between LANL and Q-drive. This cooler fits into a restricted, narrow, tubular space of a drill tip and survives operation at over 250^{o}C, plus vibration of rock drilling and huge shock loads.

The Naval Postgraduate School (NPS) has built a Thermoacoustically Driven Thermoacoustic Refrigerator (TADTAR). A solar power-driven prime mover is used to generate the sound necessary to drive the refrigerator instead of a loudspeaker. A cooling power capacity of 2.5 watts corresponding to a temperature span of 17.7^{o}C has been achieved (Adeff & Hofler, 2000).

Pennsylvania State University has designed, constructed and tested a prototype thermoacoustic chiller used in Ben and Jerry's ice cream (Poese *et al.,* 2004). The prototype machine is 483 mm tall and 254 mm in diameter with a cooling capacity of 119W at a temperature of -24.6^{o}C. The overall coefficient of performance of the chiller is measured to be 19% of the Carnot coefficient of performance (COP).

Noticeable research on thermoacoustic devices, other than listed previously, is as follows:

- small-scale thermoacoustic coolers which vary in length from 40 mm down to 8 mm, operating at frequencies from 4 kHz to 25 kHz, were developed by Abdel-Rahman *et al.* (2002). The diameter varied from 6 mm to 41 mm. The 5 kHz refrigerator has achieved a COP of 1.2 and a cooling power level of 0.5-1 watts;
- a prototype of a thermoacoustic refrigerator designed and tested by Tijani (2001) with a cooling power of 4W at a temperature of -65^{o}C;
- a thermoacoustically-driven pulse tube refrigerator built and tested by Jin *et al.* (2003) reaching a cryogenic temperature lower than 120 K;
- a study on the effect of heat exchanger surface area on the performance of thermoacoustic refrigerator, conducted by Akhavanbazaz *et al.* (2007); and
- the development of small-scale prime mover which is 5.7 cm long, conducted by Junj *et al.* (2010).

From these previous examples, it is evident that thermoacoustic devices have an impressive potential number of applications. Prime movers, or loudspeakers, can be used to drive

thermoacoustic refrigerators or generate electricity. Thermoacoustic coolers offer the following advantages:

- high reliability (no tight tolerance, no moving parts);
- environmentally safe (no CFCs, using only inert gases); and
- economical and compact (interesting in space shuttles, cooling of electronics and situations where environmental concerns are critical).

The reliability of thermoacoustic coolers can be improved by replacing the source of high intensity sound wave, namely the electrodynamics loudspeaker. Significant progress has been made in developing a variety of other energy sources (e.g. solar energy and waste heat) to drive the device and provide refrigeration. Such a device is useful for providing cooling or refrigeration in locations where refrigeration would otherwise be unavailable or too expensive. Thermoacoustic coolers driven by waste heat can be used in air conditioning units of passenger cars or mobile refrigeration units for transportation of perishable goods because of the abundance of waste heat in vehicles. Therefore, there is a strong motivation to switch to thermoacoustic coolers that can provide cooling without the use of any environmentally harmful substances, with no internal moving parts, and using a low grade of energy.

Researchers in thermoacoustics are focussing on optimising the method so that thermoacoustic coolers can compete with commercial refrigerators. Four main components of thermoacoustic refrigerators are considered critical to optimisation (Figure 1.2). These four vital components include:

- a thermoacoustic core (or stack);
- a resonance tube (or resonator);
- heat exchangers; and
- an acoustic driver.

This modular description is suitable for design purposes as it allows the designer to optimise each module separately and obtain maximum global thermodynamic performance of the thermoacoustic refrigerator as a result.

Much research seeks to optimise the geometry of thermoacoustic coolers in order to improve their performance. Special attention should be given to the stack, as the energy conversion takes place within it. This process happens in complex simultaneous oscillations of the compressible fluid parcels and the solid surface of the stack material through the boundary

layer. The resonator optimisation problem, the speaker problem and heat exchanger design are all outside the scope of this work.

2.3 Optimisation in thermoacoustics

This work will focus on thermoacoustic heat engines (TAEs) and thermoacoustic refrigerators (TARs). More specifically, the geometric optimisation of current designs will be discussed. In order to utilise the inherent benefits of thermoacoustic technology and expand its use into wider markets, miniaturization of TARs and TAEs is necessary. During TAR and TAE operation, they exhibit certain unique loss mechanisms (Zink *et al.,* 2009):

- acoustic streaming losses;
- gas streaming losses; and
- thermal losses.

The impact of the acoustic and streaming losses on miniaturization is well understood. The effect of thermal losses has been highlighted through the work of McLaughlin (2008), Zink *et al.* (2009), and Trapp *et al.* (2011). It is the goal of this particular work to expand the previous investigations and detail the incorporations of those losses in the modelling and optimisation of thermoacoustic coolers.

a. Thermoacoustic engines

Optimisation techniques as a design supplement have been under-utilised prior to Zink *et al.* (2009) and Trapp *et al.* (2011) studies. Some existing efforts include studies by Minner *et al.* (1997), Wetzel (1997), Besnoin (2001) and Tijani *et al*. (2002). A common factor of all these studies is the utilisation of a linear approach while trying to optimise the device. Additionally, most studies (the exception being the 1997 Minner *et al.* study) have been limited to parametric studies to estimate the effect of single design parameters on device performance while ignoring thermal losses to the surroundings. These parametric studies are unable to capture the nonlinear interactions inherent in thermoacoustic models with multiple variables, only guaranteeing locally optimal solutions.

Considering these optimisation efforts, Zink *et al.* (2009) and Trapp *et al.* (2011) illustrate the optimisation of thermoacoustic systems, while taking into account thermal losses to the surroundings that are typically disregarded. Zink *et al*. (2009) have targeted thermoacoustic engines as a starting point. A model has been constructed to develop an understanding of the importance of the trade-offs between the acoustic and thermal parameters. The

optimisation conducted with the Nelder-Mead Simplex method, considers four weighted objectives: 1) the conductive heat flux from the stack's outer surface, 2) the conduction through the stack, 3) acoustic work, and 4) viscous resistance). A recent study by Trapp *et al.* (2011) presented analytical solutions for cases of single objective optimisation that identify globally optimal parameter levels. Optimisation of multiple objective components—acoustic work, viscous resistance and heat fluxes—has been considered. Efficient frontiers of Pareto optimal solutions corresponding to selected weights have been generated and two profiles have been constructed to illustrate the conflicting nature of those objective components. In spite of the introductory nature of their works in respect of their plans to expand and include driven thermoacoustic refrigerators, the presented works are important contributions to thermoacoustics as they merge the theoretical optimisation approach with thermal investigation in thermoacoustics.

b. Thermoacoustic refrigerators

Various parameters affecting the performance of TARs are well understood from previous studies.

- A network model to evaluate the temperature differences across the stack was developed by Tu *et al*. (2005). The results show that the stack position, the oscillating pressure ratios and the stack geometries all affect the temperature differences.
- The optimisation of inertance sections of thermoacoustic devices using DeltaEC (Design Environment for Low-Amplitude Thermoacoustic Energy Conversion) by varying individual parameters to determine optimal designs is illustrated by Zoontjens *et al.* (2006). Their results highlight a vast array of variables that must be considered interdependent for robust device operation.
- The performance of standing wave thermoacoustic coolers to achieve the best possible COPRs (coefficient of performance compared to Carnot) for various temperature spans between the hot and cold side of the stack was evaluated by Peak *et al.* (2007) using DeltaEC. The results show that thermoacoustic cooling seems to make less sense for applications with either low or high temperature spans such as air conditioning or cryogenic cooling.
- The impact of the gas blockage with small and large thermal contact areas between stack and heat exchanges on the performance of a TAR was investigated by Akhavanbazaz *et al.* (2007), with results revealing that increasing the thermal contact area of heat exchangers reduces the cooling load and increases the acoustic power required due to the gas blockage.

- The performance of a thermoacoustic refrigeration system with respect to temperature difference, the pressure and the frequency was investigated by Nsofor *et al.* (2009). Results determined that there is an optimum pressure and an optimum frequency at which the system should be operated in order to obtain maximum cooling load.
- The relationship between cooling load and plate spacing was derived by Wu *et al.* (2009) using a constructural principle. Results showed that the plate spacing and the number of plates influence the cooling load.
- A two-dimensional numerical simulation of thermoacoustic refrigerator driven at large amplitude was conducted by Ke *et al.* (2010). Optimised parameters of plate thickness, length and plate spacing of heat exchangers have been identified.
- The effect of operation conditions and geometrical parameters on heat exchanger performance in TAR was investigated by Piccolo *et al.* (2011). Relevant guidance has been drawn for heat exchanger design insofar as fin length, fin spacing, blockage ratio, gas and secondary fluid-side heat transfer coefficients are concerned.
- More recently, Hariharan N. and Sivashanmugam (2013) optimised the parameters such as frequency, stack position, stack length, and plate spacing involved in designing TARs using the Response Surface Methodology (RSM). Their results showed that geometrical variables chosen for their investigation are interdependent.

This is by no means a complete list of the 'optimisation' of refrigerators components, but it provides a comprehensive overview of optimisation targets.

CHAPTER 3: THERMOACOUSTIC REFRIGERATOR MODELLING DEVELOPMENT

3.1 Introduction

Thermoacoustic refrigerators offer a solution to the current search for alternative refrigerants and alternative technologies (such as absorption refrigeration, thermoelectric refrigeration and pulse-tube refrigeration) necessary to reduce harsh environmental impact (Joshi & Garimella, 2003). Thermoacoustics is a field of study that combines both acoustic waves and thermodynamics. The interaction of the temperature oscillation accompanied by the pressure oscillation in a sound wave with solid boundaries initiates an energy conversion processes. In ordinary experience, this interaction between heat and sound cannot be observed. But it can be amplified under suitable conditions to give rise to significant thermodynamic effects such as convective heat fluxes, steep thermal gradients and strong sound fields. Thermoacoustic refrigerators (TARs) use acoustic power to cause heat flow from a low temperature source to high temperature sink. In contrast, thermoacoustic engines (TAEs) produce acoustic power using heat flow from a high temperature source to low temperature sink (Swift, 2002).

Thermoacoustic refrigerators (Figure 3.1) consist mainly of a loudspeaker (a vibrating diaphragm or thermoacoustic prime mover) attached to a resonator filled with gas, a stack usually made of thin parallel plates, and two heat exchangers placed at either side of the stack. The stack forms the heart of the refrigerator where the heat-pumping process takes place, and it is thus a critical element for determining the performance of the refrigerator (Swift, 1988). For the temperature gradient along the stack walls to remain steady, the material selected should have higher heat capacity and lower thermal conductivity than the gas; otherwise the stack won't be affected by the temperature oscillations of the nearby gas. In addition, a material of low thermal conductivity should be chosen for the stack and the resonator to prevent leaking from the hot side of the resonator back to the cold side and to withstand higher pressure (Tijani *et al.,* 2002).

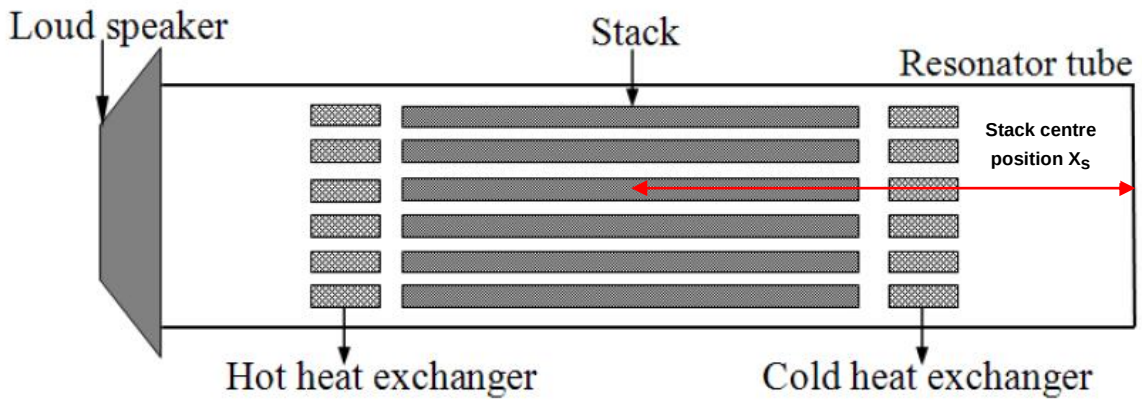

Figure 3.1: Schematic diagram of a typical thermoacoustic refrigerator

Using a sound source such as a loudspeaker, an acoustic wave is generated to make the gas resonant. As the gas oscillates back and forth within the chamber, the standing sound wave creates a temperature difference along the length of the stack. This temperature change is a result of compression and expansion of gas by sound pressure and thermal interaction between the oscillating gas and the surface of the plate. Heat is exchanged with the surroundings through heat exchangers at the cold and hot side of the stack (Swift, 2002). The basic mechanics behind thermoacoustics are already well-understood. A detailed explanation of the way thermoacoustic coolers work is given by Swift (1988) and Wheatly *et al.* (1985). Recent research focuses on improving the performance of the devices so that thermoacoustic coolers can compete with commercial refrigerators. One way to improve the performance of current devices is by developing novel modelling approaches in order to understand the interaction between design parameters.

This chapter presents thermodynamics and the concepts associated with thermoacoustics. The thermodynamic efficiencies of the refrigerators and the engines, the principle of thermoacoustic theory, governing equations and important parameters in thermoacoustics are discussed. The remainder of this chapter includes the model development. The fundamental parameters and equations in our mathematical models characterising the standing wave thermoacoustic refrigerators are presented.

3.2 Thermodynamics

Thermodynamics and acoustics are the two pillars of thermoacoustics. While thermodynamics deals with the energy conversion, heat transfer and efficiency, acoustics deals with the dynamic properties of gas oscillations such as type of gas, velocity, pressure

and phase. The energy conversion from heat to sound or from sound to heat follows the First Law of Thermodynamics which states that energy can neither be created nor destroyed. The rate of increase or decrease of internal energy ($\dot{U}$) of a system is equal to the algebraic sum of the heat flow ($\dot{Q}$) and work done by the system ($\dot{W}$) (Swift, 2002). It is described mathematically by the following Equation:

$$\dot{U} = \sum \dot{Q} + \dot{W} \qquad \textbf{Equation 3.1}$$

The Second Law of Thermodynamics limits the interchange between work and heat in a system. The second law states that for a system change in entropy ($\dot{S}$) for a process is given by the following Equation:

$$\dot{S} = \sum \frac{\dot{Q}}{T} + \dot{S}_i \qquad \textbf{Equation 3.2}$$

Where $\dot{S}_i \geq 0$

A thermodynamic prime mover or engine produces work ($\dot{W}$) after receiving heat ($\dot{Q}_H$) from a high temperature source (T_H) and rejecting heat ($\dot{Q}_C$) to a low temperature sink (T_C). Similarly, a refrigerator absorbs heat ($\dot{Q}_C$) from the low temperature source (T_C) and rejects heat ($\dot{Q}_H$) to a high temperature sink at temperature (T_H) using work ($\dot{W}$). The First Law of Thermodynamics for the engine and the refrigerator becomes:

$$\dot{Q}_H = \dot{Q}_C + \dot{W} \qquad \textbf{Equation 3.3}$$

For an engine the second law becomes:

$$\frac{Q_C}{T_C} - \frac{Q_H}{T_H} \geq 0 \qquad \textbf{Equation 3.4}$$

Similarly for the refrigerator:

$$\frac{Q_H}{T_H} - \frac{Q_C}{T_C} \geq 0 \qquad \textbf{Equation 3.5}$$

As a prime mover, the application of thermal energy from two reservoirs of different temperatures will generate useful work within the engine. A prime mover uses heating power ($\dot{Q}_H$) to produce as much acoustic power ($\dot{W}$) as possible. In the case of a prime mover, the efficiency can be defined as follows:

$$\eta = \frac{\dot{W}}{\dot{Q}_H} \leq \frac{T_H - T_C}{T_H} \qquad \textbf{Equation 3.6}$$

where the ratio $\frac{T_H - T_C}{T_H}$ is the Carnot efficiency describing the maximum efficiency limit for all engines working between two temperatures, T_H and T_C.

When analysing a refrigerator, we are interested in maximising the cooling load ($\dot{Q}_C$) extracted at temperature (T_C) while at the same time minimising the net required acoustic power ($\dot{W}$). In the case of an engine operating as a refrigerator, efficiency is called coefficient of performance (COP). It is given as follows:

$$COP = \frac{Q_C}{W} \leq \frac{T_C}{T_H - T_C}$$ **Equation 3.7**

where $\frac{T_C}{T_H - T_C}$ is the Carnot coefficient of performance describing the maximum performance limit for a given refrigerator between two temperatures.

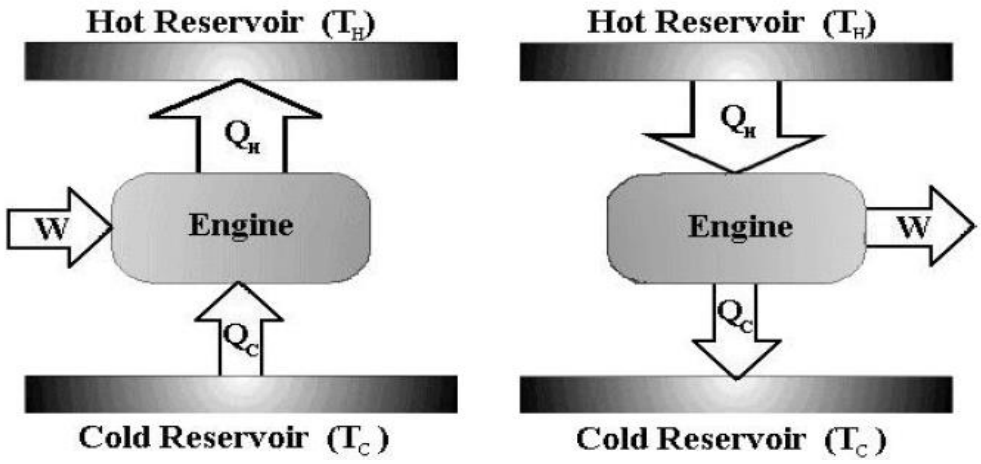

(a) Refrigerator or heat pump (b) Prime mover

Figure 3.2: Heat engine operation

(Adapted from Livvarcin, 2000)

3.3 The thermoacoustic effect

The thermoacoustic refrigerator principle is best illustrated by Figure 3.3. Consider a long tube filled with gas containing a solid material of low thermal conductivity and high specific heat capacity known as ‘stack’. The stack geometry has pores, as illustrated in Figure 1.6, with channels through which the acoustic wave will travel. A sufficiently large temperature gradient is applied across the ends of the stack to generate the thermoacoustic effect. This is done by placing two heat exchangers, one high temperature and one low temperature, in contact with the ends of the stack material.

Using the Lagrangian approach, we follow the parcel of gas as it oscillates sinusoidally in the system. For the sake of clarity, it is described in a step by step motion:

- **Step 1:** As the sound waves resonate back and forth within the resonator, the gas is compressed as it is shifted to the right. As a result of compression, the temperature of the gas parcel increases and becomes higher than that of the neighbouring stack material.
- **Step 2:** The compressed parcel of gas transfers heat to the solid. This phase is the refrigeration part of the cycle.
- **Step 3:** The gas parcel oscillates back in the other direction; it expands and cools down sufficiently. Its temperature is less than that of the adjoining stack material.
- **Step 4:** The gas parcel reabsorbs heat from the stack material to repeat the heat transfer process.

The thermoacoustic effect consists of picking up heat from a solid at a lower temperature and transferring it to a solid at a higher temperature.

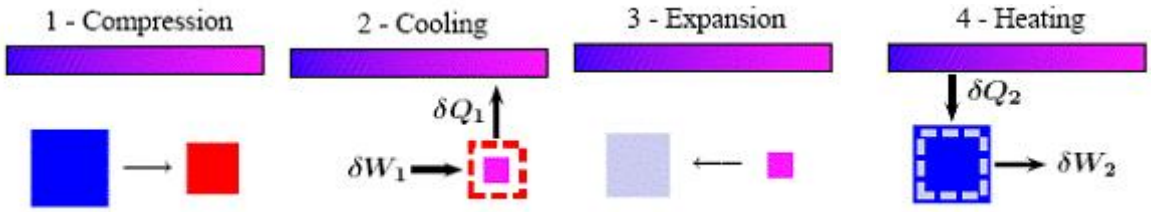

Figure 3.3: Typical fluid parcels of the thermodynamic cycle in a stack-based standing wave refrigerator

Despite the fact that an individual parcel of gas transfers only a small amount of heat, thermoacoustic refrigeration is induced by combining all gas parcels, acting like a bucket brigade (Swift, 2002), to transfer heat from the cold end to the hot end. Two reasons explain the temperature variations of the gas:

- first, adiabatic compression and expansion of the acoustic wave itself; and
- secondly, the interaction of this acoustic wave with the adjacent stack material.

The heat transfer takes place within the thermal penetration depth δ_k (Figure 3.4). For optimal heat transfer between the gas and the solid in the stack, the spacing in the stack should be about two to four times the thermal penetration depth (Tijani, 2001). The gas parcels that are present in the resonator, or those farther away than the thermal penetration depth in the stack material, undergo simple adiabatic acoustic expansion and compression

without experiencing heat transfer. It is also important to note that the temperature gradient plays a great role in describing a system as a refrigerator or engine, since both systems are interchangeable. A relatively higher temperature gradient is required for an engine, whereas a small to moderate temperature gradient is an essential condition for a refrigerator.

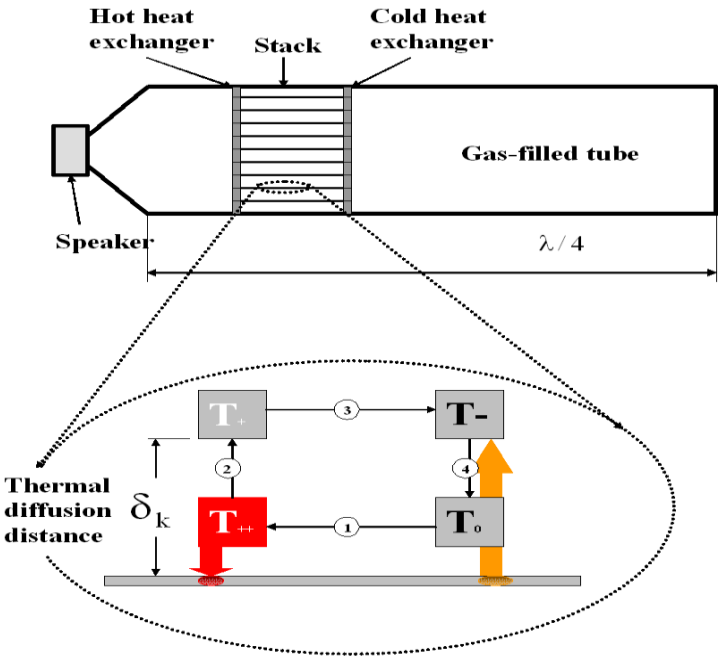

Figure 3.4: Schematic diagram of one quarter length wavelength thermoacoustic refrigerator

With regards to electronics cooling, the heat transfer can be described as follows (Abdel-Rahman *et al.,* 2002):

- absorption of heat from circuit (to be cooled) by direct metallic contact with cold heat exchanger;
- transfer of heat from cold exchanger to stack elements by the pumping action of the sound field (unique to thermoacoustics);
- pumping of heat along stack elements by sound field;
- transfer of heat across stack-hot heat exchanger interface enhanced by acoustic pumping; and
- dissipation of heat by hot heat exchanger by conduction through thermal fins and air convection.

3.4 Principle of Thermoacoustics

This section discusses the basic equations that govern the thermoacoustic phenomena. A detailed description has been developed Swift (1988), Wheatley *et al.* (1983) and Rott (1973, 1974, 1975). These authors have developed thermoacoustic equations starting with the linearization of the continuity, Navier-Stokes, and energy equations. The thermoacoustic equations are three-fold:

- the Rott's wave equation, which describes the wave equation for the pressure in the presence of a temperature gradient along the stack;
- the energy equation, which describes the energy flow in thermoacoustic systems; and
- the acoustic power absorbed (refrigerator) or produced (engine) in the stack.

In this Chapter, as well as in Chapter 4, no attempt is made to derive these equations, as detailed derivations of the equations are available in both Mahmud (2005) and Tijani (2001). However, approximations in order to derive the thermoacoustic equations used as objective functions in the modelling approach are discussed, and also are utilised in Chapters 5 and 6. The notations used by Swift (1988) and Tijani (2001) are adopted.

To assist in our derivation of the mathematical programming models, we consider a simple parallel plate stack in a gas filled resonator, as illustrated in Figure 3.5. A sustained one-dimensional acoustic wave is transmitted through the system. The following assumptions are made:

- the plates are stationary and rigid;
- the length of the plates is relatively smaller than the acoustic wavelength of the resonator;
- the acoustic pressure is constant over the entire cross section of the plates and is x-dependent only;
- the theory is linear so higher order effects such as turbulence and acoustic streaming are neglected;
- radiation is ignored;
- the temperature difference across the stack is relatively smaller than the absolute value of temperature (viscosity is assumed independent of temperature);
- the average fluid velocity is zero; and
- steady state conditions exist.

The geometry used to derive and discuss the thermoacoustic equations is illustrated in Figure 3.5. The thickness of the plates is $2l$ while the distance between the plates is $2y_o$.

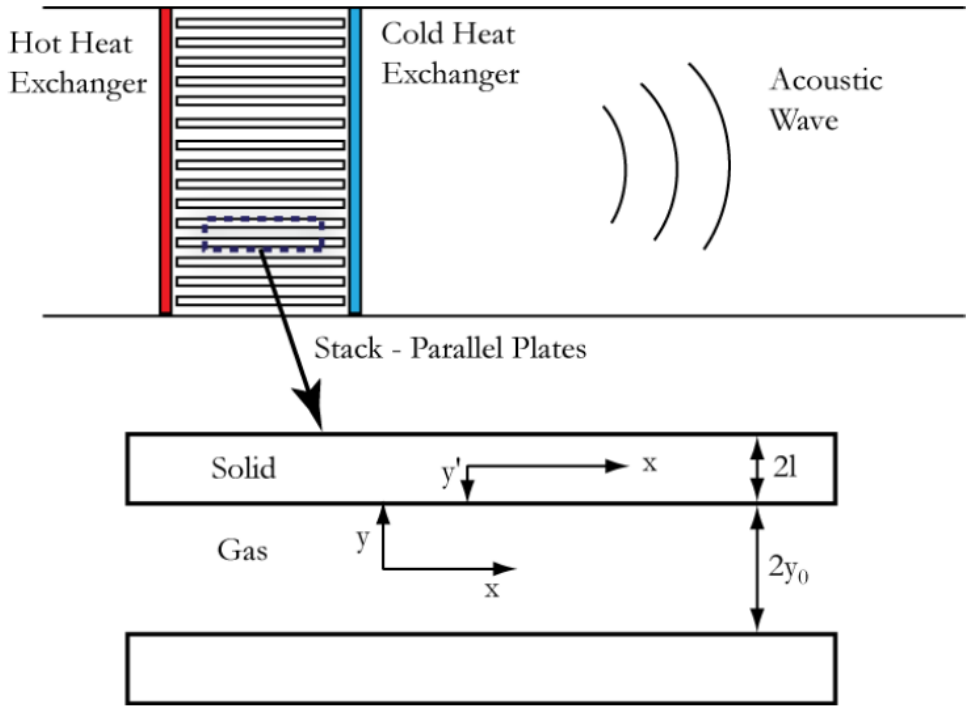

Figure 3.5: A simple short stack thermoacoustic engine with stack spacing and thickness

(Adapted from Tijani, 2001)

a. Rott wave equation

The wave equation of Rott is given as follows (Swift, 2002):

$$\left[1+\frac{(\gamma-1)}{(1+\varepsilon_s)}f_k\right]p_1+\frac{a^2}{\omega^2}\rho_m\frac{d}{dx}\left[\frac{(1-f_v)}{\rho_m}\frac{dp_1}{dx}\right]+\frac{a^2}{\omega^2}\frac{(f_k-f_v)}{(\sigma-1)(1+\varepsilon_s)}\beta\frac{dT_m}{dx}\frac{dp_1}{dx}=0 \qquad \textbf{Equation 3.8}$$

This equation relates the acoustic pressure (p_1) in a stack given a mean temperature gradient $\frac{dT_m}{dx}$ and other thermophysical properties of both an ideal gas and an ideal stack. f_v, f_k and ε_s are obtained as follows (Tijani, 2001):

$$f_v=\frac{\tanh((1+i)y_o/\delta_v)}{(1+i)y_o/\delta_v} \qquad \textbf{Equation 3.9}$$

$$f_k=\frac{\tanh((1+i)y_o/\delta_k)}{(1+i)y_o/\delta_k} \qquad \textbf{Equation 3.10}$$

$$\varepsilon_s = \frac{\sqrt{K\rho_m c_p}}{\sqrt{K_s\rho_s c_s}} \frac{\tanh((1+i)y_o/\delta_k)}{(1+i)l/\delta_s} \qquad \textbf{Equation 3.11}$$

where $\delta_k = \sqrt{\frac{2K}{\rho c_p \omega}}$

$$\delta_s = \sqrt{\frac{2K_s}{\rho_s c_s \omega}} \qquad \textbf{Equation 3.12}$$

$$Pr = \left(\frac{\delta_v}{\delta_k}\right)^2$$

where Pr is the Prandtl number for the gas; δ_k is the gas thermal penetration depth; δ_s is the solid's thermal penetration depth; δ_v is the viscous penetration depth; ω is the angular frequency; ρ is the mass density of the gas; K is the thermal conductivity; c_p is the specific heat capacity; and f is known as Rott's function, dependent on the geometry. The Rott function for various geometries have been derived and reported in Swift's studies (1997).

b. Energy equation

The energy flux equation along the direction of wave propagation is given as follows (Tijani, 2001):

$$\dot{E}_2 = \frac{A_g}{2} Re\left[p_1\langle u_1^*\rangle\left(1 - \frac{\beta T_m(f_k - f_v^*)}{(1+\sigma)(1+\varepsilon_s)(1-f_v^*)}\right)\right] +$$

$$\frac{A_g\rho_m c_p |\langle u_1\rangle|^2}{2\omega(1-\sigma)|1-f_v|^2}\frac{dT_m}{dx} Im\left[f_1^* + \frac{(f_k - f_v^*)\left(1+\frac{\varepsilon_s f_v}{f_k}\right)}{(1+\varepsilon_s)(1+\sigma)}\right] \qquad \textbf{Equation 3.13}$$

$$-\left[A_g K + A_s K_s\right]\frac{dT_m}{dx}$$

where A_g is the cross-sectional area of the gas within the stack, and A_s is the cross-sectional area of the stack material. In the above equation, the asterisk (*) denotes the complex conjugate of the individual parameter, while $Im[\ ]$ denotes the imaginary part. This equation gives the energy flux along the direction of wave propagation in terms of mean pressure $p_1(x)$, mean temperature $T_m(x)$, material properties and the geometry of the device.

c. Acoustic power

The acoustic power absorbed (or produced) in the stack per unit length is given as follows (Tijani, 2001):

$$\frac{d\dot{W}_2}{dx} = -\frac{1}{2}A_g\omega\left(\frac{\rho_m l_m(-f_v)}{|1-f_v|^2}|\langle u_1\rangle|^2 + \frac{(\gamma-1)l_m(-f_k)}{\rho_m a^2(1+\varepsilon_s)}|p_1|^2\right)$$
$$+\frac{1}{2}A_g\omega\left(\frac{\beta}{\omega(1-\sigma)(1+\varepsilon_s)}\frac{dT_m}{dx}Re\left(\frac{(f_k^* - f_v^*)}{(1-f_v^*)}p_1\langle u_1^*\rangle\right)\right) \quad \textbf{Equation 3.14}$$

To indicate that the acoustic power is a second-order quantity, the subscript 2 is used; it is obtained from the product of two first-order quantities, p_1 and u_1. The third term in Equation 3.14 contains the temperature gradient $\frac{dT_m}{dx}$. It can either produce (prime mover) or absorb (refrigerator) acoustic power depending on the magnitude of the temperature gradient along the stack. This term is unique to thermoacoustics.

3.5 Short stack and boundary layer approximations

In this section we will simplify the previous expressions using two assumptions. Additionally, we consider standing wave systems, which are more related to the modelling and experimental work in this thesis.

- **Short stack approximation**

The stack is considered short enough that the velocity and the pressure do not vary significantly: $L_s << \lambda$

- **Boundary layer approximation**

$y_o >> \delta_k$ and $l >> \delta_s$

As a result, the hyperbolic tangents in Equation 3.9, Equation 3.10 and Equation 3.11 can be set equal to unity. The standing wave acoustic pressure in the stack and the mean gas velocity in x direction are given respectively by:

$$p_1 = p_1^s = p_o\cos(kx) \quad \textbf{Equation 3.15}$$

$$\langle u_1\rangle = j\left(1+\frac{l}{y_o}\right)\frac{p_o}{\rho_m a}\sin(kx) = j\langle u_1^s\rangle \quad \textbf{Equation 3.16}$$

where k is the wave number; p_o is the pressure amplitude at the pressure antinodes; and the superscript s refers to standing waves.

The Rott's function (f) can be approximated by (Swift, 1997):

$$f = \frac{(1-j)\delta}{y_o} \qquad \textbf{Equation 3.17}$$

The cross-sectional area of the gas within the stack (A_g) and the cross-sectional area of the stack material (A_s) are approximated as follows:

$$A_g = \Pi y_o$$
$$A_s = \Pi l \qquad \textbf{Equation 3.18}$$

Using these assumptions, the approximate expressions for acoustic power ($\dot{W}_2$) and energy ($\dot{E}_2$) are obtained, respectively, as follows (Swift, 1988):

$$\dot{W}_2 = \frac{1}{4}\Pi\delta_k L_s \frac{(\gamma-1)\omega\left(p_1^s\right)^2}{\rho_m a^2(1+\varepsilon_s)}\left(\frac{\Gamma}{(1+\sqrt{\sigma})\Lambda}-1\right) - \frac{1}{4}\Pi\delta_v L_s \frac{\omega\rho_m\left\langle u_1^s\right\rangle^2}{\Lambda} \qquad \textbf{Equation 3.19}$$

and

$$\dot{E}_2 = -\frac{1}{4}\Pi\delta_k \frac{\beta T_m p_1^s\left\langle u_1^s\right\rangle}{(1+\sigma)(1+\varepsilon_s)\Lambda}\left[\Gamma\frac{1+\sqrt{\sigma}+\sigma+\sigma\varepsilon_s}{1+\sqrt{\sigma}}\right] - \left(1+\sqrt{\sigma}-\frac{\delta_v}{y_o}\right)$$
$$-\Pi\left[y_o K - l K_s\right]\frac{dT_m}{dx} \qquad \textbf{Equation 3.20}$$

where

$$\Lambda = 1-\frac{\delta_v}{y_o}+\frac{\delta_v^2}{2y_o^2}$$

$$\Gamma = \frac{\nabla T_m}{\nabla T_{crit}}$$

$$\nabla T_m = \frac{\Delta T_m}{L_s} \qquad \textbf{Equation 3.21}$$

$$\nabla T_{crit} = \frac{\beta T_m \omega p_1^s}{\rho_m c_p\left\langle u_1^s\right\rangle} = \frac{(\gamma-1)}{\left(1+\frac{l}{y_o}\right)} k T_m \cot(kx)$$

In these equations, L_s is the stack length; Π is the total perimeter of the stack plates in the direction normal to the x axis; and ΔT_m is the temperature difference across the stack.

The equations derived in this section contain a large number of parameters of the material, the working gas, and geometrical parameters of the stack. Table 3.1 gives the parameters of importance in thermoacoustics, which are contained in Equations 3.19 and 3.20.

Table 3.1: TAR parameters

Operation parameters	
Angular frequency	ω
Average pressure	p_m
Dynamic pressure amplitude	p_o
Mean temperature	T_m
Gas parameters	
Dynamic viscosity	μ
Thermal conductivity	K
Sound velocity	a
Ratio of isobaric to isochoric specific heats	γ
Stack parameters	
Thermal conductivity	K_s
Density	ρ_s
Specific heat	c_s
Length	L_s
Stack centre position	x_s
Plate thickness	2l
Plate spacing	$2y_o$
Cross section	A

3.6 Design strategy

As stated previously, thermoacoustic refrigerators primarily consist of four main components:

- a driver;
- a stack;
- two heat exchangers; and
- a resonator.

Our approach to the design and optimisation of the refrigerator consists of the design and optimisation of each part separately. However, the optimisation of the driver and the two heat exchangers are beyond the scope of this thesis.

The coefficient of performance of the stack is defined as the ratio of the heat pumped by the stack to the acoustic power used by the stack. The formulation of the expressions of acoustic power and cooling power in the stack looks complicated. They contain a large number of geometrical parameters of the stack and the gas. However, Olson and Swift

(1994) have chosen a number of dimensionless independent parameters to reduce the large number of parameters listed previously (Table 3.1). Some dimensionless parameters are derived from Equations 3.19 and 3.20, while others are obtained from the short stack and the boundary layer assumptions. The important parameters in thermoacoustics are listed in Table 3.2 and Table 3.3.

The normalisation is carried out as follows:

- the position and the length of the stack are normalised by $\lambda / 2\pi$;
- the viscous and thermal penetration depths are normalised by y_o;
- the temperature difference can be normalised by T_m;
- the thermal penetration depth (δ_k) and the viscous penetration depth (δ_v) are related using the prandtl number (σ);
- the acoustic power and the cooling power are normalised by the product of the mean pressure (p_m). the sound velocity a, and the cross sectional area of the stack A as proposed by Olson and Swift (1994); and
- the drive ratio (DR) is used to define the ratio $\frac{p_o}{p_m}$.

3.7 Model development

In this section, the model development for the physical standing wave refrigerator depicted in Figure 3.1 is presented. For our models, only the stack geometry is considered. The model does not consider any influence of the stack material or the interdependency of coefficient of performance of thermoacoustic core, effectiveness of heat exchangers and acoustic power efficiency.

3.7.1 Design parameters of the thermoacoustic core

The basic design requirements for thermoacoustic refrigerator are twofold (Herman & Travnicek, 2006):

(1) to supply the desired cooling load ($\dot{Q}_c$); and

(2) to achieve the prescribed cooling temperature (T_c) or a given temperature difference (ΔT) over the stack at the same time.

The resultant normalised operation parameters are presented in Table 3.2. The number of parameters can once more be reduced by making a choice of some normalised parameters.

Table 3.2: Normalised cooling load and acoustic power

Operation parameters	
Normalised cooling power	$\Phi_H = \frac{\dot{Q}_c}{p_m a A}$
Normalised acoustic power	$\Phi_W = \frac{\dot{W}}{p_m a A}$

The coefficient of performance of a thermoacoustic core COP is dependent on 19 independent design parameters (Wetzel & Herman, 1997). Herman and Travnicek (2006) have collapsed the number of parameters to the following six normalised parameter spaces, as shown in Table 3.3:

Table 3.3: TAR parameters

Operation parameters	
Drive Ratio (DR)	$DR = \frac{p_0}{p_m}$ Where p_0 and p_m are respectively the dynamic and mean pressure
Normalised temperature difference	$\theta = \Delta T_{mn} = \frac{\Delta T_m}{T_m}$ Where ΔT_m and T_m are respectively the desired temperature span and the mean temperature span
Gas parameters	
Normalised thermal penetration depth	$\delta_{kn} = \frac{\delta_k}{y_0}$ where $2y_0$ is the plate spacing
Stack geometry parameters	
Normalised stack length	$L_{Sn} = \frac{2\pi f}{a} L_S$ where L_S the stack length
Normalised stack position	$X_{Sn} = \frac{2\pi f}{a} X_S$ where f, a and X_S are respectively the resonant frequency, the speed of sound and the stack centre position
Blockage ratio or porosity	$BR = \frac{y_0}{(y_0 + l)}$ where $2l$ is the plate thickness

3.7.2 Design objectives

The performance of the thermoacoustic stack depends on three main stack design parameters: 1) the centre position, 2) the length, and 3) the cross-section area of the stack. The normalised cooling power (Φ_H) and acoustic power (Φ_W) neglecting axial conduction in the working fluid as well as in the stack plates are given by Tijani *et al.* (2002):

$$\Phi_H = -\left[\frac{\delta_{kn} DR^2 \sin(2X_{Sn})}{8\gamma(1+\sigma)\left(1-\sqrt{\sigma}\delta_{kn}+\frac{1}{2}\sigma\delta_{kn}^2\right)}\right]\times \left[\frac{\Delta T_{mn}\tan(X_{Sn})}{(\gamma-1)BR\ L_{Sn}}\times\frac{\left(1+\sqrt{\sigma}+\sigma\right)}{1+\sqrt{\sigma}}-\left(1+\sqrt{\sigma}-\sqrt{\sigma}\delta_{kn}\right)\right] \quad \textbf{Equation 3.22}$$

and

$$\Phi_W = \left[\frac{\delta_{kn} DR^2 L_{Sn}(\gamma-1)BR\ \cos^2(X_{Sn})}{4\gamma}\right]\times \left[\frac{\Delta T_{mn}\tan(X_{Sn})}{BR\ L_{Sn}(\gamma-1)(1+\sqrt{\sigma})\left(1-\sqrt{\sigma}\delta_{kn}+\frac{1}{2}\sigma\delta_{kn}^2\right)}-1\right] - \left[\frac{\delta_{kn} L_{Sn} DR^2}{4\gamma}\times\frac{\sqrt{\sigma}\sin^2(X_{Sn})}{BR\left(1-\sqrt{\sigma}\delta_{kn}+\frac{1}{2}\sigma\delta_{kn}^2\right)}\right] \quad \textbf{Equation 3.23}$$

The normalised cooling load (Φ_C) and the coefficient of performance of the thermoacoustic core COP can be defined respectively as follows (Wetzel & Herman, 1997):

$$\Phi_C = \Phi_H - \Phi_W \quad \textbf{Equation 3.24}$$

$$COP = \frac{\Phi_H - \Phi_W}{\Phi_W} \quad \textbf{Equation 3.25}$$

The cooling load (Φ_C) is a function of eight non-dimensional parameters (Tijani *et al.,* 2002):

$$\Phi_C = F(\sigma,\ \gamma,\ \varepsilon_S,\ \theta,\ L_{Sn},\ X_{Sn},\ BR,\ \delta_{kn}) \quad \textbf{Equation 3.26}$$

where σ, γ, ε_S and θ represent respectively the Prandtl number, the isentropic coefficient and the normalised temperature difference. The influence of the working fluid on the gas is exerted through the parameters σ, γ and ε_S. In Chapter 5, we study the influence of

normalised stack length (L_{Sn}) normalised stack position (X_{Sn}) blockage ratio (BR) and normalised thermal penetration depth on the performance of the TAR.

It should be noted that stack resistance to sound waves causes intensity attenuation and introduces nonlinearities (Kuntz & Blackstock, 1987). Therefore, the viscous and thermal relaxation dissipation in the penetration depth and along the surface of the resonator has to be considered. In the boundary layer approximation, the acoustic power loss per unit area of the resonator is given by Tijani *et al.* (2002):

$$\overset{o}{W}_2 = \frac{dW_2}{dS} = \left[\frac{\delta_{kn} DR^2 L_{Sn}(\gamma - 1) BR \cos^2(X_{Sn})}{4\gamma}\right] + \left[\frac{\delta_{kn} L_{Sn} DR^2}{4\gamma} \times \frac{\sqrt{\sigma}\sin^2(X_{Sn})}{BR\left(1 - \sqrt{\sigma}\delta_{kn} + \frac{1}{2}\sigma\delta_{kn}^2\right)}\right] \quad \textbf{Equation 3.27}$$

where the first term on the right-hand side is the kinetic energy dissipated by viscous shear. The second term is the energy dissipated by thermal relaxation.

3.7.3 Design constraints

Using the dimensionless parameters, the parameter (Γ) in Equation 3.21 can be rewritten as follows (Tijani, 2001):

$$\Gamma = \frac{\Delta T_{mn}}{(\gamma - 1) BR L_{sn}} \tan(x_n) \quad \textbf{Equation 3.28}$$

The normalised temperature gradient is the parameter that determines whether the thermoacoustic device operates as engine ($\Gamma > 1$) or as refrigerator ($\Gamma < 1$). For the design optimisation, Equation 3.28 can be used as constraint in the mathematical programming models.

Figure 3.6 represents the energy flux as a function of the normalised stack length. It identifies two limits, $L_{sn_{min}}$ and $L_{sn_{max}}$. If the designer chooses a normalised stack length longer than $L_{sn_{max}}$, corresponding to the intersection B in Figure 3.6, the coefficient of performance takes a negative value. The cooling load obtained is negative as well. This result does not have any physical meaning. Subsequently, the following constraint could be enforced in the mathematical programming models:

$$\Phi_C = \Phi_H - \Phi_W > 0 \quad \textbf{Equation 3.29}$$

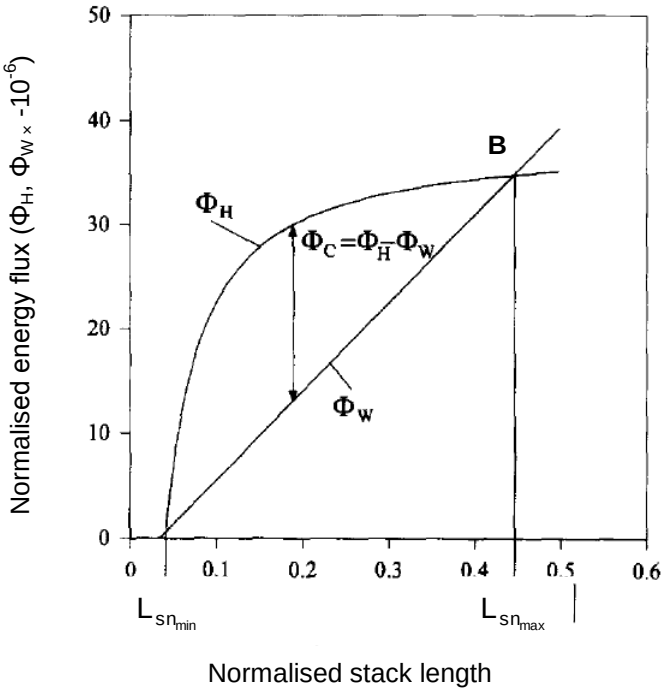

Figure 3.6: Example of limits of normalised stack length

(Adapted from Wetzel & Herman, 1997)

CHAPTER 4: THERMOACOUSTIC ENGINE MODELLING DEVELOPMENT

4.1 Introduction

This work demonstrates how a multi-objective approach can be used to optimise the design and performance of small-scale thermoacoustic devices. Thermoacoustics relates to the physical phenomenon that a temperature difference can create and amplify a sound wave and vice versa (Swift, 1988). Hereto the sound wave is brought into interaction with a porous solid material with a much higher heat capacity compared to the gas through which the sound wave propagates. The solid material acts as a regenerator. When a temperature difference is applied across the stack and a sound wave passes through it from the cold to the hot side, a parcel of gas executes a thermoacoustic cycle. The gas will subsequently be compressed, displaced and heated, expanded, displaced again, and cooled (Figure 4.1). During this cycle the gas is being compressed at low temperature, while expansion takes place at high temperature. This means that work is performed on the gas.

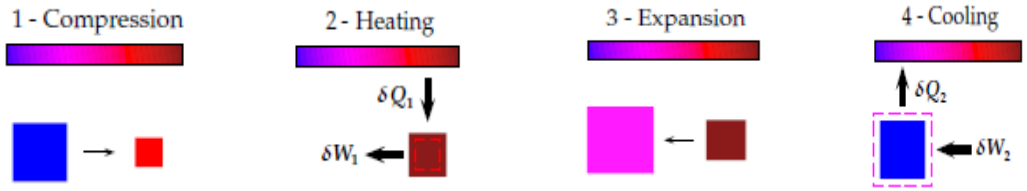

Figure 4.1: Typical fluid parcels, near a stack plate, executing the four steps of the thermodynamic cycle in a stack-based standing wave thermoacoustic engine.

The effect of this work is that the pressure amplitude of the sound wave is increased. In this way, it is possible to create and amplify a sound wave by a temperature difference. The thermal energy is converted into acoustic energy. Within thermoacoustics, this is referred to as a thermoacoustic engine (TAE). In a thermoacoustic refrigerator (TAR), as described previously, the thermodynamic cycle is run the reverse way, and heat is pumped from a low-temperature level to a high-temperature level by the acoustic power. The basic mechanics behind thermoacoustic engines are already well-understood. In this chapter, some fundamental physical properties are reviewed and previous optimisation efforts underlying thermoacoustic engines are presented. Finally, the fundamental components of the mathematical model characterising the standing wave thermoacoustic heat engines are presented.

4.2 Thermoacoustic engines

The most important part of the thermoacoustic engine is the core, where the stack of plates is located. Thermoacoustic effects actually occur within a very small layer next to the plate, the thermal boundary layer. This is defined as follows (Tijani *et al.,* 2002):

$$\delta_k = \sqrt{\frac{2K}{\rho_m c_p \omega}} \qquad \textbf{Equation 4.1}$$

with K being the thermal conductivity; ρ_m the mean density; and c_p the constant pressure specific heat of the working fluid. Heat transfer by conduction is encouraged by a thick boundary layer during a period of $1/\omega$, where ω is the angular frequency of the vibrating fluid. However, another layer that occurs next to the plate, the viscous boundary layer, discourages the thermoacoustic effects. It is defined as follows (Tijani *et al.,* 2002):

$$\delta_v = \sqrt{\frac{2\mu}{\rho_m \omega}} \qquad \textbf{Equation 4.2}$$

where μ is the diffusivity of the gas. Losses due to viscous effects occur in this region. A thinner viscous boundary layer than the thermal boundary layer is desirable for effective thermoacoustic effects. Swift (1988) started with the equation of heat transfer to come up with a theoretical critical mean temperature gradient, $\nabla T_{crit.}$ that describes the difference between a thermoacoustic heat engine as follows:

$$\nabla T_{crit.} = \frac{\omega p_1^s}{\rho_m c_p u_1^s} \qquad \textbf{Equation 4.3}$$

This critical temperature gradient depends on the angular frequency (ω) the first order pressure (p_1^s) and velocity (u_1^s) in the standing wave, as well as the mean gas density (ρ_m) and specific heat (c_p). In a TAE, the imposed temperature gradient must be greater than this critical temperature gradient $(dT/dx)/(dT/dx_{crit.}) > 1$. Figure 4.2 shows a very simple prototypical standing wave TAE.

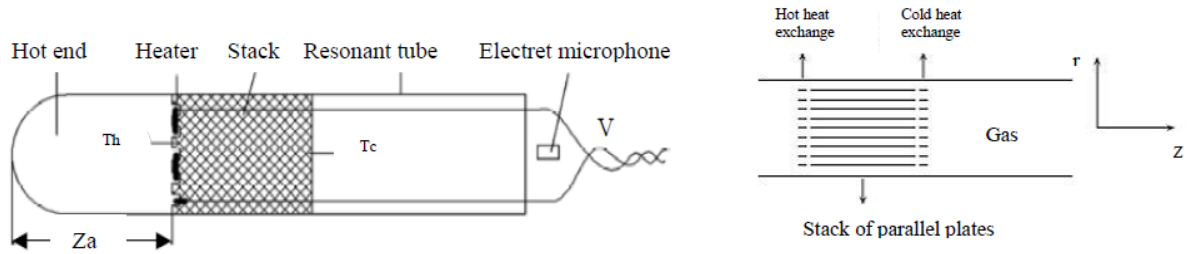

Figure 4.2: Prototype of a small-scale thermoacoustic engine or prime mover

The closed end of the resonance tube is the velocity node and the pressure antinode. The porous stack is located near the closed end and the interior gas experiences large pressure oscillations and relatively small displacement. Heat input is provided by a heating wire, causing a temperature gradient to be established across the stack (in the axial direction). A gas in the vicinity of the walls inside the regenerative unit experiences compression, expansion and displacement when it is subject to a sound wave. Over the course of the cycle, heat is added to the gas at high pressure, and heat is withdrawn from it at low pressure. This energy imbalance results in an increase of the pressure amplitude from one cycle to the next, until the acoustic dissipation of the sound energy equals the addition of heat to the system (Swift, 2000; Bastyr & Keolian, 2003; Poese, 2004; Backhaus & Swift, 2000).

4.3 Modelling approach

In this section, our modelling approach for the physical standing wave engine depicted in Figure 4.2 is discussed; the development of our mathematical model equations is included in Section 4.4. The problem is reduced to a two-dimensional domain because of the symmetry present in the stack. Two constant temperature boundaries are considered; namely, one convective boundary and one adiabatic boundary, as shown in Figure 4.3. For our model, only the stack geometry is considered. The model considers variations in operating conditions and the interdependence of stack location and geometry.
Five different parameters are considered to characterise the stack:

- L: stack length,
- H: stack height,
- Za: stack placement (with Za=0 corresponding to the closed end of the resonator tube),
- dc: channel dimension, and
- N: number of channels.

Those parameters have been allowed to vary simultaneously. Five different objectives as described by Trapp *et al.* (2011) (Swift, 2002), namely two acoustic objectives—acoustic work (W) and viscous resistance (R_V)—and three thermal objectives—convective heat flux (Q_{conv}), radiative heat flux (Q_{rad}) and conductive heat flux (Q_{cond})—are considered to measure the quality of a given set of variable values that satisfy all the constraints. Ultimately, optimising the resulting problem generates optimal objective function value

$G^* = \left[W^*, R^*_{V,} Q^*_{conv}, Q^*_{rad}, Q^*_{cond}\right]$ and optimal solution $x^* = \left[L^*, H^*, dc^*, Za^*, N^*\right]$. Since the five objectives are conflicting in nature (Trapp *et al.,* 2011), a multi-objective optimisation approach has been used. In this approach, the five objective components will be considered simultaneously. Therefore, each objective component has been given a weighting factor (w_i) to provide appropriate user-defined emphasis.

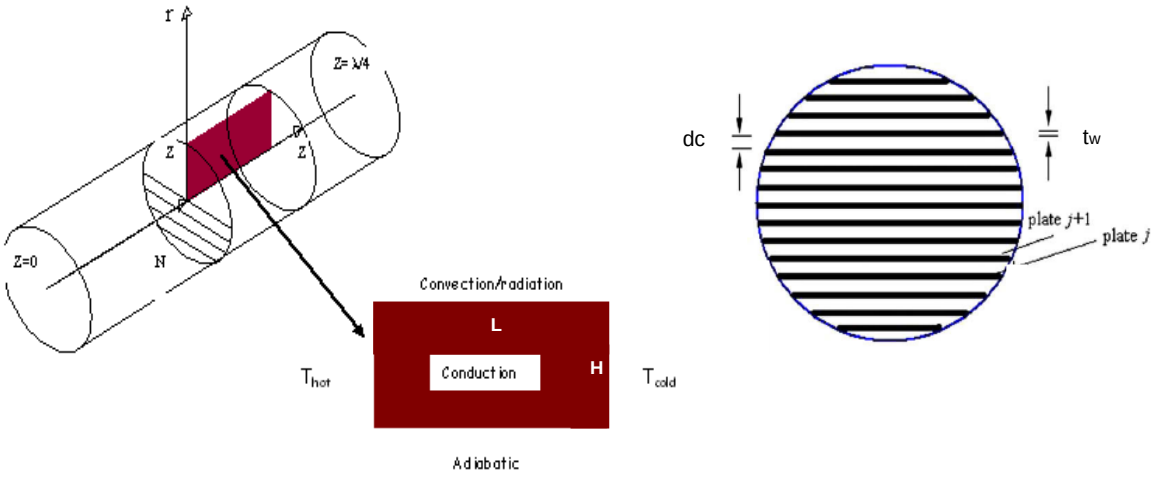

Figure 4.3: Computational domain

4.4 Illustration of the optimisation procedure of the stack

4.4.1 Boundary conditions

The five variables—L, H, dc, Za, N--may only take values within the certain lower and upper bounds. The feasible domains for a thermoacoustic stack are defined as follows:

$$
\begin{aligned}
&L_{min} \le L \le L_{max} \\
&H_{min} \le H \le H_{max} \\
&dc_{min} \le dc \le dc_{max} \\
&Za_{min} \le Za \le Za_{max} - L \\
&N_{min} \le N \le N_{max}
\end{aligned}
\qquad \textbf{Equation 4.4}
$$

$L,\ H,\ dc,\ Za \in \Re+$ and $N \in Z+$

with $dc_{min} = 2\delta_k$ and $dc_{max} = 4\delta_k$ (Tijani et al., 2002) **Equation 4.5**

Additionally, the total number of channels (N) of a given diameter (dc) is limited by the cross-sectional radius of the resonance tube (H). Therefore, the following constraint relation can be determined:

$$N(dc + t_w) \leq 2H$$ **Equation 4.6**

where t_w represents the wall thickness around a single channel and N_{min} and N_{max} predetermined values corresponding respectively to H_{min} and H_{max}

The following boundary conditions are defined:

1. constant hot side temperature (T_h);

2. constant cold side temperature (T_C);

3. adiabatic boundary, modelling the central axis of the cylindrical stack:

$$\left.\frac{\partial T}{\partial r}\right|_{r=0} = 0;$$ **Equation 4.7**

4. free convection and radiation to surroundings (at T_∞) with temperature dependent heat transfer coefficient (h), emissivity (ε), and thermal conductivity (K):

$$K\left.\frac{\partial T}{\partial r}\right|_{r=H} = h(T_S - T_\infty) + \varepsilon k_b\left(T_S^4 - T_\infty^4\right)$$ **Equation 4.8**

4.4.2 Acoustic power

The acoustic power per channel has been derived by Swift (2002). The following equation can be derived for N channel:

$$W = \omega LN\left(\frac{\pi H^2}{2(dc + t_w)}\right)\left[\delta_k \frac{(\gamma - 1)p^2}{\rho c^2 (1+\varepsilon)}(\Gamma - 1) - \delta_v \rho u^2\right]$$ **Equation 4.9**

The relation between the stack perimeter Π and the cross sectional area A as determined by Swift (2002) is given as follows:

$$\Pi = \frac{2A}{dc + t_w}$$ **Equation 4.10**

The amplitudes of the dynamic pressure (p) and gas velocity (u) due to the standing wave in the tube are given by the following equations:

$$p = p_{max}\cos\left(\frac{2\pi Za}{\lambda}\right)$$ **Equation 4.11**

$$u = u_{max}\sin\left(\frac{2\pi Za}{\lambda}\right)$$ **Equation 4.12**

with $u_{max} = \frac{p_{max}}{\rho c}$ **Equation 4.13**

The heat capacity ratio can be expressed by (Zink et al., 2009):

$$\varepsilon = \frac{(\rho c_p \delta_k)_g}{(\rho c_p \delta_s)_s} \frac{\tanh((i+1)y_0/\delta_k)}{\tanh((i+1)l/\delta_s)}$$ **Equation 4.14**

This expression can be simplified to values of $\varepsilon = y_0/\delta_k$ if $y_0/\delta_k < 1$ or $\varepsilon = 1$ if $y_0/\delta_k > 1$ (Zink *et al.,* 2009).

where y_0 represents half of the channel height; l is half of the wall thickness; and δ_s is the solid's thermal penetration depth.

4.4.3 Viscous resistance

Just as the total acoustic power of the stack is dependent on the total number of channels, the viscous resistance also depends on it. The following equation can be derived (Swift, 2002):

$$R_V = \frac{\mu \prod L}{A_C^2 \delta_V N} = \frac{2\mu}{\delta_V} \frac{L}{(d+t_w)\pi H^2 N}$$ **Equation 4.15**

4.4.4 Convective heat flux

The mechanism of convection for the thermoacoustic devices in this study is free convection with air at room temperature. The rate of heat transfer (Long, 1999), ($\dot{Q}_{conv}$) to surround air due to convection is given as follows:

$$\dot{Q}_{conv} = hA(T_S - T_\infty)$$ **Equation 4.16**

The heat transfer coefficient (h) and the heat flux to the surroundings were estimated using a linear temperature profile. In this models, the actual temperature distribution throughout the stack is taken into account by utilising MATLAB finite element toolbox (MATLAB, 2007), which captures the temperature dependence of the heat transfer coefficient. Only the temperature distribution at the shell surface and the temperature gradient at the cold side are of interest. Trapp *et al*. (2011) have derived the final surface temperature distribution as a function of axial direction (Za). It is given by the following equation:

$$T_S = T_h e^{\ln\left(\frac{T_C}{T_h}\right)\frac{Za}{L}}$$ **Equation 4.17**

The convective heat transfer coefficient and the radiative heat flux to the surroundings are assumed to be dependent on this temperature. The total convective heat transfer across the cylindrical shell in its integral form can be described by the following:

$$Q_{conv} = H\int_0^{2\pi}\int_0^{L} h(T(z))(T(z) - T_\infty)dz d\rho \qquad \textbf{Equation 4.18}$$

For the case of a horizontal tube subject to free convection (Baehr & Stephan, 2004), the heat transfer coefficient (h) is derived from the Nusselt number, which is a non-dimensional heat transfer coefficient as follows:

$$h(Ts) = \frac{k_g}{2H} Nu \qquad \textbf{Equation 4.19}$$

$$Nu = 0.36 + \frac{0.518 Ra_D^{\frac{1}{4}}}{\left[1 + \left(\frac{0.559}{Pr}\right)^{\frac{9}{16}}\right]^{\frac{4}{9}}} \qquad \textbf{Equation 4.20}$$

This expression depends on the Prandtl number, which can be expressed as follows:

$$Pr = \frac{\nu}{\alpha} \qquad \textbf{Equation 4.21}$$

$$Ra = \frac{g\beta(T_S - T_\infty)8H^3}{\nu\alpha} \qquad \textbf{Equation 4.22}$$

where Pr is the Prandtl number; T_S is the surface temperature; T_∞ is the (constant) temperature of the surroundings; ν is the viscosity of the surrounding gas; and α is the thermal diffusivity of the surrounding gas (air). The temperature distribution stated in Equation 4.17 is then used to determine the convective heat transfer to the surroundings. After integrating, the following heat flow expression is derived:

$$Q_{conv} = 2\pi HLh\left[\frac{T_C - T_H}{\ln\left(\frac{T_C}{T_H}\right)} - T_\infty\right] \qquad \textbf{Equation 4.23}$$

The following constraint can be derived from Equation 4.17 and Equation 4.22:

$$Za \geq L \log\left(\frac{T_{inf}}{T_C}\right) \qquad \textbf{Equation 4.24}$$

4.4.5 Radiative heat flux

For an object having a surface area (A) a temperature (T) surrounded by air at temperature (T_∞) the object will radiate heat at a rate ($\overset{o}{Q}_{rad}$) given as follows (Seaway, 1996):

$$\overset{o}{Q}_{rad} = k_B \varepsilon A\left(T^4 - T_\infty^4\right) \qquad \textbf{Equation 4.25}$$

The radiative heat flux becomes increasingly important as T_H increases, as shown in the following equation:

$$Q_{rad} = Hk_B \int_0^{2\pi L} \int \varepsilon\left(T_{(z)}{}^4 - T_\infty^4\right) dz d\rho \qquad \textbf{Equation 4.26}$$

where k_B is the Stefan Boltzmann constant and ε is the surface emissivity which depends on the emitted wavelength. After integrating, the following heat flow expression is derived:

$$Q_{rad} = 2\pi HLk_B \varepsilon \left[\frac{T_C^4 - T_H^4}{4 \ln\left(\frac{T_C}{T_H}\right)} - T_\infty^4 \right] \qquad \textbf{Equation 4.27}$$

4.4.6 Conductive heat flux

The temperature distribution is used to determine the temperature gradient at the top surface $Za,\ r = H$. According to Fourier's law (Long, 1999), the heat flow ($\overset{o}{Q}_{cond}$) in the z direction, through a material is expressed as follows:

$$\frac{\Delta Q}{\Delta t} = -kA \frac{\Delta T}{\Delta x} \qquad \textbf{Equation 4.28}$$

The rate at which the flow of heat occurs depends on the material, the geometry and the temperature gradient; it is specified by its conductivity. Similar to the cylindrical shell, this heat flux has to be integrated over the whole surface representing the cold side:

$$Q_{cond} = \int_0^{2\pi H} \int \left(k_{zz} \frac{\partial T}{\partial r} \right) dr d\rho \qquad \textbf{Equation 4.29}$$

where the value of the axial thermal conductivity (k_{zz}) is determined by Equation 4.30 (Zink *et al.*, 2009).

$$k_{zz} = \frac{k_S t_w + k_g dc}{t_w + dc} \qquad \textbf{Equation 4.30}$$

Therefore: $\left.\frac{\partial T}{\partial z}\right|_{z=L} = \frac{\ln\left(\frac{T_C}{T_H}\right)\left(\frac{T_C}{T_H}\right)}{L}$ **Equation 4.31**

And after integration $Q_{cond} = \frac{k_{zz}}{L}\pi H^2 T_C \ln\left(\frac{T_H}{T_C}\right)$ **Equation 4.32**

CHAPTER 5: OPTIMAL DESIGN OPTIMISATION USING A LEXICOGRAPHIC METHOD

5.1 Introduction

The need to provide cooling without environmentally harmful refrigerants is driving the development of technology that will significantly reduce the global warming potential of refrigeration and air conditioning in current systems. One of the most successful examples of such a shift is the Ben and Jerry ice cream cooler (Poese *et al.,* 2004). Thermoacoustic refrigeration is a technology that has already proven its potential for replacing conventional vapour compression driven cycles. In locations where waste heat can be used for the necessary heat input, the potential saving of environmentally harmful materials can be enough to justify a push in the use of thermoacoustic refrigerators in the long term to become a feasible and very reasonable replacement for current technology.

Despite efforts thus far in the development of efficient devices, there are still some important aspects that merit further attention. In particular, the key points that still remain open concern ways of determining the optimal geometry of the device capable of achieving the highest performance and efficiency. This is not a trivial task, since it requires the understanding of the complex interactions between acoustic power, viscous losses and thermal losses for thermoacoustic engines and maximum coefficients of performance and maximum cooling for thermoacoustic refrigerators.

Engineering optimisation has two different parts (Andersson, 2001):

- one, the evaluation of the design proposals; and
- two, the generation of new and hopefully better solutions.

Thus, engineering optimisation consists of both analysis (evaluation) and synthesis (generation of new solutions). The evaluation is usually conducted by means of an objective function which consists of a figure of merit describing how good a design is. The formulation of such an objective function is crucial to the outcome of the optimisation. Neither the objectives nor the constraints are clearly defined in engineering design. However, the focus of this research is on optimisation with stated objective functions or adaptation of previously derived formulations.

The generation of new solutions depends on the optimisation strategy. Within the scope of this research, one optimisation method is used, namely the lexicographic ε-constraint method as this method rests upon a set of design proposals which evolve as the

optimisation progresses. Technically speaking, there is no synthesis or anything creative involved in the solutions generated by this optimisation method when considering a small space. We are merely finding solutions that are already out there waiting to be found. However, the solution space for thermoacoustic engine and refrigerator design is enormous and expanding. Therefore, sophisticated search methods are mandatory to find the best, or even a very good, solution. Optimisation, then, is used as a technique of innovation.

In this chapter, we have developed several advanced mathematical strategies for the optimal design of thermoacoustic refrigerators and thermoacoustic engines. These tools, which aim to facilitate decision-making in these areas, include novel features. First, they optimise the geometry of thermoacoustic devices in addition to the understanding of thermal losses. Secondly, they account for all design parameters simultaneously. Thirdly, they expedite the search for an optimal solution by the use of a lexicographic method.

5.2 General objectives

The objectives of this chapter are as follows:

- to develop a systematic framework for the single objective optimisation of thermoacoustic engines and thermoacoustic refrigerators, all parameters known in advance;
- to develop mathematical programming models to expedite the search for optimal solutions;
- to extend this framework to account for thermal losses typically disregarded in thermoacoustic engines modelling;
- to develop a multi-objective optimisation framework of thermoacoustic refrigerator designs for electronics cooling; and
- to develop effective methods for facilitating the decision-making process in practical applications.

5.3 Mathematical programming

Mathematical programming deals with the problem of minimising or maximising an objective function in the presence of constraints which are either equalities $(h_{n'}(x))$ or inequalities $(g_n(x))$. Consider the following single-objective SO minimisation problem:

$$SO(X) = \min_{x \in X} (f(x))$$

Subject to

$$h_{n'}(x) = 0, \quad n' = 1, 2, ..., N'$$

$$g_n(x) \leq 0, \quad n = 1, 2, ..., N$$

Equation 5.1

where $f(x)$ is an objective function. N' and N are respectively the number of equalities and inequality constraints. X is the search space, and x is a vector of decision variables. If the objective function is linear and the equality or the inequality constraints are all linear, it is a linear programming (LP) problem. The problem takes the form of a nonlinear programming (NLP) model if at least one of the functions defining the objective function or the constraints is nonlinear. In general, different solution algorithms are required for solving LP and NLP problems. In case where a LP problem contains discrete variables (logical or integer) in addition to continuous ones, it is described as a mixed-integer linear programming (MILP) problem. A mixed-integer nonlinear programming (MINLP) problem is defined if the problem contains at least one nonlinear equation. A nonlinear programming with discontinuous derivatives (DNLP) problem is the same as NLP, except that non-smooth functions (abs, min, max) can appear in objective function or constraint. The models developed in this thesis have NLP, MINLP and DNLP formulations.

5.4 Method for solving mathematical programming problems

The NLPs, MINLPs and DNLP models were written and solved in the General Algebraic Modelling System (GAMS). The GAMS optimisation platform was selected due to its wide range of solvers and its availability. GAMS is a high level modelling system for mathematical programming and optimisation. It consists of an integrated development environment (IDE). The user is allowed to express optimisation models in the special programming language called Algebraic Modelling Languages (AML) and then call an appropriate solver to obtain a solution (Figure 5.1). Specifically, LINDOGLOBAL solver (GAMS Development Corporation, 2011) was used to solve the NLP, MINLP and DNLP problems in this work.

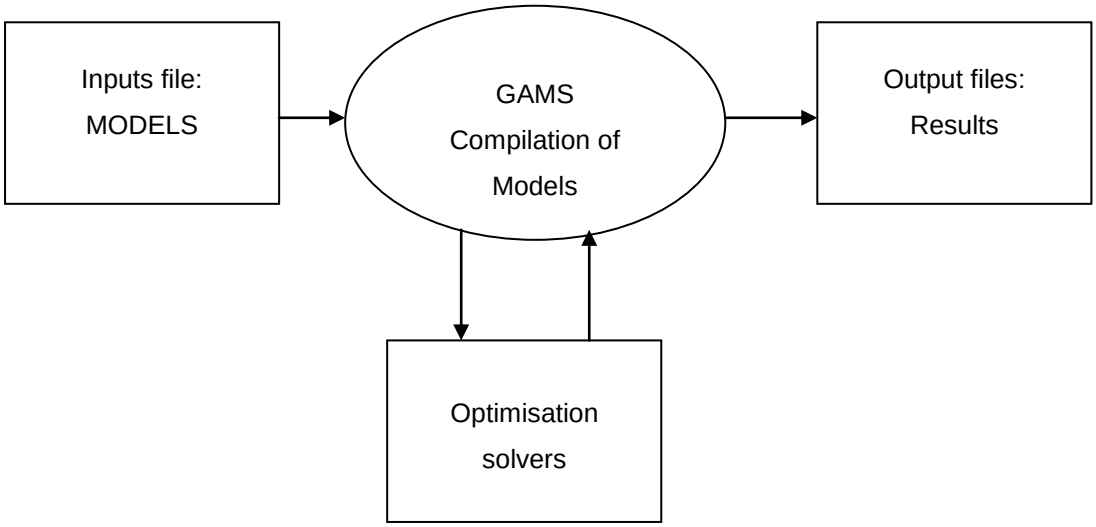

Figure 5.1: GAMS process illustration

5.5 The multi-objective programming problems

5.5.1 Problem definition

The MOO problem, $MO(X)$, can be presented as follows:

$$MO(X) = \min_{x \in X} (F(x) = \{f_1(x), ..., f_k(x), ..., f_o(x)\})$$

subject to

$$h_{n'}(x) \leq 0, \quad n' = 1, 2, ..., N' \qquad \text{Equation 5.2}$$

$$g_n(x) \leq 0, \quad n = 1, 2, ..., N$$

where $F(x)$ denotes the vector of objective functions $f_k(x)$ of the (O) objective functions to be optimised. The set of values taken by the objective functions $f_k(x)$ in the feasible solutions of $MO(X)$ constitutes the feasible objective space (Z).

5.5.2 Pareto optimality

In contrast to single objective optimisation, a solution to a multi-objective optimisation is more of a concept than a definition. Typically, no single or global solution can be considered as such, and often, a set of points that all fit a predetermined definition for an optimum is necessary. The predominant concept in defining the optimal point is that of Pareto optimality (Marler, 2009). A formal definition for a Pareto optimal point in terms of the design space is provided by Vincent and Gratham (1981), Eschenauer *et al.* (1990) and Miettinen (1999). Central to the performance of a particular multi-objective optimisation formulation is deciding whether solving it serves as a necessary and/or sufficient condition for Pareto optimality. Marler and Arora (2009) discuss theoretically necessary and sufficient conditions as a

means of qualifying Pareto optimality. The terms “necessary” and “sufficient” are used in a more practical sense to describe the ability of a method to provide Pareto optimal solutions by Marler (2009).

5.5.3 Classification of some methods to conduct multi-objective optimisation

Most engineering optimisation problems are multi-objective in nature. Many methods are available to tackle this kind of problems. References to multi-objective optimisation in a general sense can be found in Hwang *et al.* (1980), Ringuest (1992) and Steuer (1986). Multi-objective optimisation with applications to engineering design can be found in Marler (2009), Eschenauer *et al.* (1990) and Osyczka (1984).

Depending on when the decision maker articulates his preference concerning the different objectives, the multi-objective optimisation problem can be handled in four different ways: 1) never, 2) before, 3) during, or 4) after the actual optimisation procedure.

- In the first two approaches, the different objective functions are aggregated to one overall objective function. As a result, optimisation is then conducted with one single objective. The solution is strongly dependent on how the objectives were aggregated. To support the decision maker in aggregating the objectives, different methods have been developed in the literature (Gonzalez-Pachon & Romero, 2001; Gonzalez-Pachon & Romero, 2007).
- In the third approach, the decision maker progressively articulates his preferences on the different objectives as an iterative process. This approach works under the assumption that the decision maker has been presented with some alternatives before the search for an optimal solution starts. He will be better equipped to value the objectives.
- In the fourth approach, the decision maker doesn’t articulate any preferences among the objectives. The outcome of this optimisation is a set of Pareto optimal solutions which elucidate the trade-off between the objectives. In order to select the final design, the decision maker then has to trade the objectives against each other. Thus, optimisation is conducted before the decision maker articulates his preferences.

The methods developed for this research belong to the fourth approach. The four different approaches, exemplified with suitable methods, are detailed in Figure 5.2. The Pareto-optimal solutions in this work are obtained by means of the ε-constraint method.

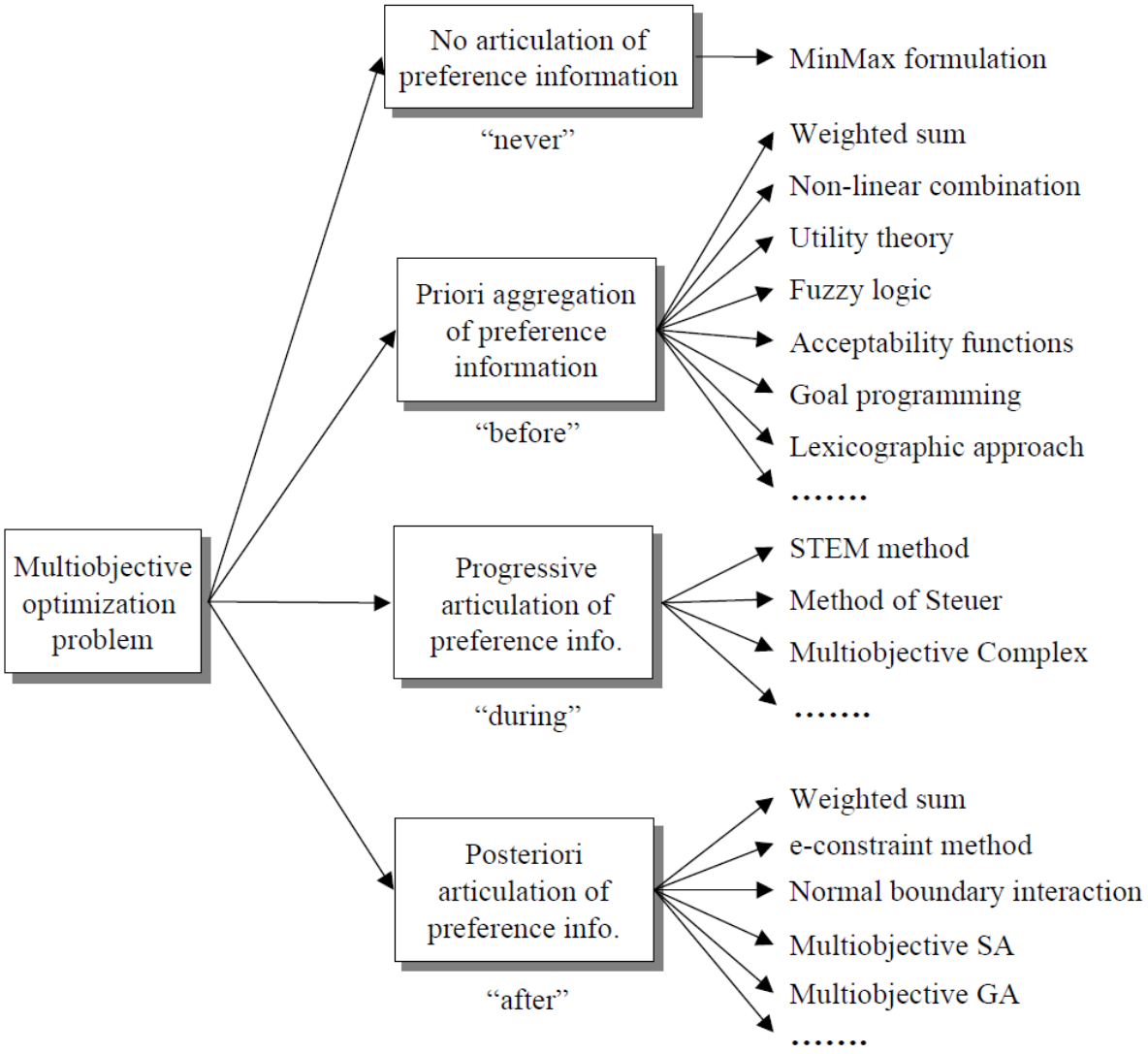

Figure 5.2: Classification of multi-objective optimisation methods

(Adapted from Hwang *et al.*, 1980)

5.5.4 E-constraint method

In this method, the decision maker specifies the trade-off among multiple objectives. This method is also known as the trade-off method, or reduced feasible space Ω method, because the technique involves a search in a progressively reduced criterion space. The original problem is converted to a new problem in which one objective is minimised (or maximised) while the other objectives are added as constraints to the feasible solution space of Ω as follows:

$$SO_e(X) = \min_{x \in \Omega} (f_1(x))$$

subject to

$$f_2(x) \le \varepsilon_2,\ f_3(x) \le \varepsilon_3,\ ..., f_p(x) \le \varepsilon_p,\ x \in \Omega$$

Equation 5.3

By solving iteratively problem $SO_e(X)$ for different values of ε_p, different Pareto solutions can be obtained. The range of at least p-1 objectives functions is necessary in order to determine grid points for $\varepsilon_1,...,\varepsilon_p$ values and apply the ε-constraint method. The most common approach is to calculate these ranges from the payoff table. Each objective function is optimised individually. The mathematical details of computing payoff table for a Multi-objective Mathematical Programming (MMP) problem can be found in Cohon (1978). The payoff table for a MMP problem with (p) competing objective functions is calculated as follow:

- The individual optima of the objective functions (f_i) are calculated. The optimum value of the objective functions (f_i) and the vector of decision variables which optimises the objective function (f_i) are indicated respectively by $f_i^*\left(\bar{x}_i^*\right)$ and $\bar{x}_i^*$.
- Represent the payoff table including $f_1^*\left(\bar{x}_1^*\right),\ f_2^*\left(\bar{x}_{2i}^*\right),...,\ f_p^*\left(\bar{x}_p^*\right)$ as follows:

$$\Phi = \begin{pmatrix} f_1^*\left(\bar{x}_1^*\right) & \cdots & f_i^*\left(\bar{x}_1^*\right) & \cdots & f_p^*\left(\bar{x}_1^*\right) \\ \vdots & \ddots & & & \vdots \\ f_1^*\left(\bar{x}_i^*\right) & \cdots & f_i^*\left(\bar{x}_i^*\right) & \cdots & f_p^*\left(\bar{x}_i^*\right) \\ \vdots & & & \ddots & \vdots \\ f_1^*\left(\bar{x}_p^*\right) & \cdots & f_i^*\left(\bar{x}_p^*\right) & \cdots & f_p^*\left(\bar{x}_p^*\right) \end{pmatrix}$$

Equation 5.4

- Determine the range of each objective function in the payoff table based on utopia and pseudo-nadir points. The Utopia point (f^U) refers to a specific point where all objectives are simultaneously at their best possible values. It is generally outside the feasible region. However, the Nadir point (f^{SN}) is a point where all objective functions are simultaneously at their worst values. It is generally in the objective space

$$f_i^U \le f_i\left(\bar{x}\right) \le f_i^{SN}$$

Equation 5.5

- Divide the range of $p-1$ objectives functions $f_2,...,f_p$ to $q_2,...,q_p$ into equal intervals using $(q_2 - 1),...,(q_p - 1)$ intermediate equidistant points, respectively.
- Convert the MMP problem into $\prod_{i=2}^{p}(q_i + 1)$ single objective optimisation sub-problems as follows:

$$\min f_1(\bar{x})$$

subject to

$$f_2(\bar{x}) \le \varepsilon_{2,n2}, \ldots, f_p(\bar{x}) \le \varepsilon_{p,np}$$

Equation 5.6

$$\varepsilon_{2,n2} = f_2^{SN} - \left(\frac{f_2^{SN} - f_2^{U}}{q_2} \right) \times n2, \quad n2 = 0, 1, \ldots, q_2$$

$$\varepsilon_{2,n2} = f_2^{SN} - \left(\frac{f_2^{SN} - f_2^{U}}{q_2} \right) \times n2, \quad n2 = 0, 1, \ldots, q_2$$

- Each sub-problem is a candidate solution or Pareto optimal solution of the MMP problem. At the same time, some of these optimisation sub-problems may have infeasible solution space due to the added constraints for $f_2, \ldots, f_p$; such sub-problems are discarded.
- Selection of the most preferred solution out of the obtained Pareto optimal solutions by the decision maker.

The detailed explanation of the algorithm can be found in Ehrgott (2000).

5.5.5 Augmented ε-constraint method

In the ordinary ε-constraint method, the efficiency of Pareto solutions is not guaranteed. Inefficient solutions can be generated. The obtained solution is considered inefficient if there is another Pareto solution that can improve at least one objective function without deteriorating the other objectives functions. In order to overcome this drawback, we consider the following:

a. The objective functions constraints in Equation 5.6 are transformed into equality constraints by means of the slack variable technique (Bard, 1998; Mavrotas, n.d). Therefore, the augmented ε-constraint method can be formulated as follows:

$$\min \left(f_1(\bar{x}) - \delta \left(\frac{s_2}{r_2} + \frac{s_3}{r_3} + \ldots + \frac{s_p}{r_p} \right) \right)$$

subject to

Equation 5.7

$$f_2(\bar{x}) + s_2 = \varepsilon_2, \ldots, f_p(\bar{x}) + s_p = \varepsilon_p \qquad s_2, \ldots, s_p \in R^+$$

where $s_2, \ldots, s_p$ represent the slack variables for the constraints in Equation 5.6 of the Multi-objective Mathematical Programming (MMP) problem and δ is a small number usually between 10^{-3} and 10^{-6} (Mavrotas, 2009). This formulation (Equation 5.7), preventing the generation of an inefficient solution, is known as 'augmented ε-

constraint method' due to the augmentation of the objective function (f_1) by the second term. Its proof can be found in Mavrotas (2009).

b. The concept of relative importance of objective in generating the Pareto solutions is introduced to be consistent with the decision maker policy. Although each objective has its own relative importance in the MMP problem, the previous formulations consider all slack variables with equivalent importance. In MMP problems, the concept of optimality stipulates that we search for the most preferred solution among the generated Pareto set. To remedy the inconsistency in the decision making process, the formulation of the augmented ε-constraint method is modified by the use of a lexicographic optimisations of these series of objective functions. Practically, the first objective function of higher priority is optimised, obtaining $\min f_1 = x_1^*$. Then the second objective function is optimised by adding the constraint $f_1 = x_1^*$ in order to keep the solution of the first optimisation. Assume that we obtain $\min f_2 = x_2^*$. Subsequently, the constraints $f_1 = x_1^*$ and $f_2 = x_2^*$ are added to optimise the third objective function in order to keep the previous optimal solutions and so on, until all objective functions are dealt with. The flowchart of the lexicographic optimisation of a series of objective functions is illustrated in Figure 5.3.

By the combination of the lexicographic optimisation and augmented ε-constraint method, the range of the objective functions in the payoff table is optimised and results in the generation of *only* efficient solutions within the identified ranges. This is illustrated by the flowchart in Figure 5.4.

The proposed augmented ε-constraint method is expected to provide a representative subset of the Pareto set which in most cases is adequate. The basic step towards further penetration of the generation methods in our multi-objective mathematical problems is to provide appropriate codes in a GAMS environment and produce efficient solutions. Two different case studies are used to illustrate the proposed MMP methodology in a context of thermoacoustic coolers modelling and design optimisation.

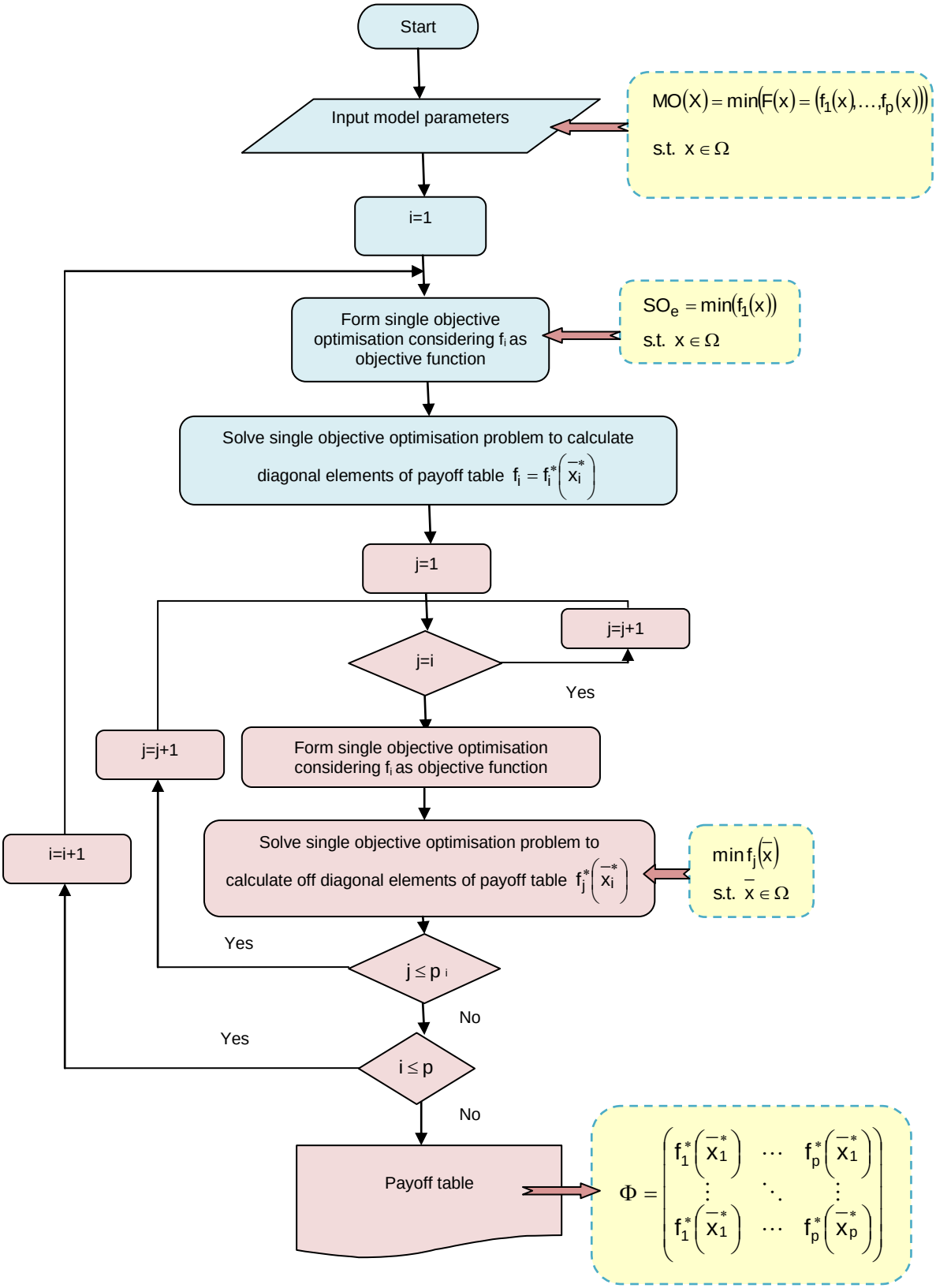

Figure 5.3: Flowchart of the lexicographic optimisation for calculation of payoff table.

(Adapted from Aghaei *et al*, 2009)

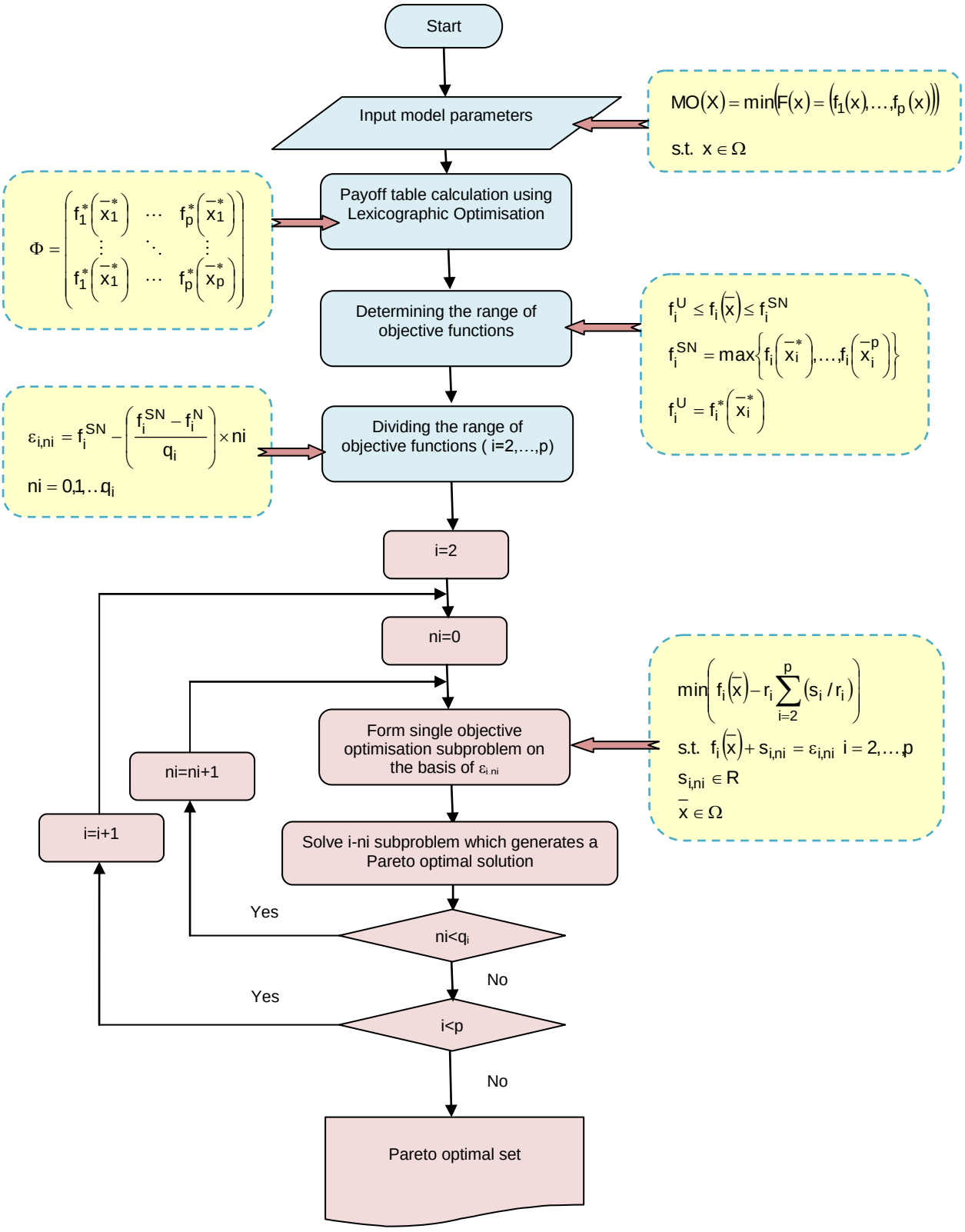

Figure 5.4: Flowchart of the proposed MMP solution method including augmented ε - constraint with lexicographic optimisation.

(Adapted from *Aghaei et al*, 2009)

5.6 Solution methodology of the multi-objective mathematical programming problems

5.6.1 Engine

5.6.1.1 Single objective optimisation

All the expressions involved in our mathematical programming formulation (MPF) have been presented in Chapter 4. Together with the following expressions, they represent a mixed-integer nonlinear programming (MINLP) problem:

$$(MPF)\ \min_{L,H,Za,dc,N} \xi = w_1(-W) + w_2 R_V + w_3 Q_{conv} + w_4 Q_{rad} + w_5 Q_{cond} \qquad \textbf{Equation 5.8}$$

This mathematical model characterises the essential elements of a standing wave thermoacoustic engine. In the following discussion, we analyse restricted cases of our objectives and identify general tendencies of the structural variables to influence individual objective components. To illustrate our approach, we consider the thermoacoustic couple (TAC) as described in Atchley *et al.,* (1990) which consists of a parallel-plate stack placed in helium-filled resonator. All relevant parameters are given in Table 5.1 and Table 5.2.

Table 5.1: Specifications for thermoacoustic couple

Parameter	Symbol	Value	Unit
Isentropic coefficient	ν	1.67	
Gas density	ρ	0.16674	kg/m^3
Specific heat capacity	c_p	5193.1	J/kg.K
Dynamic viscosity	μ	$1.9561.10^{-5}$	kg/m.s
Maximum velocity	u_{max}	670	m/s
Maximum pressure	p_{max}	114003	Pa
Speed of sound	c	1020	m/s
Thickness plate	t_w	1.91.10-4	m
Frequency	f	696	Hz
Thermal conductivity Helium	k_g	0.16	W/(m.K)
Thermal conductivity stainless steel	k_S	11.8	W/(m.K)
Isobaric specific heat capacity	c_p	5193.1	J/(kg.K)

Table 5.2: Additional parameters used for programming

Parameter	Symbol	Value	Unit
Temperature of the surrounding	T_∞	298	K
Constant cold side temperature	T_C	300	K
Constant hot side temperature	T_H	700	K
Wavelength	λ	1.466	m
Thermal expansion	β	$1/T_\infty$	1/K
Thermal diffusivity	α	2.1117E-5	m^2s-1

5.6.1.2 Emphasising acoustic work

All proposed MINLP models are solved by GAMS 23.8.1, using LINDOGLOBAL solver on a personal computer Pentium IV 2.1 GHz with 4 GB RAM. The following constraints (upper and lower bounds) have been enforced on variables in order for the solver to carry out the search of the optimal solutions in those ranges:

$$\begin{aligned} &L.lo = 0.005;\ L.up = 0.05; \\ &Za.lo = 0.005;\ Za.up = 0.050 \\ &N.lo = 20;\ N.up = 50; \\ &H.lo = 0.005;\ H.up = 0.050 \\ &dc.lo > 2.\delta_k;\ dc.up < 4.\delta_k \end{aligned}$$

Equation 5.9

Setting the objective function weights to $w_2 = w_3 = w_4 = w_5 = 0$ and $w_1 = 1$, the problem reduces to Equations 4.1-4.3, Equation 4.9, Equations 4.11-4.13, constraints in Equation 4.6 and 4.24 and variable restrictions in Equation 5.9. Objective function (Equation 5.8) becomes:

$$\min_{L,H,dc,Za,N} \xi_W = (-W)$$

Equation 5.10

In our approach, the geometry range is small in order to illustrate the behaviours of the objective functions and optimal solution of a small-scale thermoacoustic engine. The detailed model is reported in the Appendix A. In Table 5.3, the optimal solutions that maximise ξ_W are represented with letters subscripted with an asterisk:

Table 5.3: Optimal solutions maximising acoustic work

	L^*	H^*	Za^*	dc^*	N^*	W^*	CPU time (s)
x^*	0.050	0.034	0.005	0.001	50	4.5536E+9	18.171

Physically, this optimal solution can be interpreted as:

- making the stack as long as possible $\left(L^* = L_{max}\right)$;
- making the stack spacing wider;
- moving the stack as near as possible to the closed end $\left(Za^* = Za_{min}\right)$ maximising the available pressure amplitude for the thermodynamic cycle and thus work output W;
- increasing the number of channels $\left(N^* = N_{max}\right)$ and the channel diameter dc so that we maximise the thermoacoustically active surface area; and
- Setting $N^* = N_{max}$ and $dc^* = dc_{max}$ ensures that H can take its maximum value in constraint Equation 4.6.

5.6.1.3 Emphasising viscous resistance

We emphasise R_V by setting objective function weights $w_1 = w_3 = w_4 = w_5 = 0$ and $w_2 = 1$. The problem then simplifies to Equations 4.2 and 4.15, constraints Equation 4.6 and 4.24, and variable restrictions in Equation 5.9. Objective function (Equation 5.8) becomes:

$$\min_{L,H,dc,Za,N} \xi_{R_V} = R_V \qquad \textbf{Equation 5.11}$$

The detailed model is reported in Appendix B. In Table 5.4, the optimal solutions that minimise ξ_{R_V} are represented with letters subscripted with an asterisk:

Table 5.4: Optimal solutions minimising viscous resistance

	L^*	H^*	Za^*	dc^*	N^*	R_v^*	CPU time (s)
x^*	0.005	0.008	0.005	5.8140E-4	20	3.467	1.062

Physically, this optimal solution can be interpreted as:

- making the stack as small as possible $\left(L^* = L_{min}\right)$, thereby reducing the individual (viscous) resistance of each channel to its minimum;
- moving the stack as near as possible to the closed end $\left(Za^* = Za_{min}\right)$;
- decreasing the number of channels $N^* = N_{min}$; and
- setting $N^* = N_{min}$ and $dc^* = dc_{min}$ to ensure that H can take its minimum value in constraint Equation 4.6.

5.6.1.4 Emphasising convective heat flux

We can emphasise Q_{conv} by setting objective function weights $w_1 = w_2 = w_4 = w_5 = 0$ and $w_3 = 1$. The problem then reduces to Equations 4.17 and 4.19 and Equations 4.20-4.22, constraints Equations 4.6 and 4.24, and variable restrictions in Equation 5.9. Objective function (Equation 5.8) becomes:

$$\min_{L,H,dc,Za,N} \xi_{Q_{conv}} = Q_{conv} \qquad \textbf{Equation 5.12}$$

The detailed model is reported in Appendix C. In Table 5.5, the optimal solutions that minimise $\xi_{Q_{conv}}$ are represented with letters subscripted with an asterisk:

Table 5.5: Optimal solutions minimising convective heat flux

	L^*	H^*	Za^*	dc^*	N^*	Q^*_{conv}	CPU time (s)
x^*	0.005	0.008	0.005	5.93522E-4	20	0.1623	0.718

Physically, this optimal solution can be interpreted as:

- making the stack as short as possible $\left(L^* = L_{min}\right)$;
- moving the stack as near as possible to the closed end $\left(Za^* = Za_{min}\right)$;
- decreasing the number of channels $\left(N^* = N_{min}\right)$; and
- setting $N^* = N_{min}$ and $dc^* = dc_{min}$ to ensure that H can take its minimum value in constraint Equation 4.6.

5.6.1.5 Emphasising radiative heat flux

We can emphasise Q_{rad} by setting objective function weights $w_1 = w_2 = w_3 = w_5 = 0$ and $w_4 = 1$, so that only Equation 4.27, constraints Equation 4.6 and 4.24 and variable restrictions in Equation 5.9 are active. For these restricted optimisation problems, objective function (Equation 5.8) becomes

$$\min_{L,H,dc,Za,N} \xi_{Q_{rad}} = Q_{rad} \qquad \textbf{Equation 5.13}$$

The detailed model is reported in Appendix D. In Table 5.6, the optimal solutions that minimise $\xi_{Q_{rad}}$ are represented with letters subscripted with an asterisk:

Table 5.6: Optimal solutions minimising radiative heat flux

	L^*	H^*	Za^*	dc^*	N^*	Q^*_{rad}	CPU time (s)
x^*	0.005	0.008	0.005	5.93522E-4	20	0.7305	5.750

Physically, this optimal solution can be interpreted as:

- making the stack as short as possible $\left(L^* = L_{min}\right)$;
- moving the stack as near as possible to the closed end $\left(Za^* = Za_{min}\right)$;
- decreasing the number of channels $\left(N^* = N_{min}\right)$; and
- setting $N^* = N_{min}$ and $dc^* = dc_{min}$ ensures that H can take its minimum value in constraint Equation 4.6.

5.6.1.6 Emphasising conductive heat flux

We emphasise Q_{cond} by setting objective function weights $w_1 = w_2 = w_3 = w_4 = 0$ and $w_5 = 1$, so that only Equations 4.30 and 4.32, constraints in Equation 4.6 and 4.24, and variable restrictions in Equation 5.9 are active. Objective function (Equation 5.8) becomes:

$$\min_{L,H,dc,Za,N} \xi_{Q_{cond}} = Q_{cond} \qquad \textbf{Equation 5.14}$$

The detailed model is reported in Appendix E. In Table 5.7, the optimal solutions that minimise $\xi_{Q_{cond}}$ are represented with letters subscripted with an asterisk:

Table 5.7: Optimal solutions minimising conductive heat flux

	L^*	H^*	Za^*	dc^*	N^*	Q^*_{cond}	CPU time (s)
x^*	0.050	0.008	0.005	5.8140E-4	20	2.8951	0.656

Physically, this optimal solution can be interpreted as:

- making the stack as large as possible $\left(L^* = L_{max}\right)$;
- moving the stack as near as possible to the closed end $\left(Za^* = Za_{min}\right)$;
- decreasing the number of channels $\left(N^* = N_{min}\right)$; and
- Setting $N^* = N_{min}$ and $dc^* = dc_{min}$ to ensure that H can take its minimum value in constraint Equation 4.6.

5.6.1.7 Emphasising all objective components

Lastly, we simultaneously considered all five objective components by regarding acoustic work (W), viscous resistance (R_V), convective heat flux (Q_{conv}), radiative heat flux (Q_{rad}) and conductive heat flux (Q_{cond}) as five distinct objective components. All the expressions involved in the multi-objective mathematical programming (MMP) have been presented in the previous section. The optimisation task is formulated as a five-criteria mixed-integer nonlinear programming problem (MPF) that simultaneously minimises the negative magnitude of the acoustic work (W) (since it is the only objective to be maximised), the viscous resistance (R_V), the convective heat flux (Q_{conv}), the radiative heat flux (Q_{rad}) and the conductive heat flux (Q_{cond}).

$$(MPF)\ \min_{L,H,Za,dc,N} \xi = \begin{Bmatrix} -W_{(L,H,Za,dc,N)}, R_{V(L,H,Za,dc,N)}, Q_{conv(L,H,Za,dc,N)}, \\ Q_{rad(L,H,Za,dc,N)}, Q_{cond(L,H,Za,dc,N)} \end{Bmatrix} \qquad \textbf{Equation 5.15}$$

subject to constraints in Equations 4.6 and 4.24, and variable restrictions in Equation 5.17.

In this formulation, (L,H,Za,dc,N) denotes the geometric parameters.

There is no single optimal solution that simultaneously optimises all the five objectives functions. In these cases, the decision makers are looking for the “most preferred” solution. To find the most preferred solution of this multi-objective model, the augmented ε-constraint method (AUGMECON) as proposed by Mavrotas (2009) is applied. The AUGMECON method has been coded in GAMS. The code is available in the GAMS library (http://www.gams.com/modlib/libhtml/epscm.htm) with an example. While the part of the code that has to do with the example (the specific objective functions and constraints), as well as the parameters of AUGMENCON have been modified in this case, the part of the code that performs the calculation of payoff table with lexicographic optimisation and the production of the Pareto optimal solutions is fully parameterized in order to be ready to use.

Practically, the ε-constraint method is applied as follows: from the payoff table the range of each one of the p-1 objective functions that are going to be used as constraints is obtained. Then the range of the ith objective function is divided into qi equal intervals using (q_i-1) intermediate equidistant grid points. Thus in total (q_i + 1) grid points that are used to vary parametrically the right hand side (ε_i) of the ith objective function are obtained. The total number of runs becomes (q_2 + 1)$\times$(q_3 + 1) $\times \ldots \times$ (q_p + 1). The augmented ε-constraint method for solving model (Equation 5.15) can be formulated as:

$$\max\left(W_{(L,H,Za,dc,N)} + dir_1\ r_1 \times \left(\frac{s_2}{r_2} + \frac{s_3}{r_3} + \frac{s_4}{r_4} + \frac{s_5}{r_5} \right) \right)$$

Subject to

$$R_{V(L,H,Za,dc,N)} - dir_2\ s_2 = \varepsilon_2$$

$$Q_{conv(L,H,Za,dc,N)} - dir_3\ s_3 = \varepsilon_3 \qquad \textbf{Equation 5.16}$$

$$Q_{rad(L,H,Za,dc,N)} - dir_4\ s_4 = \varepsilon_4$$

$$Q_{conv(L,H,Za,dc,N)} - dir_5\ s_5 = \varepsilon_5$$

$$s_i \in \Re^+$$

where dir_i is the direction of the ith objective function, which is equal to -1 when the ith function should be minimised, and equal to +1, when it should be maximised. Efficient solutions to the problem are obtained by parametrical iterative variations in the ε_i. s_i are the introduced surplus variables for the constraints of the MMP problem. $r_1\ s_i / r_i$ are used in the second term of the objective function, in order to avoid any scaling problem. The formulation of Equation 5.16 is the augmented ε-constraint method due to the augmentation of the objective function W by the second term. The following constraints (upper and lower bounds) have been enforced on variables in order for the solver to carry out the search of the optimal solutions within each identified ranges:

$$\begin{aligned} &L.lo = 0.005;\ \ L.up = 0.05; \\ &Za.lo = 0.005; \\ &H.lo = 0.005; \\ &dc.lo > 2.\delta_k;\ \ dc.up < 4.\delta_k \end{aligned} \qquad \textbf{Equation 5.17}$$

We use lexicographic optimisation for the payoff table; the application of the model (Equation 5.16) will provide *only* the Pareto optimal solutions, avoiding the weakly Pareto optimal solutions. Efficient solutions to the proposed model have been found using AUGMENCON method and the LINDOGLOBAL solver. To save computational time, the early exit from the loops as proposed by Mavrotas (2009) has been applied. The range of each five objective functions is divided in four intervals (five grid points). The integer variable N has been given values from 20 to 50. This process generates optimal solutions corresponding to each integer variable. Three different solutions representing sets of Pareto solutions obtained have been reported in Table 5.8. The maximum CPU time taken to complete the results is 1029.700 sec. The detailed model is reported in Appendix F.

Table 5.8: Non-dominated solutions found using AUGMENCON

(a) Solutions 1

N	L*	dc*	H*	Za*	W^*	$R_V{}^*$	$Q_{cond}{}^*$	$Q_{conv}{}^*$	$Q_{rad}{}^*$	CPU time (s)
21 channels	0.047	0.00098521	0.012	0.005	13752.67	671.112	1.803	9.301	1.312	1029.700
25 channels	0.043	0.00100000	0.016	0.005	23061.14	292.007	3.010	10.230	1.552	1024.989
26 channels	0.043	0.00100000	0.017	0.005	25924.46	243.410	3.367	10.464	1.614	1017.766
35 channels	0.044	0.00100000	0.022	0.005	63219.01	110.627	5.783	13.081	2.171	47.409
36 channels	0.045	0.00100000	0.022	0.005	68794.08	113.043	5.790	13.461	2.233	94.506
37 channels	0.047	0.00097718	0.022	0.005	74687.64	125.216	5.557	13.927	2.295	118.498
42 channels	0.040	0.00100000	0.028	0.005	108740.00	47.243	9.780	14.533	2.594	446.288
43 channels	0.049	0.00092090	0.024	0.005	117420.00	97.351	6.763	15.798	2.672	386.976

(b) Solutions 2

N	L*	dc*	H*	Za*	W^*	$R_V{}^*$	$Q_{cond}{}^*$	$Q_{conv}{}^*$	$Q_{rad}{}^*$	CPU time (s)
21 channels	0.050	0.00100000	0.014	0.031	16532.19	467.927	1.975	8.776	1.606	1029.700
25 channels	0.050	0.00100000	0.017	0.031	27895.99	277.342	2.799	9.952	1.911	1024.989
26 channels	0.050	0.00100000	0.018	0.031	31384.93	246.556	3.027	10.257	1.988	1017.766
35 channels	0.050	0.00100000	0.024	0.031	76558.06	101.072	5.485	12.701	2.676	47.409
36 channels	0.050	0.00100000	0.024	0.031	83310.46	92.881	5.803	12.965	2.753	94.506
37 channels	0.050	0.00100000	0.025	0.031	90448.66	85.552	6.130	13.226	2.829	118.498
42 channels	0.050	0.00100000	0.028	0.031	131330.00	58.420	7.961	14.426	3.186	446.288
43 channels	0.050	0.00100000	0.029	0.031	141980.00	54.504	8.280	14.760	3.288	386.976

(c) Solutions 3

N	L*	dc*	H*	Za*	W^*	$R_V{}^*$	$Q_{cond}{}^*$	$Q_{conv}{}^*$	$Q_{rad}{}^*$	CPU time (s)
21 channels	0.050	0.00100000	0.014	0.005	16829.09	467.927	1.975	10.959	1.606	1029.700
25 channels	0.050	0.00100000	0.017	0.005	28393.75	277.342	2.799	12.427	1.911	1024.989
26 channels	0.050	0.00100000	0.018	0.005	31939.10	246.535	3.027	12.785	1.988	1017.766
35 channels	0.050	0.00100000	0.024	0.005	77912.46	101.072	5.485	15.865	2.676	47.409
36 channels	0.050	0.00100000	0.024	0.005	84783.29	92.881	5.803	16.195	2.753	94.506
37 channels	0.050	0.00100000	0.025	0.005	92046.64	85.552	6.130	16.522	2.829	118.498
42 channels	0.050	0.00100000	0.028	0.005	133580.00	58.420	7.934	17.987	3.186	446.288
43 channels	0.050	0.00100000	0.029	0.005	144480.00	54.504	8.280	18.439	3.288	386.976

Figure 5.5 represents the Pareto optimal solutions graphically; it shows that there is not one single optimal solution that optimises the geometry of the stack and highlights the fact that the geometrical parameters are interdependent, supporting the use of a multi-objective approach for optimisation of thermoacoustic engines. To maximise acoustic work W and minimise viscous resistance and thermal losses simultaneously, there is a specific stack length (L) to which correspond a specific stack height (H), a specific stack position (Za), a specific stack spacing (dc) and a specific number of channels (N). This study highlights the

fact that the geometrical parameters are interdependent, which support the use of a multi-objective approach for optimisation. It should be noted that in all cases, locating the stack closer to the closed end produced the desired effect. All Pareto optimal solutions can be identified to reinforce the decision maker's final decision and preferred choice.

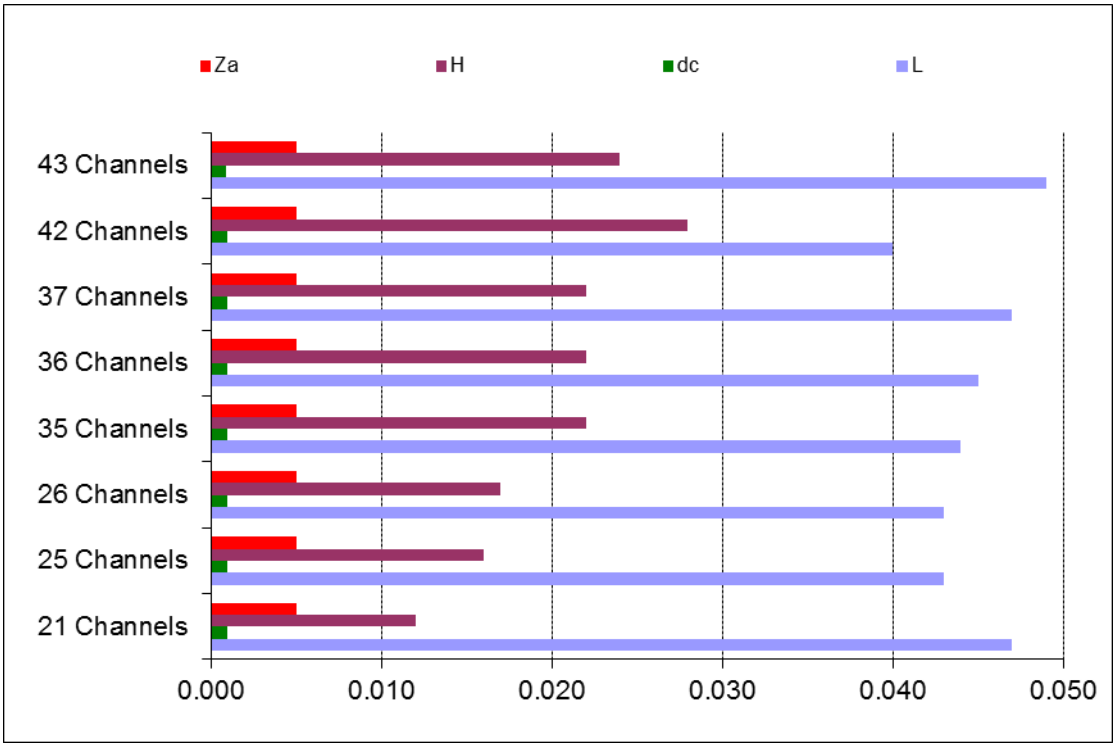

Figure 5.5: Optimal structural variables

These optimal solutions are then used to construct Figure 5.6 and Figure 5.7 representing, respectively, acoustic work, viscous resistance, conductive, convective and radiative heat fluxes as a function of the number of channels. It can be seen that an increase in number of channels results in a similar increase of the acoustic work, the convective heat flux and the radiative heat flux. The conductive heat flux shows a slightly different trend, especially between 35 and 40 and above 42 channels. Unlike the previous trend, the viscous resistance decreases with the number of channels. These graphs highlight the conflicting nature of the five objective functions in the design and optimisation of thermoacoustic engines.

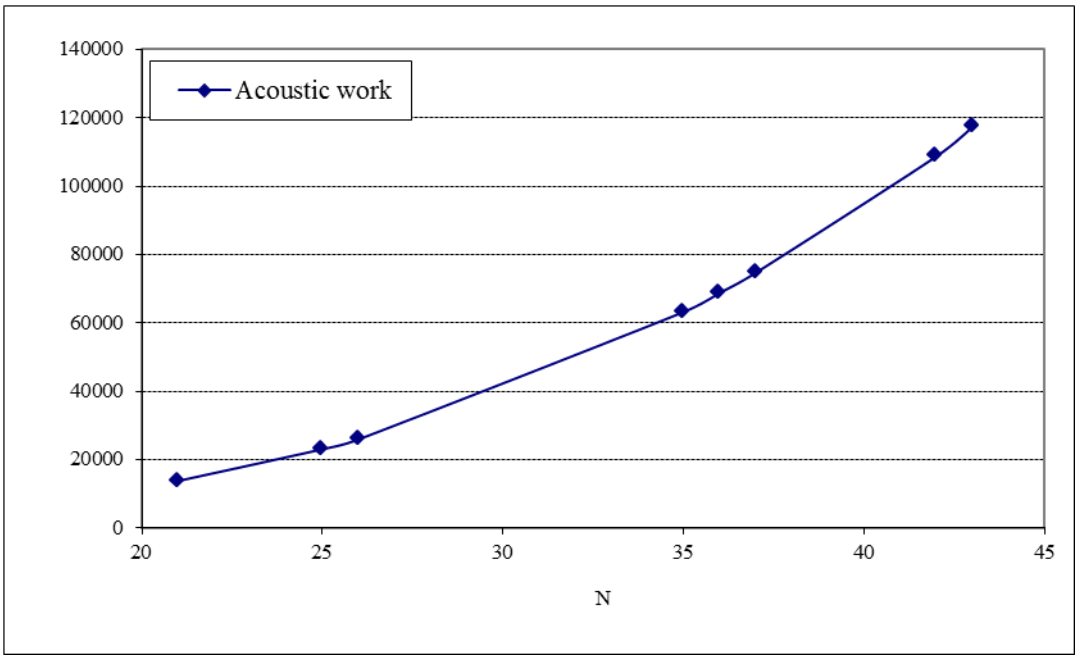

(a)

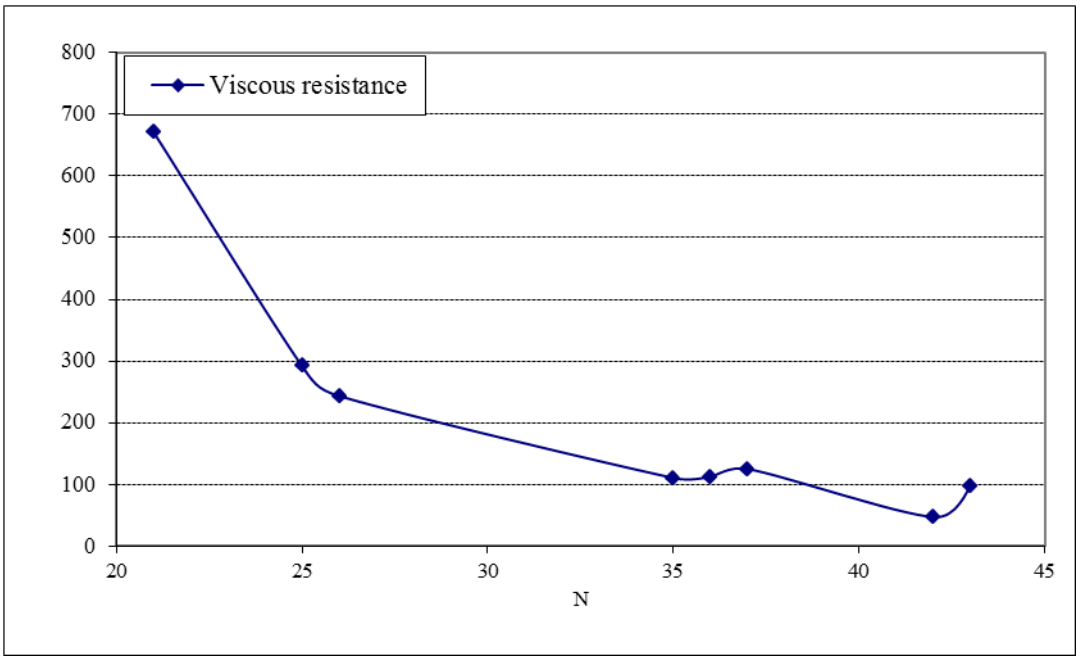

(b)

Figure 5.6: (a) Acoustic power and (b) viscous resistance plotted as a function of N

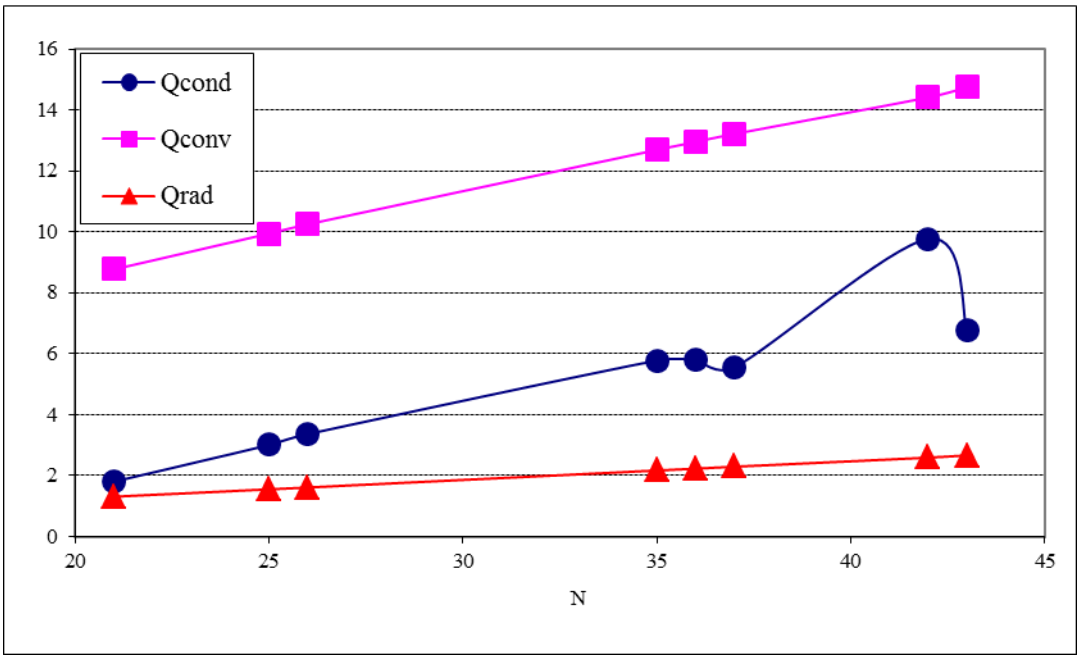

Figure 5.7: Conductive, convective and radiative heat fluxes plotted as a function of N

The optimal dimension functions of the number of channels are presented in Figures 5.8 through 5.15. The corresponding acoustic work, viscous resistance, conductive, convective and radiative heat fluxes are shown respectively in Figures 5.16 through 5.20. Considering the decision maker's preference, these figures are good indications of expected values of objective functions for specific geometrical parameters. While maximum value is expected for greater number of stack channels, thermal losses increase as well. The conflicting nature of the five objectives can be observed in these profiles. These results clarify the trade-offs between the geometrical parameters of the stack for maximum performance of thermoacoustic engines.

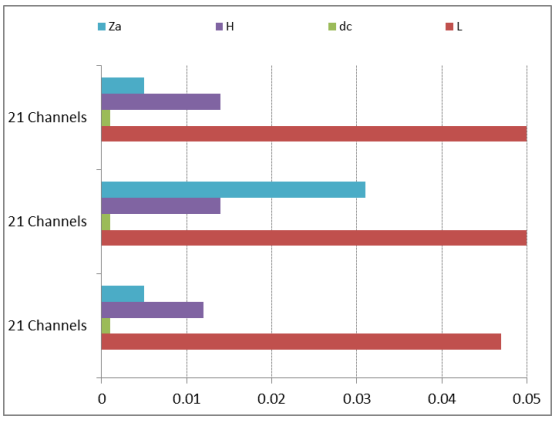

Figure 5.8: Optimal dimensions for N=21

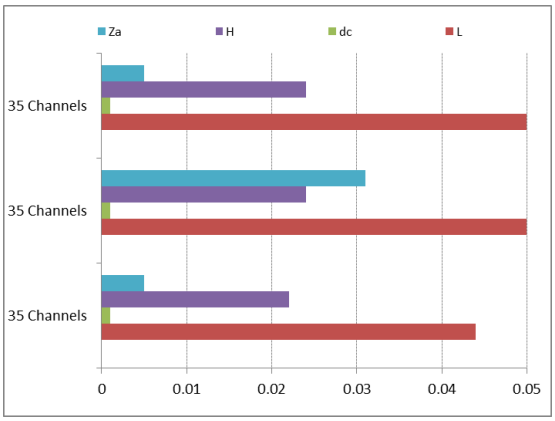

Figure 5.11: Optimal dimensions for N=35

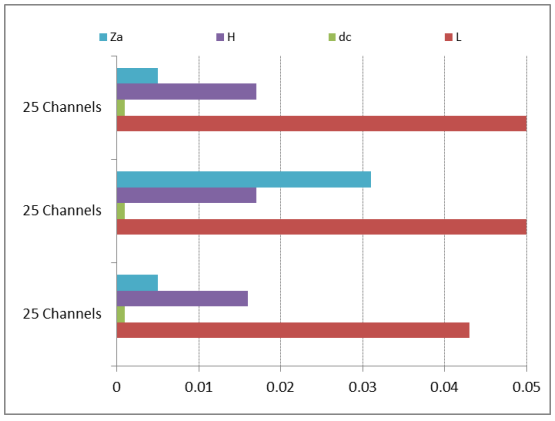

Figure 5.9: Optimal dimensions for N=25

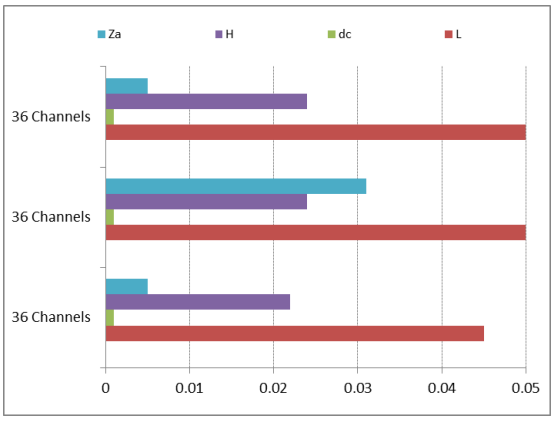

Figure 5.12: Optimal dimensions for N=36

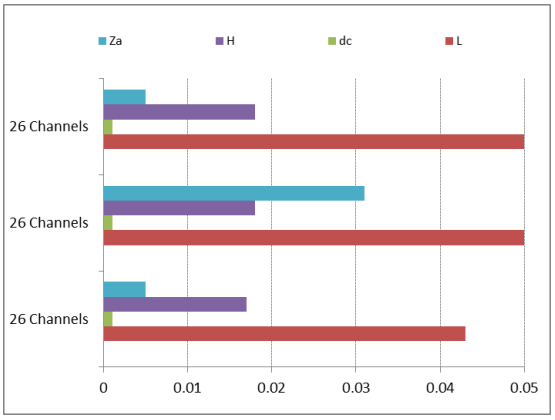

Figure 5.10: Optimal dimensions for N=26

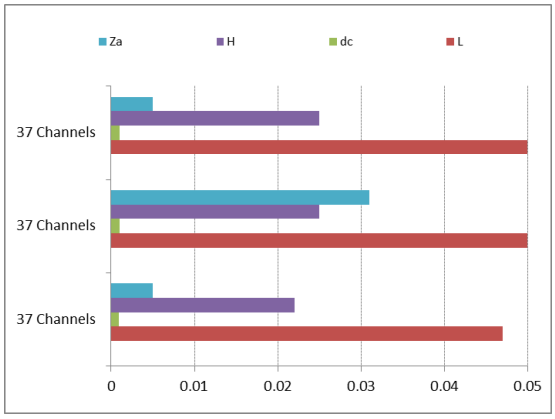

Figure 5.13: Optimal dimensions for N=37

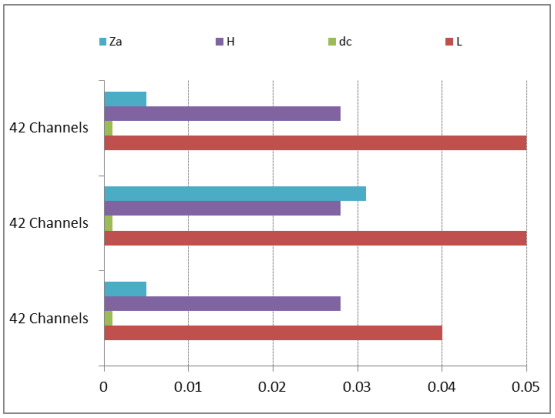

Figure 5.14: Optimal dimensions for N=42

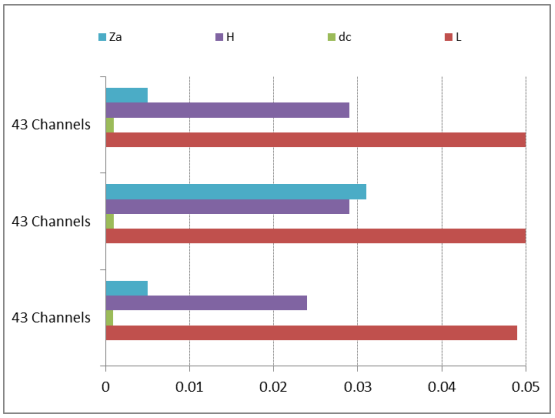

Figure 5.15: Optimal dimensions for N=43

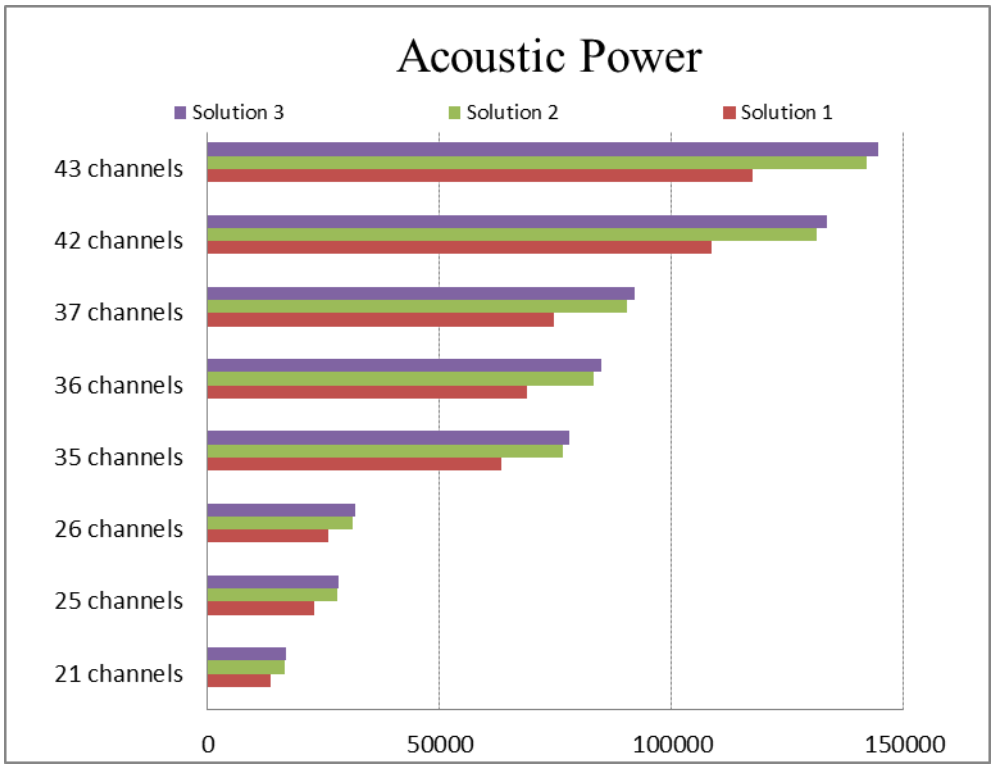

Figure 5.16: Acoustic power function of N describing three solution sets

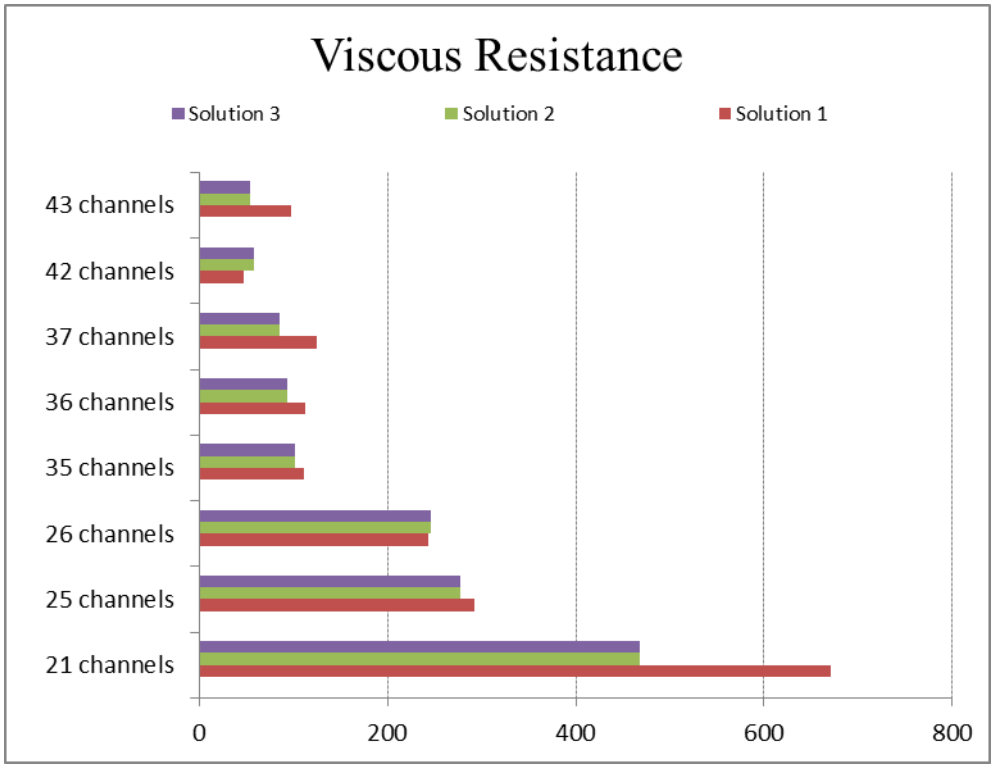

Figure 5.17: Viscous resistance function of N representing three solution sets

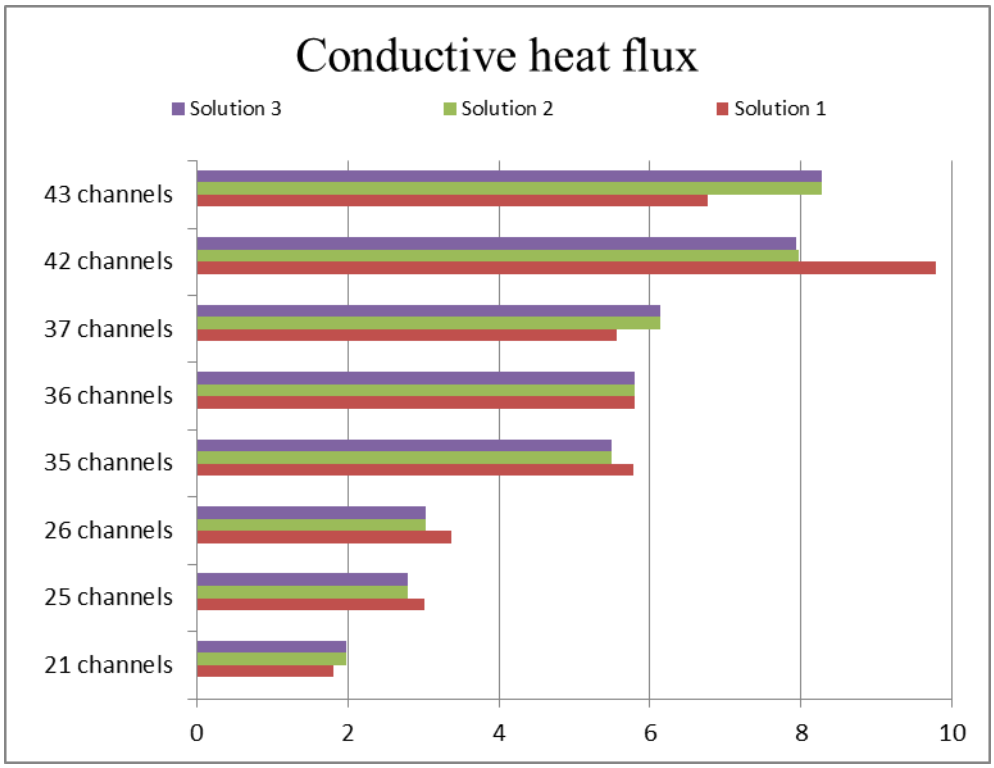

Figure 5.18: Conductive het flux function of N representing three solution sets

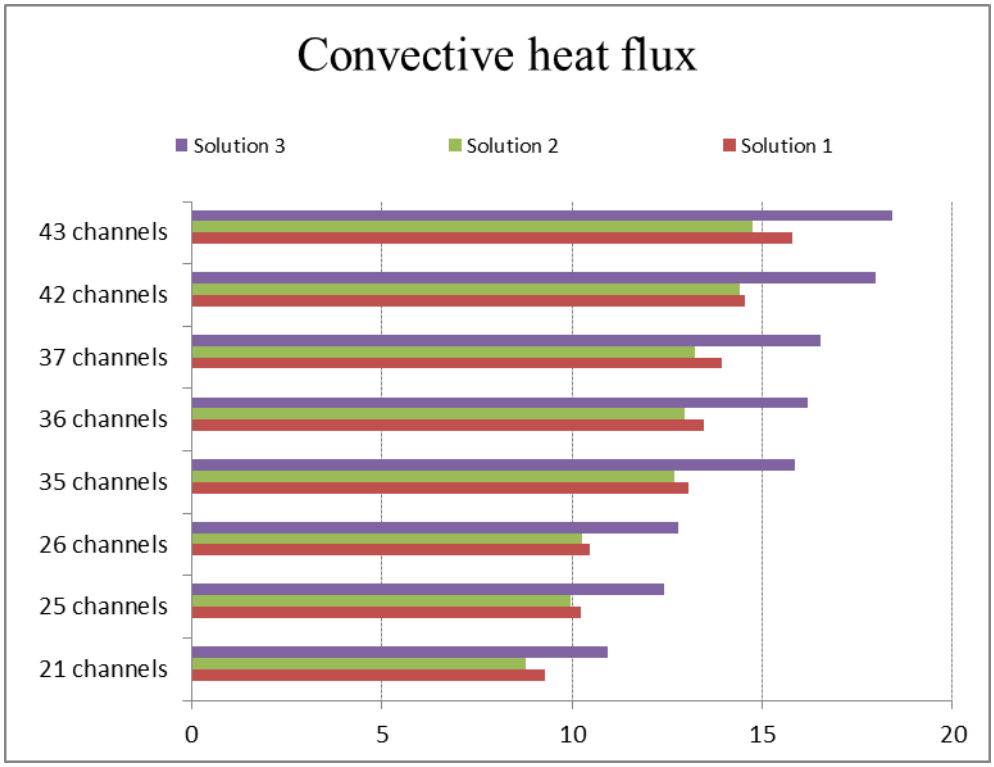

Figure 5.19: Convective heat flux function of N representing three solution sets

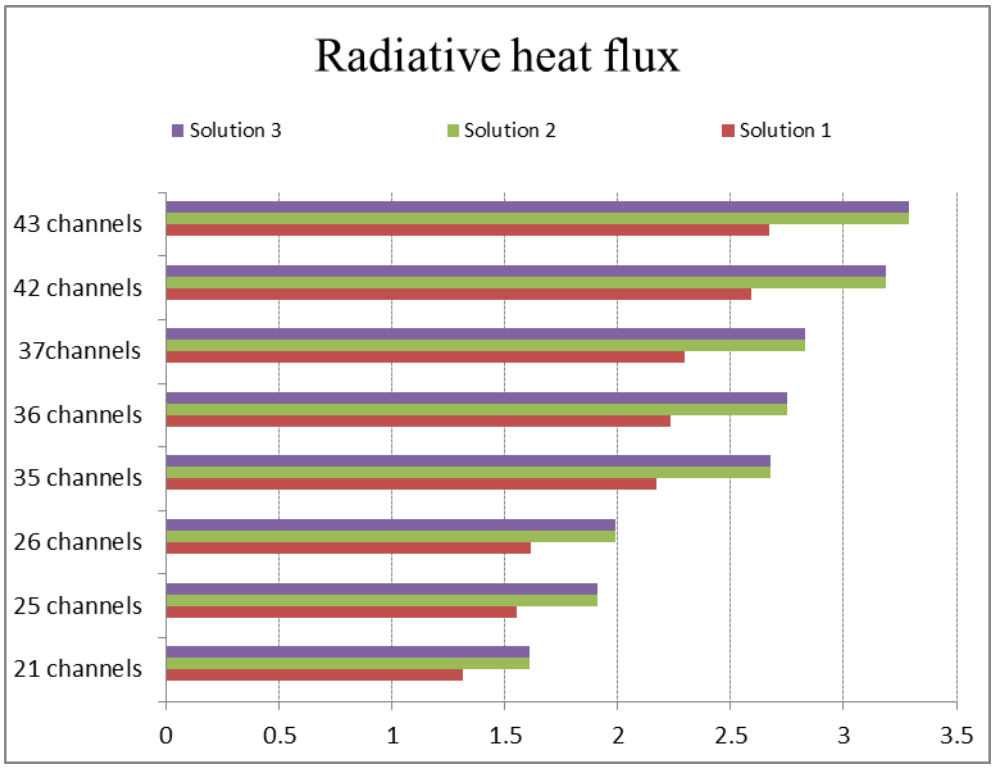

Figure 5.20: Radiative heat flux function of N representing three solution sets

5.6.1.8 Solutions' comparison

An alternative way to simultaneously maximise acoustic work and minimise losses (viscous resistance as well as heat flows) is to consider the thermal efficiency (η) which can be defined as the ratio of the work output over the sum of the work output and losses as follows:

$$\eta = \frac{W}{W + R_v + Q_{conv} + Q_{rad} + Q_{cond}} \qquad \textbf{Equation 5.18}$$

The viscous resistance in Equation 4.15 has the units [kg/m^{4}s]. In order to express this in terms similar to the other variables used in Equation 5.18, we multiply Equation 4.15 (subsequently R_v* in Table 5.8) by the volumetric velocity [m^3/s] and the oscillating frequency [1/s], yielding [W/m] as final unit for the viscous resistance per channel used in Equation 5.18. This ratio can be used to compare the results obtained previously and identify the preferred solution. Figure 5.21 represents the comparison of results based on Equation 5.18. Based on the magnitude of work output, viscous resistance and heat fluxes, the following solution 2 / 42 channels, solution 2 / 43 channels and solution 3 / 43 channels are the best solutions for this application.

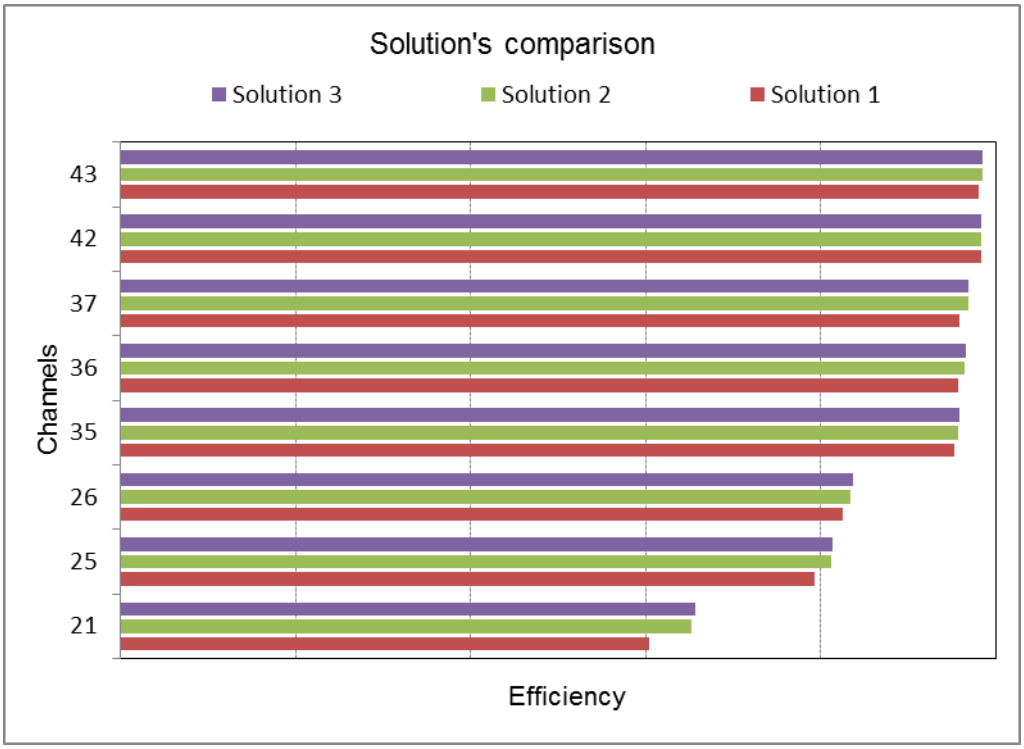

Figure 5.21: TAE results comparisons

5.6.1.9 Conclusion

Optimisation as a design aid is required for a thermoacoustic engine to be competitive on the current market. Previous studies have relied heavily upon parametric studies. This section

targets the geometry of the thermoacoustic stack and uses a multi-objective optimisation approach to find the optimal set of geometrical parameters that optimises the device. Five different parameters describing the geometry of the device (stack length, stack height, stack placement, stack spacing and number of channels) have been studied. Five different objectives have been identified; a weight has been given to each of them to allow the designer to place a desired emphasis on each. A mixed-integer nonlinear programming problem for thermoacoustic stack has been implemented in GAMS. We have determined design statements for each single case of objective emphasis. In the case of multiple objectives considered simultaneously, we have applied an improved version of a multi-objective solution method, the epsilon-constraint method called augmented epsilon-constraint method (AUGMENCON). This process generates optimal solutions which are then used to illustrate the conflicting nature of objective functions. The results demonstrate the interdependence between the geometrical parameters of the stack, again supporting the use of our multi-objective approach to optimise the geometry of thermoacoustic engines. The Pareto optimal solutions obtained will assist the decision maker in selecting the preferred alternatives. It is a personal choice whether to emphasise the thermal behaviour or the acoustic behaviour.

5.6.2 Refrigerator

5.6.2.1 Single objective optimisation

All the expressions involved in our mathematical programming formulation (MPF) have been presented in Chapter 3. Together with the following expressions, they represent a nonlinear programming problem with discontinuous derivatives (DNLP):

$$(MPF)\ \min_{BR,\delta_{kn},L_{Sn},X_{Sn}} \xi = w_1(\Phi_C) + w_2(COP) + w_3\left(\overset{o}{W}_2\right) \qquad \textbf{Equation 5.19}$$

This mathematical model characterises the essential elements of a standing wave thermoacoustic refrigerator. In the following discussion we analyse restricted cases of our objectives, and identify general tendencies of the parameters to influence individual objective components. To illustrate our approach, we consider the design requirement as described by Herman and Travnicek (2006) consisting of a parallel-plate stack placed in helium-filled resonator. All relevant parameters are given in Table 5.9 and Table 5.10.

Table 5.9: Design parameters

Design requirements		
Mean pressure	Pm [Pa]	500,000
Drive ratio	DR [%]	3.5
Normalised temperature difference	θ or ΔT_{mn}	0.030
Stack material	Mylar	

Table 5.10: Additional parameters

Working fluid: Helium		
Prandtl number	σ	0.67
Isentropic coefficient	γ	1.63
Calculated parameters		
Sound speed	a [m/s]	1054.4
Resonant frequency, c/λ	f [Hz]	24,752
Thermal penetration depth	δ_k [mm]**	0.23

**This value was divided by 10 in this study to reduce significantly the computational time that could otherwise take several days for multiple objective emphasis. Therefore, the values obtained in this study should be multiplied by 10 to compute the actual value.

5.6.2.1.1 Emphasising acoustic cooling load

All proposed DNLP models are solved by GAMS 23.8.1, using LINDOGLOBAL solver on a personal computer Pentium IV 2.1 GHz with 4 GB RAM. The following constraints (upper and lower bounds) have been enforced on variables to facilitate the solver in searching for the optimal solutions in those ranges:

$$\begin{aligned} &L_{Sn}.lo = 0.001;\ L_{Sn}.up = 0.500; \\ &X_{Sn}.lo = 0.010;\ X_{Sn}.up = 1.000 \\ &BR.lo = 0.700;\ BR.up = 0.900; \\ &\delta_{kn}.lo = 2\delta_k;\ \delta_{kn}.up = 4\delta_k; \end{aligned} \qquad \textbf{Equation 5.20}$$

Setting the objective function weights to $w_2 = w_3 = 0$ and $w_1 = 1$ in Equation 5.18, the problem reduces to Equations 3.22-3.24, and variable restrictions in Equation 5.20. Objective function (Equation 5.18) becomes:

$$\max_{BR,\delta_{kn},L_{Sn},X_{Sn}} \xi_{\Phi_C} = (\Phi_C) \qquad \textbf{Equation 5.21}$$

In our approach, the geometry range is small so as to illustrate the behaviours of the objective functions and optimal solution of a small-scale thermoacoustic refrigerator. The detailed model is reported in Appendix G. In Table 5.11, the optimal solutions that maximise ξ_{Φ_C} are represented with letters superscripted with an asterisk:

Physically, this optimal solution can be interpreted as:

- making the stack as short as possible $\left(L_{Sn}^{*} = L_{Sn\min}\right)$,
- moving the stack as near as possible of the closed end $\left(X_{Sn}^{*} = X_{Sn\min}\right)$ and,

  reducing the porosity of the stack $\left(BR^{*} = BR_{\min} \text{ and } \delta_{kn} = \delta_{kn\min}\right)$

Table 5.11: Optimal solutions maximising cooling load

	L_{Sn}^{*}	X_{Sn}^{*}	BR^{*}	δ_{kn}^{*}	Φ_C^{*}	CPU time (s)
X^{*}	0.001	0.010	0.700	0.046	7.2659E-4	10.383

The maximum cooling load reported in Table 5.11 is given by:

$\Phi_{C\max}$=7.2659E-4

The decision maker can also determine the minimum cooling load by formulating the problem as follows:

Setting the objective function weights to $w_2 = w_3 = 0$ and $w_1 = 1$ in Equation 5.18, the problem reduces to Equations 3.22-3.24, and variable restrictions in Equation 5.19. Objective function (Equation 5.18) becomes:

$$\min_{BR,\delta_{kn},L_{Sn},X_{Sn}} \xi_{\Phi_C} = (\Phi_C) \qquad \textbf{Equation 5.22}$$

The minimum cooling load $\Phi_{C\,min}$=4.3339E-8

$\Phi_{C\,max}$ and $\Phi_{C\,min}$ have been used as upper and lower bounds for the objective Φ_C in the models.

5.6.2.1.2 Emphasising coefficient of performance (COP)

We emphasise COP by setting objective function weights $w_1 = w_3 = 0$ and $w_2 = 1$ in Equation 5.18. The problem then simplifies to Equations 3.22, 3.23 and 3.25, and variable restrictions in Equation 5.19. The maximal performance for all refrigerators is given by the Carnot coefficient of performance obtained as follows (Wetzel & Herman, 1997):

$$COP_C = \frac{(2-\theta)}{2\theta} \qquad \textbf{Equation 5.23}$$

This value is used as the upper bound for the objective COP. Objective function (Equation 5.18) becomes:

$$\max_{BR,\delta_{kn},L_{Sn},X_{Sn}} \xi_{COP} = (COP) \qquad \textbf{Equation 5.24}$$

The detailed model is reported in Appendix H. In Table 5.12, the optimal solutions that maximise ξ_{COP} are represented with letters superscripted with an asterisk.

Physically, this optimal solution can be interpreted as:

- making the stack as short as possible $\left(L_{Sn}^{*} = L_{Sn\,min}\right)$,
- moving the stack slightly from the closed end $\left(X_{Sn}^{*} > X_{Sn\,min}\right)$ and,
- reducing the porosity of the stack and making the stack spacing greater then $\delta_{kn\,min}$ $\left(BR^{*} = BR_{min} \text{ and } \delta_{kn} > \delta_{kn\,min}\right)$.

Table 5.12: Optimal solutions maximising COP

	L_{Sn}^{*}	X_{Sn}^{*}	BR^{*}	δ_{kn}^{*}	COP^{*}	CPU time (s)
x^{*}	0.001	0.014	0.700	0.065	32.8	0.206

5.6.2.1.3 Emphasising acoustic power loss

We emphasise $\overset{o}{W}_2$ by setting objective function weights $w_1 = w_2 = 0$ and $w_3 = 1$ in Equation 5.18. The problem then simplifies to Equations 3.27 and variable restrictions Equation 5.19. The objective function (Equation 5.18) becomes:

$$\max_{BR,\delta_{kn},L_{Sn},X_{Sn}} \xi_{\overset{o}{W}_2} = \left(\overset{o}{W}_2\right) \qquad \textbf{Equation 5.25}$$

The detailed model is reported in Appendix I. In Table 5.13, the optimal solutions that minimise $\xi_{\overset{o}{W}_2}$ are represented with letters superscripted with an asterisk.

Table 5.13: Optimal solutions minimising acoustic power loss

	L_{Sn}^*	X_{Sn}^*	BR^*	δ_{kn}^*	$\overset{o}{W}_2^*$	CPU time(s)
x^*	0.001	0.010	0.700	0.046	3.8121E-9	0.347

Physically, this optimal solution can be interpreted as:

- making the stack as short as possible $\left(L_{Sn}^* = L_{Snmin}\right)$,
- moving the stack as near as possible to the closed end $\left(X_{Sn}^* = X_{Snmin}\right)$ and,
- reducing the porosity of the stack $\left(BR^* = BR_{min} \text{ and } \delta_{kn}^* = \delta_{knmin}\right)$

5.6.2.1.4 Single objective optima: variable analysis

Table 5.14 summarises the results of Sections 5.6.2.1.1, 5.6.3.1.2 and 5.6.2.1.3, highlighting the behaviour of parameters. For these objectives, ↑ indicates an increasing tendency, ↓ indicates a decreasing tendency, and ǂ indicates a conflicting tension between parameters. Note the lack of tension in parameters for the cooling load (Φ_C) and the acoustic power loss ($\overset{o}{W}_2$), which share the same optimal solution.

Table 5.14: Tendency of parameters when optimising individual components

	Φ_C	COP	$\overset{o}{W}_2$
L_{Sn}	↓	↓	↓
X_{Sn}	↓	↑ ǂ	↓
BR	↓	↓	↓
δ_{kn}	↓	↑ ǂ	↓

5.6.2.2 Emphasising all objective components

Lastly, we simultaneously consider all three objective components by regarding cooling load (Φ_C), coefficient of performance (COP) and acoustic power lost ($\overset{o}{W}_2$) as three distinct objective components. Most of the expressions involved in the formulation of the multi-objective mathematical programming problem (MPF) have been presented in the previous section. The optimisation task is formulated as a three-criterion nonlinear programming problem with discontinuous derivatives (DNLP) that simultaneously maximise the magnitude of the cooling load (Φ_C), maximise the coefficient of performance (COP) and minimise acoustic power lost ($\overset{o}{W}_2$).

$$(MPF)\ \max_{L_{Sn},X_{Sn},BR,\delta_{kn}} \xi = \left\{ \begin{array}{l} \Phi_{C(L_{Sn},X_{Sn},BR,\delta_{kn})}, \\ COP_{(L_{Sn},X_{Sn},BR,\delta_{kn})}, \\ \overset{o}{X}_{2\,(L_{Sn},X_{Sn},BR,\delta_{kn})} \end{array} \right\} \qquad \textbf{Equation 5.26}$$

subject to bound limits Φ_{Cmax} - Φ_{Cmin}, Equation 5.22 and the following constraint:

$$\Phi_C = \Phi_H - \Phi_W > 0 \qquad \textbf{Equation 5.27}$$

A negative cooling load does not have any physical meaning and thus the solutions for which this condition is not met have been eliminated. In Equation 5.26, $(L_{Sn}, X_{Sn}, BR, \delta_{kn})$ denotes the parameters of the thermoacoustic refrigerator.

The lexicographic optimisation for each objective function to construct the payoff table for the multi-objective mathematical programming models (MPF) is proposed in order to yield only Pareto optimal solutions, avoiding the generation of weak, non-efficient solutions (Mavrotas, 2009). In the formulation of the problem, the selection of the primary objective function (most important function) depends on the decision maker. Frequently, this decision is based on problem information and can lead to partial representation of Pareto optimal sets due to the tendency of the solution to cluster toward the maximum of the primary objective function. We have, therefore, articulated the preferences and specific limits on objective functions rather than relying on relative importance of objectives as suggested by Marler (2009) to identify the best problem formulation. Subsequently, the augmented ε-constraint method for solving the model (Equation 5.26) has been formulated twice and the preferred optimal solutions have been identified based on the value of the obtained cooling load (Φ_C) and coefficient of performance (COP):

a. Model A

$$\max\left(\Phi_{C(L_{Sn},X_{Sn},BR,\delta_{kn})} + dir_1\ r_1 \times\left(\frac{s_2}{r_2}+\frac{s_3}{r_3}+\frac{s_4}{r_4}+\frac{s_5}{r_5}\right)\right)$$

Subject to

$$COP_{(L_{Sn},X_{Sn},BR,\delta_{kn})} - dir_2\ s_2 = \varepsilon_2 \qquad \textbf{Equation 5.28}$$

$$\overset{o}{W}_{2(L_{Sn},X_{Sn},BR,\delta_{kn})} - dir_3\ s_3 = \varepsilon_3$$

$$s_i \in \Re^+$$

b. Model B

$$\max\left(COP_{(L_{Sn},X_{Sn},BR,\delta_{kn})} + dir_1\ r_1 \times\left(\frac{s_2}{r_2}+\frac{s_3}{r_3}+\frac{s_4}{r_4}+\frac{s_5}{r_5}\right)\right)$$

Subject to

$$\Phi_{C(L_{Sn},X_{Sn},BR,\delta_{kn})} - dir_2\ s_2 = \varepsilon_2 \qquad \textbf{Equation 5.29}$$

$$\overset{o}{W}_{2(L_{Sn},X_{Sn},BR,\delta_{kn})} - dir_3\ s_3 = \varepsilon_3$$

$$s_i \in \Re^+$$

where dir_i is the direction of the ith objective function, which is equal to -1 when the ith function should be minimised, and equal to +1 when it should be maximised. Efficient solutions to the problem are obtained by parametrical iterative variations in the ε_i. s_i are the introduced surplus variables for the constraints of the MP problem. $r_1\ s_i / r_i$ are used in the second term of the objective function in order to avoid any scaling problem. The formulation of Equations 5.27 and 5.28 are known as the augmented ε-constraint method due to the augmentation of the objective function (Φ_C) and COP by the second term. The following constraints (upper and lower bounds) have been enforced on variables in order for the solver to search for the optimal solutions in those ranges:

$$\begin{aligned} &X_{Sn}.lo = 0.010;\ \ X_{Sn}.up = 1.000 \\ &BR.lo = 0.700;\ \ BR.up = 0.900; \\ &\delta_{kn}.lo = 2\delta_k;\ \ \delta_{kn}.up = 4\delta_k \end{aligned} \qquad \textbf{Equation 5.30}$$

We use lexicographic optimisation for the payoff table; the application of models (Equations 5.27 and 5.28) will provide only the Pareto optimal solutions, avoiding the weakly Pareto optimal solutions. Efficient solutions for the proposed model have been found using the AUGMENCON method and the LINDOGLOBAL solver. To save computational time, the early exit from the loops as proposed by Mavrotas (2009) has been applied. The range of each five objective functions is divided into four intervals (five grid points). The normalised stack length (L_{Sn}) has been arbitrarily given successive values of 0.05-0.1-0.15-0.2-0.25-0.3-0.35-0.4-0.5. This process generates optimal solutions corresponding to each value of L_{Sn}. The following section reports only the best sets of Pareto solutions obtained successively with models A and B. These results suggest that for an arbitrary chosen fixed value of L_{Sn}, a maximum value of Φ_C and COP can be found. The maximum CPU time taken to complete the results is 324.981 sec. The detailed models are reported in Appendices J and K.

In Figure 5.21 and Figure 5.22, the results of performance calculations illustrating the efficiency of thermoacoustic core are shown. They are represented in terms of maximum cooling and coefficient of performance relative to Carnot COPR. Presenting the results in the form of COPR instead of COP is advantageous in the fact that it does not take into account the trivial part of the Carnot part of the performance, accounting for the temperature dependence of the efficiency. In terms of normalised design parameters, the COPR can be determined as follows (Wetzel & Herman, 1997):

$$COPR = \frac{COP}{COP_C} = \frac{\left(|\Phi_H| - |\Phi_W|\right)/|\Phi_W|}{(2-\theta)/(2\theta)} \qquad \textbf{Equation 5.31}$$

5.6.2.3 Results and discussions

5.6.2.3.1 Optimisation for best coefficient of performance

In Figure 5.21, results that quantify the effect of the normalised stack length on the COPR are displayed. For this purpose, the normalised stack length (L_{Sn}) the normalised stack position (X_{Sn}) the blockage ratio (BR) and the normalised thermal penetration depth δ_{kn} were allowed to vary simultaneously. Optimal solutions describing the best parameters have been presented in Table 5.16. The results suggest the COPR increases by locating the stack centre position closer (as compared to the cooling load) to the pressure antinode (closed end) and making the stack length (L_{Sn}) shorter. This concurs with previous studies by

Herman and Travnicek (2006) who suggest that higher pressure amplitudes at the pressure antinode (closed end) cause more pronounced temperature change.

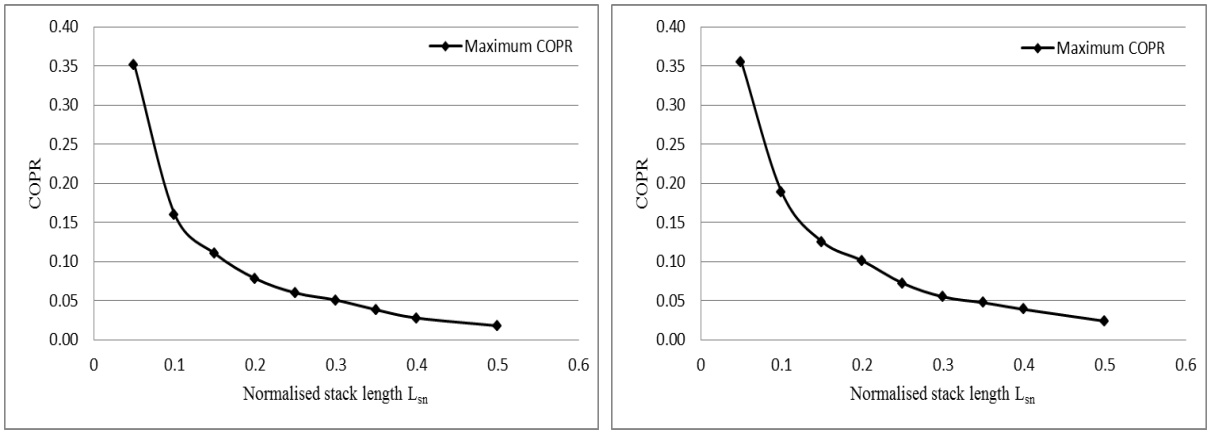

(a) (b)

Figure 5.22: (a) Cooling load as function of the normalised stack length for model A and (b) Cooling load function of the normalised stack length for model B.

The results suggest that there is a distinct optimum of the coefficient of performance for a selected set of design parameters, and depending on the formulation adopted (model A or B) with the maximum value described by:

Model A

$$COPR^{*} = \begin{bmatrix} L_{Sn}^{*} \\ X_{Sn}^{*} \\ BR^{*} \\ \delta_{kn}^{*} \end{bmatrix} = \begin{bmatrix} 0.050 \\ 0.193 \\ 0.700 \\ 0.046 \end{bmatrix}$$

Model B

$$COPR^{*} = \begin{bmatrix} L_{Sn}^{*} \\ X_{Sn}^{*} \\ BR^{*} \\ \delta_{kn}^{*} \end{bmatrix} = \begin{bmatrix} 0.050 \\ 0.413 \\ 0.720 \\ 0.089 \end{bmatrix}$$

5.6.2.3.2 Optimisation for maximum cooling

In this approach, we have taken the interaction between design parameters into account. As shown in Table 5.16 and Figure 5.23, the maximum of the cooling load ($\Phi_{C\,MAX}$) is located further away (as compared with best COPR) from the closed end as suggested by values of optimal stack centre position X_{Sn} obtained.

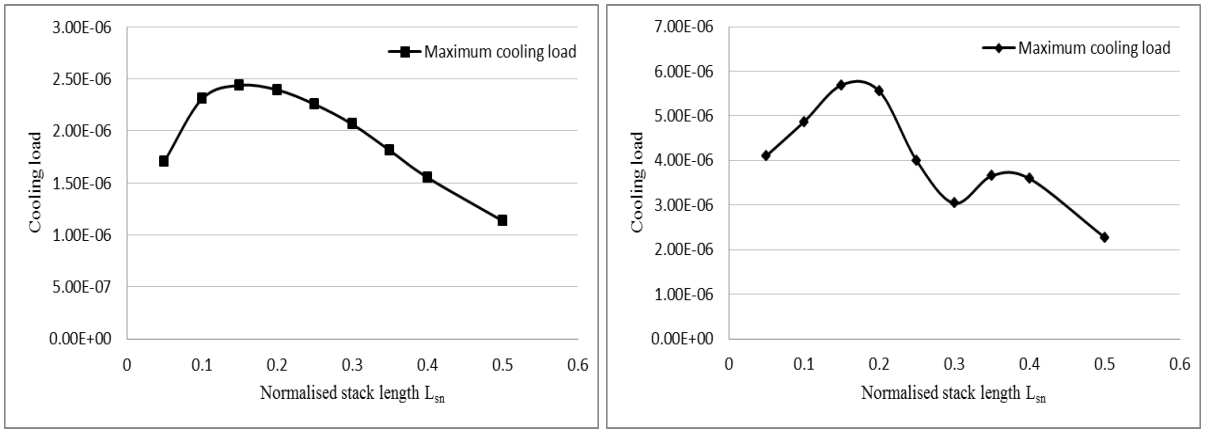

(a) (b)

Figure 5.23: (a) Coefficient of performance relative to Carnot for model A and (b) Coefficient of performance relative to Carnot for model B.

The results suggest that there is a distinct optimum of the cooling load for a selected set of design parameters and depending on the formulation adopted (model A or B) with the maximum value described by:

Model A

$$\Phi_C^* = \begin{bmatrix} L_{Sn}^* \\ X_{Sn}^* \\ BR^* \\ \delta_{kn}^* \end{bmatrix} = \begin{bmatrix} 0.150 \\ 0.459 \\ 0.700 \\ 0.046 \end{bmatrix}$$

Model B

$$\Phi_C^* = \begin{bmatrix} L_{Sn}^* \\ X_{Sn}^* \\ BR^* \\ \delta_{kn}^* \end{bmatrix} = \begin{bmatrix} 0.150 \\ 0.561 \\ 0.900 \\ 0.083 \end{bmatrix}$$

Based on Table 5.16, Figure 5.22 and Figure 5.23, one will suspect that the normalised stack length (L_{Sn}), the normalised stack position (X_{Sn}), the blockage ratio (BR) and the normalised thermal penetration depth (δ_{kn}) are somehow related. Indeed, that is the case.

5.6.2.3.3 Best coefficient of performance and maximum cooling load results comparisons

A comparison of Figure 5.23 (a) and (b) leads to the conclusion that the maxima of the functions $\Phi_{C\,MAX}$ and $COPR^*$ depend on the mathematical programming formulation. It can be seen that model B (with the COP as primary objective function) produces a different

configuration for the highest cooling load (Φ_C^*) and coefficient of performance ($COPR^*$). This choice is in line with the a priori articulation of preferences by the decision maker which consists of selecting the most preferable solution. Additionally, the maxima of the functions Φ_C^* and $COPR^*$ do not coincide. While the former is far away from the closed end, the latter is close to it. For electronic cooling, the main objective is to achieve high cooling loads; thus, maximising Φ_C^* while maximising the $COPR^*$, is the goal for large-scale devices. Therefore, the solution to this problem exists, given as follow:

Large scale applications:

$$COPR^* = \begin{bmatrix} L_{Sn}^* \\ X_{Sn}^* \\ BR^* \\ \delta_{kn}^* \end{bmatrix} = \begin{bmatrix} 0.050 \\ 0.413 \\ 0.720 \\ 0.089 \end{bmatrix} \text{ or } \begin{bmatrix} 0.050 \\ 0.193 \\ 0.700 \\ 0.046 \end{bmatrix}$$

Electronic cooling applications:

$$\Phi_C^* = \begin{bmatrix} L_{Sn}^* \\ X_{Sn}^* \\ BR^* \\ \delta_{kn}^* \end{bmatrix} = \begin{bmatrix} 0.150 \\ 0.561 \\ 0.900 \\ 0.083 \end{bmatrix} \text{ or } \begin{bmatrix} 0.150 \\ 0.459 \\ 0.700 \\ 0.046 \end{bmatrix}$$

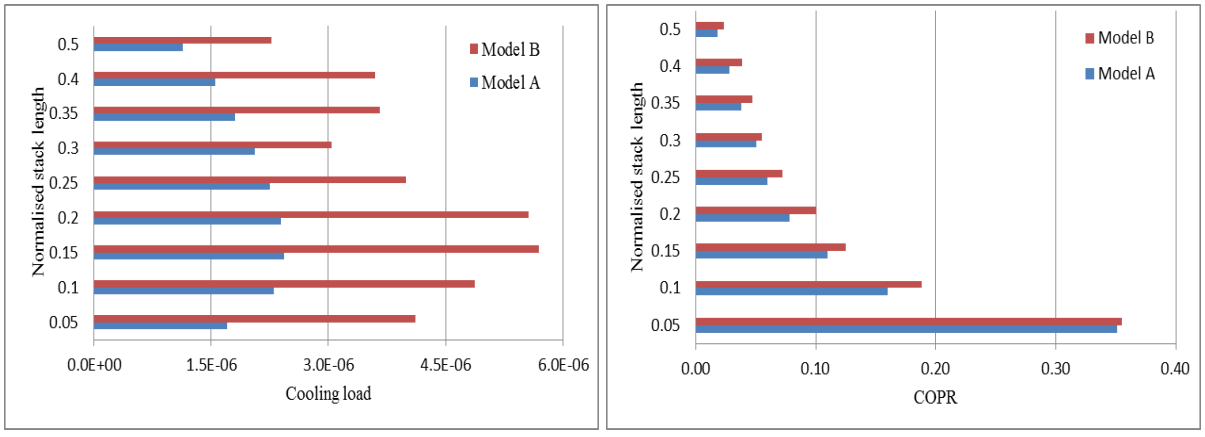

(a) (b)

Figure 5.24: Results comparison of (a) Maximum cooling and (b) Coefficient of performance for model A and B

5.6.2.4 Influence of the working fluid on the performance of TAR

Equation 3.27 shows the negative effect of viscosity on the acoustic power of TAE and the performance of TAR. A reduction of the effect of viscosity will result in an increase in efficiency. This can be done by decreasing the Prandtl number σ. The Prandtl number is an important parameter in thermoacoustics as can be seen from Equation 3.22 and Equation 3.23. Values of Prandtl number calculated by Tijani *et al.* (2002) for binary gas mixtures are presented in Table 5.15. These Prandtl number values have been incorporated in the models to predict the performance of the TAR for different gas mixtures.

Table 5.15: Working fluids specifications

Working fluid		He	He-Ne	He-Ar	He-Xe	He-Kr	He-Xe 62-38%
Prandtl number	σ	0.67	0.53	0.39	0.27	0.23	0.18
Ratio c_p/c_v	γ	1.63	1.64	1.65	1.67	1.65	1.64
Sound speed	a [m/s]	1054.4	628.9	485.0	500.6	353.6	292.4
Resonant frequency	f [Hz]	24,752	14,763	11,384	11,751	8,300	6,864

Figure 5.24 and Figure 5.25 represent graphically the results obtained in Table 5.17 (a), (b) and (c). These results show the influence of the normalised stack length on the coefficient of performance (COP) and the cooling load (Φ_C) for different working fluids. Optimal parameters describing the geometry of the device (BR, δ_{kn}, X_{Sn} and L_{sn}) are reported. Model B formulation has been adopted for illustration. The best configuration has been highlighted as guidance for a decision maker. These results suggest that the highest COP and Φ_C will be obtained with a mixture of He-Ne 62-38%. Interestingly, similar trends have been obtained by Wetzel and Herman (1997) and Herman and Travnicek (2006) using different approaches.

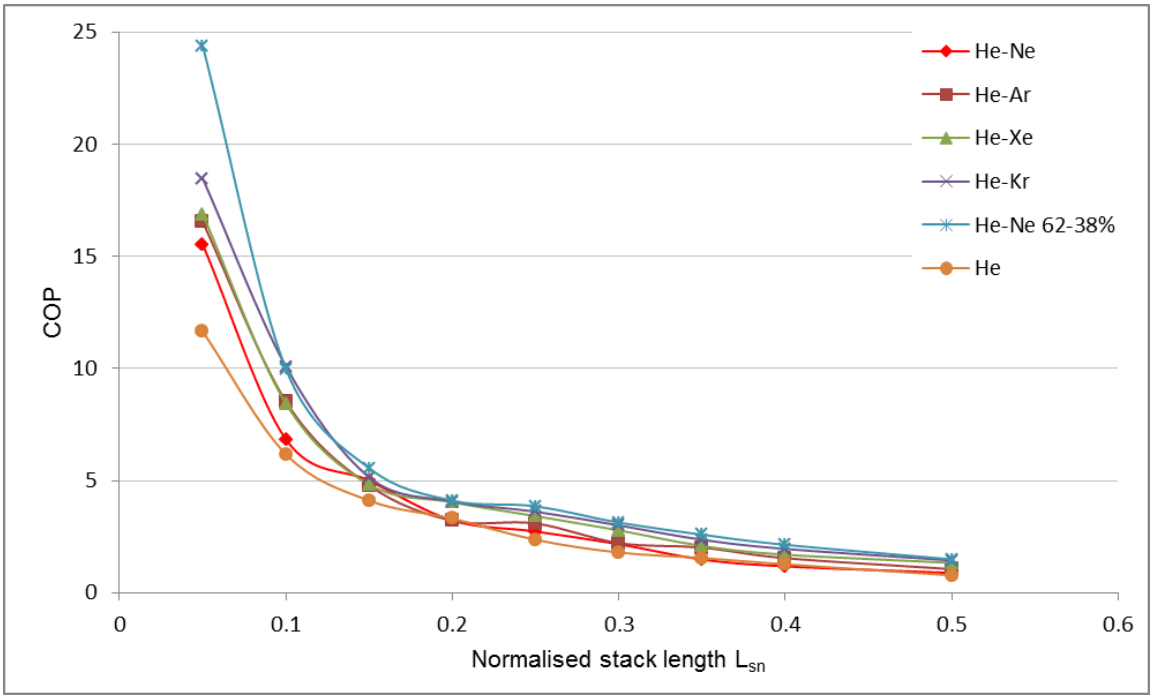

Figure 5.25: COP function of normalised stack length for different working fluid

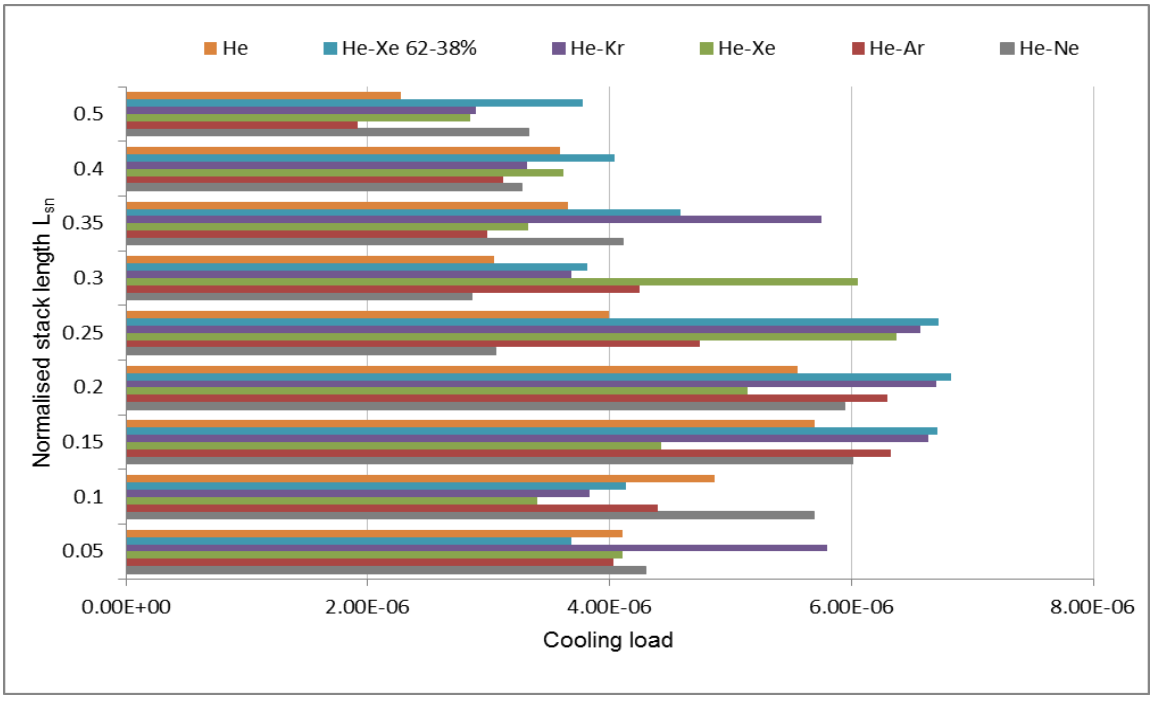

Figure 5.26: Cooling load function of normalised stack length for different working fluid

Table 5.16: Non-dominated solutions obtained using AUGMENCON/Air

		L_{Sn}	**0.050**	**0.100**	**0.150**	**0.200**	**0.250**	**0.300**	**0.35**	**0.4**	**0.5**
Model A	COP_{MAX}	BR	**0.700**	0.700	0.700	0.700	0.700	0.700	0.700	0.700	0.700
		δ_{kn}	**0.046**	0.046	0.046	0.046	0.046	0.046	0.046	0.046	0.046
		X_{Sn}	**0.193**	0.426	0.303	0.388	0.321	0.479	0.467	0.454	0.473
		Φ_C	**1.26E-06**	2.31E-06	1.81E-06	2.09E-06	1.59E-06	2.05E-06	1.81E-06	1.55E-06	1.13E-06
		COP	**11.521**	5.250	3.603	2.559	1.958	1.660	1.250	0.910	0.584
	$\Phi_{C\ MAX}$	BR	0.700	0.700	**0.700**	0.700	0.700	0.700	0.700	0.700	0.700
		δ_{kn}	0.046	0.046	**0.046**	0.046	0.046	0.046	0.046	0.046	0.046
		X_{Sn}	0.331	0.426	**0.459**	0.478	0.484	0.483	0.467	0.454	0.473
		Φ_C	1.71E-06	2.31E-06	**2.44E-06**	2.39E-06	2.25E-06	2.06E-06	1.81E-06	1.55E-06	1.13E-06
		COP	9.475	5.250	**3.434**	2.432	1.921	1.590	1.250	0.91	0.584
Model B	COP_{MAX}	BR	**0.720**	0.900	0.835	0.890	0.760	0.860	0.817	0.728	0.808
		δ_{kn}	**0.089**	0.082	0.060	0.460	0.046	0.046	0.046	0.046	0.046
		X_{Sn}	**0.413**	0.521	0.503	0.575	0.610	0.610	0.610	0.517	0.610
		Φ_C	**4.11E-0.6**	4.87E-06	3.74E-06	2.54E-06	2.47E-06	2.33E-06	2.33E-06	2.12E-06	1.31E-06
		COP	**11.65**	6.176	4.109	3.306	2.362	1.795	1.795	1.271	0.778
	$\Phi_{C\ MAX}$	BR	0.720	0.900	**0.900**	0.900	0.900	0.900	0.700	0.835	0.700
		δ_{kn}	0.089	0.082	**0.083**	0.084	0.070	0.059	0.078	0.078	0.048
		X_{Sn}	0.413	0.521	**0.561**	0.582	0.656	0.609	0.489	0.628	0.519
		Φ_C	4.11E-06	4.87E-06	**5.70E-06**	5.56E-06	3.99E-06	3.04E-06	3.66E-06	3.59E-06	2.27E-06
		COP	11.65	6.176	**3.429**	2.427	2.118	1.361	1.324	0.928	0.455

Table 5.17: Non-dominated solutions obtained using AUGMENCON/gas mixture

(a)		L_{Sn}	**0.050**	**0.100**	**0.150**	**0.200**	**0.250**	**0.300**	**0.35**	**0.4**	**0.5**
He-Ne	COP_{MAX}	BR	**0.700**	0.900	0.700	0.820	0.836	0.878	0.862	0.848	0.807
		δ_{kn}	**0.046**	0.069	0.046	0.070	0.046	0.046	0.055	0.044	0.046
		X_{Sn}	**0.359**	0.620	0.481	0.466	0.665	0.634	0.737	0.728	0.708
		Φ_C	**2.81E-06**	4.22E-06	3.31E-06	3.87E-06	2.76E-06	2.86E-06	3.26E-06	2.21E-06	1.59E-06
		COP	**15.529**	6.838	4.999	3.225	2.732	2.169	1.484	1.179	0.882
	$\Phi_{C\ MAX}$	BR	0.788	0.900	**0.700**	0.900	0.900	0.900	0.900	0.839	0.900
		δ_{kn}	0.089	0.081	**0.092**	0.083	0.047	0.048	0.065	0.071	0.092
		X_{Sn}	0.451	0.544	**0.478**	0.611	0.664	0.635	0.644	0.620	0.661
		Φ_C	4.30E-06	5.70E-06	**6.014E-06**	5.94E-06	3.06E-06	2.86E-06	4.11E-06	3.27E-06	3.33E-06
		COP	11.757	5.773	**3.807**	2.725	2.643	2.024	1.223	1.096	0.694
He-Ar	COP_{MAX}	BR	**0.600**	0.700	0.700	0.720	0.900	0.749	0.756	0.900	0.700
		δ_{kn}	**0.070**	0.050	0.083	0.092	0.046	0.048	0.046	0.046	0.046
		X_{Sn}	**0.307**	0.386	0.519	0.537	0.737	0.622	0.608	0.763	0.540
		Φ_C	**2.81E-0.6**	2.61E-06	5.18E-06	6.30E-06	3.43E-06	2.83E-06	2.39E-06	2.51E-06	1.92E-06
		COP	**16.538**	8.526	4.789	3.218	3.091	2.215	2.015	1.544	1.052
	$\Phi_{C\ MAX}$	BR	0.900	0.795	**0.900**	0.720	0.900	0.733	0.700	0.745	0.700
		δ_{kn}	0.071	0.072	**0.092**	0.092	0.072	0.071	0.049	0.061	0.046
		X_{Sn}	0.470	0.532	**0.647**	0.537	0.665	0.620	0.609	0.641	0.540
		Φ_C	4.04E-06	4.40E-06	**6.32E-06**	6.30E-06	4.75E-06	4.24E-06	2.98E-06	3.12E-06	1.92E-06
		COP	13.430	7.521	**4.282**	3.218	2.356	2.160	1.969	1.447	1.052

(b)		L_{Sn}	**0.050**	**0.100**	**0.150**	**0.200**	**0.250**	**0.300**	**0.35**	**0.4**	**0.5**
He-Xe	COP_{MAX}	BR	**0.700**	0.856	0.900	0.700	0.787	0.843	0.745	0.821	0.757
		δ_{kn}	**0.048**	0.051	0.046	0.048	0.046	0.048	0.046	0.046	0.046
		X_{Sn}	**0.414**	0.577	0.672	0.506	0.657	0.693	0.639	0.693	0.659
		Φ_C	**2.73E-06**	3.41E-06	3.25E-06	3.04E-06	3.09E-06	4.16E-06	2.76E-06	2.65E-06	2.84E-06
		COP	**16.873**	8.435	4.826	4.336	3.419	2.782	2.088	1.700	1.332
	$\Phi_{C\ MAX}$	BR	0.900	0.856	0.900	0.900	**0.900**	0.861	0.900	0.716	0.757
		δ_{kn}	0.066	0.051	0.062	0.070	**0.092**	0.092	0.048	0.066	0.046
		X_{Sn}	0.501	0.577	0.670	0.693	**0.707**	0.692	0.822	0.596	0.659
		Φ_C	4.11E-06	3.41E-06	4.42E-06	5.14E-06	**6.38E-06**	6.05E-06	3.32E-06	3.62E-06	2.84E-06
		COP	16.100	8.435	4.418	3.973	**2.684**	2.455	2.076	1.692	1.332
He-Kr	COP_{MAX}	BR	**0.700**	0.792	0.900	0.767	0.700	0.900	0.849	0.900	0.848
		δ_{kn}	**0.046**	0.048	0.046	0.046	0.046	0.048	0.046	0.046	0.050
		X_{Sn}	**1.000**	0.567	0.678	0.662	0.603	0.756	0.803	0.822	0.725
		Φ_C	**3.39E-0.6**	3.44E-06	3.31E-06	3.23E-06	3.08E-06	3.68E-06	2.91E-06	3.32E-06	2.84E-06
		COP	**18.473**	10.090	5.148	4.707	3.616	3.004	2.364	1.957	1.443
	$\Phi_{C\ MAX}$	BR	0.700	0.844	0.900	**0.900**	0.900	0.900	0.781	0.900	0.773
		δ_{kn}	0.092	0.047	0.092	**0.092**	0.082	0.048	0.092	0.046	0.046
		X_{Sn}	1.000	0.519	0.656	**0.689**	0.720	0.756	0.619	0.822	0.704
		Φ_C	5.80E-06	3.83E-06	6.64E-06	**6.70E-06**	6.57E-06	3.68E-06	5.76E-06	3.32E-06	2.89E-06
		COP	15.199	9.303	5.119	**3.762**	2.900	3.004	2.180	1.957	1.370

(c)		L_{Sn}	**0.050**	**0.100**	**0.150**	**0.200**	**0.250**	**0.300**	**0.35**	**0.4**	**0.5**
He-Xe (62-38)	COP_{MAX}	BR	**0.700**	0.700	0.900	0.900	0.788	0.858	0.782	0.728	0.846
		δ_{kn}	**0.046**	0.056	0.046	0.046	0.048	0.048	0.051	0.046	0.058
		X_{Sn}	**1.000**	0.529	0.696	0.727	0.760	0.742	0.792	0.779	0.860
		Φ_C	**3.68E-06**	4.14E-06	3.34E-06	3.39E-06	3.34E-06	3.82E-06	3.82E-06	2.82E-06	3.13E-06
		COP	**24.389**	9.996	5.552	4.107	3.856	3.127	2.591	2.140	1.492
	$\Phi_{C\ MAX}$	BR	0.700	0.700	0.900	**0.900**	0.900	0.858	0.900	0.700	0.775
		δ_{kn}	0.046	0.056	0.083	**0.092**	0.092	0.048	0.069	0.053	0.069
		X_{Sn}	1.000	0.529	0.692	**0.690**	0.712	0.742	0.811	0.656	0.788
		Φ_C	3.68E-06	4.14E-06	6.71E-06	**6.82E-06**	6.73E-06	3.82E-06	4.58E-06	4.04E-06	3.78E-06
		COP	24.389	9.966	5.531	**4.073**	3.157	3.127	2.204	1.910	1.408
He	COP_{MAX}	BR	**0.720**	0.900	0.835	0.890	0.760	0.860	0.817	0.728	0.808
		δ_{kn}	**0.089**	0.082	0.060	0.460	0.046	0.046	0.046	0.046	0.046
		X_{Sn}	**0.413**	0.521	0.503	0.575	0.610	0.610	0.610	0.517	0.610
		Φ_C	**4.11E-0.6**	4.87E-06	3.74E-06	2.54E-06	2.47E-06	2.33E-06	2.33E-06	2.12E-06	1.31E-06
		COP	**11.65**	6.176	4.109	3.306	2.362	1.795	1.795	1.271	0.778
	$\Phi_{C\ MAX}$	BR	0.720	0.900	**0.900**	0.900	0.900	0.900	0.700	0.835	0.700
		δ_{kn}	0.089	0.082	**0.083**	0.084	0.070	0.059	0.078	0.078	0.048
		X_{Sn}	0.413	0.521	**0.561**	0.582	0.656	0.609	0.489	0.628	0.519
		Φ_C	4.11E-06	4.87E-06	**5.70E-06**	5.56E-06	3.99E-06	3.04E-06	3.66E-06	3.59E-06	2.27E-06
		COP	11.65	6.176	**3.429**	2.427	2.118	1.361	1.324	0.928	0.455

5.6.2.5 Conclusion

In this section, a multi-objective approach that provides fast initial engineering estimates to initial design calculation of thermoacoustic refrigerators is discussed. Their performances were evaluated using three criteria: 1) maximum cooling, 2) best coefficient of performance, and 3) the acoustic power loss. Four different parameters - stack length, stack centre position, stack spacing and blockage ratio - describing the geometry of the device have been studied. Nonlinear programming models with discontinuous derivatives (DNLPs) have been formulated and implemented in GAMS. For the case of multiple objectives considered simultaneously, we have applied an improved version of a multi-objective solution method, the epsilon-constraint method called augmented epsilon-constraint method (AUGMENCON). We have adopted a lexicographic method in order to avoid dominated Pareto optimal solutions. We were able to identify the best mathematical programming formulation leading to the highest performance of the device. For different arbitrary values of stack length, this process generates optimal solutions describing geometry of the TAR, solutions which depend on the a priori design goal for maximum cooling or maximum coefficient of performance. This present study reveals and quantifies that the results obtained with these two objectives are different. There is a specific stack length which corresponds to a specific stack centre position, specific stack spacing and a specific blockage ratio depending on the design goal. In conclusion, it was determined that the design parameters are interdependent. This clearly supports the use of a lexicographic multi-objective optimisation scheme to design TARs.

CHAPTER 6: EXPERIMENTAL SCHEME

6.1 Introduction

Experiments in engineering provide the basis for scientific knowledge by testing theories and investigating novel components, novel techniques or materials for a specific application. Numerical and analytical models are insignificant if they are not based on valid experimental evidence, logical discussion and criticism. Therefore, a major objective of the comprehensive experimental scheme is to provide knowledge on the influence of the geometry and the position of the stack in a resonator tube relative to the standing wave as they affect the acoustic work produced or absorbed and the cooling power of thermoacoustic devices. The second objective, then, is to provide insight into models developed in Chapter 5. Finally, the experimental scheme will be utilised to evaluate the ability of the models to compute optimal solutions describing the stack geometries.

6.2 Thermoacoustic refrigerators

6.2.1 Experimental objectives

The main objectives of this experimental scheme are to obtain the following characteristics of the stack:

- measurements of temperature difference (ΔT) obtained across the stack ends at steady state for different stack geometries (lengths of the stacks varying from 26 to 100 mm) and stack spacing (homogenous stacks ranging from 64 to 300 Cells Per Square Inch, or CPSI).
- measurements of the temperature difference (ΔT) obtained across the stack ends at steady state for different positions of the stack (the hot end of the stack varies from 100 to 600 mm from the closed end).

6.2.2 Experimental facility

The TAR experimentation was carried out using a quarter-wavelength resonator design. A speaker-driven system was used to ensure equal acoustic environments for each test instead of a heat driven one. The experimental facility has the following subsections:

• Experimental Set-up
• Sensors
• Data Acquisition and Recording
• Test Procedure

6.2.2.1 Experimental set-up

An experimental set-up (thermoacoustic refrigerator) for measuring the performance of the device function of the geometry of the stack has been designed and assembled. The set-up has the following components:

- a resonator tube;
- a loudspeaker; and
- a stack.

As this set-up does not have hot heat exchanger and cold heat exchanger at the ends of the stack, it is similar to a thermoacoustic couple (TAC). For this study, the stack is not cooled actively. The main function of this experiment is to evaluate the models, rather than achieving highest temperature drop or cooling power.

a. Resonator and loudspeaker

The resonator is an acrylic tube (thermal conductivity 0.20 W/m K at 23^{o}C) of a length of 780 mm and an inner diameter of 44 mm, as illustrated in Figure 6.1. The resonator is filled with air at atmospheric pressure. The position of the stack can be adjusted at any location on the resonator. One end of the tube is closed with an end cap. At the other end, a commercially available loudspeaker (4 Ω) constitutes the acoustic power source (driver). The loudspeaker has a frequency range of 45 – 26000 Hz and 180 W maximum acoustic power output. This driver is located in PVC housing (130×130×72 mm) to which the resonator is connected. A function generator (model Agilent 33220A) and an 80 W amplifier have been used to drive the system at the operating frequency and with the selected power. The accuracy of the amplitude and the frequency of the output signal are 0.1mV and 1μHz, respectively.

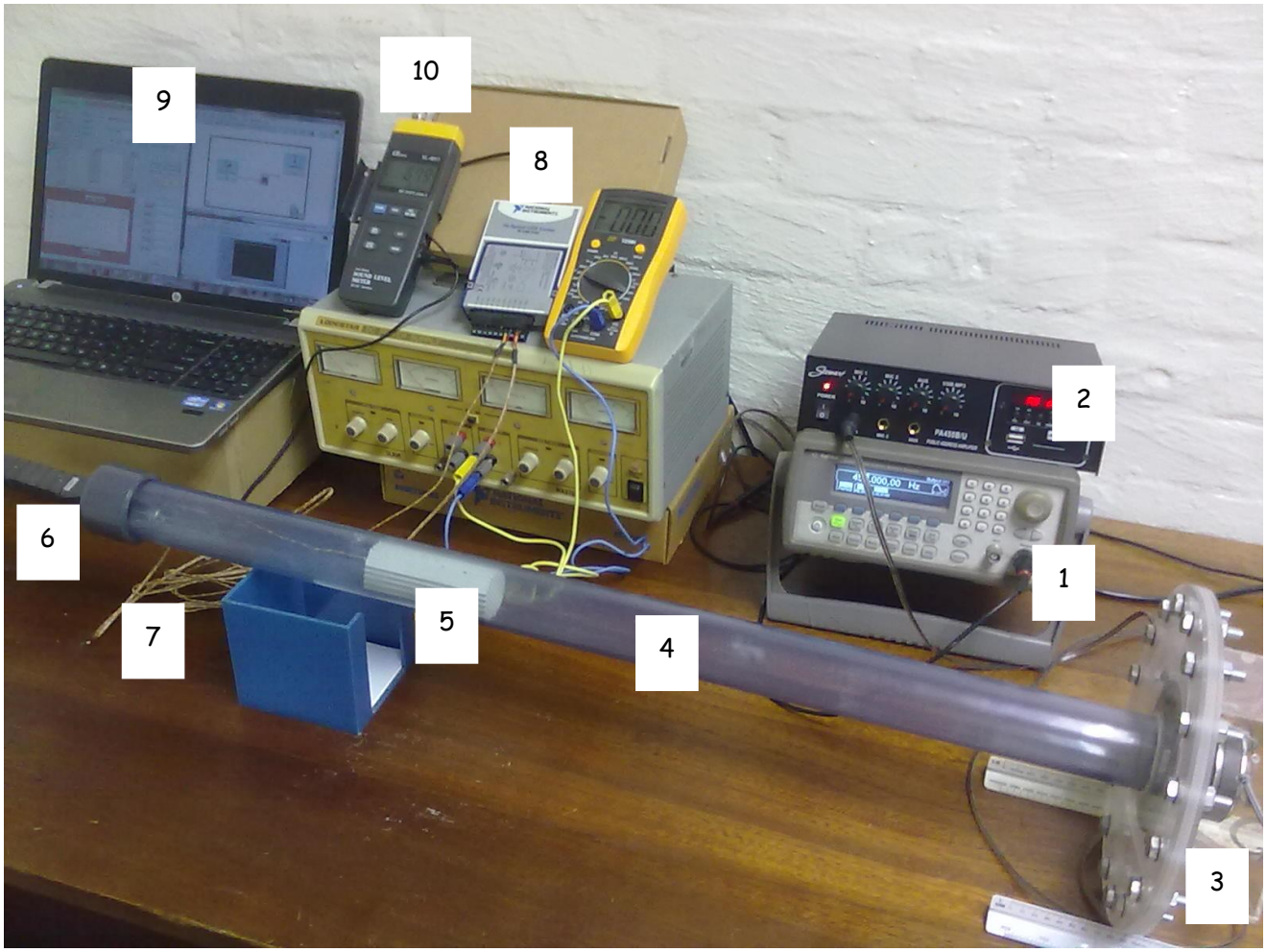

Figure 6.1: Thermoacoustic refrigerator and the measuring systems.

1	Function generator
2	Amplifier
3	Speaker
4	Resonant chamber
5	Honeycomb ceramic stack
6	Microphone
7	Thermocouples
8	NI Data Acquisition System
9	Labview and sound level meter software interface
10	Sound level meter

b. Stack

The stacks studied in the measurement set-up are prefabricated stacks made of 64, 100, 230 and 300 CPSI respectively, manufactured by Applied Ceramics Inc. (2011). The cordierite honeycomb ceramic is selected because of its low thermal conductivity, high surface area for conversion efficiency, high thermal capability (up to 1400^0C), ability to

sustain large temperature gradients and highest sound pressure level output. Additionally, such stacks are relatively cheaper and easier to make, especially when the channel size goes down into tens of microns range. Sixteen cordierite honeycomb ceramic stacks with square cross sections (as shown in Figure 6.2) having four different lengths - 26 mm, 48 mm, 70 mm and 100 mm - are considered. Cordierite honeycomb ceramic stack properties and specifications are provided in Table 6.1. Measurements are taken at six different locations of the stack hot ends from the pressure antinode, namely 100 mm, 200 mm, 300 mm, 400 mm, 500 mm and 600 mm respectively.

Table 6.1: Properties and dimensions of stack materials

(Applied Ceramics, 2011)

Material: Cordierite Ceramic Honeycomb				
Density [Kg/m^3]		2500		
Thermal conductivity [W/m K]		0.42		
Specific heat [J/Kg K]		1047		
Melting point [^{o}C]		1450		
Coefficient of thermal expansion ^{o}C×10^{-6}		0.7		
	Engine	Refrigerator		
Stack Lengths [mm]	25	100		
	22	70		
	17	48		
	13	26		
	7			
Stack position (from closed end) [mm]	52	100		
	72	200		
	92	300		
	112	400		
	132	500		
	152	600		
	172			
	Size (pore sizes)			
	Size 4: 64 CPSI	Size 3: 100 CPSI	Size 2: 230 CPSI	Size 1: 300 CPSI
Plate thickness [mm]	0.690	0.550	0.160	0.140
Plate spacing [mm]	3.175	2.540	1.675	1.467
Porosity [BR]	≈0.8	≈0.8	≈0.9	≈0.9

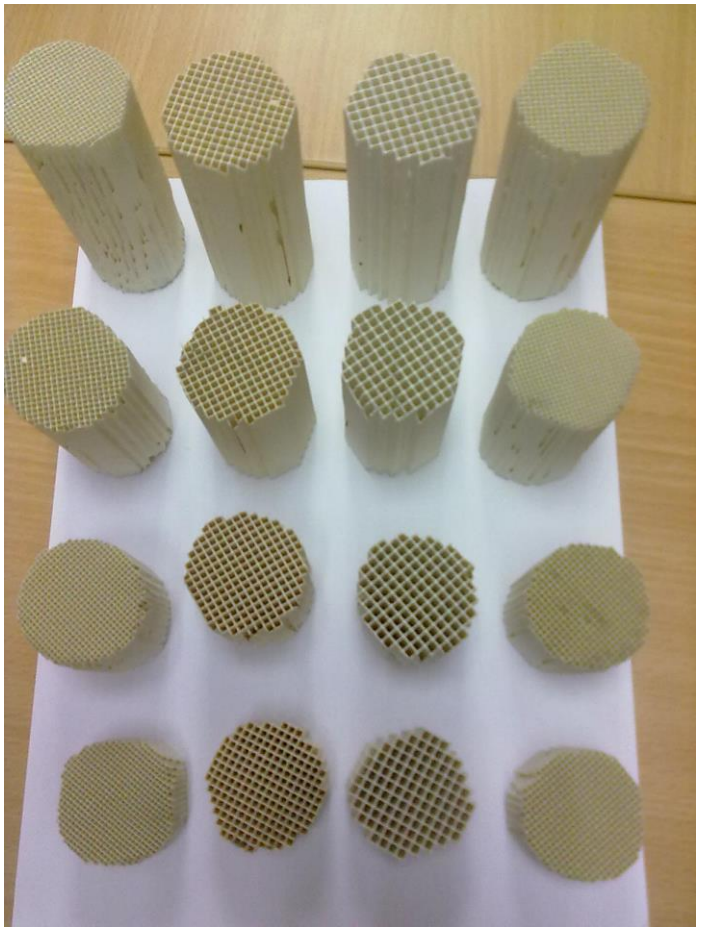

Figure 6.2: Stack samples used in the experiments/ TAR

6.2.2.2 Sensors

A variety of equipment is utilised to perform the measurements. Thermocouples are used to measure thermal response, and pressure measurements are made with a sound level meter, while a data acquisition system records the measurements (as shown in Figure 6.1).

Temperature measurement

A common method to record temperature is through the use of thermocouples. K-Type thermocouples wires have been selected for this work. They are made of chromel and alumael from National Instruments (National Instruments, n.d). Based on National Instruments, these exposed junction type thermocouples which feature fiberglass insulation (melting point 482^{o}C) allow for a temperature range of 0^{o}C to 482^{o}C. The accuracy of the thermocouple is $\pm$ 2.2^{o}C (National Instruments, n.d).

Pressure Measurement

The acoustic pressure measurements are made by a sound level meter (Lutron SL 4013) which, when placed near the driver end, measures the dynamic pressure (P_0). The drive ratio (DR) is evaluated using this dynamic pressure measurement. The accuracy of the sound level meter, as indicated by Lutron Electronic (Lutron Electronic, n.d) is ±1.5 dB. To convert the sound level meter data from decibel (dB) to Pascal (Pa), the following expression is used:

$$L_P = 10\log_{10}\left(\frac{P^2}{P_{ref}^2}\right) = 20\log_{10}\left(\frac{P}{P_{ref}}\right)\text{dB} \qquad \textbf{Equation 6.1}$$

where L_P =sound pressure level in dB

P =root mean square sound pressure = $\frac{P_0}{\sqrt{2}}$

P_{ref} =20×10^{-6} Pa or 20 μPa = reference pressure

Accuracy of instruments

Instrument	Accuracy
Function generator	10μHz
Amplifier	1 mV
K-type thermocouple	$\pm$ 2.2^{o}C
Sound level meter	±1.5 dB

6.2.2.3 Data acquisition and logging

The analog signals generated by sensors are obtained using data acquisition (DAQ) hardware (as shown in Figure 6.1). Once these signals are interpreted by the DAQ, a digital signal is sent to a computer for processing, recording and analysing. Although there are numerous possible solutions for acquiring and processing analog data, LabVIEW 11 (National Instrument, 2011) has been selected as the environment for data visualisation and processing, together with a National Instruments (NI) DAQ hardware (NI USB-9211A and NI myDAQ).

6.2.2.4 Thermocouple and sound level meter data acquisition

A portable USB based DAQ is chosen for thermocouple measurement (National instruments hardware NI USB-9211). The module is compatible with J, K, R, S, T, N, E, and B type thermocouples and offers 24-bit resolution allowing for temperatures of 0 to 750°C to be read from any thermocouple type (National Instrument, n.d). This module includes antialiasing filters and cold-junction compensation for high accuracy thermocouple measurements. It has four channels. The sampling rate is 14 samples per second and per channel. The sound level meter is a portable five digits, compact sized, digital display sound level meter designed for long term measurements, with an operating environment of 0 to 50^{o}C. This sound level meter has been connected to the NI myDAQ hardware to compute the Fast-Fourier Transformation (FFT) for analysing and measuring the signals from DAQ devices. FFTs are computed to evaluate the resonant frequency of thermoacoustic engine.

6.2.2.5 Test procedure

Experiments are performed using the samples presented in Table 6.2. The effect of stack geometry (pore sizes and stack length) and position of the stack in the resonator are investigated during the experiment. For each test (for a particular stack geometry), the position of the stack is varied between 100 mm to 600 mm from the pressure antinode. Each test is allowed to reach a steady state over a certain period of time (about 250 to 350

seconds) that is confirmed by LabVIEW graphics for the temperature measurements at the stack ends. The thermocouples are read with NI USB-9211, a module for which National Instruments present a graph to quantify the error associated with K-type thermocouples. In the range of interest, namely 10°C to 65°C, the error is ±2.2°C, an error associated with the following considerations:

- gain errors;
- offset errors;
- mechanical disturbances;
- noise errors; and
- isothermal errors.

It should be noted that this error is independent of any error associated with the thermocouple itself. The measurement positions are accurate to about ±5 mm. The uncertainty analysis of the measurements is discussed in Section 6.3.6.7. The measurements related to the experimental set-up are discussed in the next section.

6.2.3 Results, thermoacoustic refrigerator

To evaluate the thermal performance, the temperature difference across the stack end temperature is the main focus of the present work. Several authors (Tu *et al*., 2005; Akhavanbazaz *et al*., 2007; Herman & Travnicek, 2006; Zink *et al*., 2009) have studied the influence of the temperature difference at the stack extremities either mathematically, numerically or experimentally in an effort to improve the performance of thermoacoustic refrigerators through the use of optimisation. But there is inconsistency in the literature about the interdependency between design parameters in the search of optimal solutions describing the geometry of the device. Therefore, the present research aims to investigate the temperature difference across the stack ends with the objective of highlighting the influence and the interdependency of the stack parameters (length, pore size and position) on the performance of the device.

6.2.3.1 Temperature behaviour as a function of driving frequency

In this set of experiments, the effect of the driving frequency on the temperature difference across the stack was investigated. During these experiments, the hot end of a 100 mm stack (size 2) remained 100 mm from the closed end and the function generator voltage was kept at 150 mV_{RMS}. The data for this test was collected beginning at 50 Hz and ranging up to 350 Hz in increments of 5 Hz. The response time of the temperature was much slower than the pressure amplitude; hence, each frequency was maintained for approximately 250 to 350

seconds. Figure 6.3 illustrates the hot side temperature, the cold side temperature and the temperature difference across the stack end as obtained and recorded in this study.

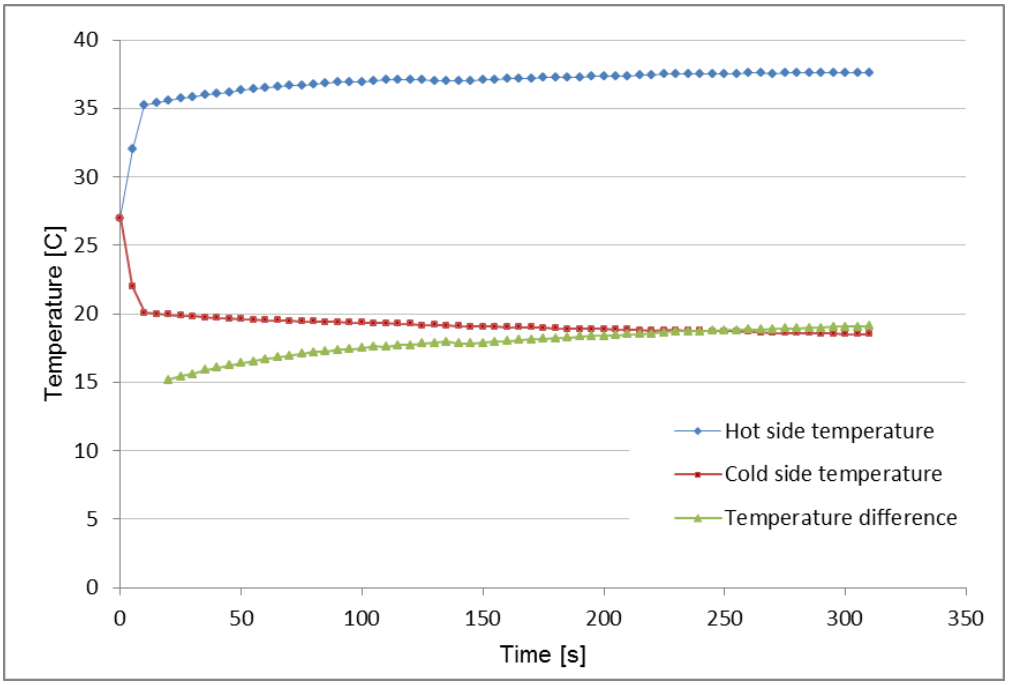

Figure 6.3: Hot side and cold side temperature across the ceramic stack/TAR

A second test was run with a frequency increment of 1 Hz, starting at 130 Hz and ranging beyond the first peak (140 Hz) in order to illustrate a more exact picture of the temperature behaviour in the range of frequencies present in the first peak. Figure 6.2 shows the temperature difference for the entire range of frequencies. The optimal driving frequency identified results in the highest temperature difference across the stack, as suggested by previous studies (Zink, 2009). The total length of this TAR set-up was 780 mm, which corresponds to an optimal operating frequency of ≈ 110 Hz. This is not in agreement with the results reported in Figure 6.4 evaluating the standing wave resonator frequency at 135 Hz. Similar findings are reported by Kim and Kim (2000) who suggest that the frequency of the peak temperature difference won't be in satisfactory agreement with the system resonance frequency if the stack position is not optimum. Therefore, all remaining results were taken under the same operating conditions, with the driving frequency fixed at 135 Hz.

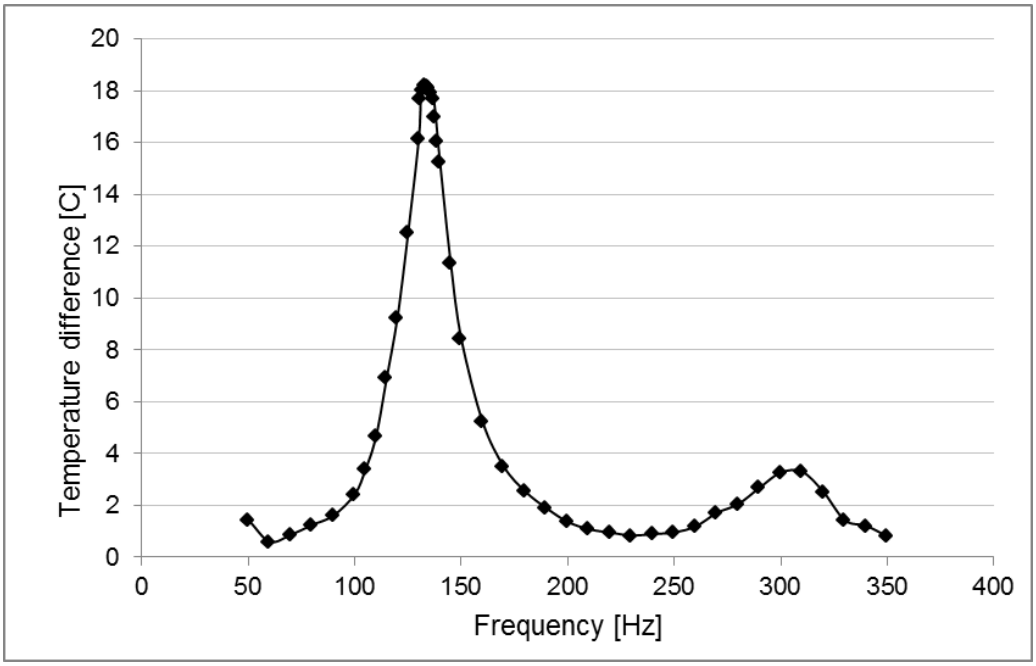

Figure 6.4: Temperature difference function of the frequency

6.2.3.2 Temperature behaviour as a function of power input

In this set of experiments, the effect of the output voltage of the function generator and the power input on the temperature difference across the stack was investigated. During these experiments, the hot end of a 100 mm stack (size 2) remained 100 mm from the closed end and the frequency of the acoustic wave was kept at 135 Hz. The experiments were carried out at eight different function generator output voltages ranging from 50 mV_{RMS} to 500 mV_{RMS} corresponding to eight different power inputs, ranging from 5 W to 18 W. During each experiment, the temperature was measured at both ends of the stack, with results revealed in Figures 6.5 and 6.6. The plots show that the temperature difference across the stack is larger for the output voltage of 250 mV_{RMS}. Therefore, the generator output voltage has been set to 250 mV_{RMS} corresponding to 18.5 W for the remainder of the experiments.

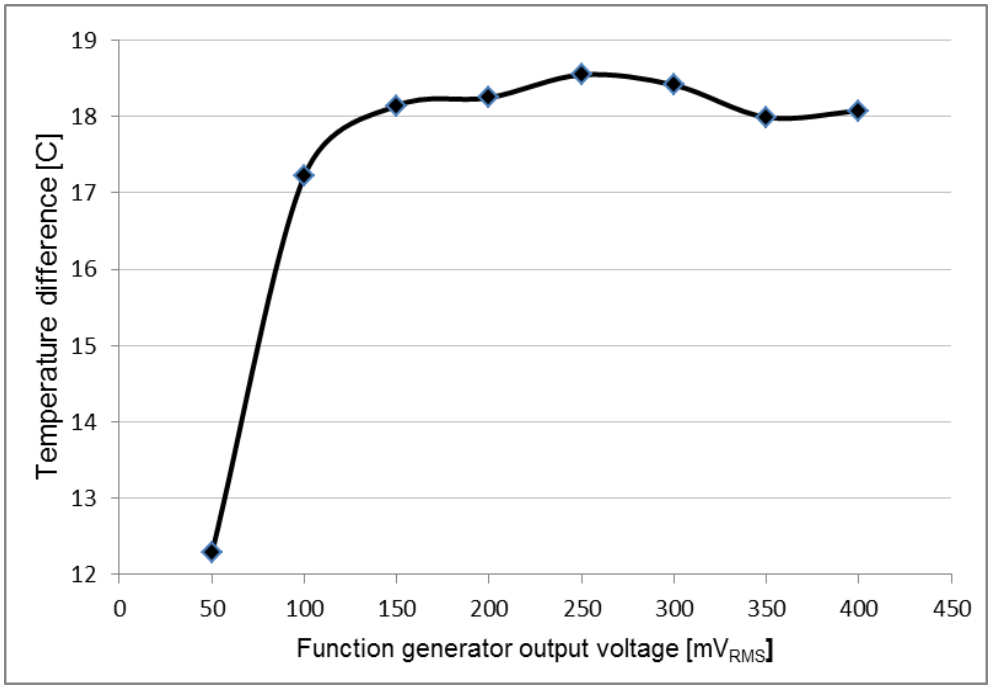

Figure 6.5: Temperature difference across the stack ends versus the function generator output voltage

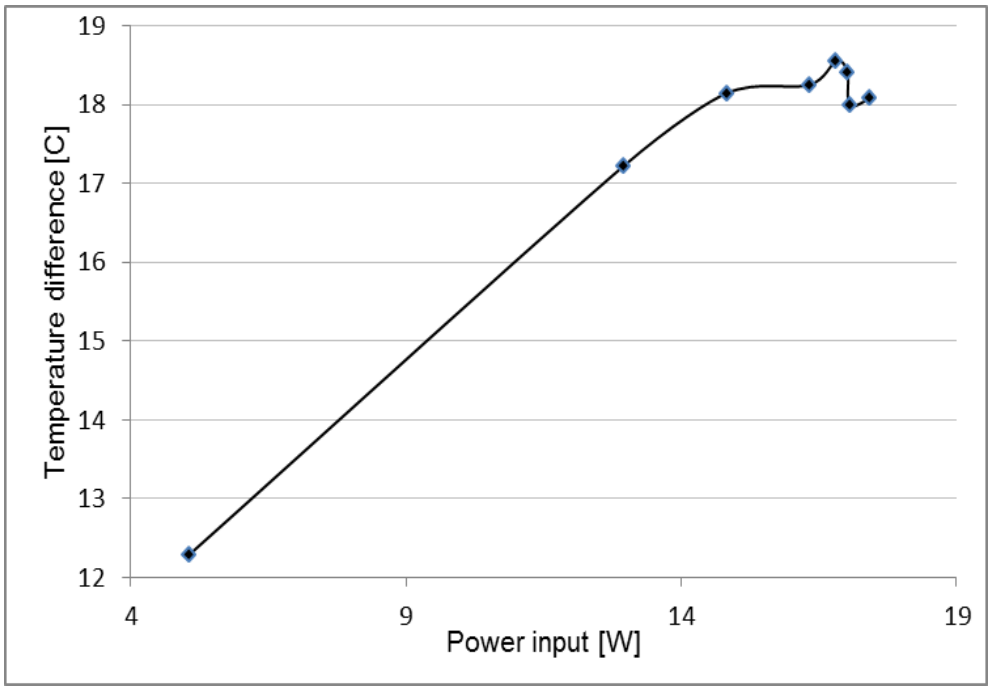

Figure 6.6: Temperature difference across the stack ends versus the power input

6.2.3.3 Temperature behaviour as a function of stack length

The influence of the stack length on the temperature difference was also studied. For this investigation, four different sizes of ceramic stacks (64 CPSI, 100 CPSI, 230 CPSI and 300

CPSI) having four different lengths (26 mm, 48 mm, 70 mm, and 100 mm) were used. Figures 6.5 through 6.8 show the temperature difference as a function of the stack length corresponding respectively to size 1, size 2, size 3 and size 4. It shows that there is a peak in temperature difference corresponding to the optimal stack length in each configuration. The highest temperature peaks obtained for size 1, size 2 and size 3 were 13.147^{o}C, 19.136 ^{o}C and 14.722 ^{o}C respectively, corresponding to a 70 mm stack. However, a maximum temperature of 10.552 ^{o}C has been obtained with a 48 mm stack of size 4. These results demonstrate that there is no clear trend of temperature difference function of the stack length.

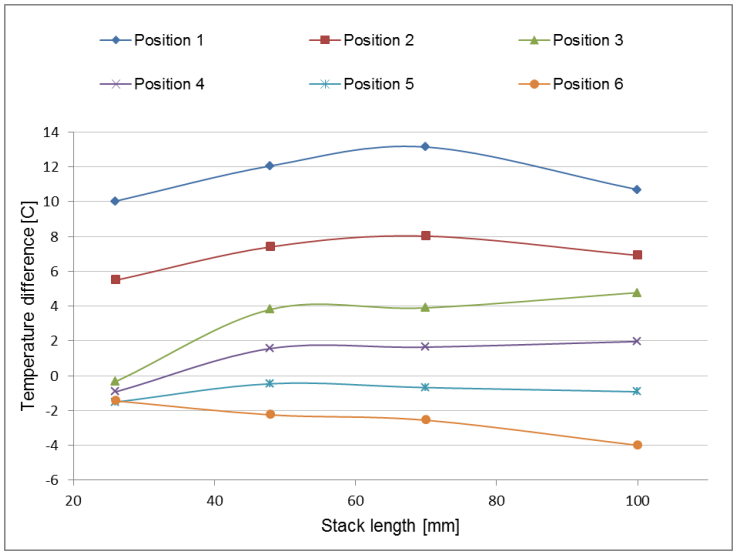

Figure 6.7: Temperature behaviour as a function of stack length/size 1

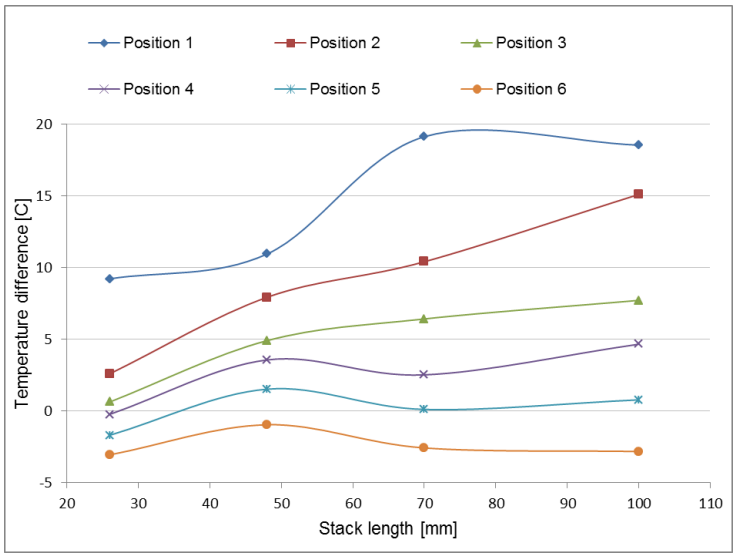

Figure 6.8: Temperature behaviour as a function of stack length/size 2

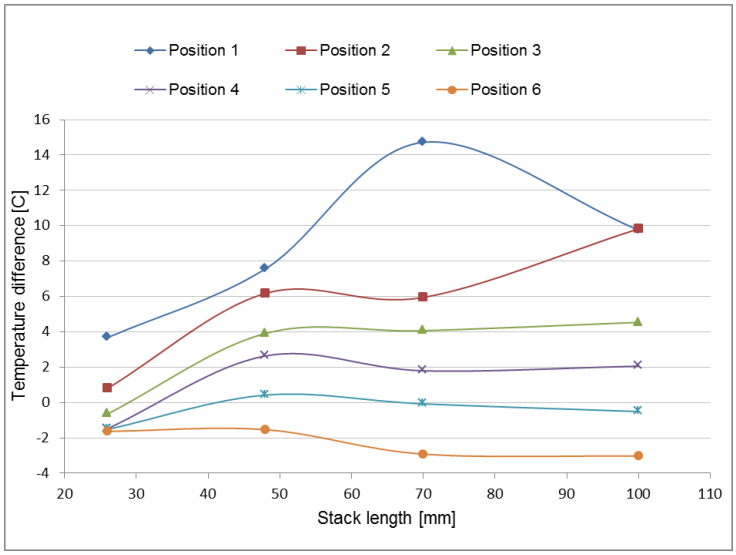

Figure 6.9: Temperature behaviour as a function of stack length/size 3

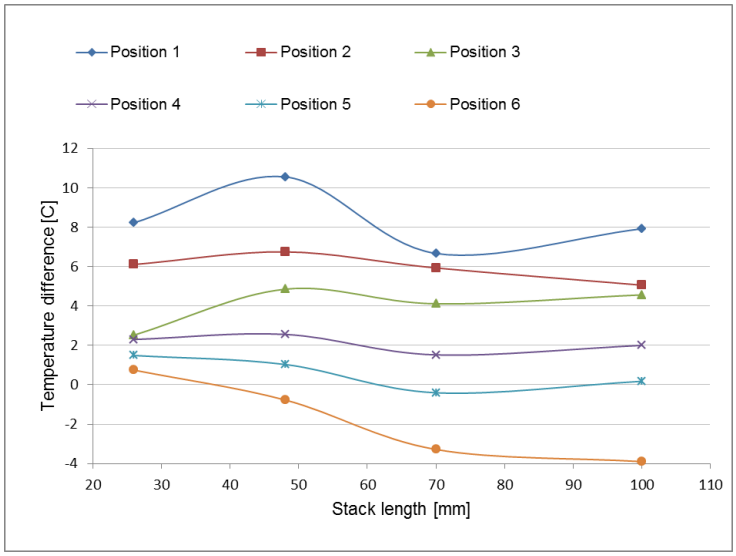

Figure 6.10: Temperature behaviour as a function of stack length/size 4

6.2.3.4 Temperature behaviour as a function of stack position

The influence of stack locations on the temperature difference was studied. The stack location is measured relative to the closed end of the resonator. For good resolution, this study was conducted at six locations, starting at 100 mm to 600 mm from the closed end (Table 6.1). The temperature difference between the two ends was used as the indicator for optimal placement. Figure 5.8 shows this temperature difference as a function of the stack location. A logarithmic curve fit is shown for visual guidance, allowing for a peak in temperature difference to suggest positioning the stack closer to the pressure antinode which is in complete agreement with previous studies (Wetzel & Herman, 1997). Additionally, locating the stack further away from the closed end results in an obvious drop in

temperature difference because of the decrease in pressure amplitude away from the pressure antinode.

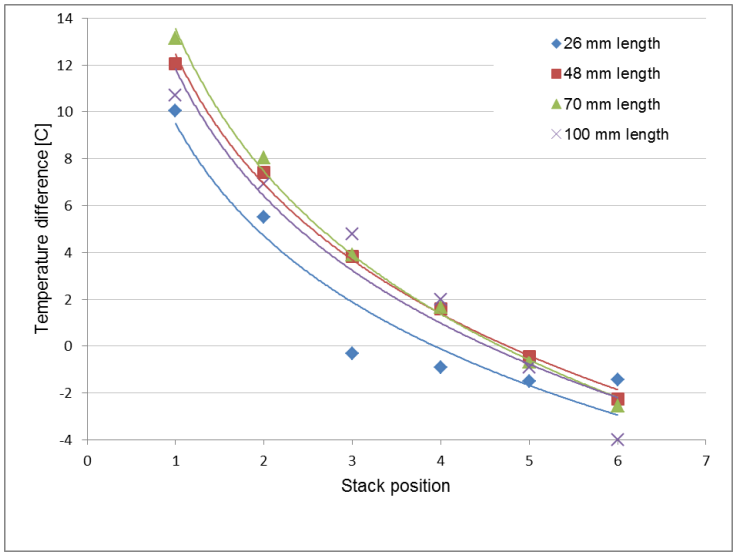

Figure 6.11: Temperature behaviour as a function of stack position/size 1

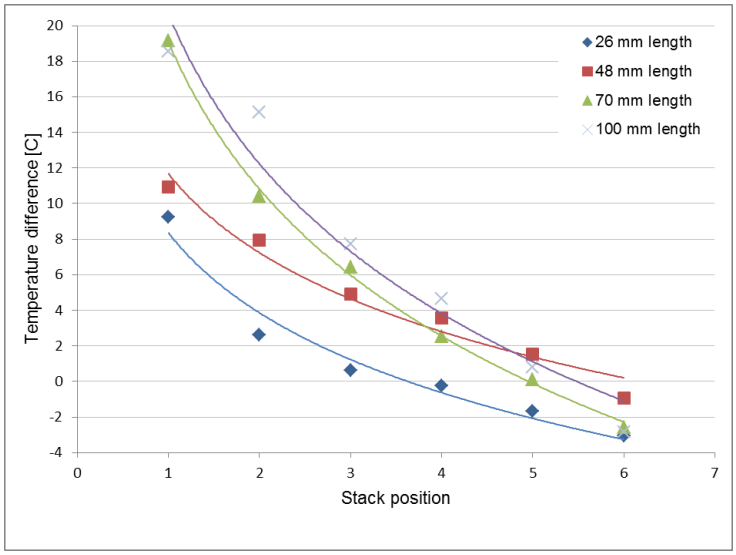

Figure 6.12: Temperature behaviour as a function of stack position/size 2

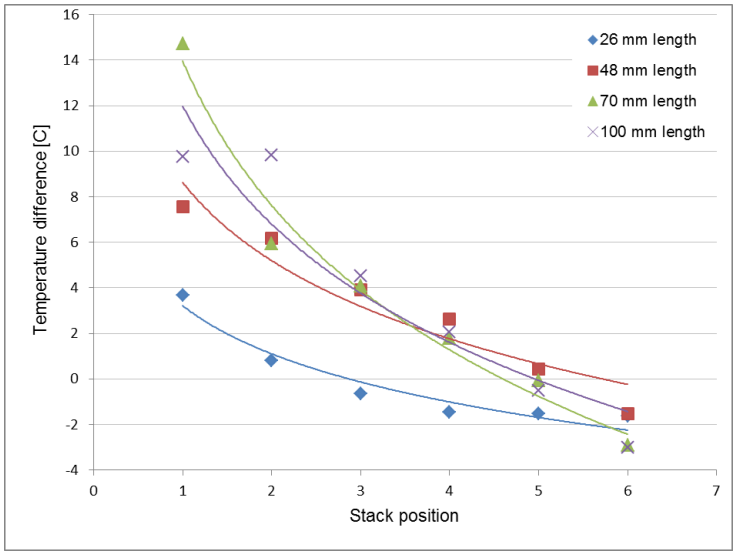

Figure 6.13: Temperature behaviour as a function of stack position/size 3

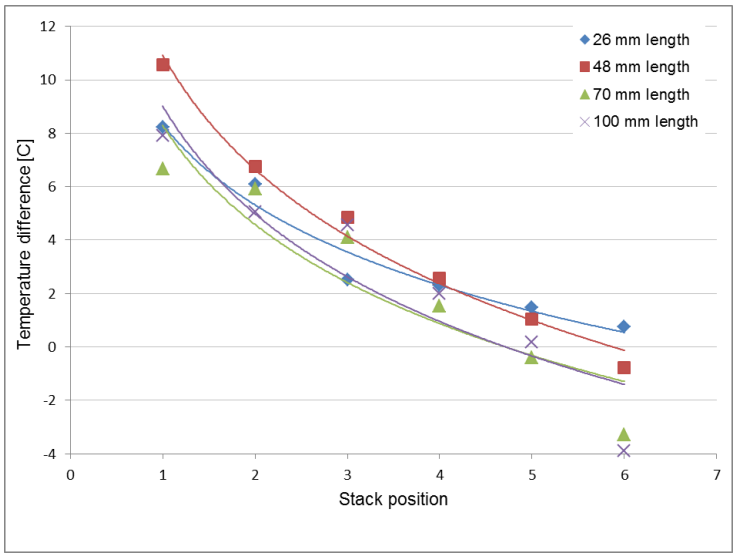

Figure 6.14: Temperature behaviour as a function of stack position/size 4

6.2.3.5 Temperature behaviour as a function of stack pore size

The influence of the stack spacing was studied. The gas thermal penetration depth (δ_k) has been evaluated to 0.214 mm using Equation 2.4. Although Tijani *et al.* (2002) recommend a spacing of 2 to 4 δ_k for optimal transfer between the gas and the surface of the stack, this experimental investigation was performed with stacks having larger spacing (Table 6.1) as per the experimental objectives. It should be noted, however, that the models developed in this work were constrained as per Tijani *et al.* (2002) requirements. The results found in Figure 6.15 and 6.16 suggest a peak of temperature difference for size 1 corresponding to 10.044 ^{o}C and 12.067 ^{o}C respectively. These results show a similar trend for the 26 mm and the 48 mm stacks. However, different profiles are observed from the results reported in

Figures 6.17 and 6.18. The highest temperature difference is observed for size 2. The temperature differences of 19.136 ^{o}C and 18.547 ^{o}C corresponding respectively to 70 mm and 100 mm stacks have been measured.

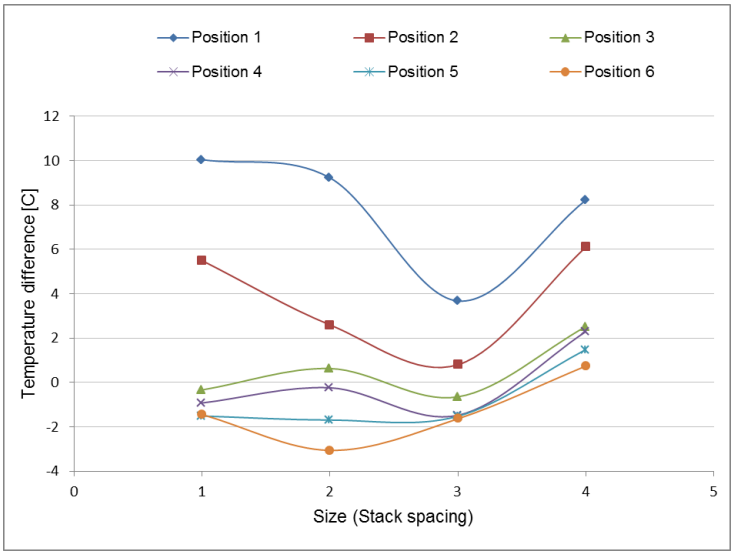

Figure 6.15: Temperature behaviour as a function of pore size/26 mm

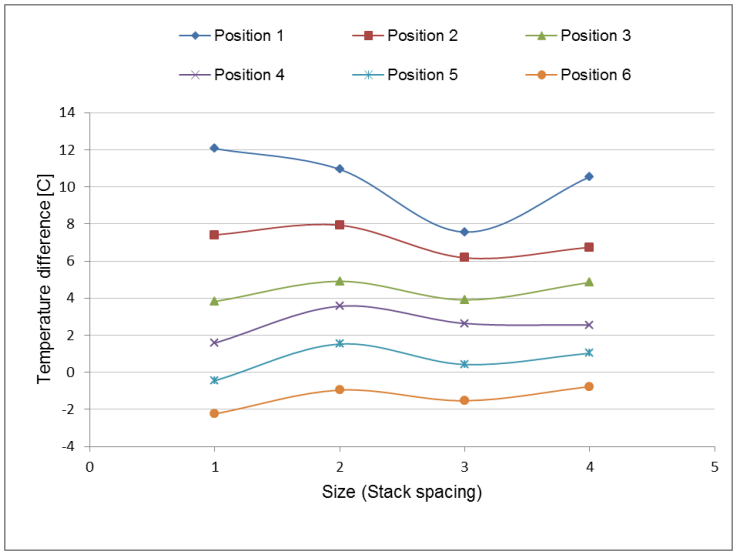

Figure 6.16: Temperature behaviour as a function of pore size/48 mm

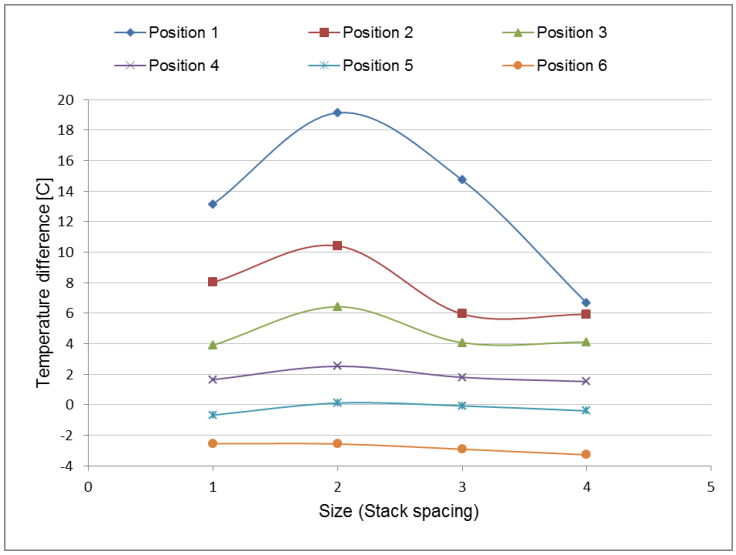

Figure 6.17: Temperature behaviour as a function of pore size/70 mm

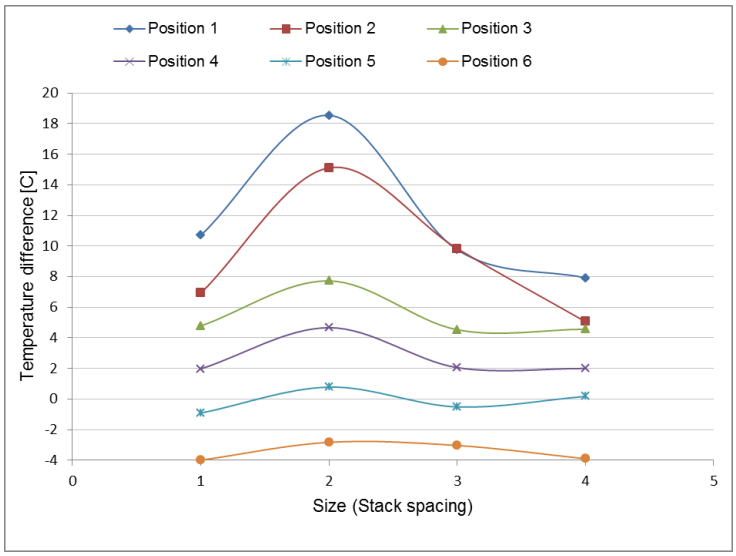

Figure 6.18: Temperature behaviour as a function of pore size/100 mm

Figures 6.7 to 6.18 demonstrate that the magnitude of maximum temperature difference generated at the stack ends depends on the geometry and the position of the stack. To better understand the performance of a thermoacoustic refrigerator, the cooling load and the coefficient of performance of the prototype presented in Figure 6.1 is calculated and presented in the following section.

6.2.3.6 Cooling load and Carnot coefficient of performance

The coefficient of performance (COP) of a thermoacoustic refrigerator indicates how effective the device is in converting and producing cooling load by absorbing sound energy. Therefore the coefficient of performance is given by Equation 3.25. The cooling power, the acoustic power and the cooling load are calculated respectively using Equations 3.22, 3.23, 3.24 and 5.30. Table 6.2 presents the parameters as estimated for the cordierite honeycomb ceramic stack used in this experiment. The normalised values are obtained from Table 3.3 and Table 6.1.

For all the stack lengths considered, the values of COPR decrease as the distance from the pressure antinode (closed end) increases (Figure 6.19). In particularly, the shortest stack length shows the highest COPR for Figure 5.19 (a), (b) and (d) corresponding respectively to sizes 1, 2 and 4. Interestingly, this behaviour has been observed in Figures 5.21 and 5.24 for the TAR models. From Equation 3.23, the acoustic power is proportional to the length of the stack and the viscous loss is increased as the velocity amplitude increases. Therefore, a shorter stack length absorbs less acoustic power and exhibits higher COPR.

Figure 6.20 represents the cooling load function of the normalised stack centre position. There is maximum cooling load when the stack is moved away from the pressure antinode. This finding has also been observed when comparing maximum cooling and maximum coefficient of performance in Table 5.16 for the TAR models. Contrary to the maximum COPR presented in Figure 6.19, increasing the stack length leads to an increase in cooling load for TAR.

The COPR presented in this study is roughly 70% of Carnot COP. While considering the losses (viscous *and* thermal) along the stack, the heat exchangers, the resonator, the heat leaks through the stack and the resonator and the efficiency of a loudspeaker, the COPR of a complete thermoacoustic refrigerator will be lower than the COPR of a stack as presented in this study.

Table 6.2: Estimated parameters of TAR

Lsn	Xsn						δkn	F [Hz]	Tm [K]	DR
0.065	0.280	0.528	0.777	1.024	1.272	1.520	0.135	135	250	0.025
0.119	0.307	0.555	0.803	1.051	1.299	1.547	0.168			
0.173	0.334	0.582	0.830	1.078	1.326	1.574	0.255			
0.248	0.372	0.620	0.868	1.116	1.364	1.612	0.291			

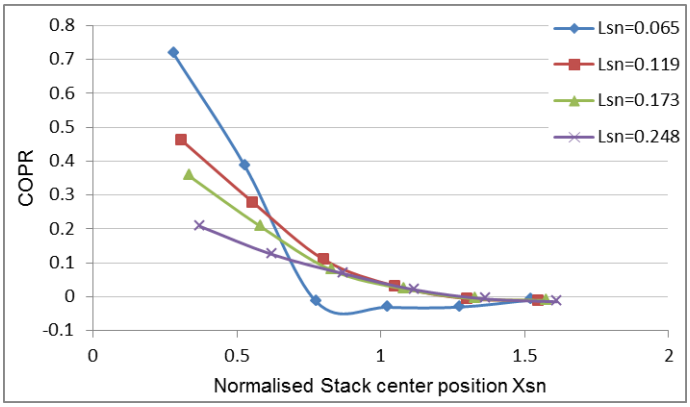

(a)

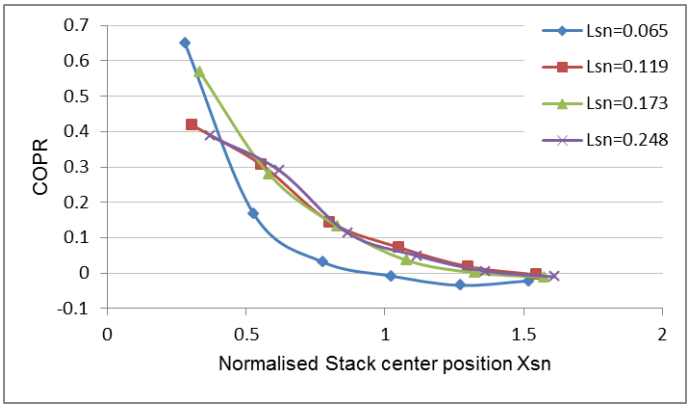

(b)

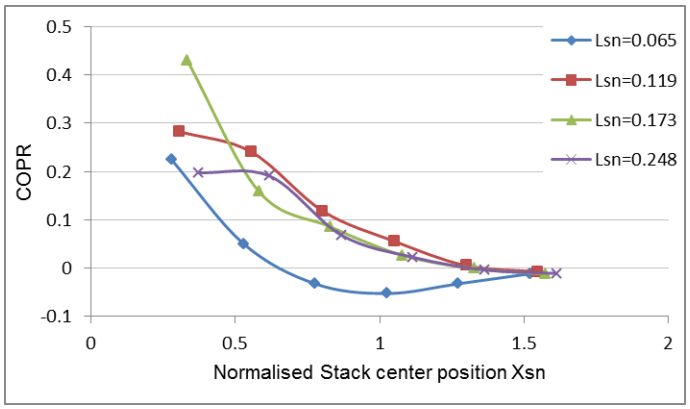

(c)

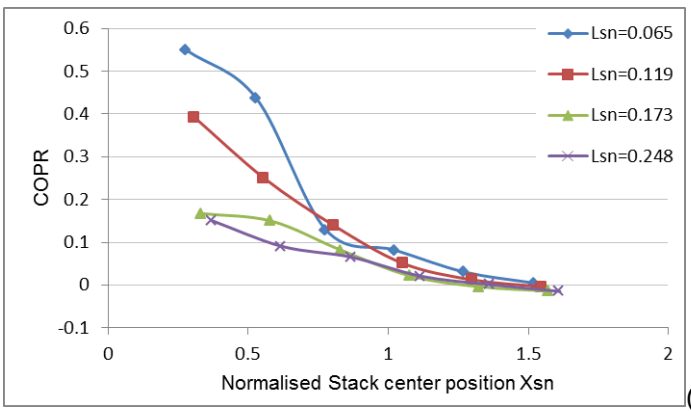

(d)

Figure 6.19: COPR for (a) size 1, (b) size 2, (c) size 3 and (d) size 4 honeycomb ceramic stacks

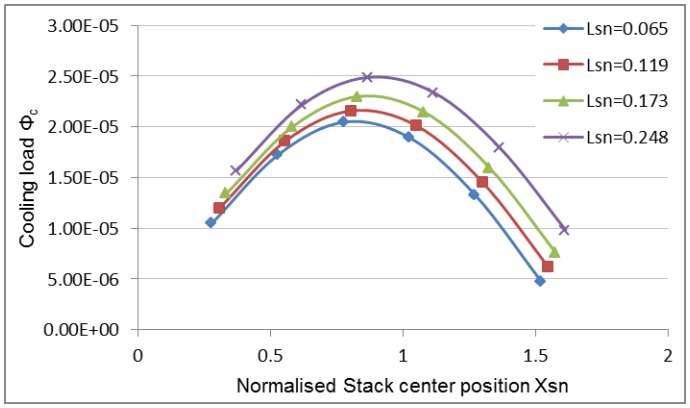

(a)

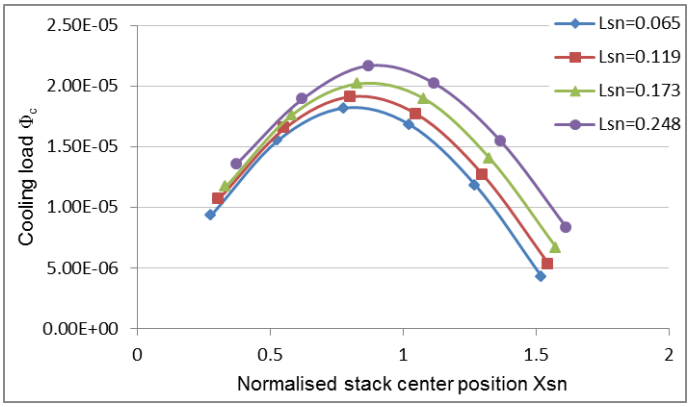

(b)

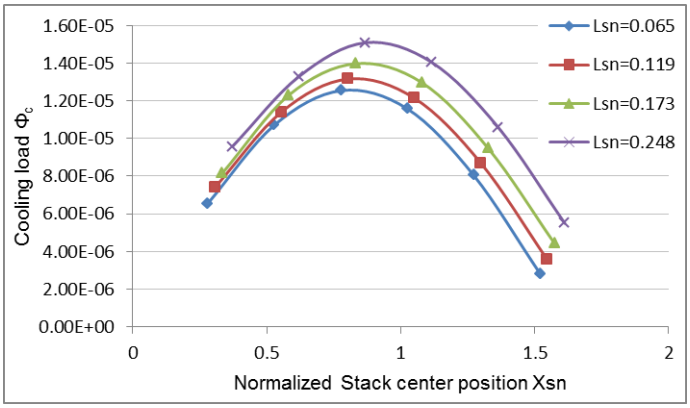

(c)

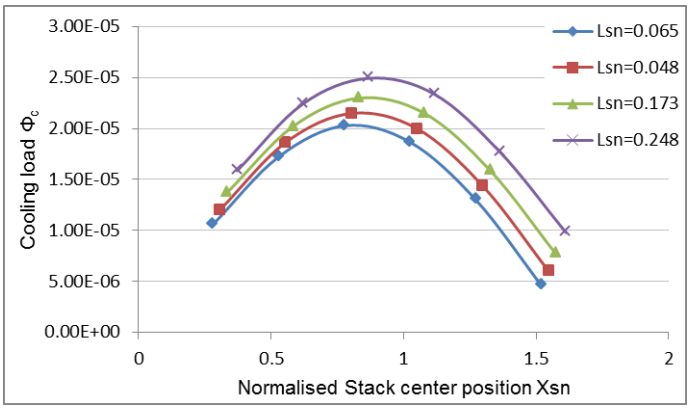

(d)

Figure 6.20: Cooling load for (a) size 1, (b) size 2, (c) size 3, and (d) size 4 honeycomb ceramic stacks

6.2.3.7 TAR models evaluations

In Chapter 5, mathematical programming models were presented to compute optimal solutions corresponding to the optimal geometry of the stack in a thermoacoustic refrigerator. A thermoacoustic resonator tube was constructed, and experiments with a 'thermoacoustic couple' were conducted in this section. These experimental results have been compared with the mathematical programming results of the models. The ε-constraint method as formulated in Equation 5.28 was applied. The following constraints (upper and lower bounds) have been enforced in order for the solver to carry out the search for the optimal solution in those ranges:

$X_{Sn}.lo = 0.280;\ \ X_{Sn}.up = 1.612$

$\delta_{kn}.lo = 0.05;\ \ \delta_{kn}.up = 0.1$

The thermal penetration depth range has been shortened to reduce the computational time (as that could take several days) since the result trends were more important. The normalised temperature difference (θ) is set to be equal to 0.030. The blockage ratio has been set to 0.8. More input parameters are shown in Table 6.2. The normalised stack length has been arbitrarily given values of 0.065-0.119-0.173-0.248 successively. Table 6.3 reports the results obtained representing the optimal parameters, namely BR, δ_{kn}, and X_{sn}, giving the highest performance.

For a specific value of normalised temperature difference (θ), the trend of the COPR and the cooling load (Φ_c) is the same as the ones reported in Figures 6.19 and 6.20 (the trendlines are shown for visual guidance). These results suggest that the COPR is maximised closer to the closed end while the cooling (Φ_c) reaches its maximum value away from the closed end.

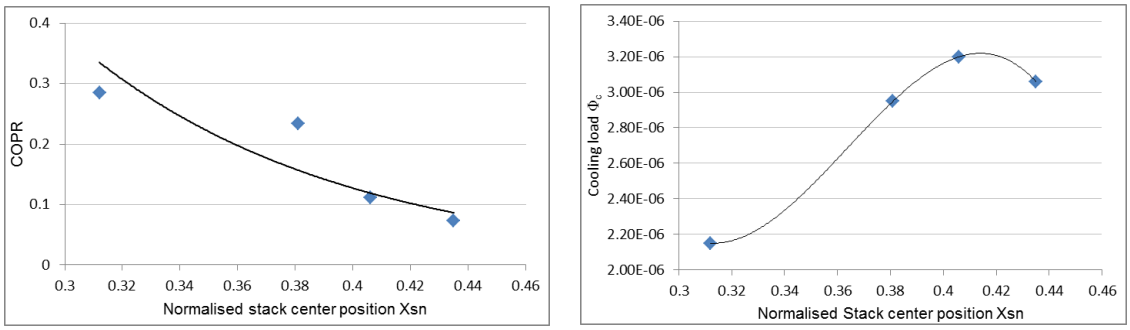

Figure 6.21: AUGMENCON results representing COPR and Φ_c for cordierite honeycomb ceramic stack

Table 6.3: Computation results obtained using AUGMENCON

	Results	1	2	3	4	5	6	7	8	9	10
$L_{sn} = 0.065$	BR	**0.800**	0.800	0.800	0.800	0.800	0.800	0.800	0.800	0.800	0.800
	δ_{kn}	**0.061**	0.075	0.081	0.100	0.100	0.100	0.100	0.075	0.075	0.050
	X_{Sn}	**0.312**	0.312	0.313	0.310	0.311	0.311	0.311	0.314	0.376	1.390
	Φ_C	**2.15E-06**	1.92E-06	1.69E-06	2.07E-06	2.88E-07	2.09E-06	3.04E-08	2.15E-07	1.55E-06	5.21E-6
	COP	**9.372**	9.357	8.990	8.992	8.992	8.992	8.993	8.988	8.988	13.711
$L_{sn} = 0.119$	BR	**0.800**	**0.800**	0.800	0.800	0.800	0.800	0.800	0.800	0.800	0.800
	δ_{kn}	**0.050**	**0.100**	0.100	0.084	0.073	0.061	0.050	0.095	0.095	0.084
	X_{Sn}	**0.381**	**0.355**	0.340	0.377	0.379	0.381	0.382	0.376	0.376	0.379
	Φ_C	**1.35E-06**	**2.88E-06**	2.57E-06	2.27E-06	1.96E-06	1.66E-06	1.35E-06	2.88E-06	2.57E-06	1.96E-6
	COP	**7.686**	**6.484**	6.677	5.361	5.362	5.363	5.364	5.360	5.360	5.362
$L_{sn} = 0.173$	BR	0.800	0.800	0.800	0.800	0.800	0.800	**0.800**	0.800	0.800	0.800
	δ_{kn}	0.050	0.089	0.089	0.085	0.073	0.062	**0.100**	0.097	0.097	0.050
	X_{Sn}	0.413	0.407	0.407	0.408	0.409	0.411	**0.406**	0.406	0.406	0.413
	Φ_C	1.44E-0.6	3.14E-06	2.80E-06	2.46E-06	2.12E-06	1.78E-06	**3.20E-06**	2.80E-06	3.14E-06	4.30E-7
	COP	3.651	3.660	3.660	3.647	3.649	3.650	**3.661**	3.645	3.645	3.651
$L_{sn} = 0.248$	BR	**0.800**	**0.800**	0.800	0.800	0.800	0.800	0.800	0.800	0.800	0.800
	δ_{kn}	**0.050**	**0.089**	0.089	0.085	0.074	0.062	0.098	0.050	0.071	0.097
	X_{Sn}	**0.435**	**0.428**	0.428	0.430	0.432	0.433	0.427	0.435	0.400	0.428
	Φ_C	**1.43E-06**	**3.12E-06**	2.78E-06	2.44E-06	2.11E-06	1.77E-06	3.12E-06	1.43E-06	2.27E-06	2.78E-6
	COP	**2.381**	**2.377**	2.377	2.377	2.379	2.380	2.375	2.381	2.886	2.376

6.3 Thermoacoustic engines

6.3.1 Experimental objectives

The main objectives of this experimental scheme are to obtain the following characteristics of the stack:

- Measurements of sound pressure level (SPL) obtained at the resonant tube open end using different stack geometries (lengths of the stacks varying from 7 mm to 25 mm) and stack spacing (cordierite honeycomb ceramic stacks ranging from 64 CPSI-300 CPSI).
- Measurements of the sound pressure level (SPL) obtained at the resonant tube end for different positions of the stack (the hot end of the stack varied from 52 mm to 172 mm from the closed end).
- Measurements of the temperature difference (ΔT) obtained across the stack ends in each case.

6.3.2 Experimental Facility

The TAE experimentation was carried out using a quarter wavelength resonator design. Data acquisition was handled by the same system as for the thermoacoustic refrigerator in Section 6.2.

The experimental facility has the following subsections:

- Experimental set-up
- Test Procedure

6.3.2.1 Experimental set-up

The experimental prototype shown in Figure 6.13 is a standing wave thermoacoustic engine, including the following components:

- a heater;
- a resonant tube; and
- a stack.

The lack of a heat exchanger at the stack's cold end leads to natural cooling for the stack's cold end which is made of cordierite honeycomb ceramic stack with square pores.

The total length of the present prototype is 200 mm and the resonant tube inner diameter is 22 mm. The location of the stack inside the resonant tube is variable during experiments. The Nicrome (NiCr) wire, embedded at one end of the stack, is used as a heater. This wire

allows for a maximum temperature of approximately 1100^{o}C, sufficiently high for this application. The heating input is controlled by a LODESTAR DC power supply PS-303D. This research intends to study the effect of the geometry and stack position on the performance of the standing wave engine. Therefore, particular care was given to making stack profiles that were geometrically identical to each other.

Similar to the measurement set-up of TAR, the prefabricated stacks were made of 64, 100, 230 and 300 CPSI (cells per square inch) respectively manufactured by Applied Ceramics, Inc. (Applied Ceramics, 2011). Twenty cordierite honeycomb ceramic stacks with square pores (as shown in Figure 6.14) and five different lengths (7 mm, 13 mm, 17 mm, 22 mm and 25 mm) were considered. Measurements were taken at seven different locations of the stack hot ends from the pressure antinode (closed end), namely 52 mm, 72 mm, 92 mm,112 mm, 132 mm, 152 mm and 172 mm respectively.

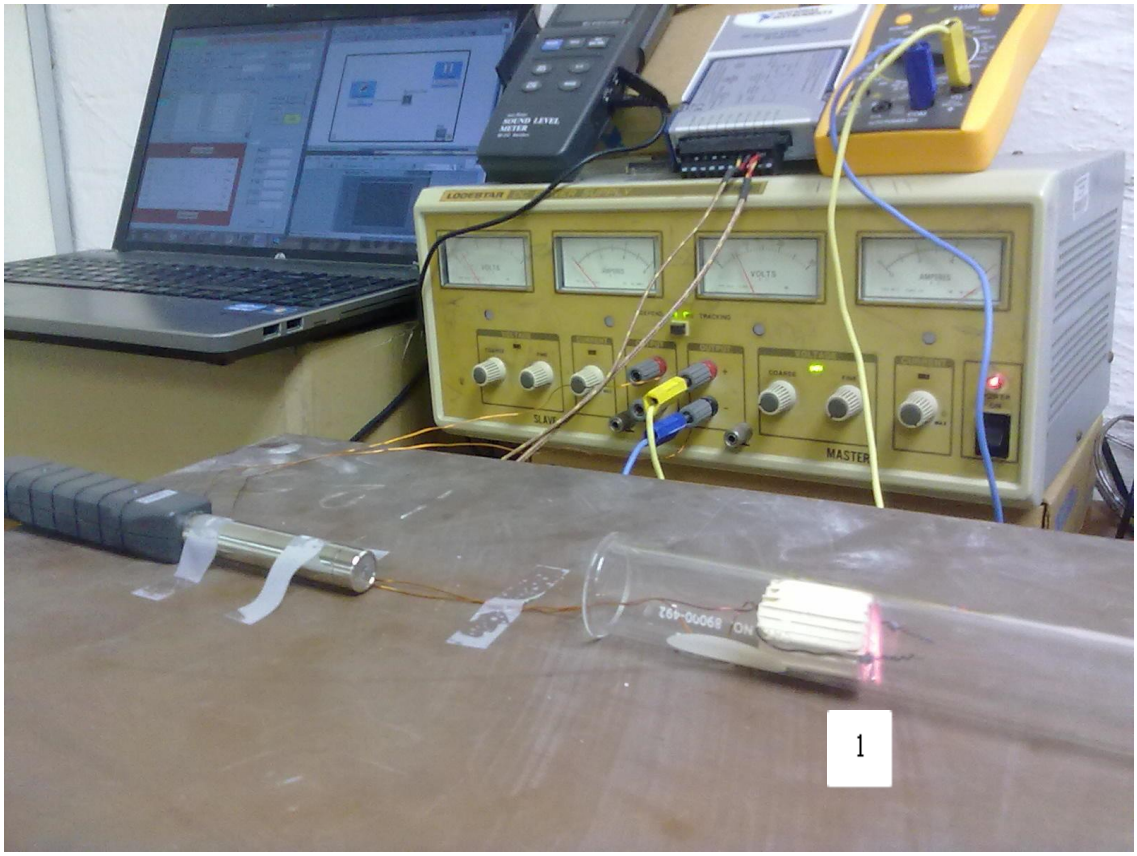

Figure 6.22: Thermoacoustic engine and the measuring systems.

1	Nichrome (NiCr) resistance heater wire

Figure 6.23: Stack samples used in the experiments/TAE

6.3.2.2 Test procedure

In order to investigate the influence of the stack geometry and position on the performance of the device, thermocouples (K-type) were mounted on the hot and cold side of the stack for temperature measurements. The sound level meter was mounted coaxially with the resonator (Figure 6.21), 100 mm from the open end, in order to record the sound output of the engine. Prior to the start of the experiment, the stack was adjusted at a certain position. The electric voltage from the DC power supply was connected across the NiCr wire. Each test was run over 250 to 350 seconds (Figure 6.24). The thermocouples were read with NI USB-9211 like previously. Figure 6.24 illustrates the hot side temperature, the cold side temperature and the temperature difference across the stack end as obtained and recorded in this study.

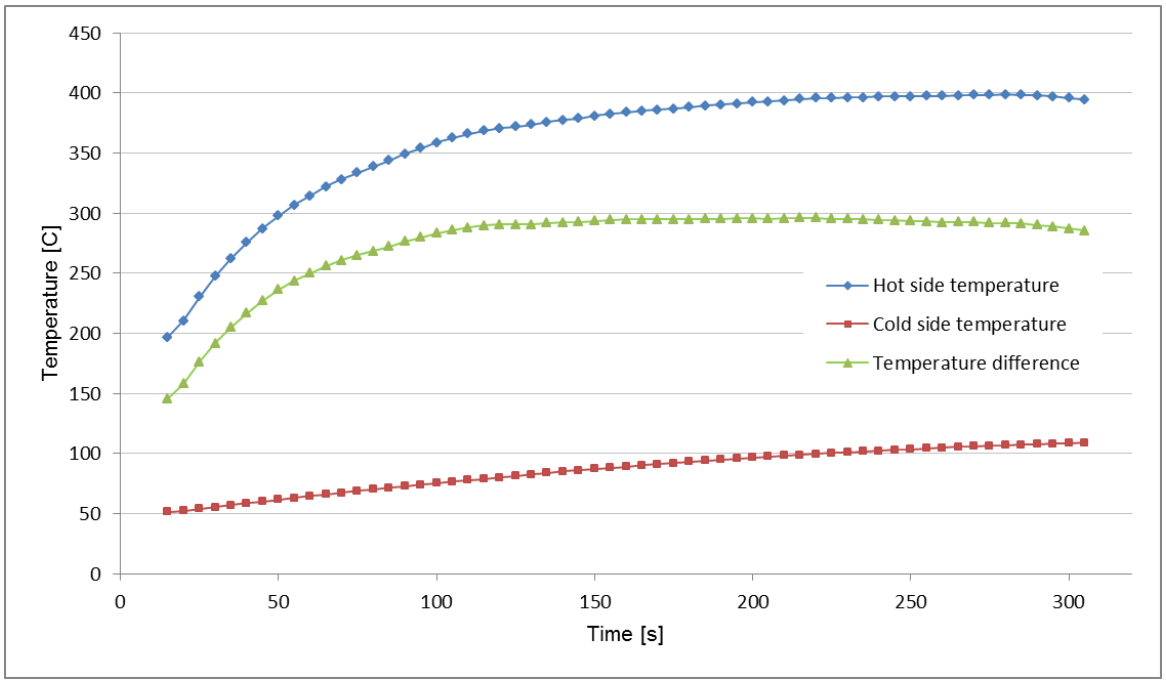

Figure 6.24: Hot side and cold side temperature across the ceramic stack/TAE

Before discussing the results from the stack geometry and position variation, two main sources of error should be identified:

- The NiCr wire used as the hot side heat exchanger failed several times, prompting replacement. Although great care was given to ensuring that each assembly was identical to the previous version, this must be considered as a potential source of error.
- The location of thermocouples could not be determined exactly. As a result, placement of the thermocouple leads was not trivial and visual access was the only means to confirm placement in the assembly. This may very well be the cause of variation in data collected from the thermocouples.

6.3.3 Results, thermoacoustic refrigerator

During the tests of the different stacks in the aforementioned engine set-up, temperature data at each end of the stack and sound pressure level (SPL) were recorded. In addition, the voltage applied to the heating wire was recorded. In conjunction with the resistance data from the heating wire, the applied electrical power was calculated using the direct correlation derived from Ohm's Law $P = \frac{U^2}{R}$. The resulting sound pressure level was recorded in case of oscillations (all other values are assumed to be zero even though this is not physically achievable). The most useful way to disseminate the findings is by analysing the temperatures on each end of the stack as it is this temperature difference that is directly responsible for the acoustic output of the engine.

6.3.3.1 Frequency spectrum of the emitted sound

When one side of the stack near the closed end of the tube is heated and the open end of the tube is maintained at room temperature, the engine begins to emit sound. The total length of the TAE is 200 mm, which corresponds to a resonant frequency of 430 Hz. A test was performed to identify the frequency of the emitted sound. An electrical energy of 25W was supplied to the hot side of the stack. After approximately 10 seconds, a large temperature gradient parallel to the engine axis builds up in the ceramic stack and the engine begins to emit sound with a frequency of around 450 Hz, corresponding to the highest peak as shown in the frequency spectrum of Figure 6.15.

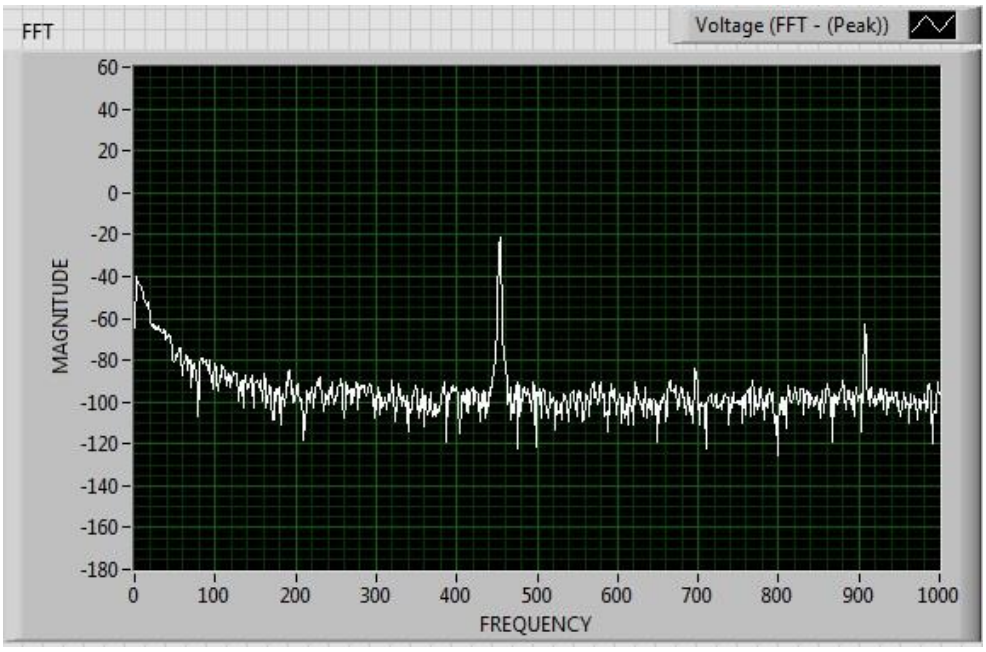

Figure 6.25: Frequency spectrum of sound output

6.3.3.2 Temperature behaviour of stacks as a function of power input

In this set of experiments, the effect of the input power on the temperature difference across the stack was investigated. During these experiments, the twenty different stacks were moved successively from 52 mm to 152 mm (respectively, position 1 to position 7) relative to the closed end. The temperature differences were measured at the seven different configurations (positions). Additionally, the input power was changed from 15 W to 29 W. Figure 6.26 shows the plots for the temperature difference as a function of input power for the 300 CPSI cordierite honeycomb ceramic stacks. The individual data for all stack sizes (64 CPSI, 100 CPSI and 230 CPSI) is provided in Appendices L, M and N. These results suggest a nonlinear behaviour of the temperature difference as a function of the electrical input power. The cordierite honeycomb ceramic stack exhibits a high temperature difference for all the sizes and positions examined herein. In particular, the 25 mm stack clearly exhibits the highest temperature difference for a 300 CPSI cordierite honeycomb ceramic stack (Figure 6.25). Therefore, the heat fluxes to the surroundings can be assumed to be large. It can be suggested that at high powers, the heat losses will be large enough to make further increases in temperature differences across the stack impossible. However, this range has not been investigated further due to limitations of the heating wire employed in this study.

6.3.3.3 Temperature behaviour of stacks as a function of stack length

The effect of stack length on temperature difference across the stack end was investigated. The results obtained in Figure 6.26 show a positive slope in all cases, suggesting that the cordierite honeycomb ceramic stack isolated the hot from the cold side. Another indication of this fact is the higher slope exhibited when the input power increased. Figure 6.26 shows that an increase of the stack's length results in an increase in the temperature difference. This finding can be added to the models of TAE suggested in this study, especially in Equation 4.9, as it gives a relation between the expected temperature gradient ratio (Γ) and the stack length.

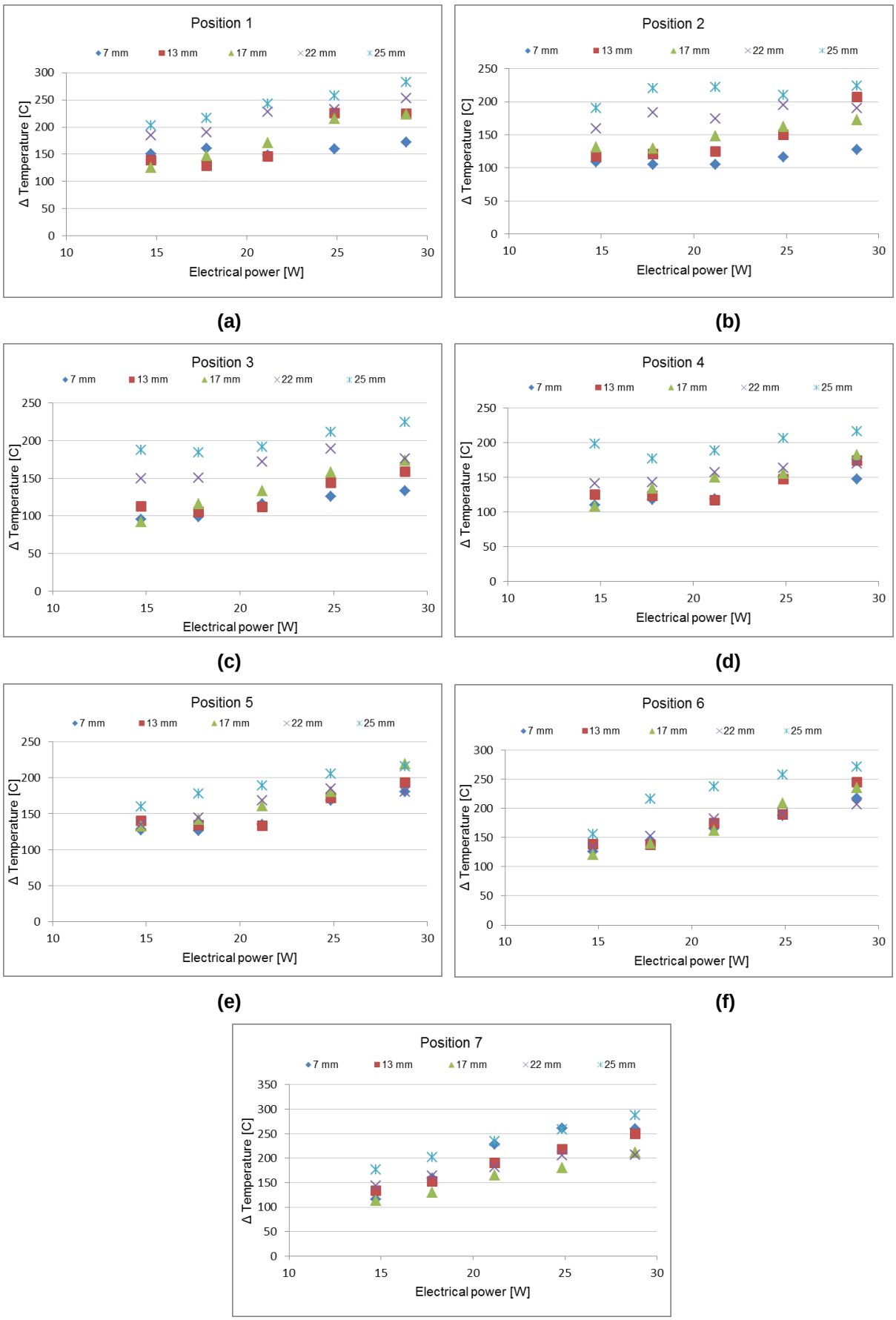

Figure 6.26: Temperature difference across stack ends as a result of variation of input power/300 CPSI

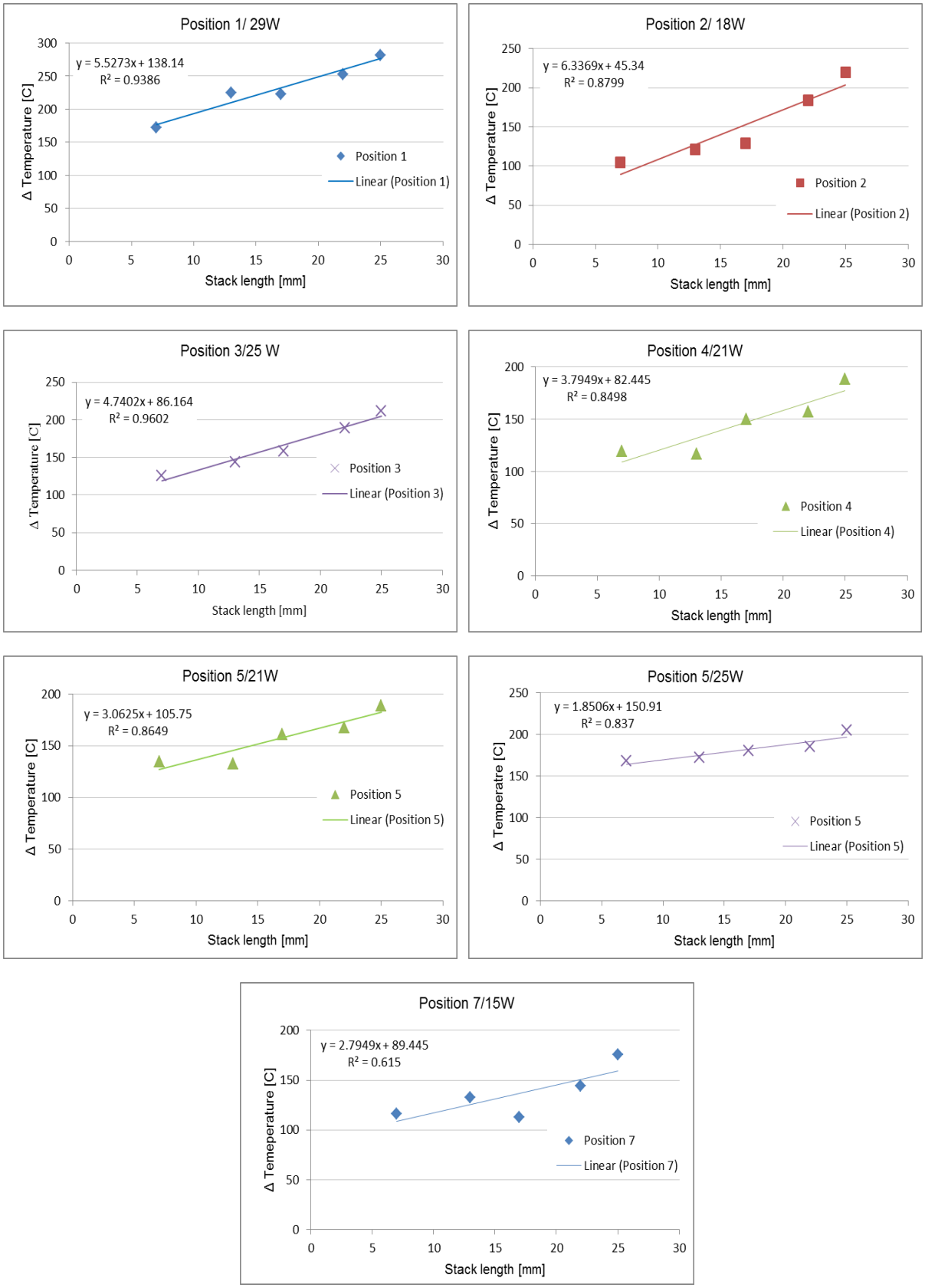

Figure 6.27: Illustration of the temperature difference across the stack as function of the length

6.3.3.4 SPL as a function of power input

This section presents the resulting sound pressure level (SPL) as a function of the input power. As shown in Figure 6.26, the temperature difference across each stack increases with the power input; it is expected that the resulting SPL will increase similarly. As stated before, the SPL value was assumed to be zero when no sound output was produced. In addition, sound was heard and recorded briefly in many measurements; these results were also discarded and considered as zero sound output. Additionally, size 3 and size 4 results were not reported in this study because the sound output couldn't be sustained for a relatively long period (more than one minute) in all measurements. This can be explained by pore size of the considered stack (Table 6.1) exceeding the 4 δ_k suggested by Tijani *et al.* (2002) as the limit for thermoacoustic effect to take place. In addition, Tao *et al.* (2007) suggest that the oscillation may disappear after a temperature fluctuation if the heat input is near the critical value, a phenomenon caused by the thermal energy consumption by the oscillation.

The highest measured SPL for cordierite honeycomb ceramic stack is about 112 dB corresponding to the highest input power of 29 W. An interesting aspect of these results is the magnitude of the SPL function of the stack length. Figure 6.28 and Appendix O suggest using a larger stack when the power is 29 W and recommend a smaller stack when the input power is relatively low. It can be seen that at low power input, no sound output was produced for larger stacks. However, experiments conducted by Tao *et al.* (2007) on a similar ceramic stack suggest that higher power input should lead to lower temperature onset. This result can be attributed to the temperature rise at the stack's cold end, due to the lack of a cold heat exchanger. This result will be elaborated in more detail in the next section.

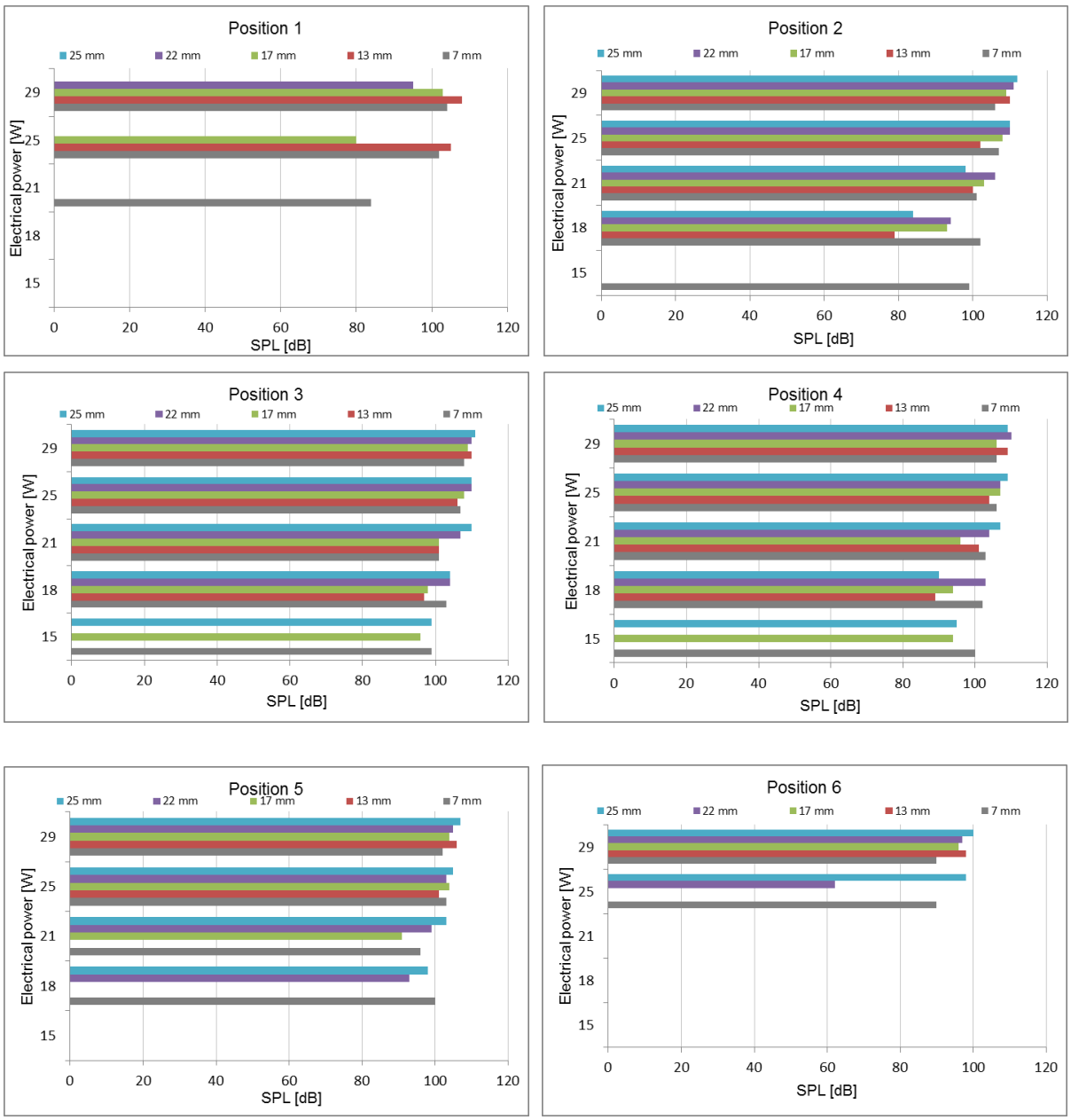

Figure 6.28: SPL as a function of power input for different stack positions, size 1

6.3.3.5 SPL as a function of stack position

This section presents the resulting sound pressure level (SPL) as a function of the stack position. As shown in Section 6.3.3.5, there is a relation between the input power and the expected SPL. Concerning the stack position, most of the oscillations take place at position 3 and position 4, corresponding respectively to 92 and 112 mm from the closed end. In Appendix V, the mathematical model equation based on cordierite honeycomb ceramic stack geometry is presented. We can analyse the structural variables based on individual objective components as based on the results obtained in Section 5.6.1. It should be noted that the acoustic power is proportional to the SPL. The tendency of structural variable for individual objective components is presented in Table 6.4.

Table 6.4: Tendency of structural variable for Cordierite honeycomb ceramic stack

	W	R_v	Q_{conv}	Q_{rad}	Q_{cond}
L	↑	↓	↓	↓	↑
H	↑	↓	↓	↓	↑
d	↑	↓	↓	↓	↓
Za	↓	↓	↓	↓	↓
N	↑	↓	↓	↓	↓

The investigation of the relation between the SPL and the power input cannot be dissociated from the stack geometry, namely the length and the stack spacing. With respect to the stack position, a smaller stack results in a decrease of the acoustic power W and the conductive heat flux, with an increase in viscous resistance, conductive and radiative heat fluxes. The results obtained in Figure 6.28 and Appendix P show that this effect is small enough to cancel out the SPL for low input power. However, when the stack is relatively large, the acoustic power, the viscous resistance, the convective, the radiative and the conductive heat fluxes increase, cancelling out the SPL at low input power. For higher input power and large TAE, the effect of conductive, radiative and convective heat fluxes can be minimised.

An interesting investigation would be to make quantitative measurements of the acoustic pressure amplitude (p_{max}) in Equation 5.11, at the closed end of the test tube and derive the total radiated acoustic power. The results presented in this section suggest that only a small fraction of this input power is ultimately transformed into acoustic power. The remaining energy is lost to the surroundings via convection and radiation and conduction. The optimal geometrical parameters emphasising all the objectives listed in Table 6.4 could then be computed with the models proposed in this study.

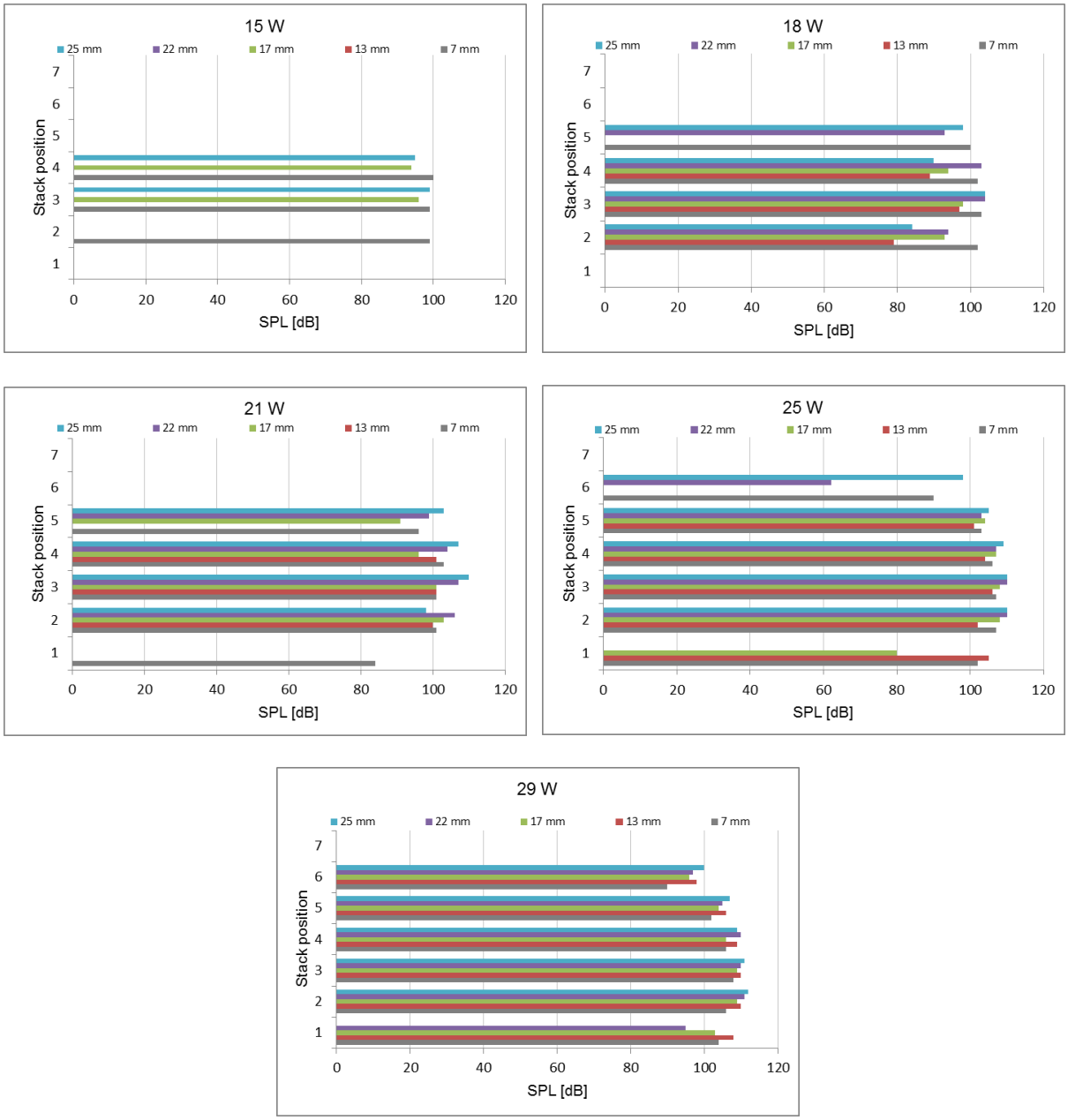

Figure 6.29: SPL as a function of stack position, size 1

6.3.3.6 SPL as a function of stack pore sizes

This section presents the comparison of results between the sound pressure levels (SPL) as function of the stack pore sizes. Looking at size 1 and size 2 (Table 6.1), most of the oscillations take place at position 3 and position 4, corresponding respectively to 92 and 112 mm from the closed end. With respect to the pore sizes, size 1 is preferable when the length of the stack is relatively short, as demonstrated from results obtained in Figure 6.29, in Appendix Q and Appendix R. This choice is dependent on the input power for larger stacks (Appendices S and T). This can be explained as follows: a smaller stack spacing (dc) results in a decrease of the acoustic power, viscous resistance, convective, radiative and conductive

heat fluxes. However, when the stack spacing increases, the acoustic power increases but the viscous resistance and the thermal losses decrease (Table 6.4). The effect of the viscous resistance and the thermal losses is strong enough when the stack length is short and the input power is low, as shown in Figure 6.29 and Appendices Q, R, S and T.

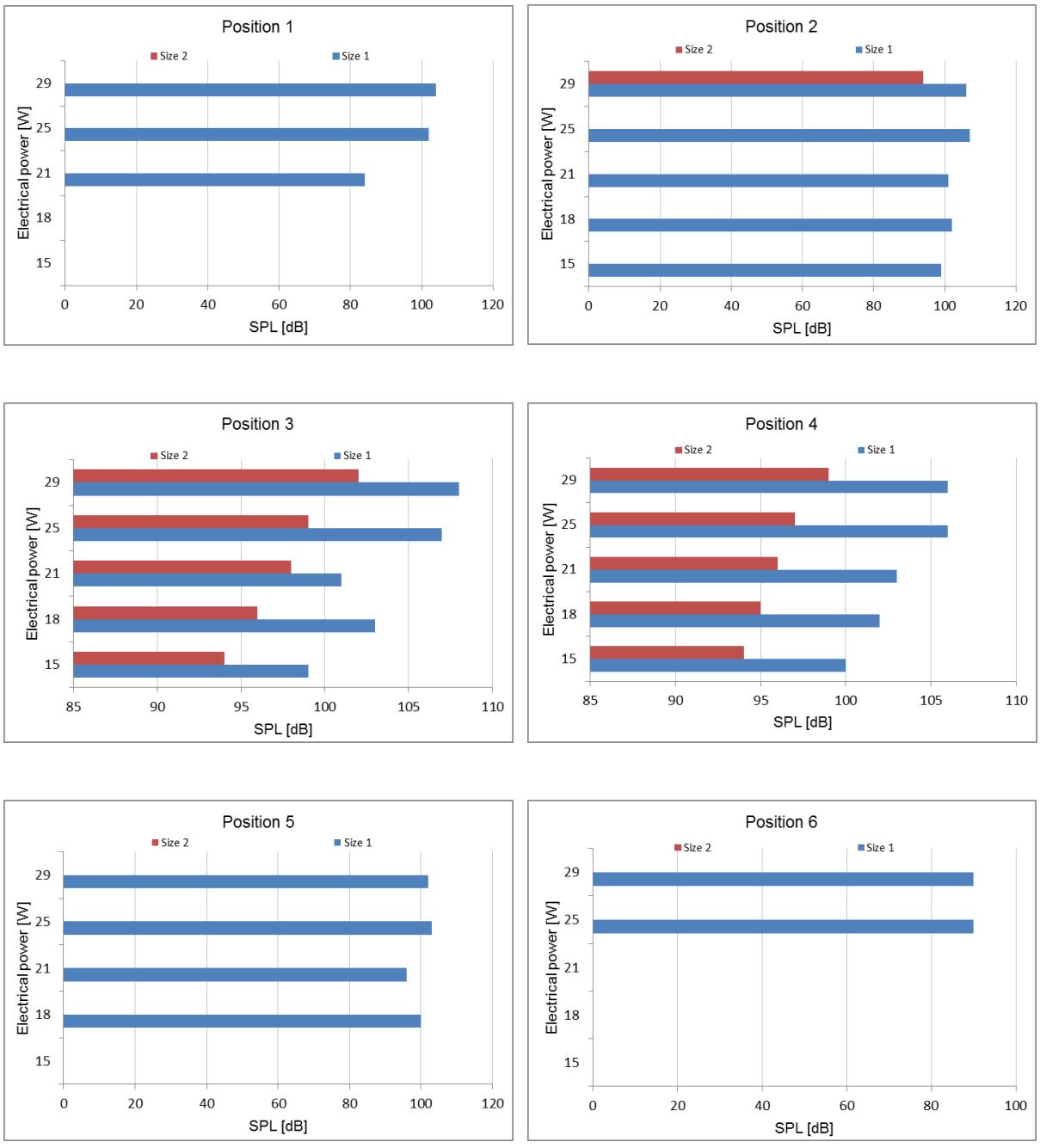

Figure 6.30: SPL as a function of stack pore size, L=7 mm

6.3.3.7 Comments on experimental uncertainty

Every measurement is subject to some uncertainty. The uncertainty of a measurement is defined as the difference between the measured value and the true value of the measurand. Errors in experiments generally fall into two categories (Bell, 1999):

- precision errors (random errors); and
- bias errors (systematic errors).

Major sources of the bias errors pertain to accuracy of the instrument and calibration errors. Precision errors are detected by a lack of repeatability in the measurement output.

A rigorous error analysis in a system with multiple geometries, positions and measurements such as described in this chapter is relatively difficult. Although individual errors of each type of measurement are known (pressure transducers, thermocouples, etc.), the important aspect of the experiment is whether or not the observed thermoacoustic processes are fully repeatable for the same experimental conditions. In order to obtain some indication of the compounded value of measurement error, its repeatability is investigated.

As a demonstration of this principle, Figure 6.30 shows the values of temperature difference measured for three independent experiments carried out on three different times. The stack length and size are respectively 25 mm and 300 CPSI. It can be seen that the spread of the results is within 5% for these high temperature differences. This cannot be attributed to the thermocouple 'accuracy' which is 2.2^{o}C, but to the repeatability of the independent experiments that indeed give the spread of temperature within that range.

Similar investigation on repeatability/uncertainty can be associated with the sound pressure level (SPL). Figure 6.31 shows the corresponding sound pressure level measurements. It can be seen that the spread of results is within 2% of the sound pressure value.

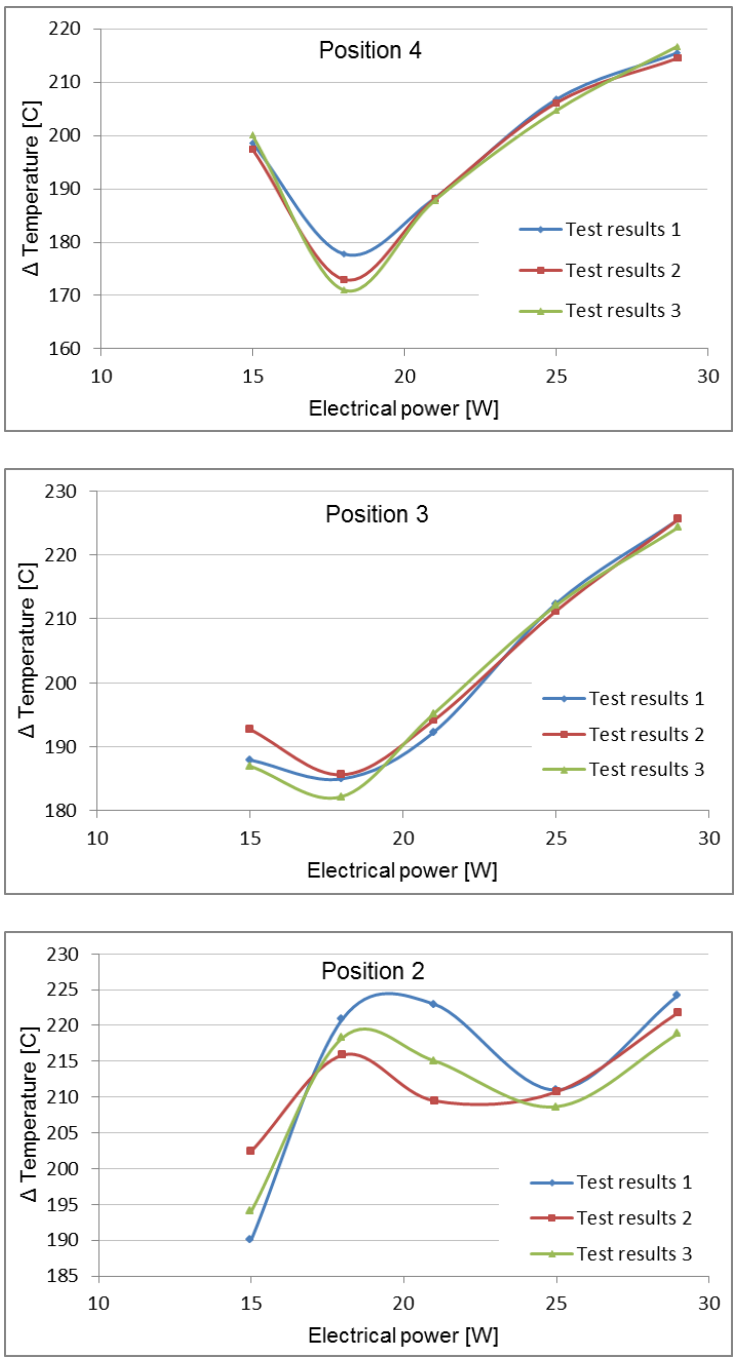

Figure 6.31: Illustration of the experimental uncertainty through repeatability test results for temperature difference

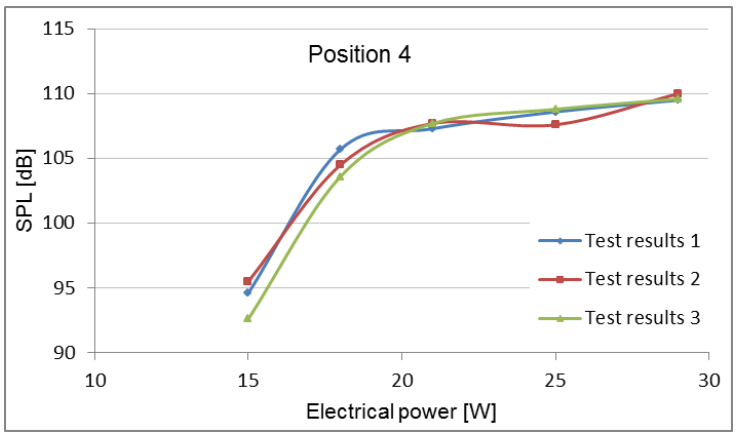

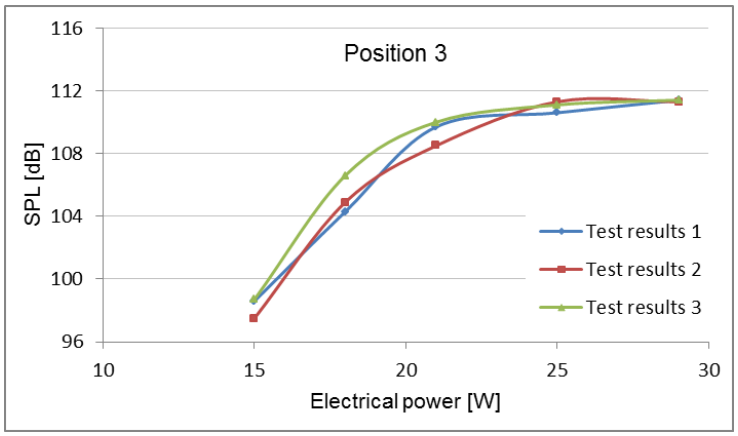

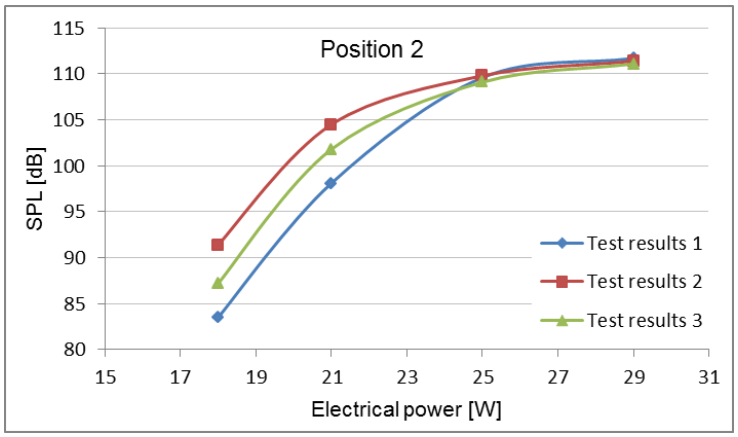

Figure 6.32: Illustration of the experimental uncertainty through repeatability test results for SPL

6.4 Conclusion

The goal of these experiments was to investigate the influence of stack geometry and position on the performance of thermoacoustic engines and refrigerators and evaluate the ability of the proposed models to predict the performance of the device. Detailed conclusions for both cases are presented below.

6.4.1 Refrigerators

In order to investigate the influence of stack geometry and position on the performance of the device, an acoustically-driven thermoacoustic refrigerator was built. This system utilises a loudspeaker to create strong sound waves in a quarter wavelength resonator. Sixteen different cordierite honeycomb ceramic stacks of four different pore sizes were investigated. These stacks were moved successively at six different locations inside the resonator. The temperature differences across the stack in each configuration were used to measure the performance of the refrigerator. The influence of the stack length, the stack position and the stack pore sizes reveal that there is a peak of temperature difference. The results suggest that the stack should be located closer to the pressure antinode for maximum temperature difference in all cases. However, the stack length and the stack pore sizes cannot be treated independently based on the profile of the temperature differences measured. This study reveals that these are indeed interdependent.

The data obtained were used to calculate the coefficient of performance and the cooling load. While locating the stack closer to the pressure antinode for maximum performance of the device is confirmed through this study, the design for maximum cooling implies moving the stack *away* from the pressure antinode. This finding is relevant to electronic cooling where maximum cooling is more important.

Finally, the proposed models were tested to evaluate their ability to predict the best parameters describing the geometry of the stack. Similar trends were obtained to reinforce the use of the proposed approach in the design of thermoacoustic refrigerators.

6.4.2 Engines

For the investigation of the thermoacoustic engine, a simple standing wave demonstrator device was used. A NiCr wire connected across a DC power supply supplied the heating input. Twenty different cordierite honeycomb ceramic stacks of four different pore sizes were investigated. The sound output was used as the metric to quantify the performance of each stack. The temperature behaviour of the stack functions of the electrical heating power

shows that longer stacks exhibit higher temperature difference. This study reveals that the temperature difference function of the electrical heating power was nonlinear. The study on the influence of the length on the temperature difference shows that increasing the stack length results in an increase of temperature difference.

The influence of the SPL on the electrical heating power was also investigated. This study reveals that wider pore sizes result in minimum radiated sound or no sound output. That was the case for more than half of the considered cordierite ceramic honeycomb stacks. Higher electrical heating input results in higher radiated sound in most of the cases. The highest SPL recorded was 112 dB. The study on the influence of the stack position on the radiated sound reveals that positioning the stack on a specific location results in the highest sound output. The study on the influence of the stack pore sizes on the SPL reveals that length and pore size cannot be considered independently. The results obtained show that smaller pore size is preferable when the length of the stack is relatively short, and the opposite is observed for large stacks.

Finally, the results obtained were analysed based on the proposed approach in this study. An important finding reveals that the effect of the viscous resistance and the thermal losses is strong enough when the stack length is short and the input heating power is lower. This is important for electronic cooling application and suggests that cooling an array of components instead of a single one could minimise the effect of viscous and thermal losses of the thermoacoustic engine.

CHAPTER 7: CONCLUSIONS AND RECOMMENDATIONS

7.1 Conclusion

In order to manage the ever-increasing levels of waste heat in electronics, a thermoacoustic approach is presented in this study. It is simple, efficient and capable of coping with higher power densities. Two different devices have been investigated: 1) a simple thermoacoustic engine, and 2) a simple thermoacoustic refrigerator. Scaling down these devices plays a significant role. Firstly, it raises questions concerning efficiency and the performance. Secondly, there are limitations as well as fabrication issues when the device size is reduced by an order of magnitude or even more. Several engineering tools are proposed to model and optimise the design and the performance of the thermoacoustic device. The relevant parameters determining the performance are mostly used during the optimisation process. This work focuses on the stack, considered the heart of the thermoacoustic system, as it critically affects its performance.

Recent studies reveal that scaling down the device leads to an increase of the ratio between the surface area and the active volume, resulting in higher thermal losses. These thermal losses - the convective, radiative and conductive heat fluxes - need careful attention since they are not adequately included in current modelling approaches. An estimate of heat losses shows that they are significant relative to the total energy supplied to the thermoacoustic engine (TAE). This provides a clear motivation to include the aforementioned losses in the modelling approach in an effort to improve the performance of the devices.

In addition, much work related to the modelling and optimisation of thermoacoustic refrigerators has contributed to the theoretical and practical advances of large scale systems due to geometrical and thermo-mechanical limitations. Two similar outcomes, maximum cooling and maximum coefficient of performance, were found not to be the same. While the former was the required criteria for electronics cooling, the latter is required for large-scale thermoacoustic systems. This aspect is important for the success of the design and raises questions pertaining to its implication on the geometry of the device.

In order to tackle these issues, this research takes a step forward by conducting research into three major areas, with narrowed focus on the geometry and the position of the stack. The three major areas of research are as follows:

- thermoacoustic refrigerators modelling and design optimisation;
- thermoacoustic engines modelling and design optimisation; and

- experimental works with cordierite honeycomb ceramic stack.

The major areas of research and their outcomes are elaborated in the next paragraphs.

A new mathematical modelling approach is proposed to model and optimise thermoacoustic engines while taking into account thermal losses. The idea of incorporating thermal losses in the modelling and optimisation of TAE gives the decision maker a clear picture of expected magnitude and the ability to search for the configuration that will simultaneously minimise them.

- A multi-objective optimisation approach is used to compute the optimal set of parameters describing the geometry of the device: the stack length, stack height, stack position from the closed end of the TAE, stack spacing and the number of channels. These are the variables in the mathematical modelling formulation.
- The performance of the device is measured through the acoustic (work output and viscous resistance) and the thermal losses (convective, radiative and conductive heat fluxes) that have been used as objective functions to measure the quality of each set of variable values that satisfies all of the constraints. These objectives have been derived in this work.
- This problem has been formulated as a five-criterion mixed-integer nonlinear programming problem. This formulation allows for identifying the implication of each objective emphasis on the geometry of the stack. It has been implemented in the software GAMS (General Algebraic Modelling System). The detailed models are reported in Appendices A, B, C, D, E and F.
- For multiple objective optimisations, the ε-constraint method combined with a lexicographic method (AUGMENCON) is proposed to generate only non-dominated Pareto optimal solutions.
- A case study is used for illustration. A complete set of objective functions and Pareto optimal solutions are computed in this work and guidance for the decision maker's selection of the preferred solution is suggested.
- The unique finding of this approach is the interdependency between geometrical parameters which makes a multi-objective optimisation approach relevant and useful for the modelling of TAEs. The results clearly suggest that there is a specific stack length corresponding to a specific stack position, specific stack spacing, specific stack height and specific number of channels for maximum performance of the TAE.

A new mathematical modelling approach is proposed to model and optimise thermoacoustic refrigerator. It provides fast engineering estimates to the design calculation and selection for large-scale and small-scale applications.

- A multi-objective optimisation approach is used to compute the optimal set of parameters describing the geometry of the device. These are the stack length, stack centre position, stack spacing and blockage ratio of the TAR. These are the variables in the mathematical modelling formulation.
- The performance of the device is measured through the maximum cooling, coefficient of performance and acoustic power loss that have been used as objective functions to measure the quality of each set of variable values that satisfies all the constraints.
- This problem has been formulated as a three-criterion mixed-integer nonlinear programming problem. This formulation allows for identifying the implication of each objective emphasis on the geometry of the stack. It has been implemented in the software GAMS (General Algebraic Modelling System). The detailed models are reported in the Appendices G, H, I, J, K and U.
- For multiple objective optimisations, the ε-constraint method combined with a lexicographic method (AUGMENCON) is proposed to generate only non-dominated Pareto optimal solutions. The best mathematical programming formulation leading to the highest performance has been identified.
- A case study is included for illustration. A complete set of objectives functions and Pareto optimal solutions are computed in this work and guidance for the decision maker's selection of the preferred solution is suggested.
- The unique finding of this approach is the interdependency between geometrical parameters which makes a multi-objective optimisation approach relevant and useful for the modelling of TARs. The results reveal that there is a specific stack length corresponding to a specific stack centre position, specific stack spacing and specific blockage ratio for maximum performance of the TAR.

Experimentally, the present study has investigated a simple acoustically-driven thermoacoustic refrigerator and a simple thermoacoustic engine. The influence of the stack geometry and position on the performance of the devices is reported. In addition, the proposed models are evaluated.

For the TAR:

- Sixteen different cordierite honeycomb ceramic stacks of four different pore sizes were investigated. These stacks were moved successively at six different locations inside the resonator.
- The temperature differences across the stack in each configuration were used to measure the performance of the refrigerator. The influence of the stack length, the stack position and the stack pore sizes reveal that there is a peak of temperature difference. The highest temperature difference obtained was 19.136 ^{o}C.

- The results suggest that the stack should be located closer to the pressure antinode for maximum temperature difference in all cases. However, the stack length and the stack pore sizes cannot be treated independently based on the profile of the temperature difference measured. This study reveals that there are undeniably interdependent.
- The coefficient of performance and the cooling load were calculated with the data obtained. While locating the stack closer to the pressure antinode for maximum performance of the device is confirmed through this study, the design for maximum cooling suggests moving the stack away from the pressure antinode. This finding is relevant to electronic cooling where maximum cooling is more important.
- The test of the proposed models to evaluate their ability to predict the best parameters describing the geometry of the stack has revealed similar trend with experimental results. This finding reinforces the use of the proposed approach in the design of thermoacoustic refrigerators.

For the TAE:

- Twenty different cordierite honeycomb ceramic stacks of four different pore sizes were investigated.
- A NiCr wire connected across a DC power supply was used to supply the heating input. The resulting sound output was used as the metric to quantify the performance of each stack.
- The temperature behaviour of the stacks functions of the electrical heating power shows that longer stacks exhibit higher temperature difference. This study reveals that the temperature difference function of the electrical heating power was nonlinear.
- The influence of the length on the temperature difference shows that increasing the stack length results in an increase of the temperature difference.
- The influence of the SPL on the electrical heating power was also investigated. This study reveals that wider pore sizes result in minimum radiated sound or no sound output. That was the case for more than half of the considered cordierite ceramic honeycomb stack. Higher electrical heating input results in higher radiated sound in most of the case. The highest SPL recorded was 112 dB.
- The influence of the stack position on the radiated sound reveals that positioning the stack on a specific location results on a highest sound output.
- The influence of stack pore sizes on the SPL was studied. The results obtained reveals that the length and the stack pores sizes are dependants. Smaller pore size is preferable when the length of the stack is relatively short and the opposite is observed for large stack.

- The analysis of the obtained results based on the proposed approach in this study was done. An important finding reveals that the effects of the viscous resistance and the thermal losses are strong enough when the stack length is short and the input heating power is lower. This is important for electronic cooling application and suggests that cooling an array of components instead of a single one could minimise the effects of viscous and thermal losses of the thermoacoustic engine.

7.2 Recommendations

- A multi-objective approach is proposed in this study for a TAE and a TAR considered separately. This approach can be used for the development of a multi-objective optimisation approach of a thermoacoustically-driven thermoacoustic refrigerator.
- An improved engine setup will yield a better understanding of thermal losses. This will allow measurement of the maximum pressure at the closed end and clarify the phenomenon observed at low input power for a short stack.
- The models proposed in this study can be expanded to incorporate the heat exchangers and the resonator losses.
- This new mathematical approach can be implemented in the design and optimisation of devices employing traveling wave to streamline their designs.

7.3 Publications

- Tartibu, L.K., Sun, B. & Kaunda M.A.E. 2013. Optimal design study of thermoacoustic regenerator with lexicographic optimisation method. *Journal of Engineering, Design and Technology*. DOI 10.1108/JEDT-09-2012-0039.
- Tartibu, L.K., Sun, B. & Kaunda M.A.E. 2013. Geometric optimisation of micro-thermoacoustic cooler for heat management in electronics. *IEEE International Conference on Industrial Technology (ICIT)*, Cape Town, South Africa, pp. 527 – 532.
- Tartibu, L.K., Sun, B. & Kaunda M.A.E. 2015. Multi-objective optimisation of a thermoacoustic regenerator using GAMS. *Journal of Applied Soft Computing*. vol. 28, pp. 30–43.
- Tartibu, L.K., Sun, B. & Kaunda M.A.E. 2014. Lexicographic multi-objective optimisation of thermoacoustic refrigerator's stack. *Journal of Heat and Mass Transfer*. DOI 10.1007/s00231-014-1440-z.

REFERENCES

Abdel-Rahman, E., Azenui, N.C., Korovyanko, I. & Symko, O.G. 2002. Size considerations in interfacing thermoacoustic coolers with electronics. *Thermomechanical Phenomena in Electronic Systems, Proceedings of the Intersociety Conference*, 421.

Abdel-Rahman, E., Behunin, R., Kwon, Y. & Symko, O.G. 2003. Heat Transfer by High-Frequency Thermoacoustic Engines, in: J.P. Meyer (Ed.), *Proceedings of the Second International Conference on Heat Transfer, Fluid Mechanics, and Thermodynamics,* HEFAT.

Adeff J.A. & Hofler T.J. 2000. Design and construction of a solar powered, thermoacoustically driven thermoacoustic refrigerator. *The Journal of the Acoustical Society of America*, 107(6): 37-42.

Adeff J.A. & Hofler T.J. 2000. Performance improvements for the solar powered, thermoacoustically driven, thermoacoustic refrigerator. *The Journal of the Acoustical Society of America*, 108 (5): Pt. 2.

Aghaei, J, Amjady, N. & Shayanfar. H. A. 2009. Multi-objective electricity market clearing considering dynamic security by lexicographic optimisation and augmented epsilon constraint method. *Applied Soft Computing*, 11(4): 3846-3858.

Akhavanbazaz M., Kamran Siddiqui M. H. & Bhat R. B. 2007. The impact of gas blockage on the performance of a thermoacoustic refrigerator. *Experimental Thermal and Fluid Science,* 32(1): 231-239.

Andersson J. 2001. Multiobjective Optimisation in Engineering Design - Application to Fluid Power Systems, Dissertation, Thesis No. 675, Linköping University, Sweden.

Applied Ceramics Inc. 2011. Versagrid™ Product Offering, viewed 10 September 2013, from http://appliedceramics.com/products_versagrid.htm.

Atchley, A.A., Hofler, T., Muzzerall, M. L., Kite & Chianing. A.O. 1990. Acoustically generated temperature gradients in short plates. *Journal of Acoustical Society of America*, 88: 251.

Backhaus, S. & Swift, G.W. 1999. A Thermoacoustic Stirling Heat Engine. *Nature,* 399: 335-338.

Backhaus, S. & Swift, G.W. 2000. A Thermoacoustic Stirling Heat Engine: Detailed Study. *Journal of the Acoustical Society of America*, 107(6): 3148-66.

Baehr, H.D. & Stephan, K. 2004. Wärme - und Stoffübertragung. (transl: Heat and Mass Transfer), fourth ed. Springer, Heidelberg.

Bard, J.F. 1998. Practical Bi-Level Optimisation-Algorithms and Applications, Kluwer, Norwell, MA.

Bastyr, K.J. & Keolian, R.M. 2003. High-frequency thermoacoustic Stirling heat engine demonstration device. *Acoustics Research Letters Online*, 4 (2): 37-40.

Bell, S. 1999. A Beginner's Guide to Uncertainty of Measurement. *Measurement Good Practice Guide,* 11 (2), National Physical Laboratory, Teddington, UK.

Besnoin, E. 2001. Numerical study of thermoacoustic heat exchangers, Ph.D. thesis, Johns Hopkins University.

Cao, N., Olson, J.R., Swift, G.W. & Chen, S. 1996. Energy flux density in a thermoacoustic couple. *Journal of the Acoustical Society of America,* 99 (6): 3456-3464.

Ceperley, 1982. P.H. US Pat. No. 4355517.

Ceperley, P.H. 1979. A Pistonless Stirling Engine - The traveling wave heat engine. *Journal of the Acoustical Society of America*, 66 (5): 1508-1513.

Cohon JL. 1978. Multiobjective programming and planning. New York: Academic Press.

DeBlok, C.M. 2001. Hendrikus, N.A., Rijt, J.V. US Pat. No. 6314740.

Ehrgott, M.2000. Multicriteria optimisation, Springer: Berlin.

Eschenauer, H., Koski, J. & Osyczka, A. 1990. Multicriteria design optimisation procedures and applications, Springer-Verlag, Berlin.

GAMS Development Corporation, 2011. *GAMS: The Solver Manuals*. GAMS Development Corporation, 1217 Potomac Street, NW Washington, DC 20007, USA.

Garrett, S. & Hofler, T. 2001. Thermoacoustic Refrigeration, Technology. NASA Conference Publication 3136, 2, 1991: 397.

Garrett, S. L., Hofler, T.J. & Perkins, D.K. 1993. Thermoacoustic refrigeration. *Refrigeration and air conditioning technology workshop*. June 23-25.

Garrett, S.L. & Hofler, T.J. 1992. Thermoacoustic Refrigeration. *American Society of Heating, Refrigerating and Air-Conditioning Engineers Journal,* 34: 28-36.

Garrett, S.L., Adeff, J.A. & Hofler, T.J. 1993. Thermoacoustic refrigerator for space applications. *Journal of Thermophysics and Heat Transfer,* 7(4): 595-599.

Gartner, Inc. 2014, Press Release, viewed 10 April 2014, from http://www.gartner.com/newsroom/id/2665715.

Generalized Algebraic modelling Systems, (GAMS), [online] available: http://www.gams.com.

Gonzales-Pachon, J. & Roble, J. 2001. Aggregation of partial ordinary rankings: an interval goal programming approach. *Computers and Operations Research,* 28(8): 827-834.

Gonzales-Pachon, J. & Roble, J. 2007. Inferring consensus weights from pairwise comparison matrices with suitable properties. *Annals of Operations Research,* 154:123-132.

Hariharan N. M. & Sivashanmugam P. 2013. Optimisation of thermoacoustic refrigerator using response surface methodology. *Journal of Hydrodynamics,* 25(1):72-82.

Herman, C. & Travnicek, Z. 2006. Cool sound: The future of refrigeration? Thermodynamic and heat transfer issues in thermoacoustic refrigeration. *Heat and Mass Transfer*, 42 (6): 492-500.

Hofler T.J. 1986. Thermoacoustic refrigeration design and performance. Ph.D. dissertation, University of California, San Diego, USA.

Hofler, T.J. & Adeff, J.A. 2001. An optimised miniature Hofler tube. *Acoustics Research Letters Online*, 2: 37-42.

http://www.lanl.gov/thermoacoustics/press.html, Hot is cool in hell, *Qdrive News*, June 18, 2010.

http://www.lanl.gov/thermoacoustics/press.html, Sound makes electricity for space: *Technology Research News,* October 6/13, 2004.

Hwang C., Paidy S. & Yoon K. 1980. Mathematical programming with multiple objectives: a tutorial. *Computers and Operations Research*, 7: 5-31.

Hwang, C.L. & Masud, A. 1979. Multiple Objective Decision Making. Methods and Applications: A state of the art survey. Lecture Notes in Economics and Mathematical Systems, 164. Springer-Verlag, Berlin.

IDC Corporate, 2014, Worldwide Mobile Phone 2014–2018 Forecast and Analysis, viewed 10 April 2014, from http://www.idc.com/getdoc.jsp?containerId=247105.

IDC Worldwide Mobile Phone Tracker, 2014, Press release, viewed 10 April 2014, from http://www.idc.com/getdoc.jsp?containerId=prUS24645514.

Jin T., Chen G.B., Wang B.R. & Zhang S.Y. 2003. Application of thermoacoustic effect to refrigeration. *Review of Scientific Instruments,* 74 (1): 677–679.

Joshi, Y.K. & Garimella, S.V. 2003. Thermal challenges in next generation electronic systems. *Microelectronics Journal,* 34 (3): 169.

Junj S. & Matveev K. I. 2010. Study of a small-scale standing-wave thermoacoustic engine. *Journal of Mechanical Engineering Science*, 224 (1): 133-141.

Ke H.B., Liu Y.W. & He Y.L. 2010. Numerical simulation and parameter optimisation of thermoacoustic refrigerator driven at large amplitude. *Cryogenics*, 50(1): 28-35.

Kuntz, H.L. & Blackstock, D.T. 1987. Attenuation of intense sinusoidal waves in air-saturated, bulk porous materials. *Journal of the Acoustical Society of America,* 81(6): 1723-1731.

Livvarcin, O. 2000. Design and Cost-Benefit Analysis of a Mini Thermoacoustic Refrigerator Driver, September.

Long, C. 1999. Essential Heat Transfer. Longman, Essex: 5, 84, 173, 175-181, 184.

Lutron Electronic. n.d. Sound level meter model SL-4013, viewed 10 September 2013, from http://www.instrumentsgroup.co.za/index_files/Lutron/database/pdf/SL-4013.pdf.

Mahmud S. 2005. MHD and porous media thermoacoustic stacks optimisation, Ph.D. thesis, Department of Mechanical Engineering, University of Waterloo, Waterloo, ON, Canada.

Marler, T. & Arora, J. S. 2009. Multi-Objective Optimisation: Concepts and Methods for Engineering, VDM Verlag, Saarbrucken, Germany.

Marler, T. 2009. A Study of Multi-Objective Optimisation Methods for Engineering Applications, VDM Verlag, Saarbrucken, Germany.

Mavrotas, G. 2009. Effective implementation of the ε-constraint method in multi-objective mathematical programming problems. *Applied Mathematics and Computation*. 213: 455-465.

Mavrotas, G. Generation of efficient solutions in multi-objective mathematical programming problems using GAMS, effective implementation of the ε-constraint method [Online]. Available: www.gams.com/modlib/adddocs/epscm.pdf.

McLaughlin B.J. 2008. Study and development of high frequency thermoacoustic prime movers with piezoelectric transducers, Ph.D. thesis, University of Utah.

Merkli, P. & Thomann, H. 1975, Thermoacoustic effects in a resonance tube. *Journal of Fluid Mechanics,* 70(1):161-177.

Miettinem, K. 1999. Non-linear Multiobjective Optimisation, Kluwer Academic Publishers, Boston.

Miettinen, K. 1999. Non-linear Multiobjective Optimisation. Springer.

Minner, B.L., Braun, J.E. & Mongeau, L.G. 1997. Theoretical evaluation of the optimal performance of a thermoacoustic refrigerator. *American Society of Heating, Refrigerating and Air-Conditioning Engineers Journal.* 103: 873-887.

Mozurkewich, G. 1998. Time-average temperature distribution in a thermoacoustic stack. *Journal of the Acoustical Society of America,* 103 (1): 380-388.

National Instruments. 2011. http://www.ni.com/labview/.

National Instruments. 2013. Operating Instructions and Specifications NI 9211 4-Channel Thermocouple Input Module, viewed 10 September 2013, from http://www.ni.com/pdf/manuals/373466d.pdf.

National Instruments. 2013. User guide and Specifications NI myDAQ, viewed 10 September 2013, from http://www.ni.com/pdf/manuals/373060e.pdf.

National Instruments. n.d. Thermocouple and RTD sensors, viewed 10 September 2013, from http://www.ni.com/pdf/products/us/3daqsc350-351.pdf.

Nsofor E. C. & Ali A. 2009. Experimental study on performance of thermoacoustic refrigerating system. *Applied Thermal Engineering*, 29(13*):* 2672-2679.

Olson, J.R. & Swift, G.W. 1994. Similitude in thermoacoustics. *Journal of the Acoustical Society of America.* 95: 1405.

Osyczka A. 1984.Multicriterion Optimisation in Engineering - with FORTRAN Programs, Ellis Horwood, Chichester.

Paek I., Braun J. E. & Mongeau L. 2007. Evaluation of standing-wave thermoacoustic cycles for cooling applications. *International Journal of Refrigeration*, 30(6): 1059-1071.

Piccolo A. 2011. Numerical computation for parallel plate thermoacoustic heat exchangers in standing wave oscillatory flow. *International Journal of Heat and Mass Transfer*, 54(21-22): 4518-4530.

Poese M.E. & Garrett S.L. 2000. Performance measurement on a thermoacoustic refrigerator driven at high amplitude. *Journal of the Acoustical Society of America*, 107: 2480–2486.

Poese, M. 2004. An Evolution of Compact Thermoacoustic Refrigeration Devices, Ph.D. thesis, Pennsylania State University.

Poese, M.E., Robert W. M. & Garret, S.L. 2004. Thermoacoustic Refrigeration for Ice Cream Sales. *Journal Acoustical Society of American,* 107(5): 2480- 2486.

Poese, M.E., Smith, R.W., Garrett, S.L., Van Gerwen, R. & Gosselin, P. 2004. Thermoacoustic refrigeration for ice cream sales. Proceedings of the 6th IIR Gustav Lorentzen Conference.

Rao, S.S. 1996. Engineering Optimisation: Theory and Practice, 3rd Edition, John Wiley & Sons.

Ringuest J. 1992. Multiobjective Optimisation: Behavioral and Computational Considerations, Kluwer Academic Publishers, Boston.

Rott, N. 1969. Damped and thermally driven acoustic oscillations in wide and narrow tubes. *Zeitschrift für angewandte Mathematik und Physik ZAMP*, 20 (2): 230-243.

Rott, N. 1973. Thermally driven acoustic oscillations. Part II: Stability limit for helium. *Zeitschrift Fur Angewandte Mathematik Und Physik,* 24: 54-72.

Rott, N. 1974. The heating effect connected with non linear oscillations in a resonance tube. *Zeitschrift Fur Angewandte Mathematik Und Physik,* 25: 619-634.

Rott, N. 1974. The influence of heat conduction on acoustic streaming. *Zeitschrift Fur Angewandte Mathematik Und Physik,* 25: 417-421.

Rott, N. 1975. Thermally driven acoustic oscillations. Part III: Second order heat flux. *Zeitschrift Fur Angewandte Mathematik Und Physik,* 26: 43-49.

Rott, N. 1980. Thermoacoustics. *Advances in Applied Mechanics,* 20(135): 327.

Seaway, R. A. 1996. Physics for Scientist & Engineers with Modern Physics, College Publishing, Philadelphia, 4th edition.

Steuer R. 1986. Multiple criteria optimisation: theory, computation and application, John Wiley & Sons, Inc, New York.

Swift, G.W. 1988. Thermoacoustic engines. *Journal of Acoustical Society of America,* 4: 1146–1180.

Swift, G.W. 1997. Thermoacoustic engines and refrigerators. *Encyclopedia of Applied Physics,* 21: 245.

Swift, G.W. 2002. Thermoacoustics: a unifying perspective for some engines and refrigerators. *Acoustical Society of America,* Melville NY.

Swift, G.W., Backhaus, S.N. & Gardner, D.L. 2000. US Patent No. 6032464.

Tao, J., Bao-Sen, Z., Ke, T., Rui, B. & Guo-Bang, Ch. 2007. Experimental Observation on A Small-Scale Thermoacoustic Prime Mover. *Journal of Zhejiang University SCIENCE A*, 8 (2): 205-209.

The MathWorks, Inc., MATLAB User's Guide. 2007. The Math Works, Inc.

Tijani M.E.H. 2007. Loudspeaker-driven thermo-acoustic refrigeration, Ph.D. thesis, Eindhoven University of Technology, Netherlands.

Tijani, M.E.H., Zeegers, J.C.H. & De Waele, A.T.A.M. 2002. The optimal stack spacing for thermoacoustic refrigeration. *Journal of the Acoustical Society of America,* 112(1): 128-133.

Tijani, M.E.H., Zeegers, J.C.H. & De Waele, A.T.A.M. 2002. Construction and performance of a thermoacoustic refrigerator. *Cryogenics,* 42(1): 59-66.

Tijani, M.E.H., Zeegers, J.C.H. & De Waele, A.T.A.M. 2002. Design of thermoacoustic refrigerators. *Cryogenics,* 42(1): 49-57.

Tijani, M.E.H., Zeegers, J.C.H. & Waele, A.T.A.M. 2002. Prandtl number and thermoacoustic refrigerators. *Journal of Acoustical Society of America,* 112 (1): 134-143.

Trapp, A.C., Zink, F., Prokopyev, O.A. & Schaefer, L. 2011. Thermoacoustic heat engine modelling and design optimisation. *Journal of Applied Thermal Engineering,* 31: 2518-2528.

Tu Q., Chen Z. J. & Liu J. X. 2005. Numerical simulation of loudspeaker-driven thermoacoustic refrigerator. Proceedings of the Twentieth International Cryogenic Engineering Conference (ICEC 20). Beijing, China.

Ueda, Y., Biwa, T., Mizutani, U. & Yazaki, T. 2003. Experimental studies of a thermoacoustic Stirling prime mover and its application to a cooler. *Journal of the Acoustical Society of America,* 72 (3): 1134-1141.

Vincent, T.L. & Grantham, W.J. 1981. Optimality in parametric systems, John Wiley and Sons, New York.

Wetzel, M., & Herman, C. 1997. Design optimisation of thermoacoustic refrigerators. *International Journal of Refrigeration,* 20(1): 3-21.

Wheatley J., Hofler T., Swift G.W. & Migliori A. 1983. An intrinsically irreversible thermoacoustic heat engine. *The Journal of the Acoustical Society of America*, 74: 153–170.

Wheatley, J.C., Hofler, T., Swift, G.W. & Migliori, A. 1985. Understanding some simple phenomena in thermoacoustics with applications to acoustical heat engines. *American Journal of Physics*, 53: 147-162.

Wu F., Chen L. & Shu A. *et al.* Constructal design of stack filled with parallel plates in standing-wave thermo-acoustic cooler. *Cryogenics*, 2009, 49(3-4): 107-111.

Xiao, J.H. 1995. Thermoacoustic heat transportation and energy transformation, part 3: Adiabatic wall thermoacoustic effects. *Cryogenics*, 35(1): 27-29.

Yong Tae Kim & Min Gon Kim 2000. Optimum positions of a stack in a thermoacoustic heat pump. *Journal of the Korean Physical Society*, 36(5): 279-286.

Zink, F. 2009. Identification and attenuation of losses in thermoacoustics: issues arising in the miniaturization of thermoacoustic devices. Ph.D. thesis, University of Pittsburgh, United States.

Zink, F., Waterer, H., Archer, R. & Schaefer, L. 2009. Geometric optimisation of a thermoacoustic regenerator. *International Journal of Thermal Sciences*, 48(12): 2309-2322.

Zoontjens L., Howard C. Q. & Zander A. C. 2006. Modelling and optimisation of acoustic inertance segments for thermoacoustic devices. First Australasian Acoustical Societies Conference: Acoustics 2006: Noise of Progress, Clearwater Resort. Christchurch, New Zealand: 435-441.

APPENDICES

APPENDIX A: TAE models "Emphasising acoustic work"

```
$ Title Thermoacoustic engine
Scalars pi  /3.141592654/
        K thermal conductivity /0.16/
        tw wall thickness /0.000191/
        dens density /0.16674/
        isco  isentropic coefficient /1.67/
        cp heat capacity /5193.1/
        af angular frequency /696/
        c speed of sound /1020/
        densm  mean gas density /0.16674/
        dynv dynamic viscosity /0.000019561/
        kg thermal conductivity of the gas /0.16/
        ks solid thermal conductivity /11.8/
        umax maximum velocity /670/
        pmax maximum pressure /114003/
        wavel wavelength /1.466/
        epsi emissivity /1/
        Th constant hot side temperature /700/
        Tc constant cold side temperature /300/
        Tinf temperature of the surrounding /298/;
         scalar starttime;
         starttime=jnow;

Positive VARIABLES L, H, za, d;
Integer VARIABLE N;
L.lo = 0.005; L.up = 0.05;
za.lo =0.005; za.up=0.05;
N.lo =20; N.up =50;
H.lo=0.005; H.up =0.05;

Free VARIABLE W;
Equations
eWORKOUTPUT  objective function
ebound1 equation
ebound2 equation
ebound3 equation
ebound5 equation;
ebound1.. N*(d+tw)=e=2*H;
```

```
ebound2.. d=g= 2*SQRT((2*K)/(2*dens*cp*pi*af));
ebound3.. d=l= 4*SQRT((2*K)/(2*dens*cp*pi*af));
ebound5.. za =g= L*log(Tinf/Tc);
eWORKOUTPUT.. W*2*(d+tw)
=e=(2*pi*af*((SQRT((2*K)/(2*dens*cp*pi*af)))*(isco-
1)*((pmax**2)*cos(2*pi*Za/wavel)*cos(2*pi*Za/wavel))*(((2*pi*af*(pmax*(cos(
2*pi*Za/wavel))))/(densm*cp*(umax*(sin(2*pi*Za/wavel)))))-1)-
((SQRT((2*dynv)/(2*dens*pi*af)))*dens*(umax**2)*sin(2*pi*Za/wavel)*(sin(2*p
i*Za/wavel))))/(dens*SQR(c)*(1+(SQRT(3)/2)))*L*N*pi*SQR(H));

MODEL thermoacoustic /ALL/;
Solve thermoacoustic using minlp maximising W;
Display "-------------------------------------------------------------------
----------------------------",
        "nlp solver",
        L.l, H.l, za.l, d.l, N.l;

scalar elapsed;elapsed =(jnow-starttime)*24*3600;
display elapsed;
```

APPENDIX B: TAE models “Emphasising viscous resistance”

```
$ Title Thermoacoustic engine
scalars
         dens density /0.16674/
         af angular frequency /696/
         dynv dynamic viscosity /0.000019561/
         tw wall thickness /0.000191/
         K thermal conductivity /0.16/
         Th constant hot side temperature /700/
         Tc constant cold side temperature /300/
         Tinf temperature of the surrounding /298/
         pi  /3.141592654/
         cp heat capacity /5193.1/;
         scalar starttime;
         starttime=jnow;

Positive VARIABLES L, H, Za, d;
Integer VARIABLE N;
L.lo = 0.005; L.up = 0.05;
za.lo =0.005; za.up=0.05;
N.lo =20; N.up =50;
H.lo=0.005; H.up =0.05;

Free VARIABLE Rv;

Equations
eVISCOUSRESISTANCE objective function
ebound1 equation
ebound2 equation
ebound3 equation
ebound5 equation;
ebound1.. N*(d+tw)=e=2*H;
ebound2.. d=g= 2*SQRT((2*K)/(2*dens*cp*pi*af));
ebound3.. d=l= 4*SQRT((2*K)/(2*dens*cp*pi*af));
ebound5.. za =g= L*log(Tinf/Tc);
eVISCOUSRESISTANCE..
Rv*N*((SQRT((2*dynv)/(2*dens*pi*af))))*2*pi*SQR(H)*(d+tw) =e= (4*dynv*L);

MODEL thermoacoustic /ALL/;
Solve thermoacoustic using minlp minimising Rv;
Display "-----------------------------------------------------------------
```

```
----------------------------",
        "nlp solver",
        L.l, H.l, Za.l, d.l, N.l;
scalar elapsed;elapsed =(jnow-starttime)*24*3600;
display elapsed;
```

APPENDIX C: TAE models “Emphasising convective heat flux”

```
$ Title Thermoacoustic engine
Scalars
         pi  /3.141592654/
         ga  acceleration of gravity /9.81/
         dens density /0.16674/
         af angular frequency /696/
         dynv dynamic viscosity /0.000019561/
         kg thermal conductivity of the gas /0.16674/
         Th constant hot side temperature /700/
         Tc constant cold side temperature /300/
         tw wall thickness /0.000191/
         Tinf temperature of the surrounding /300/
         beta themal expansion coefficient /0.00333333/
         viscos viscosity of the surrounding gas /0.000015111/
         therd thermal diffusivity of the surrounding gas /0.000021117/
         cp heat capacity /5193.1/;
         scalar starttime;
         starttime=jnow;

Positive VARIABLES L, H, Za, d;
Integer VARIABLE N;
L.lo = 0.005; L.up = 0.05;
za.lo =0.005; za.up=0.05;
N.lo =20; N.up =50;
H.lo=0.005; H.up =0.05;

Free VARIABLE Qconv;

Equations
ebound1 equation
ebound2 equation
ebound3 equation
ebound5 equation
eCONVECTIVEHEATFLOW objective function;
ebound1.. N*(d+tw)=e=2*H;
ebound2.. d=g= 2*SQRT((2*Kg)/(2*dens*cp*pi*af));
ebound3.. d=l= 4*SQRT((2*Kg)/(2*dens*cp*pi*af));
ebound5.. za =g= L*log(Tinf/Tc);
eCONVECTIVEHEATFLOW.. Qconv =e= 2*pi*H*L*(((Tc-Th)/log(Tc/Th))-
Tinf)*((0.36+((0.518*(((((ga*beta)*((Th*(exp((log(Tc/Th))*Za/L)))-
Tinf)*8*power(H,3))/(Viscos*therd)))**0.25))/((1+((0.559/(viscos/therd))**0
```

```
.5625))**0.4444)))*kg)/(2*H);

MODEL thermoacoustic /ALL/;

Solve thermoacoustic using minlp minimising Qconv;
Display "-------------------------------------------------------------------
----------------------------",
        "nlp solver",
        L.l, H.l, Za.l, d.l, N.l;
scalar elapsed;elapsed =(jnow-starttime)*24*3600;
display elapsed;
```

APPENDIX D: TAE models "Emphasising radiative heat flux"

```
$ Title geometric optimisation of a thermoacoustic refrigerator
Scalars
         pi  /3.141592654/
         kb boltzmann constant /0.00000005670373/
         Th constant hot side temperature /700/
         Tc constant cold side temperature /300/
         Tinf temperature of the surrounding /300/
         tw wall thickness /0.000191/
         kg thermal conductivity of the gas /0.16674/
         cp heat capacity /5193.1/
         af angular frequency /696/
         dens density /0.16674/ ;
         scalar starttime;
         starttime=jnow;

Positive VARIABLES L,H,Za,d;
Integer VARIABLE N;
L.lo = 0.005; L.up = 0.05;
za.lo =0.005; za.up=0.05;
N.lo =20; N.up =50;
H.lo=0.005; H.up =0.05;

Free VARIABLE Qrad;

Equations
ebound1 equation
ebound2 equation
ebound3 equation
ebound5 equation
eradiativeheatflux objective function;
ebound1.. N*(d+tw)=e=2*H;
ebound2.. d=g= 2*SQRT((2*Kg)/(2*dens*cp*pi*af));
ebound3.. d=l= 4*SQRT((2*Kg)/(2*dens*cp*pi*af));
ebound5.. za =g= L*log(Tinf/Tc);
eRADIATIVEHEATFLUX.. Qrad =e= ((Tc**4-(Th)**4)/(4*log(Tc/Th))-
(Tinf)**4)*2*pi*H*L*kb*((SQRT(3))/2);

MODEL thermoacoustic /ALL/;
Solve thermoacoustic using minlp minimising Qrad;
Display "-----------------------------------------------------------------
```

```
----------------------------",
        "nlp solver",
        L.l, H.l, Za.l, d.l, N.l;
scalar elapsed;elapsed =(jnow-starttime)*24*3600;
display elapsed;
```

APPENDIX E: TAE models "Emphasising conductive heat flux"

```
$ Title Thermoacoustic engine
Scalars
         pi  /3.141592654/
         kg thermal conductivity of the gas /0.16/
         ks solid thermal conductivity /11.8/
         Th constant hot side temperature /700/
         Tc constant cold side temperature /300/
         tw wall thickness /0.000191/
         Tinf temperature of the surrounding /300/
         umax maximum velocity /670/
         pmax maximum pressure /114003/
         cp heat capacity /5193.1/
         af angular frequency /696/
         dens density /0.16674/ ;
         scalar starttime;
         starttime=jnow;

Positive VARIABLES L, H, Za, d;
Integer VARIABLE N;
L.lo = 0.005; L.up = 0.05;
za.lo =0.005; za.up=0.05;
N.lo =20; N.up =50;
H.lo=0.005; H.up =0.05;

Free VARIABLE Qcond;

Equations
ebound1 equation
ebound2 equation
ebound3 equation
ebound5 equation
eCONDUCTIVEHEATFLUX objective function;
ebound1.. N*(d+tw)=e=2*H;
ebound2.. d=g= 2*SQRT((2*Kg)/(2*dens*cp*pi*af));
ebound3.. d=l= 4*SQRT((2*Kg)/(2*dens*cp*pi*af));
ebound5.. za =g= L*log(Tinf/Tc);
eCONDUCTIVEHEATFLUX.. Qcond =e=
(((ks*tw)+(kg*d))/(tw+d))*(pi/L)*(SQR(H))*Tc*log(Th/Tc);
MODEL thermoacoustic /ALL/;
```

```
Solve thermoacoustic using minlp minimising Qcond;
Display "-------------------------------------------------------------------
----------------------------",
        "nlp solver",
        L.l, H.l, Za.l, d.l, N.l;
scalar elapsed;elapsed =(jnow-starttime)*24*3600;
display elapsed;
```

APPENDIX F: TAE models “Emphasising all objectives functions”

```
$inlinecom [ ]
$eolcom //
$STitle Thermoacoustic engine
Scalars
         pi  /3.141592654/
         Kth thermal conductivity /0.16/
         dens density /0.16674/
         isco  isentropic coefficient /1.67/
         cp heat capacity /5193.1/
         af angular frequency /696/
         c speed of sound /1020/
         densm  mean gas density /0.16674/
         dynv dynamic viscosity /0.000019561/
         kg thermal conductivity of the gas /0.16/
         ks solid thermal conductivity /11.8/
         umax maximum velocity /670/
         pmax maximum pressure /114003/
         wavel wavelength /1.466/
         Th constant hot side temperature /700/
         Tc constant cold side temperature /300/
         tw wall thickness /0.000191/
         Tinf temperature of the surrounding /298/
         ga  acceleration of gravity /9.81/
         beta themal expansion coefficient /0.00333333/
         viscos viscosity of the surrounding gas /0.000015111/
         therd thermal diffusivity of the surrounding gas /0.000021117/
         kb boltzmann constant /0.00000005670373/
         epsi emissivity /1/
         N /25/
        ;

Sets
k objective functions /workoutput, viscousresistance, conductiveheatflux,
convectiveheatflux, radiativeheatflux/;
$set min -1
$set max +1

Parameter dir(k) direction of the objective functions
/workoutput %max%, viscousresistance %min%, conductiveheatflux %min%,
convectiveheatflux %min%, radiativeheatflux %min%/;
```

```
free Variables
z(k) objective function variables;
positive VARIABLES L,d,H,Za;

L.lo = 0.005; L.up = 0.05;
za.lo =0.005;
H.lo=0.005;

Equations
objworkoutput objective for maximising workoutput
objviscousresistance objective for minimising viscousresistance
objconductiveheatflux objective for minimising conductiveheatflux
objconvectiveheatflux objective for minimising convectiveheatflux
objradiativeheatflux objective for minimising radiativeheatflux
ebound1 equation
ebound5 equation
ebound2 equation
ebound3 equation
;

* Objective functions
ebound1.. N*(d+tw)=e=2*H;
ebound2.. d=g= 2*SQRT((2*Kth)/(2*dens*cp*pi*af));
ebound3.. d=l= 4*SQRT((2*Kth)/(2*dens*cp*pi*af));
ebound5.. za =g= L*log(Tinf/Tc);
objworkoutput.. z('workoutput')*2*(d+tw)
=e=(2*pi*af*((SQRT((2*Kth)/(2*dens*cp*pi*af)))*(isco-
1)*((pmax**2)*cos(2*pi*Za/wavel)*cos(2*pi*Za/wavel))*(((2*pi*af*(pmax*(cos(
2*pi*Za/wavel))))/(densm*cp*(umax*(sin(2*pi*Za/wavel)))))-1)-
((SQRT((2*dynv)/(2*dens*pi*af)))*dens*(umax**2)*sin(2*pi*Za/wavel)*(sin(2*p
i*Za/wavel))))/(dens*SQR(c)*(1+(SQRT(3)/2)))*L*N*pi*SQR(H));
objviscousresistance..
z('viscousresistance')*N*((SQRT((2*dynv)/(2*dens*pi*af))))*2*pi*SQR(H)*(d+t
w) =e= (4*dynv*L);
objconductiveheatflux.. z('conductiveheatflux') =e=
(((ks*tw)+(kg*d))/(tw+d))*(pi/L)*(SQR(H))*Tc*log(Th/Tc);
objconvectiveheatflux.. z('convectiveheatflux') =e= 2*pi*H*L*(((Tc-
Th)/log(Tc/Th))-
Tinf)*((0.36+((0.518*(((((ga*beta)*((Th*(exp((log(Tc/Th))*Za/L)))-
Tinf)*8*power(H,3))/(Viscos*therd)))**0.25))/((1+((0.559/(viscos/therd))**0
.5625))**0.4444)))*kg)/(2*H);
objradiativeheatflux.. z('radiativeheatflux') =e= ((Tc**4-
(Th)**4)/(4*log(Tc/Th))-(Tinf)**4)*2*pi*H*L*kb*((SQRT(3))/2);
```

```
z.lo('viscousresistance') = -100000000000000; z.up('viscousresistance') =
100000000000000;
z.lo('conductiveheatflux') = -100000000000000; z.up('conductiveheatflux') =
100000000000000;
z.lo('convectiveheatflux') = -100000000000000; z.up('convectiveheatflux') =
100000000000000;
z.lo('workoutput') = -100000000000000; z.up('workoutput') =
100000000000000;
z.lo('radiativeheatflux') = -100000000000000; z.up('radiativeheatflux') =
100000000000000;

option domlim=100;
option limrow=10, limcol=10;

Model thermoacoustic / all /;

option minlp=gamschk;
thermoacoustic.optfile =1;

$STitle eps-constraint method
Set k1(k) the first element of k, km1(k) all but the first elements of k;
k1(k)$(ord(k)=1) = yes; km1(k)=yes; km1(k1) = no;
Set kk(k) active objective function in constraint allobj
Parameter rhs(k) right hand side of the constrained obj functions in eps-
constraint
maxobj(k) maximum value from the payoff table
minobj(k) minimum value from the payoff table
Variables a_objval auxiliary variable for the objective function
obj auxiliary variable during the construction of the payoff table

Positive Variables sl(k) slack or surplus variables for the eps-constraints
Equations
con_obj(k) constrained objective functions
augm_obj augmented objective function to avoid weakly efficient solutions
allobj all the objective functions in one expression;

con_obj(km1).. z(km1) - dir(km1)*sl(km1) =e= rhs(km1);
* The first objective function is optimised and the others are used as
constraints
* The second term is added to avoid weakly efficient points
augm_obj.. sum(k1,dir(k1)*z(k1))+1e-3*sum(km1,sl(km1)/(maxobj(km1)-
minobj(km1))) =e= a_objval;
```

```
allobj.. sum(kk, dir(kk)*z(kk)) =e= obj;

Model mod_payoff / thermoacoustic, allobj / ;
Model mod_epsmethod / thermoacoustic, con_obj, augm_obj / ;
option limrow=10, limcol=10;
option solprint=on, solvelink=%solvelink.CallModule%;
option decimals=8;

Parameter payoff(k,k) payoff tables entries;
Alias(k,kp);

* Payoff table is generated by applying lexicographic optimisation
loop(kp, kk(kp)=yes;
repeat solve mod_payoff using nlp maximising obj;
payoff(kp,kk) = z.l(kk);
z.fx(kk) = z.l(kk);// The value of the last objective optimised are freezed
kk(k++1) = kk(k); // cycle through the objective functions
until kk(kp); kk(kp) = no;
* Values of the objective functions are released for the new iteration
z.up(k) = inf; z.lo(k) =-inf; );
if (mod_payoff.modelstat<>%modelstat.Optimal%, abort 'no optimal solution
for mod_payoff');

display payoff;
minobj(k)=smin(kp,payoff(kp,k));
maxobj(k)=smax(kp,payoff(kp,k));

$set fname p.%gams.scrext%
File fx solution points from eps-method / "%gams.scrdir%%fname%" /;

$if not set gridpoints $set gridpoints 5
Set g grid points /g0*g%gridpoints%/
grid(k,g) grid

Parameter
gridrhs(k,g) rhs of eps-constraint at grid point
maxg(k) maximum point in grid for objective
posg(k) grid position of objective
firstOffMax, lastZero some counters
numk(k) ordinal value of k starting with 1
numg(g) ordinal value of g starting with 0;
lastZero=1; loop(km1, numk(km1)=lastZero; lastZero=lastZero+1); numg(g) =
```

```
ord(g)-1;

grid(km1,g) = yes; // Define the grid interval for different objectives
maxg(km1) = smax(grid(km1,g), numg(g));
gridrhs(grid(km1,g))$(%min%=dir(km1)) = maxobj(km1) -
numg(g)/maxg(km1)*(maxobj(km1)- minobj(km1));
gridrhs(grid(km1,g))$(%max%=dir(km1)) = minobj(km1) +
numg(g)/maxg(km1)*(maxobj(km1)- minobj(km1));
display gridrhs;

* Walking through the grid points and taking shortcuts if the model becomes
infeasible
posg(km1) = 0;
repeat
rhs(km1) = sum(grid(km1,g)$(numg(g)=posg(km1)), gridrhs(km1,g));
solve mod_epsmethod maximising a_objval using nlp;
if (mod_epsmethod.modelstat<>%modelstat.Optimal%, // not optimal is in this
case infeasible
lastZero = 0; loop(km1$(posg(km1)>0 and lastZero=0), lastZero=numk(km1));
posg(km1)$(numk(km1)<=lastZero) = maxg(km1); // skip all solves for more
demanding values of rhs(km1)
else
loop(k, put fx z.l(k):12:2); put /);

* Proceed forward in the grid
firstOffMax=0;
loop(km1$(posg(km1)<maxg(km1) and firstOffMax=0),posg(km1)=posg(km1)+1;
firstOffMax=numk(km1));
posg(km1)$(numk(km1)<firstOffMax) = 0;
until sum(km1$(posg(km1)=maxg(km1)),1)=card(km1) and firstOffMax=0;
putclose fx; // close the point file
```

APPENDIX G: TAR models “Emphasising acoustic cooling load”

```
$ Title Thermoacoustic refrigerator
scalars
         isco isentropic coefficient /1.63/
         pn prandtl number /0.67/
         deltat temperature difference /0.030/
         tw wall thickness /0.012/
         DR drive ratio /0.035/
         ; scalar starttime;
         starttime=jnow;

positive VARIABLES  BR, thermp,Lsn, Xsn, eqA, eqB, eqC, eqD, eqE, eqF, eqG,
eqH, eqJ;

BR.lo =0.7; BR.up =0.9;
thermp.lo=0.046;thermp.up=0.092;
Lsn.lo =0.001; Lsn.up =0.5;
Xsn.lo=0.01; Xsn.up=1;

Free VARIABLE Qc;

Equations
objcoolingload objective for minimising coolingload

eqAdef equation
eqBdef equation
eqCdef equation
eqDdef equation
eqEdef equation
eqFdef equation
eqGdef equation
eqHdef equation
eqJdef equation
ebound1 equation;

* Objective functions
eqAdef.. eqA =e= 2*Xsn;
eqBdef.. eqB =e= thermp*(DR**2)*sin(eqA);
eqCdef.. eqC =e= 0.5*pn*SQR(thermp);
eqDdef.. eqD =e= SQRT(pn)*thermp;
eqEdef.. eqE =e= tan(Xsn);
```

```
eqFdef.. eqF =e= (isco-1)*BR*Lsn;
eqGdef.. eqG =e= 1+SQRT(pn)-eqD;
eqHdef.. eqH =e= cos(Xsn)*cos(Xsn);
eqJdef.. eqJ =e= sin(Xsn)*sin(Xsn);
ebound1.. abs((((deltat*eqE*(1+SQRT(pn)+pn))/(eqF*(1+SQRT(pn))))-
eqG)/((8*isco*(1+pn)*(1-eqD+eqC))/eqB)) =g=
abs((((thermp*eqF*(DR**2)*eqH)/(4*isco)))*(((deltat*eqE)/(eqF*(1+SQRT(pn))*
(1-eqD+eqC)))-1)-((eqD*Lsn*(DR**2)*eqJ)/(4*isco*BR*(1-eqD+eqC))));

objcoolingload..  Qc =e=
abs((((deltat*eqE*(1+SQRT(pn)+pn))/(eqF*(1+SQRT(pn))))-
eqG)/((8*isco*(1+pn)*(1-eqD+eqC))/eqB))-
abs((((((thermp*eqF*(DR**2)*eqH)/(4*isco)))*(((deltat*eqE)/(eqF*(1+SQRT(pn))
)*(1-eqD+eqC)))-1)-((eqD*Lsn*(DR**2)*eqJ)/(4*isco*BR*(1-eqD+eqC))))));

eqB.lo = 0.000001; eqB.up = 0.001;
eqF.lo = 0.0001; eqF.up = 0.5;

MODEL thermoacoustic /ALL/;
Option Reslim=1000000;
Solve thermoacoustic using dnlp maximising Qc;
Display "-------------------------------------------------------------------
---------------------------",
        "dnlp solver",
        BR.l, Lsn.l, thermp.l, Xsn.l;
scalar elapsed;elapsed =(jnow-starttime)*24*3600;
display elapsed;
```

APPENDIX H: TAR models "Emphasising coefficient of performance"

```
$ Title Thermoacoustic refrigerator
scalars
         isco isentropic coefficient /1.63/
         pn prandtl number /0.67/
         deltat temperature difference /0.030/
         tw wall thickness /0.012/
         DR drive ratio /0.035/
         ; scalar starttime;
         starttime=jnow;

positive VARIABLES  BR, thermp, Lsn, Xsn, eqA, eqB, eqC, eqD, eqE, eqF,
eqG, eqH, eqJ;

BR.lo =0.7; BR.up =0.9;
thermp.lo=0.046;thermp.up=0.092;
Lsn.lo =0.001; Lsn.up =0.5;
Xsn.lo=0.01; Xsn.up=1;

Free VARIABLE cop;

Equations
objcop objective for maximising cop

eqAdef equation
eqBdef equation
eqCdef equation
eqDdef equation
eqEdef equation
eqFdef equation
eqGdef equation
eqHdef equation
eqJdef equation
ebound1 equation;

* Objective functions
eqAdef.. eqA =e= 2*Xsn;
eqBdef.. eqB =e= thermp*(DR**2)*sin(eqA);
eqCdef.. eqC =e= 0.5*pn*SQR(thermp);
eqDdef.. eqD =e= SQRT(pn)*thermp;
eqEdef.. eqE =e= tan(Xsn);
eqFdef.. eqF =e= (isco-1)*BR*Lsn;
```

```
eqGdef.. eqG =e= 1+SQRT(pn)-eqD;
eqHdef.. eqH =e= cos(Xsn)*cos(Xsn);
eqJdef.. eqJ =e= sin(Xsn)*sin(Xsn);
ebound1.. abs((((deltat*eqE*(1+SQRT(pn)+pn))/(eqF*(1+SQRT(pn))))-
eqG)/((8*isco*(1+pn)*(1-eqD+eqC))/eqB)) =g=
abs((((thermp*eqF*(DR**2)*eqH)/(4*isco)))*(((deltat*eqE)/(eqF*(1+SQRT(pn))*
(1-eqD+eqC)))-1)-((eqD*Lsn*(DR**2)*eqJ)/(4*isco*BR*(1-eqD+eqC))));

objcop..
cop*abs(((((thermp*eqF*(DR**2)*eqH)/(4*isco)))*(((deltat*eqE)/(eqF*(1+SQRT(
pn))*(1-eqD+eqC)))-1)-((eqD*Lsn*(DR**2)*eqJ)/(4*isco*BR*(1-eqD+eqC))))) =e=
abs((((deltat*eqE*(1+SQRT(pn)+pn))/(eqF*(1+SQRT(pn))))-
eqG)/((8*isco*(1+pn)*(1-eqD+eqC))/eqB))-
(abs(((((thermp*eqF*(DR**2)*eqH)/(4*isco)))*(((deltat*eqE)/(eqF*(1+SQRT(pn)
)*(1-eqD+eqC)))-1)-((eqD*Lsn*(DR**2)*eqJ)/(4*isco*BR*(1-eqD+eqC))))));
cop.lo = 0.01; cop.up = 32.8;
eqB.lo = 0.000001; eqB.up = 0.001;
eqF.lo = 0.0001; eqF.up = 0.5;


MODEL thermoacoustic /ALL/;
Option Reslim=1000000;
Solve thermoacoustic using dnlp maximising cop;
Display "-------------------------------------------------------------------
----------------------------",
        "dnlp solver",
        BR.l, thermp.l, Lsn.l, Xsn.l;
scalar elapsed;elapsed =(jnow-starttime)*24*3600;
display elapsed;
```

APPENDIX I: TAR models "Emphasising acoustic power loss"

```
$ Title Thermoacoustic refrigerator
scalars
         isco isentropic coefficient /1.63/
         pn prandtl number /0.67/
         deltat temperature difference /0.030/
         tw wall thickness /0.012/
         DR drive ratio /0.035/
         ; scalar starttime;
         starttime=jnow;

positive VARIABLES  BR, thermp, Lsn, Xsn, eqA, eqB, eqC, eqD, eqE, eqF,
eqG, eqH, eqJ;

BR.lo =0.7; BR.up =0.9;
thermp.lo=0.046;thermp.up=0.092;
Lsn.lo =0.001; Lsn.up =0.5;
Xsn.lo=0.01; Xsn.up=1;

Free VARIABLE Za;

Equations
objacousticpowerlost objective for minimising acousticpowerlost

eqAdef equation
eqBdef equation
eqCdef equation
eqDdef equation
eqEdef equation
eqFdef equation
eqGdef equation
eqHdef equation
eqJdef equation
ebound1 equation;

* Objective functions
eqAdef.. eqA =e= 2*Xsn;
eqBdef.. eqB =e= thermp*(DR**2)*sin(eqA);
eqCdef.. eqC =e= 0.5*pn*SQR(thermp);
eqDdef.. eqD =e= SQRT(pn)*thermp;
eqEdef.. eqE =e= tan(Xsn);
eqFdef.. eqF =e= (isco-1)*BR*Lsn;
```

```
eqGdef.. eqG =e= 1+SQRT(pn)-eqD;
eqHdef.. eqH =e= cos(Xsn)*cos(Xsn);
eqJdef.. eqJ =e= sin(Xsn)*sin(Xsn);
ebound1.. abs((((deltat*eqE*(1+SQRT(pn)+pn))/(eqF*(1+SQRT(pn))))-
eqG)/((8*isco*(1+pn)*(1-eqD+eqC))/eqB)) =g=
abs((((thermp*eqF*(DR**2)*eqH)/(4*isco)))*(((deltat*eqE)/(eqF*(1+SQRT(pn))*
(1-eqD+eqC)))-1)-((eqD*Lsn*(DR**2)*eqJ)/(4*isco*BR*(1-eqD+eqC))));

objacousticpowerlost..  Za =e= ((thermp*eqF*(DR**2)*eqH)/(4*isco))+
((eqD*Lsn*(DR**2)*eqJ)/(4*isco*BR*(1-eqD+eqC)));

eqB.lo = 0.000001; eqB.up = 0.001;
eqF.lo = 0.0001; eqF.up = 0.5;


MODEL thermoacoustic /ALL/;
Option Reslim=1000000;
Solve thermoacoustic using dnlp minimising Za;
Display "-----------------------------------------------------------------
----------------------------",
        "dnlp solver",
        BR.l, thermp.l, Lsn.l, Xsn.l;
scalar elapsed;elapsed =(jnow-starttime)*24*3600;
display elapsed;
```

APPENDIX J: TAR Model A

```
$ Title Thermoacoustic refrigerator
scalars
         isco isentropic coefficient /1.63/
         pn prandtl number /0.67/
         deltat temperature difference /0.030/
         tw wall thickness /0.012/
         DR drive ratio /0.035/
         Lsn /0.5/
         ; scalar starttime;
         starttime=jnow;

Sets
k objective functions /coolingload, cop, acousticpowerlost/;
$ set min -1
$ set max +1
Parameter dir(k) direction of the objective functions /coolingload %max%,
cop %max%, acousticpowerlost %min%/;

positive VARIABLES  BR, thermp, Xsn, eqA, eqB, eqC, eqD, eqE, eqF, eqG,
eqH, eqJ;
BR.lo =0.7; BR.up =0.9;
thermp.lo=0.046;thermp.up=0.092;

Xsn.lo=0.01; Xsn.up=1;

Free VARIABLE
z(k) objective function variables;

Equations
objcoolingload objective for maximising coolingload
objcop objective for maximising cop
objacousticpowerlost objective for minimising acousticpowerlost

eqAdef equation
eqBdef equation
eqCdef equation
eqDdef equation
eqEdef equation
eqFdef equation
eqGdef equation
eqHdef equation
```

```
eqJdef equation
ebound1 equation
;
* Objective functions
eqAdef.. eqA =e= 2*Xsn;
eqBdef.. eqB =e= thermp*(DR**2)*sin(eqA);
eqCdef.. eqC =e= 0.5*pn*SQR(thermp);
eqDdef.. eqD =e= SQRT(pn)*thermp;
eqEdef.. eqE =e= tan(Xsn);
eqFdef.. eqF =e= (isco-1)*BR*Lsn;
eqGdef.. eqG =e= 1+SQRT(pn)-eqD;
eqHdef.. eqH =e= cos(Xsn)*cos(Xsn);
eqJdef.. eqJ =e= sin(Xsn)*sin(Xsn);
ebound1.. abs((((deltat*eqE*(1+SQRT(pn)+pn))/(eqF*(1+SQRT(pn))))-
eqG)/((8*isco*(1+pn)*(1-eqD+eqC))/eqB)) =g=
abs((((thermp*eqF*(DR**2)*eqH)/(4*isco)))*(((deltat*eqE)/(eqF*(1+SQRT(pn))*
(1-eqD+eqC)))-1)-((eqD*Lsn*(DR**2)*eqJ)/(4*isco*BR*(1-eqD+eqC))));

objcoolingload.. z('coolingload') =l=
abs((((deltat*eqE*(1+SQRT(pn)+pn))/(eqF*(1+SQRT(pn))))-
eqG)/((8*isco*(1+pn)*(1-eqD+eqC))/eqB))-
(abs(((((thermp*eqF*(DR**2)*eqH)/(4*isco)))*(((deltat*eqE)/(eqF*(1+SQRT(pn))
)*(1-eqD+eqC)))-1)-((eqD*Lsn*(DR**2)*eqJ)/(4*isco*BR*(1-eqD+eqC))))));
objcop..
z('cop')*abs(((((thermp*eqF*(DR**2)*eqH)/(4*isco)))*(((deltat*eqE)/(eqF*(1+
SQRT(pn))*(1-eqD+eqC)))-1)-((eqD*Lsn*(DR**2)*eqJ)/(4*isco*BR*(1-
eqD+eqC))))) =e= abs((((deltat*eqE*(1+SQRT(pn)+pn))/(eqF*(1+SQRT(pn))))-
eqG)/((8*isco*(1+pn)*(1-eqD+eqC))/eqB))-
(abs(((((thermp*eqF*(DR**2)*eqH)/(4*isco)))*(((deltat*eqE)/(eqF*(1+SQRT(pn))
)*(1-eqD+eqC)))-1)-((eqD*Lsn*(DR**2)*eqJ)/(4*isco*BR*(1-eqD+eqC))))));
objacousticpowerlost..  z('acousticpowerlost') =e=
((thermp*eqF*(DR**2)*eqH)/(4*isco))+ ((eqD*Lsn*(DR**2)*eqJ)/(4*isco*BR*(1-
eqD+eqC)));

z.lo('cop') = 0.01; z.up('cop') = 32.8;
z.lo('coolingload') = 4.3339E-8; z.up('coolingload') = 7.2659E-4;
eqB.lo = 0.000001; eqB.up = 0.001;
eqF.lo = 0.0001; eqF.up = 0.5;

MODEL thermoacoustic /ALL/;
Option Reslim=1000000;

$STitle eps-constraint method
```

```
Set k1(k) the first element of k, km1(k) all but the first elements of k;
k1(k)$(ord(k)=1) = yes; km1(k)=yes; km1(k1) = no;
Set kk(k) active objective function in constraint allobj
Parameter rhs(k) right hand side of the constrained obj functions in eps-
constraint
maxobj(k) maximum value from the payoff table
minobj(k) minimum value from the payoff table
Variables a_objval auxiliary variable for the objective function
obj auxiliary variable during the construction of the payoff table

Positive Variables sl(k) slack or surplus variables for the eps-constraints
Equations
con_obj(k) constrained objective functions
augm_obj augmented objective function to avoid weakly efficient solutions
allobj all the objective functions in one expression;

con_obj(km1).. z(km1) - dir(km1)*sl(km1) =e= rhs(km1);
* The first objective is optimised the others are used as constraints
* The second term is added to avoid weakly efficient points
augm_obj.. sum(k1,dir(k1)*z(k1))+1e-3*sum(km1,sl(km1)/(maxobj(km1)-
minobj(km1))) =e= a_objval;

allobj.. sum(kk, dir(kk)*z(kk)) =e= obj;

Model mod_payoff / thermoacoustic, allobj / ;
Model mod_epsmethod / thermoacoustic, con_obj, augm_obj / ;
option limrow=10, limcol=10;
option solprint=on, solvelink=%solvelink.CallModule%;
option decimals=8;

Parameter payoff(k,k) payoff tables entries;
Alias(k,kp);
* Payoff table is generated by applying lexicographic optimisation
loop(kp, kk(kp)= yes;
repeat solve mod_payoff using dnlp maximising obj;
payoff(kp,kk) = z.l(kk);
z.fx(kk) = z.l(kk);
*// Values of the last objective optimised are freezed
kk(k++1) = kk(k);
*// cycle through the objective functions
until kk(kp); kk(kp) = no;
* Values of the objective functions are released for the new iteration
z.up(k) = inf; z.lo(k) =-inf; );
```

```
if (mod_payoff.modelstat<>%modelstat.Optimal%, abort 'no optimal solution
for mod_payoff');

display payoff;
minobj(k)=smin(kp,payoff(kp,k));
maxobj(k)=smax(kp,payoff(kp,k));

$set fname p.%gams.scrext%
File fx solution points from eps-method / "%gams.scrdir%%fname%" /;

$if not set gridpoints $set gridpoints 5
Set g grid points /g0*g%gridpoints%/
grid(k,g) grid

Parameter
gridrhs(k,g) rhs of eps-constraint at grid point
maxg(k) maximum point in grid for objective
posg(k) grid position of objective
firstOffMax, lastZero some counters
numk(k) ordinal value of k starting with 1
numg(g) ordinal value of g starting with 0;
lastZero=1; loop(km1, numk(km1)=lastZero; lastZero=lastZero+1); numg(g) =
ord(g)-1;

grid(km1,g) = yes;
*// Define the grid intervals for different objectives
maxg(km1) = smax(grid(km1,g), numg(g));
gridrhs(grid(km1,g))$(%min%=dir(km1)) = maxobj(km1) -
numg(g)/maxg(km1)*(maxobj(km1)- minobj(km1));
gridrhs(grid(km1,g))$(%max%=dir(km1)) = minobj(km1) +
numg(g)/maxg(km1)*(maxobj(km1)- minobj(km1));
display gridrhs;

* Walking the grid points and taking shortcuts if the model becomes
infeasible
posg(km1) = 0;
repeat
rhs(km1) = sum(grid(km1,g)$(numg(g)=posg(km1)), gridrhs(km1,g));
solve mod_epsmethod maximising a_objval using dnlp;
if (mod_epsmethod.modelstat<>%modelstat.Optimal%,
*// not optimal is in this case infeasible
lastZero = 0; loop(km1$(posg(km1)>0 and lastZero=0), lastZero=numk(km1));
```

```
posg(km1)$(numk(km1)<=lastZero) = maxg(km1);
*// skip all solves for more demanding values of rhs(km1)
else
loop(k, put fx z.l(k):12:2); put /);

* Proceed forward in the grid
firstOffMax=0;
loop(km1$(posg(km1)<maxg(km1) and firstOffMax=0),posg(km1)=posg(km1)+1;
firstOffMax=numk(km1));
posg(km1)$(numk(km1)<firstOffMax) = 0;
until sum(km1$(posg(km1)=maxg(km1)),1)=card(km1) and firstOffMax=0;
putclose fx;
*// close the point file
```

APPENDIX K: TAR Model B

```
$ Title Thermoacoustic refrigerator
scalars
         isco isentropic coefficient /1.63/
         pn prandtl number /0.67/
         deltat temperature difference /0.030/
         tw wall thickness /0.012/
         DR drive ratio /0.035/
         Lsn /0.5/
         ; scalar starttime;
         starttime=jnow;

Sets
k objective functions / cop, coolingload,acousticpowerlost/;
$ set min -1
$ set max +1

Parameter dir(k) direction of the objective functions / cop %max%,
coolingload %max%,acousticpowerlost %min%/;

positive VARIABLES  BR, thermp, Xsn, eqA, eqB, eqC, eqD, eqE, eqF, eqG,
eqH, eqJ;
BR.lo =0.7; BR.up =0.9;
thermp.lo=0.046;thermp.up=0.092;
Xsn.lo=0.01; Xsn.up=1;

Free VARIABLE
z(k) objective function variables;

Equations

objcop objective for maximising cop
objcoolingload objective for maximising coolingload
objacousticpowerlost objective for minimising acousticpowerlost

eqAdef equation
eqBdef equation
eqCdef equation
eqDdef equation
eqEdef equation
eqFdef equation
eqGdef equation
```

```
eqHdef equation
eqJdef equation
ebound1 equation
;
* Objective functions
eqAdef.. eqA =e= 2*Xsn;
eqBdef.. eqB =e= thermp*(DR**2)*sin(eqA);
eqCdef.. eqC =e= 0.5*pn*SQR(thermp);
eqDdef.. eqD =e= SQRT(pn)*thermp;
eqEdef.. eqE =e= tan(Xsn);
eqFdef.. eqF =e= (isco-1)*BR*Lsn;
eqGdef.. eqG =e= 1+SQRT(pn)-eqD;
eqHdef.. eqH =e= cos(Xsn)*cos(Xsn);
eqJdef.. eqJ =e= sin(Xsn)*sin(Xsn);
ebound1.. abs((((deltat*eqE*(1+SQRT(pn)+pn))/(eqF*(1+SQRT(pn))))-
eqG)/((8*isco*(1+pn)*(1-eqD+eqC))/eqB)) =g=
abs((((thermp*eqF*(DR**2)*eqH)/(4*isco)))*(((deltat*eqE)/(eqF*(1+SQRT(pn))*
(1-eqD+eqC)))-1)-((eqD*Lsn*(DR**2)*eqJ)/(4*isco*BR*(1-eqD+eqC))));

objcop..
z('cop')*abs(((((thermp*eqF*(DR**2)*eqH)/(4*isco)))*(((deltat*eqE)/(eqF*(1+
SQRT(pn))*(1-eqD+eqC)))-1)-((eqD*Lsn*(DR**2)*eqJ)/(4*isco*BR*(1-
eqD+eqC))))) =e= abs((((deltat*eqE*(1+SQRT(pn)+pn))/(eqF*(1+SQRT(pn))))-
eqG)/((8*isco*(1+pn)*(1-eqD+eqC))/eqB))-
(abs(((((thermp*eqF*(DR**2)*eqH)/(4*isco)))*(((deltat*eqE)/(eqF*(1+SQRT(pn)
)*(1-eqD+eqC)))-1)-((eqD*Lsn*(DR**2)*eqJ)/(4*isco*BR*(1-eqD+eqC))))));
objcoolingload.. z('coolingload') =l=
abs((((deltat*eqE*(1+SQRT(pn)+pn))/(eqF*(1+SQRT(pn))))-
eqG)/((8*isco*(1+pn)*(1-eqD+eqC))/eqB))-
(abs(((((thermp*eqF*(DR**2)*eqH)/(4*isco)))*(((deltat*eqE)/(eqF*(1+SQRT(pn)
)*(1-eqD+eqC)))-1)-((eqD*Lsn*(DR**2)*eqJ)/(4*isco*BR*(1-eqD+eqC))))));

objacousticpowerlost..  z('acousticpowerlost') =e=
((thermp*eqF*(DR**2)*eqH)/(4*isco))+ ((eqD*Lsn*(DR**2)*eqJ)/(4*isco*BR*(1-
eqD+eqC)));

z.lo('cop') = 0.01; z.up('cop') = 32.8;
z.lo('coolingload') = 4.3339E-8; z.up('coolingload') = 7.2659E-4;
eqB.lo = 0.000001; eqB.up = 0.001;
eqF.lo = 0.0001; eqF.up = 0.5;

MODEL thermoacoustic /ALL/;
Option Reslim=1000000;
```

```
$STitle eps-constraint method
Set k1(k) the first element of k, km1(k) all but the first elements of k;
k1(k)$(ord(k)=1) = yes; km1(k)=yes; km1(k1) = no;
Set kk(k) active objective function in constraint allobj
Parameter rhs(k) right hand side of the constrained obj functions in eps-
constraint
maxobj(k) maximum value from the payoff table
minobj(k) minimum value from the payoff table
Variables a_objval auxiliary variable for the objective function
obj auxiliary variable during the construction of the payoff table

Positive Variables sl(k) slack or surplus variables for the eps-constraints
Equations
con_obj(k) constrained objective functions
augm_obj augmented objective function to avoid weakly efficient solutions
allobj all the objective functions in one expression;

con_obj(km1).. z(km1) - dir(km1)*sl(km1) =e= rhs(km1);
* The first objective function is optimised and the others are used as
constraints
* The second term is added to avoid weakly efficient points
augm_obj.. sum(k1,dir(k1)*z(k1))+1e-3*sum(km1,sl(km1)/(maxobj(km1)-
minobj(km1))) =e= a_objval;

allobj.. sum(kk, dir(kk)*z(kk)) =e= obj;

Model mod_payoff / thermoacoustic, allobj / ;
Model mod_epsmethod / thermoacoustic, con_obj, augm_obj / ;
option limrow=10, limcol=10;
option solprint=on, solvelink=%solvelink.CallModule%;
option decimals=8;

Parameter payoff(k,k) payoff tables entries;
Alias(k,kp);
* Payoff table is generated by applying lexicographic optimisation
loop(kp, kk(kp)= yes;
repeat solve mod_payoff using dnlp maximising obj;
payoff(kp,kk) = z.l(kk);
z.fx(kk) = z.l(kk);
*// The value of the last objective optimised are freezed
kk(k++1) = kk(k);
*// cycle through the objective functions
```

```
until kk(kp); kk(kp) = no;
* Values of the objective functions are released for the new iteration
z.up(k) = inf; z.lo(k) =-inf; );

if (mod_payoff.modelstat<>%modelstat.Optimal%, abort 'no optimal solution
for mod_payoff');

display payoff;
minobj(k)=smin(kp,payoff(kp,k));
maxobj(k)=smax(kp,payoff(kp,k));

$set fname p.%gams.scrext%
File fx solution points from eps-method / "%gams.scrdir%%fname%" /;

$if not set gridpoints $set gridpoints 5
Set g grid points /g0*g%gridpoints%/
grid(k,g) grid

Parameter
gridrhs(k,g) rhs of eps-constraint at grid point
maxg(k) maximum point in grid for objective
posg(k) grid position of objective
firstOffMax, lastZero some counters
numk(k) ordinal value of k starting with 1
numg(g) ordinal value of g starting with 0;
lastZero=1; loop(km1, numk(km1)=lastZero; lastZero=lastZero+1); numg(g) =
ord(g)-1;

grid(km1,g) = yes;
*// Define the grid intervals for different objectives
maxg(km1) = smax(grid(km1,g), numg(g));
gridrhs(grid(km1,g))$(%min%=dir(km1)) = maxobj(km1) -
numg(g)/maxg(km1)*(maxobj(km1)- minobj(km1));
gridrhs(grid(km1,g))$(%max%=dir(km1)) = minobj(km1) +
numg(g)/maxg(km1)*(maxobj(km1)- minobj(km1));
display gridrhs;

* Walking through the grid points and taking shortcuts if the model becomes
infeasible
posg(km1) = 0;
repeat
rhs(km1) = sum(grid(km1,g)$(numg(g)=posg(km1)), gridrhs(km1,g));
solve mod_epsmethod maximising a_objval using dnlp;
```

```
if (mod_epsmethod.modelstat<>%modelstat.Optimal%,
*// not optimal is in this case infeasible
lastZero = 0; loop(km1$(posg(km1)>0 and lastZero=0), lastZero=numk(km1));
posg(km1)$(numk(km1)<=lastZero) = maxg(km1);
*// skip all solves for more demanding values of rhs(km1)
else
loop(k, put fx z.l(k):12:2); put /);

* Proceed forward in the grid
firstOffMax=0;
loop(km1$(posg(km1)<maxg(km1) and firstOffMax=0),posg(km1)=posg(km1)+1;
firstOffMax=numk(km1));
posg(km1)$(numk(km1)<firstOffMax) = 0;
until sum(km1$(posg(km1)=maxg(km1)),1)=card(km1) and firstOffMax=0;
putclose fx;
*// close the point file
```

APPENDIX L: Temperature difference across stack ends as a result of variation of input power/230 CPSI

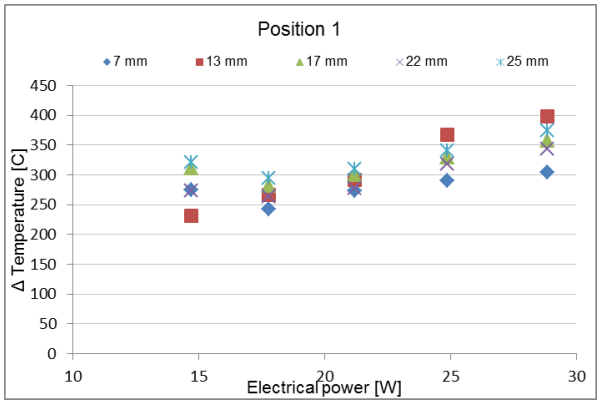

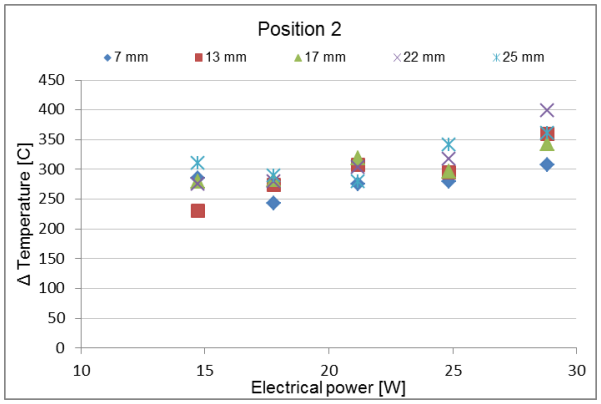

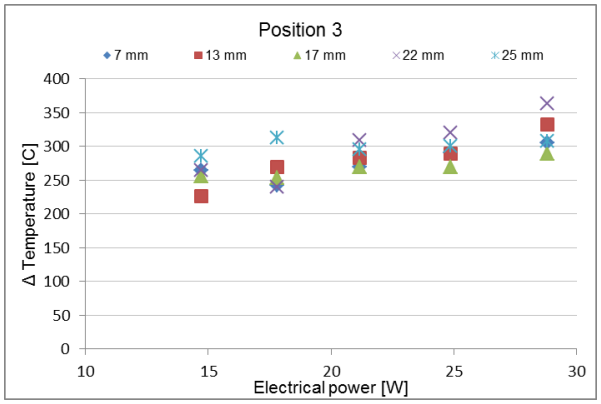

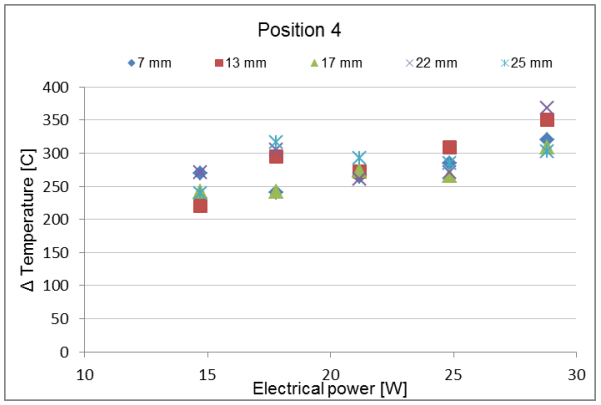

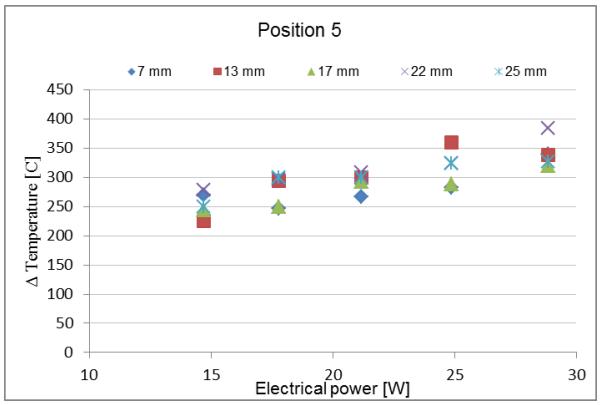

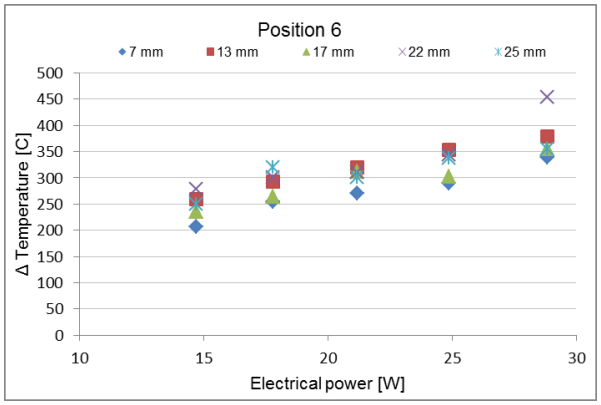

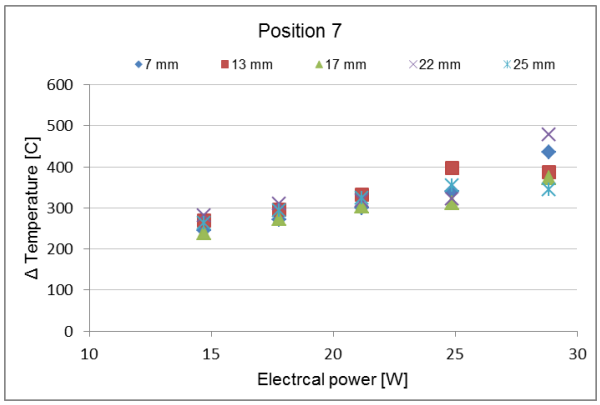

APPENDIX M: Temperature difference across stack ends as a result of variation of input power/100 CPSI

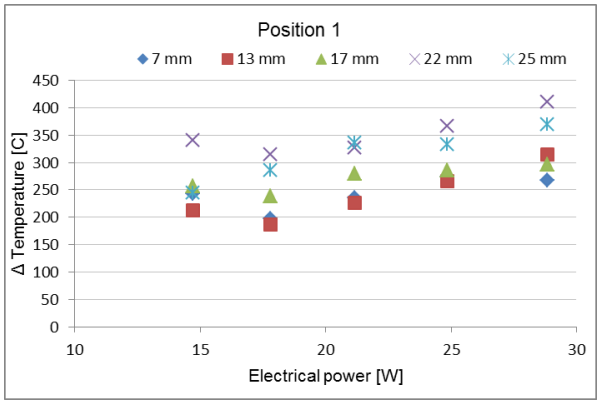

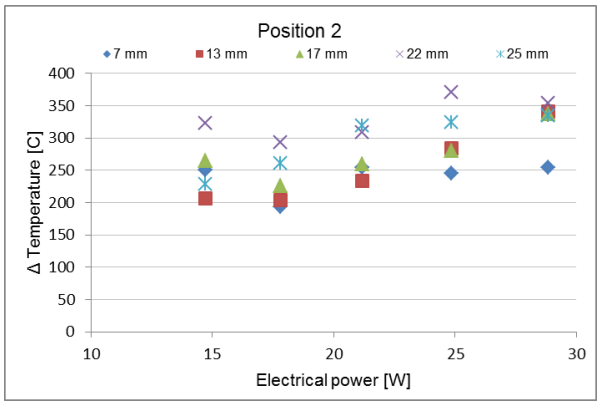

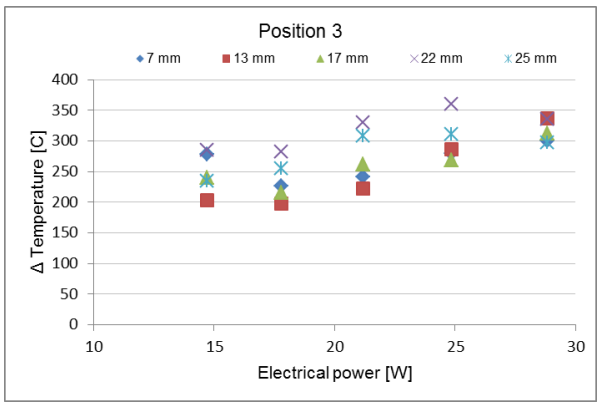

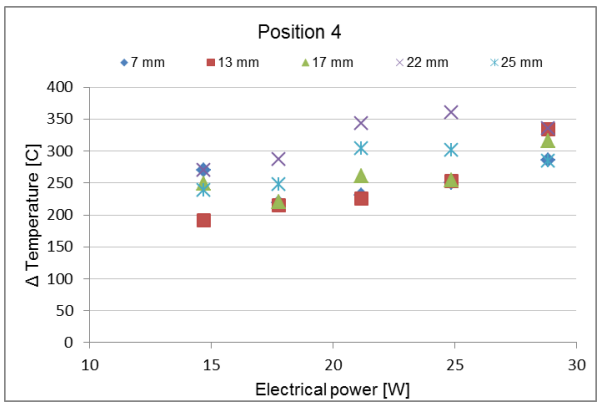

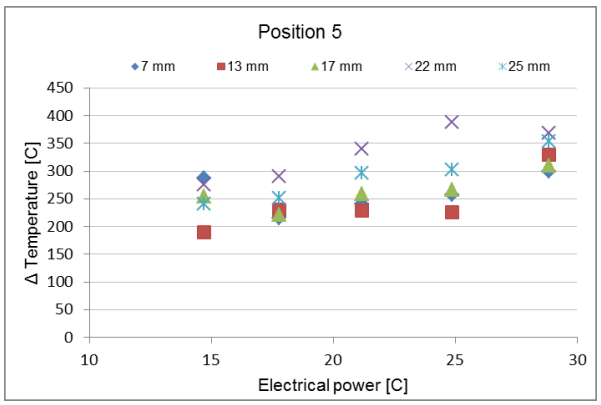

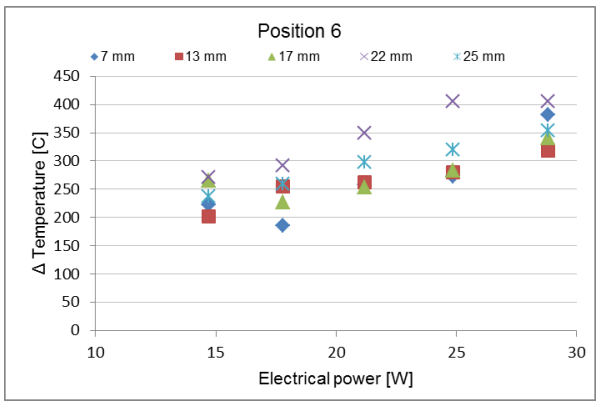

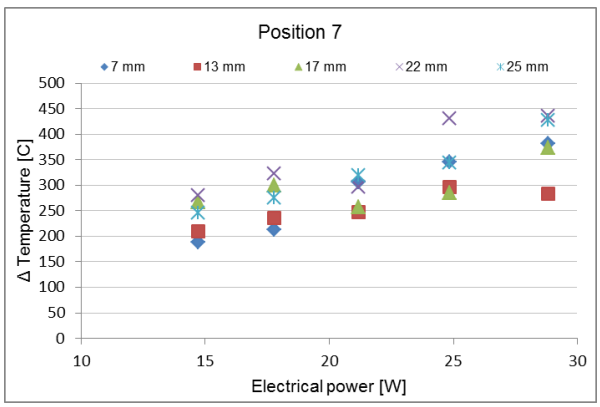

APPENDIX N: Temperature difference across stack ends as a result of variation of input power/64 CPSI

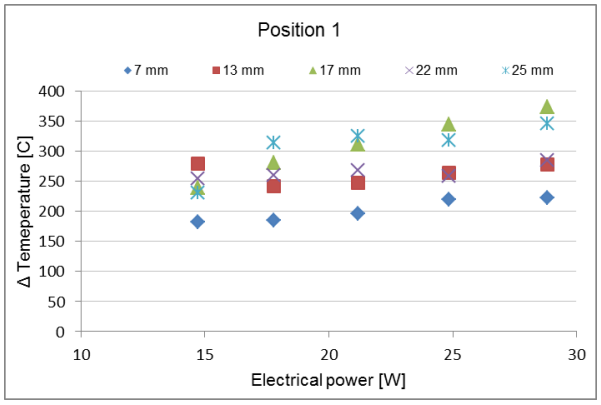

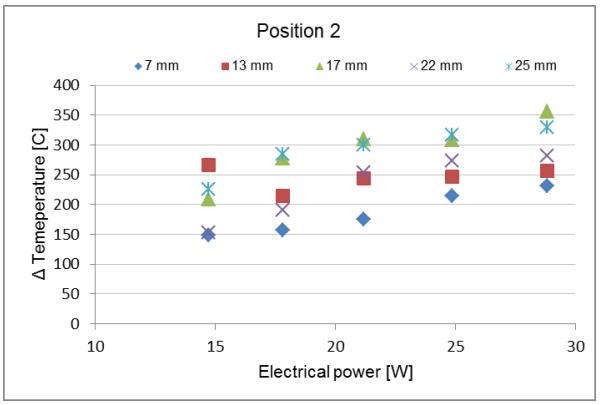

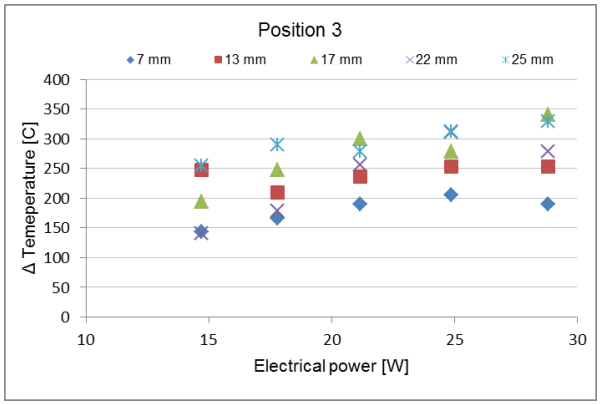

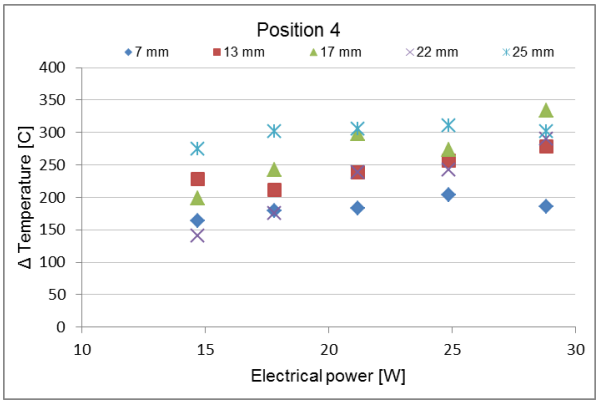

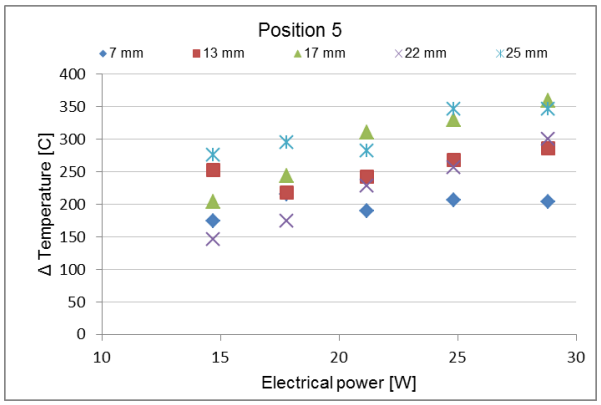

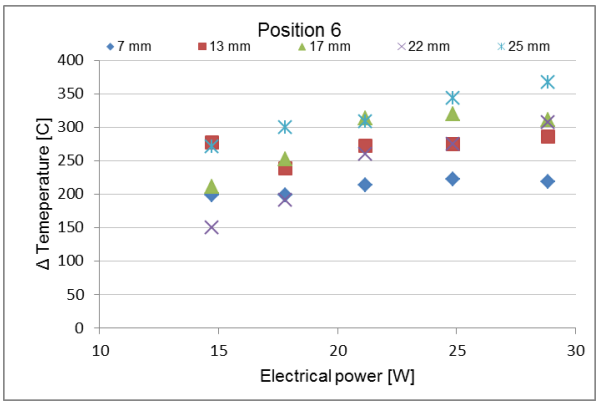

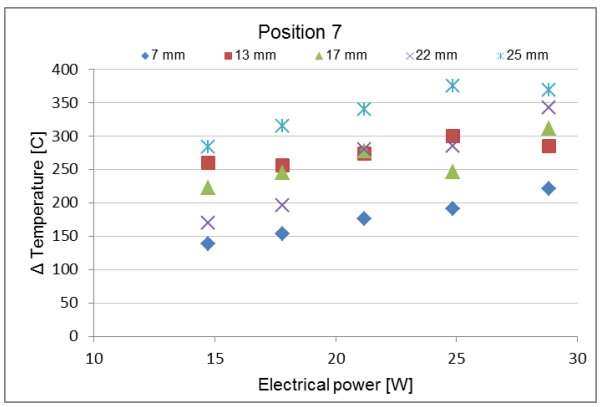

APPENDIX O: SPL as a function of input electrical power, size 2

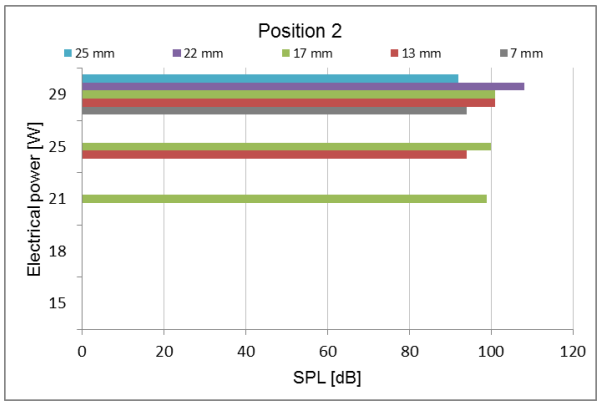

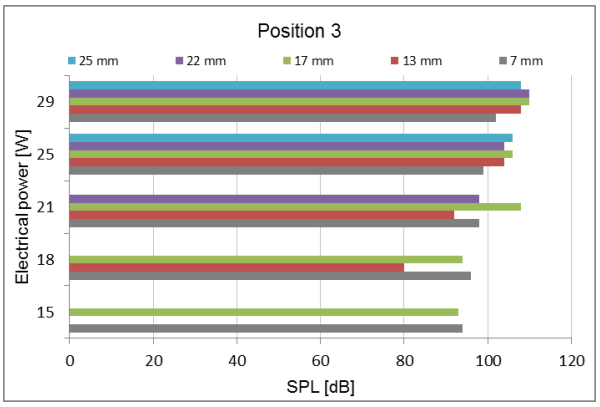

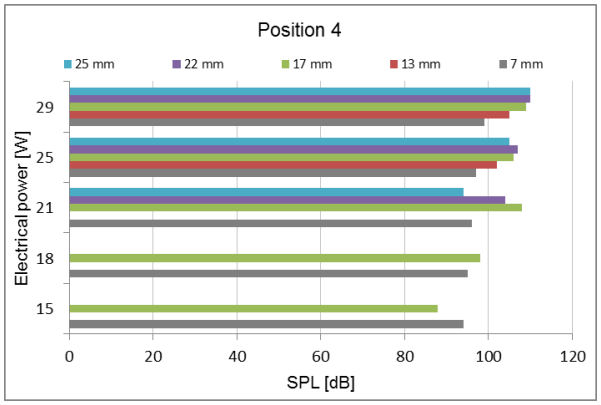

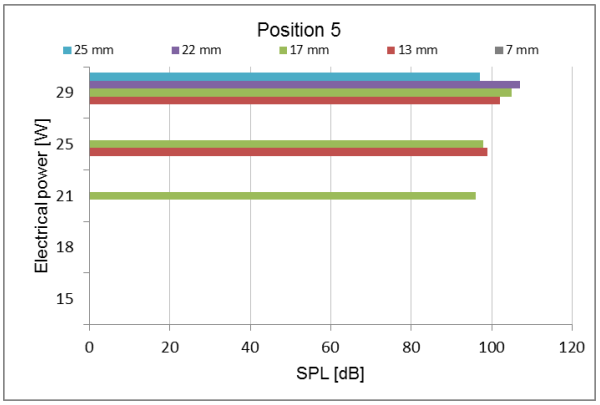

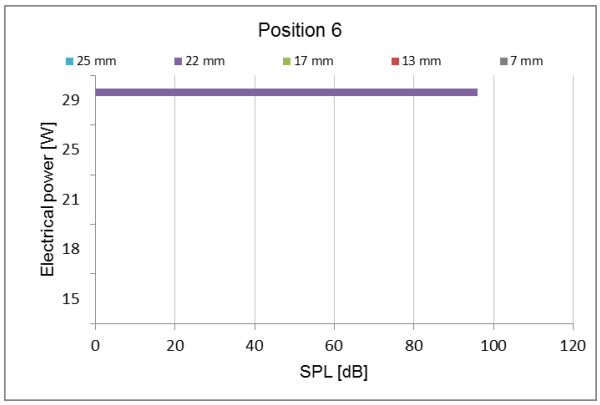

APPENDIX P: SPL as a function of stack position, size 2

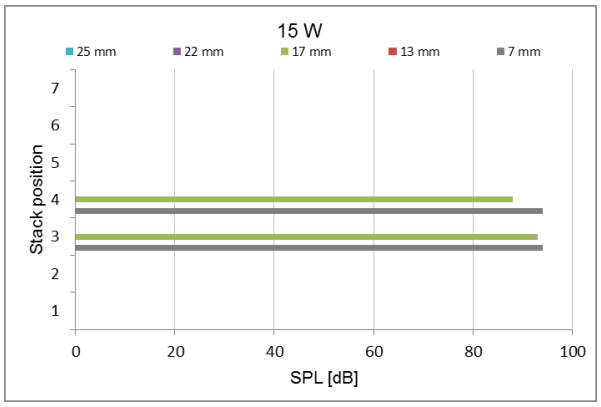

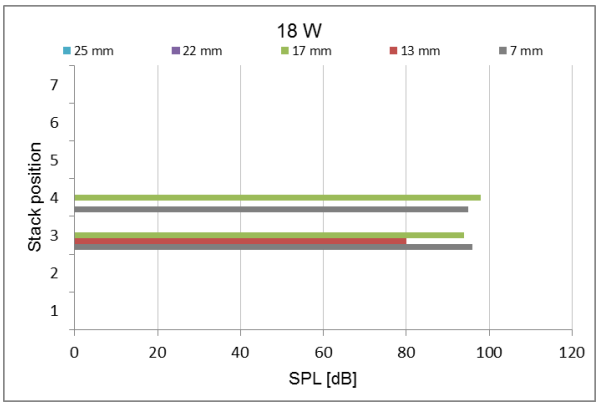

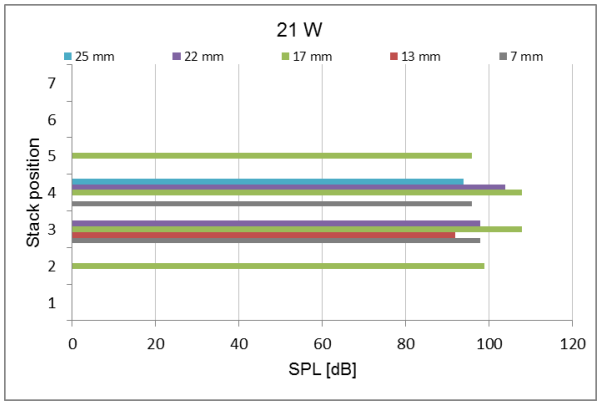

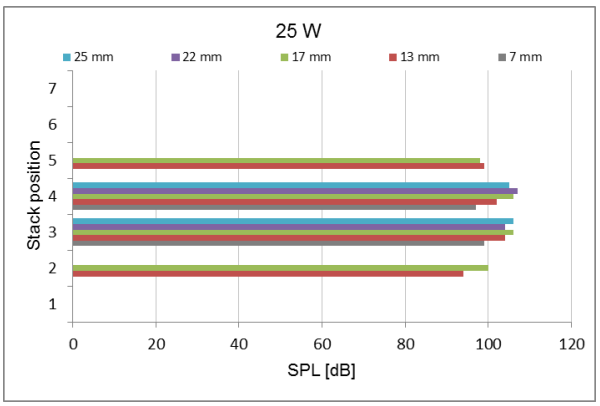

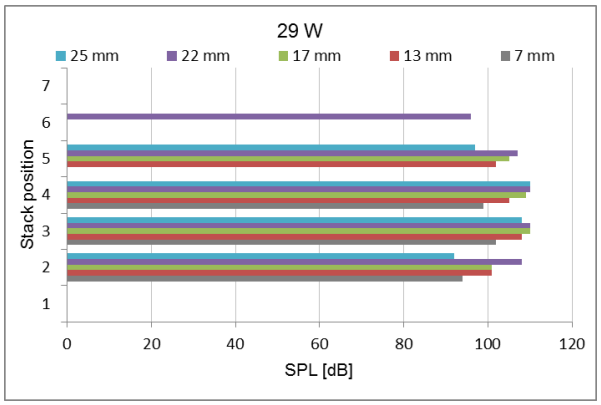

APPENDIX Q: SPL as a function of stack pore sizes, L=13 mm

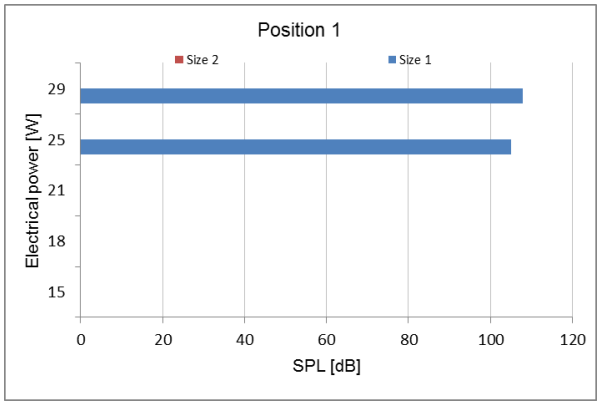

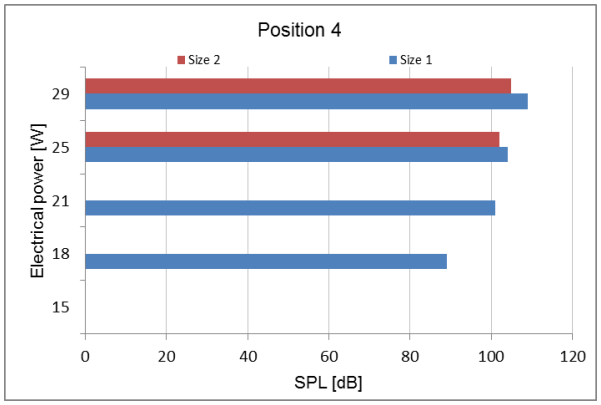

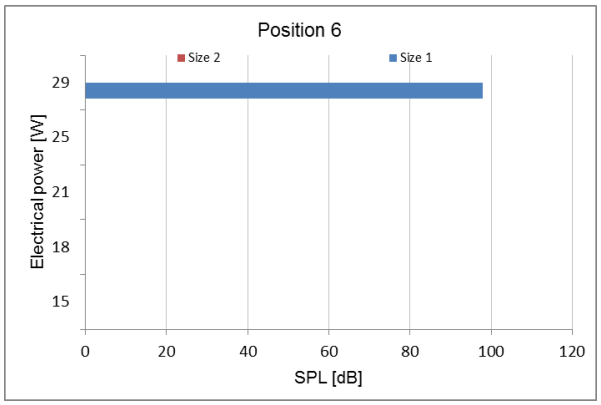

APPENDIX R: SPL as a function of stack pore sizes, L=17 mm

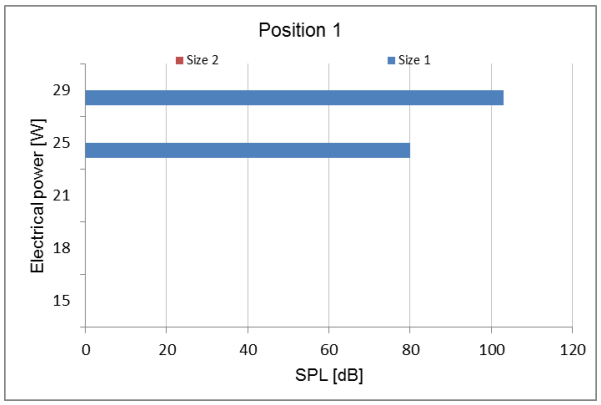

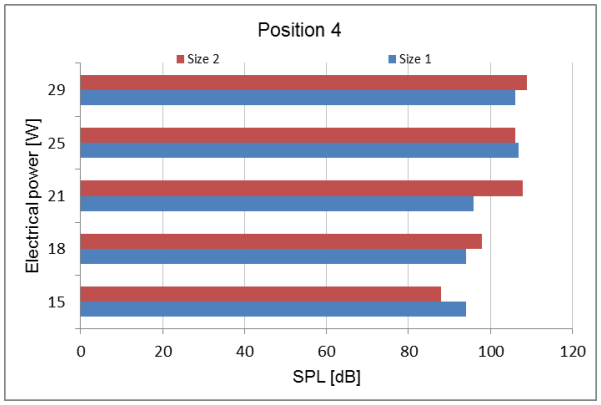

APPENDIX S: SPL as a function of stack pore sizes, L= 22 mm

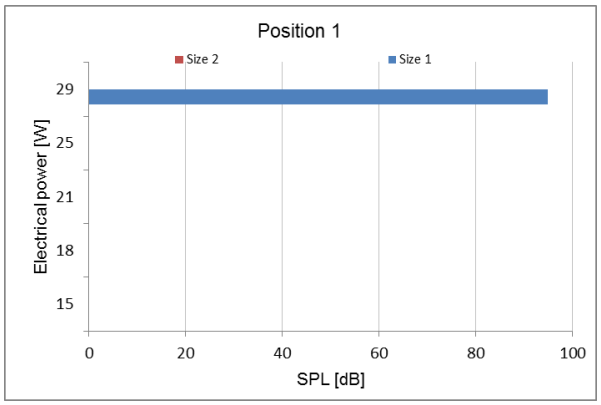

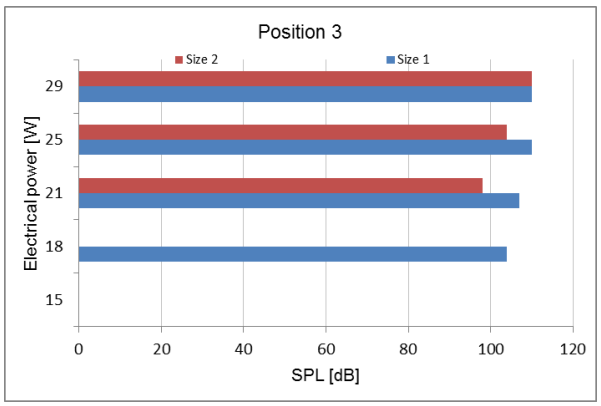

APPENDIX T: SPL as a function of stack pore sizes, L= 25 mm

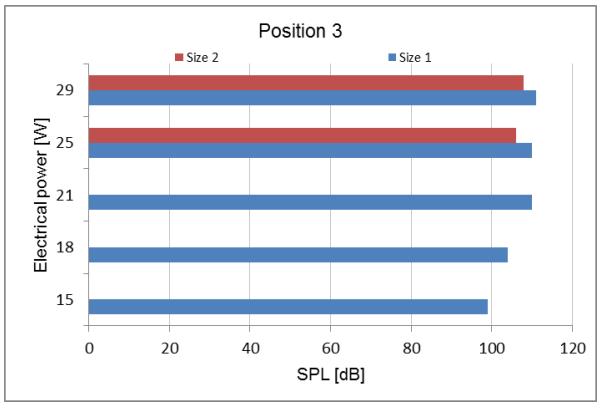

APPENDIX U: Cordierite honeycomb ceramic stack model

```
$ Title Thermoacoustic refrigerator
scalars
         isco isentropic coefficient /1.4/
         pn prandtl number /0.713/
         deltat temperature difference /0.030/
         BR /0.8/
         DR drive ratio /0.025/
         Lsn /0.065/
         ; scalar starttime;
         starttime=jnow;

Sets
k objective functions / cop, coolingload,acousticpowerlost/;
$ set min -1
$ set max +1

Parameter dir(k) direction of the objective functions / cop %max%,
coolingload %max%,acousticpowerlost %min%/;

positive VARIABLES  thermp, Xsn, eqA, eqB, eqC, eqD, eqE, eqF, eqG, eqH,
eqJ;

thermp.lo=0.05;thermp.up=0.1;
Xsn.lo=0.280; Xsn.up=1.612;

Free VARIABLE
z(k) objective function variables;

Equations

objcop objective for maximising cop
objcoolingload objective for maximising coolingload
objacousticpowerlost objective for minimising acousticpowerlost

eqAdef equation
eqBdef equation
eqCdef equation
eqDdef equation
eqEdef equation
eqFdef equation
eqGdef equation
```

```
eqHdef equation
eqJdef equation
ebound1 equation
;
* Objective functions
eqAdef.. eqA =e= 2*Xsn;
eqBdef.. eqB =e= thermp*(DR**2)*sin(eqA);
eqCdef.. eqC =e= 0.5*pn*SQR(thermp);
eqDdef.. eqD =e= SQRT(pn)*thermp;
eqEdef.. eqE =e= tan(Xsn);
eqFdef.. eqF =e= (isco-1)*BR*Lsn;
eqGdef.. eqG =e= 1+SQRT(pn)-eqD;
eqHdef.. eqH =e= cos(Xsn)*cos(Xsn);
eqJdef.. eqJ =e= sin(Xsn)*sin(Xsn);
ebound1.. abs((((deltat*eqE*(1+SQRT(pn)+pn))/(eqF*(1+SQRT(pn))))-
eqG)/((8*isco*(1+pn)*(1-eqD+eqC))/eqB)) =g=
abs((((thermp*eqF*(DR**2)*eqH)/(4*isco)))*(((deltat*eqE)/(eqF*(1+SQRT(pn))*
(1-eqD+eqC)))-1)-((eqD*Lsn*(DR**2)*eqJ)/(4*isco*BR*(1-eqD+eqC))));

objcop..
z('cop')*abs(((((thermp*eqF*(DR**2)*eqH)/(4*isco)))*(((deltat*eqE)/(eqF*(1+
SQRT(pn))*(1-eqD+eqC)))-1)-((eqD*Lsn*(DR**2)*eqJ)/(4*isco*BR*(1-
eqD+eqC))))) =e= abs((((deltat*eqE*(1+SQRT(pn)+pn))/(eqF*(1+SQRT(pn))))-
eqG)/((8*isco*(1+pn)*(1-eqD+eqC))/eqB))-
(abs(((((thermp*eqF*(DR**2)*eqH)/(4*isco)))*(((deltat*eqE)/(eqF*(1+SQRT(pn)
)*(1-eqD+eqC)))-1)-((eqD*Lsn*(DR**2)*eqJ)/(4*isco*BR*(1-eqD+eqC))))));
objcoolingload.. z('coolingload') =e=
abs((((deltat*eqE*(1+SQRT(pn)+pn))/(eqF*(1+SQRT(pn))))-
eqG)/((8*isco*(1+pn)*(1-eqD+eqC))/eqB))-
(abs(((((thermp*eqF*(DR**2)*eqH)/(4*isco)))*(((deltat*eqE)/(eqF*(1+SQRT(pn)
)*(1-eqD+eqC)))-1)-((eqD*Lsn*(DR**2)*eqJ)/(4*isco*BR*(1-eqD+eqC))))));

objacousticpowerlost..  z('acousticpowerlost') =e=
((thermp*eqF*(DR**2)*eqH)/(4*isco))+ ((eqD*Lsn*(DR**2)*eqJ)/(4*isco*BR*(1-
eqD+eqC)));

z.lo('cop') = 0.01; z.up('cop') = 40;
z.lo('coolingload') = 9.9019E-7; z.up('coolingload') = 3.1227E-6;
z.lo('acousticpowerlost')=5.2557E-7;
eqB.lo = 0.000001;
eqF.lo = 0.0001;

MODEL thermoacoustic /ALL/;
```

```
Option Reslim=1000000;

$STitle eps-constraint method
Set k1(k) the first element of k, km1(k) all but the first elements of k;
k1(k)$(ord(k)=1) = yes; km1(k)=yes; km1(k1) = no;
Set kk(k) active objective function in constraint allobj
Parameter rhs(k) right hand side of the constrained obj functions in eps-
constraint
maxobj(k) maximum value from the payoff table
minobj(k) minimum value from the payoff table
Variables a_objval auxiliary variable for the objective function
obj auxiliary variable during the construction of the payoff table

Positive Variables sl(k) slack or surplus variables for the eps-constraints
Equations
con_obj(k) constrained objective functions
augm_obj augmented objective function to avoid weakly efficient solutions
allobj all the objective functions in one expression;

con_obj(km1).. z(km1) - dir(km1)*sl(km1) =e= rhs(km1);
* The first objective function is optimised and the others are used as
constraints
* The second term is used to avoid weakly efficient points
augm_obj.. sum(k1,dir(k1)*z(k1))+1e-3*sum(km1,sl(km1)/(maxobj(km1)-
minobj(km1))) =e= a_objval;

allobj.. sum(kk, dir(kk)*z(kk)) =e= obj;

Model mod_payoff / thermoacoustic, allobj / ;
Model mod_epsmethod / thermoacoustic, con_obj, augm_obj / ;
option limrow=10, limcol=10;
option solprint=on, solvelink=%solvelink.CallModule%;
option decimals=8;

Parameter payoff(k,k) payoff tables entries;
Alias(k,kp);
* Payoff table is generated by applying lexicographic optimisation
loop(kp, kk(kp)= yes;
repeat solve mod_payoff using dnlp maximising obj;
payoff(kp,kk) = z.l(kk);
z.fx(kk) = z.l(kk);
*// Values of the last objective optimised are freezed
kk(k++1) = kk(k);
```

```
*// cycle through the objective functions
until kk(kp); kk(kp) = no;
* Values of the objective functions are released for the new iteration
z.up(k) = inf; z.lo(k) =-inf; );

if (mod_payoff.modelstat<>%modelstat.Optimal%, abort 'no optimal solution
for mod_payoff');

display payoff;
minobj(k)=smin(kp,payoff(kp,k));
maxobj(k)=smax(kp,payoff(kp,k));

$set fname p.%gams.scrext%
File fx solution points from eps-method / "%gams.scrdir%%fname%" /;

$if not set gridpoints $set gridpoints 5
Set g grid points /g0*g%gridpoints%/
grid(k,g) grid

Parameter
gridrhs(k,g) rhs of eps-constraint at grid point
maxg(k) maximum point in grid for objective
posg(k) grid position of objective
firstOffMax, lastZero some counters
numk(k) ordinal value of k starting with 1
numg(g) ordinal value of g starting with 0;
lastZero=1; loop(km1, numk(km1)=lastZero; lastZero=lastZero+1); numg(g) =
ord(g)-1;

grid(km1,g) = yes;
*// Define grid intervals for different objectives
maxg(km1) = smax(grid(km1,g), numg(g));
gridrhs(grid(km1,g))$(%min%=dir(km1)) = maxobj(km1) -
numg(g)/maxg(km1)*(maxobj(km1)- minobj(km1));
gridrhs(grid(km1,g))$(%max%=dir(km1)) = minobj(km1) +
numg(g)/maxg(km1)*(maxobj(km1)- minobj(km1));
display gridrhs;

* Walking the grid points and taking shortcuts if the model becomes
infeasible
posg(km1) = 0;
repeat
rhs(km1) = sum(grid(km1,g)$(numg(g)=posg(km1)), gridrhs(km1,g));
```

```
solve mod_epsmethod maximising a_objval using dnlp;
if (mod_epsmethod.modelstat<>%modelstat.Optimal%,
*// not optimal is in this case infeasible
lastZero = 0; loop(km1$(posg(km1)>0 and lastZero=0), lastZero=numk(km1));
posg(km1)$(numk(km1)<=lastZero) = maxg(km1);
*// skip all solves for more demanding values of rhs(km1)
else
loop(k, put fx z.l(k):12:2); put /);

* Proceed forward in the grid
firstOffMax=0;
loop(km1$(posg(km1)<maxg(km1) and firstOffMax=0),posg(km1)=posg(km1)+1;
firstOffMax=numk(km1));
posg(km1)$(numk(km1)<firstOffMax) = 0;
until sum(km1$(posg(km1)=maxg(km1)),1)=card(km1) and firstOffMax=0;
putclose fx;
*// close the point file
```

APPENDIX V: Cordierite honeycomb ceramic stack models equations

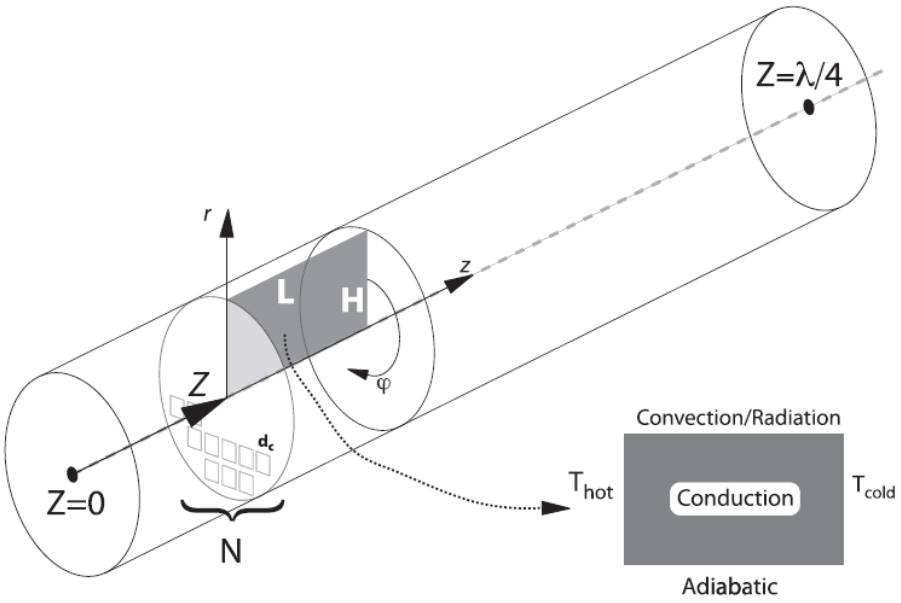

Figure A.1: Computational domain of honeycomb ceramic stack

(Adapted from Trapp et al., 2011)

a. Acoustic power:

$$W = \omega\left[\delta_k \frac{(\gamma-1)p^2}{\rho c^2(1+\varepsilon)}(\Gamma-1) - \delta_V \rho u^2\right] LNd_C \qquad \textbf{Equation A.1}$$

Where

$$\Gamma = \frac{\nabla T_m}{\nabla T_{crit}}$$

$$\nabla T_m = \frac{T_h - T_C}{L} \qquad \textbf{Equation A.2}$$

$$\nabla T_{crit} = \frac{\omega p_1^s}{\rho_m c_p u_1^s}$$

b. Viscous resistance

$$R_V = \frac{4\mu}{\delta_v}\frac{L}{Nd_c^3} \qquad \textbf{Equation A.3}$$

c. Convective heat flux

$$Q_{conv} = 2\pi HLh\left[\frac{T_C - T_H}{\ln\left(\frac{T_C}{T_H}\right)} - T_\infty\right] \qquad \textbf{Equation A.4}$$

where

$$T_S = T_h e^{\ln\left(\frac{T_C}{T_h}\right)\frac{Za}{L}}$$

$$h(Ts) = \frac{k_g}{2H} Nu$$

$$Nu = 0.36 + \frac{0.518 Ra_D^{\frac{1}{4}}}{\left[1 + \left(\frac{0.559}{Pr}\right)^{\frac{9}{16}}\right]^{\frac{4}{9}}}$$ **Equation A.5**

$$Pr = \frac{\nu}{\alpha}$$

$$Ra = \frac{g\beta(T_S - T_\infty)8H^3}{\nu\alpha}$$

d. Radiative heat flux

$$Q_{rad} = 2\pi H L k_B \varepsilon \left[\frac{T_C^4 - T_H^4}{4\ln\left(\frac{T_C}{T_H}\right)} - T_\infty^4\right]$$ **Equation A.6**

e. Conductive heat flux

$$Q_{cond} = \frac{k_{zz}}{L}\pi H^2 T_C \ln\left(\frac{T_H}{T_C}\right)$$ **Equation A.7**

Where

$$k_{zz} = \frac{k_S t_w + k_g d}{t_w + d}$$ **Equation A.8**